

## Tailored Aluminium based Coatings for Optical Appearance and Corrosion Resistance

**Aggerbeck, Martin; Ambat, Rajan**

*Publication date:*  
2014

*Document Version*  
Publisher's PDF, also known as Version of record

[Link back to DTU Orbit](#)

*Citation (APA):*  
Aggerbeck, M., & Ambat, R. (2014). Tailored Aluminium based Coatings for Optical Appearance and Corrosion Resistance. DTU Mechanical Engineering.

### DTU Library

Technical Information Center of Denmark

---

#### General rights

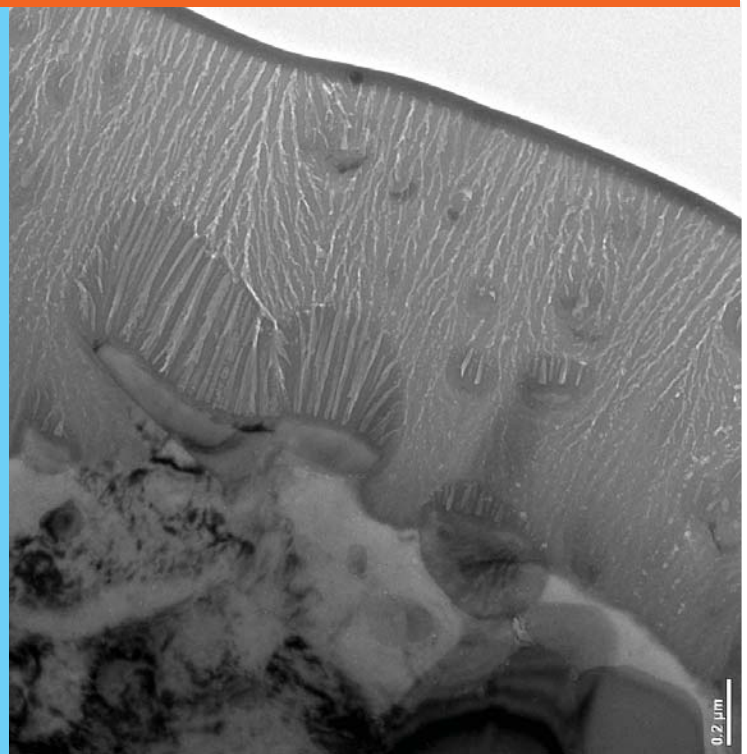
Copyright and moral rights for the publications made accessible in the public portal are retained by the authors and/or other copyright owners and it is a condition of accessing publications that users recognise and abide by the legal requirements associated with these rights.

- Users may download and print one copy of any publication from the public portal for the purpose of private study or research.
- You may not further distribute the material or use it for any profit-making activity or commercial gain
- You may freely distribute the URL identifying the publication in the public portal

If you believe that this document breaches copyright please contact us providing details, and we will remove access to the work immediately and investigate your claim.

# Tailored Aluminium based Coatings for Optical Appearance and Corrosion Resistance

## PhD Thesis



Martin Aggerbeck  
January 2014



# **Tailored Aluminium based Coatings for Optical Appearance and Corrosion Resistance**

Ph.D. thesis by

*Martin Aggerbeck*

2014

Supervisor:

*Rajan Ambat*





---

## Preface

---

The present thesis is submitted in candidacy for a Ph.D. degree at the Technical University of Denmark. The work presented was carried out under supervision by Professor Dr. Rajan Ambat during the period October 2010 – January 2014 at the Department of Mechanical Engineering in the Section for Materials and Surface Engineering.

The study was conducted as a part of the IdeAl Surfaces innovation consortium, which was funded by The Danish Agency for Science, Technology and Innovation.

---

Martin Aggerbeck, Kongens Lyngby, 8<sup>th</sup> of January 2014



---

## Acknowledgements

---

First of all, I would like to thank my supervisor, Professor Dr. Rajan Ambat, for his time, helpfulness, and support. I am impressed by his academic knowledge and ability to set up “the story” of completed studies in a good and understandable way.

The study has been done as a part of the IdeAl surfaces innovation consortium, from which I would like to thank all involved partners: Bang & Olufsen (B&O) [DK], Balliu [BE], Bremer Institut für angewandte Strahltechnik (BIAS) [GER], Danish Technological Institute (DTI) [DK], Polyteknik [DK], Sapa [DK and SE], Terma [DK], Turbocoating [IT], Vlaamse Instelling voor Technologisch Onderzoek (VITO) [BE], and Department of Photonics Engineering at DTU (DTU Fotonik) [DK], and to the Danish Agency for Science, Technology and Innovation for their financial support of the IdeAl project.

A special personal thanks to: Kristian Rechendorff from DTI for creating PVD coatings and for many good discussions and talks, and to Lars Pleth Nielsen, Bjarke Christensen, Klaus Almtoft, and colleagues for always being ready to discuss all sides of the project and for making me feel welcome at DTI. I would like to thank Flemming Jensen, Ib Kongstad, and Jørgen Dam from B&O supplying specimens when needed and always being helpful on polishing and anodisation. Jan-Olov Nilsson and Kirsten Burfelt from Sapa are thanked for discussions and answers, especially regarding the nickel salt sealing method. For laser surface cladding, I would like to thank Marleen Rombouts and Jo Verwimp from VITO as well as Knut Partes and Dias Da Silva from BIAS. Also thanks to Filip Motmans for his help during Marleen’s maternity leave. Thanks to Anne Juhl for trying to involve Terma and for showing interest in my work, and to Jørgen Schou and Stela Canulescu from DTU Fotonik for helping me with optical measurements and for discussions on the optical parts of the project. Additional thanks to Jørgen Schou and to P. S. Ramanujam for creating a special course on Solid state optics, which I truly enjoyed.

I thank Kai Dirscherl at Danish Fundamental Metrology (DFM) [DK] for always being ready to help with AFM and SKPFM measurements, for this I am very grateful. Thanks to all fellow PhD students at DTU MEK creating a nice atmosphere during the last three years, and a special thanks to Visweswara Gudla and Villads Johansen with whom I have happily been working together with. For inspiration and encouragement I would like to thank professors Marcel Somers and Per Møller. For help and support with practical work and bureaucracy, Lars Pedersen, John Troelsen, Peter Westermann, Steffen Munch, Marianne Buendia, Rolf Jensen, Grethe Saugmann, Flemming Grumsen, Flemming Jørgensen, Ewa Adamsen, Laila Leth, and Helle Bruun Brandt from DTU MEK, Christian Ravn from IPU, Jeppe Revall Frisvad from DTU Department of Applied Mathematics and Computer Science, Berit Wenzell from DTU Center for Electron Nanoscopy (DTU CEN) [DK], and Sara Engberg and Dennis Corell from DTU Fotonik are all acknowledged. Thanks to Cathrine Larsen, David Hansen, Jacob Chortsen, Alexis Herbreteau, Sigurður Stefánsson, Andreas Junker-Holst, and Daniel Nielsen who have been working on parts of my project as students.

Last but not least, many thanks to my father and the rest of my family, Søren Bredmose Simonsen, and the rest of my friends for helping me through the toughest times of the project.

---

## Abstract

---

The current project investigated the possibility of designing aluminium based coatings focusing on the effect of composition, microstructure, and surface finish on the optical appearance and on the alkaline corrosion properties using titanium as the main alloying element. The main results and discussions of this work are presented in manuscript form as four appended papers communicated for journal publication.

Aluminium is widely used in applications such as transportation, building, heat exchangers, packaging, and design products. Optical appearance after anodisation is a key aspect for many of these applications, but the use of recycled aluminium compromises this due to the presence of increased levels of impurity and alloying elements. Knowledge on how different alloying elements affect the optical appearance might therefore increase the applicability of recycled aluminium.

It was investigated how the optical appearance is affected by the alloy composition, surface morphology, and the microstructure. Four commercial aluminium alloys were studied before and after polishing, etching, anodisation, and hot water sealing, giving an overview on how the alloy composition affects the appearance. It was found that the roughness after etching increases with higher amounts of alloying elements (especially iron and silicon). Proper polishing requires some alloy hardness, while alloy purity is required for a glossy appearance after anodisation.

Magnetron sputtered aluminium based coatings containing up to 18 wt. % titanium were deposited, heat-treated, and anodised. The microstructure of the as-deposited coatings was layered, and  $\text{Al}_3\text{Ti}$  phases formed during the heat treatment. During anodisation, the heat-treated specimens containing  $\text{Al}_3\text{Ti}$  phases turned dark, and the specimens were investigated as a model system on the optical effect of partially oxidised intermetallics and the subsurface morphology after anodisation. It was suggested, that the darkening of the anodised specimens happened due to roughness of the oxide-substrate interface causing light trapping and optical scattering and absorption by the partially anodised intermetallics in the anodised layer.

The transport industry has a big share of the  $\text{CO}_2$  emission in the world, which can be decreased by reducing the weight of the vehicles itself. More than half of the weight of a car comes from steel, which can almost be reduced to half by replacing steel with aluminium. Unfortunately, aluminium corrodes heavily in the alkaline environments known e.g. from a brush less car wash ( $> \text{pH } 12$ ). Today nickel salt sealing is used to protect e.g. aluminium wheel rims, but an alternative is needed due to environmental and health reasons.

Investigations using the previously described magnetron sputtered Al-Ti coatings showed that 13 wt. % titanium and more improved the corrosion resistance at  $\text{pH } 13.5$  and this was further improved by heat

treatment, especially at 400 °C and more. The improved corrosion properties were ascribed to structural relaxation, decreased galvanic potential differences in the microstructure, and protection from the network of the  $\text{Al}_3\text{Ti}$  phases precipitated during the heat treatment.

Laser surface cladding of aluminium containing up to 20 wt. % Ti6Al4V were studied focusing on the microstructure and the alkaline corrosion properties. Due to precipitation of large  $\text{Al}_3\text{Ti}$  phases during the cladding process, the microstructure consisted of an almost pure aluminium matrix, which corroded preferentially when exposed to pH 13.5. Additional heat treatment did not break down the solidified microstructure and the corrosion properties were not improved.

---

## Resume

---

I dette projekt blev muligheden for at designe aluminiumsbaserede coatings undersøgt med fokus på hvordan den kemiske sammensætning og overfladens beskaffenhed påvirker den visuelle fremtoning og de basiske korrosionsegenskaber med titan anvendt som det primære legeringselement. De primære resultater og diskussioner fra dette arbejde præsenteres i form af i bilag som fire artikelmanuskripter indsendt til publikation i tidsskrifter.

Anvendelsen af aluminium er bred, fra transportmidler, bygninger, varmevekslere og emballage til designprodukter. Den visuelle fremtoning efter anodisering er en vigtig karakter i mange af disse anvendelser, men brugen af genbrugsaluminium kompromitterer denne pga. tilstedeværelsen af store mængder urenheder og legeringselementer. Viden om hvordan forskellige legeringselementer påvirker den visuelle fremtoning kan derfor øge anvendeligheden af genbrugsaluminium.

Det blev undersøgt, hvorledes den visuelle fremtoning påvirkes af legeringssammensætning, overflademorfologi og mikrostruktur. Fire handelslegeringer blev undersøgt før og efter polering, bejdsning, anodisering og forsegling med varmt vand, hvilket gav et overblik over, hvordan legeringssammensætning påvirker den visuelle fremtoning. Ruheden af overfladen efter bejdsning blev større ved øget mængde af legeringselementer (især jern og silicium). Behørig polering kræver nogen mængde af legeringshårdhed, mens legeringsrenhed kræves for at opnå en spejlende fremtoning efter anodisering.

Fysisk pådampede Al-Ti coatings med op til 18 vægt-% titan blev deponeret, varmebehandlet og anodiseret. Mikrostrukturen efter pådampning var lagdelt og  $\text{Al}_3\text{Ti}$ -faser blev dannet i løbet af varmebehandlingen. De varmebehandlede emner indeholdende  $\text{Al}_3\text{Ti}$ -faser blev mørke under anodisering, og emnerne blev undersøgt som et modelsystem for hvordan den visuelle fremtoning påvirkes af delvist oxiderede partikler og morfologien mellem det anodiserede lag og metallet efter anodisering. Det blev foreslået at emnerne blev mørke pga. indfangning af lyset i det anodiserede lag pga. den ru grænseflade mellem det anodiserede lag og substratet og pga. absorption og optisk spredning i de delvist oxiderede partikler i det anodiserede lag.

Transportindustrien står for en stor andel af verdens  $\text{CO}_2$ -udledning, hvilket kan mindskes ved at reducere vægten af transportmidlerne. Mere end halvdelen af en bils vægt kommer fra stål, hvilket næsten kan halveres ved at udskifte stålet med aluminium. Desværre korroderer aluminium kraftigt under de basiske forhold der f.eks. kendes fra en børsteløs bilvask ( $> \text{pH } 12$ ). I dag anvendes forsegling med nikkelsalte for at beskytte f.eks. aluminiumsfølge, men af miljø- og sundhedsmæssige årsager søges et alternativ.



Undersøgelser af de tidligere beskrevne fysisk pådampede Al-Ti coatings viste at 13 vægt-% titan og mere forbedrede modstandsdygtigheden ved pH 13.5 og denne var yderligere forbedret under varmebehandling, særligt ved 400 °C og over. De forbedrede korrosionsegenskaber blev tilskrevet strukturel afspænding, sænkede galvaniske potentialeforskelle i mikrostrukturen og beskyttelse fra netværket af  $\text{Al}_3\text{Ti}$ -faserne, der blev udfældet i løbet af varmebehandlingen.

Coatings med laser af aluminium indeholdende op til 20 vægt-% Ti6Al4V blev undersøgt med fokus på mikrostrukturen og de basiske korrosionsegenskaber. Pga. udfældning af store faser af  $\text{Al}_3\text{Ti}$  under processen bestod mikrostrukturen af et næsten rent aluminiumsmatrix, der korroderede selektivt ved pH 13.5. Varmebehandling brød ikke den størknede mikrostruktur ned og korrosionsegenskaberne blev ikke forbedret ved dette.

---

## List of abbreviations

---

AAxxxx	Aluminium Alloy, where xxxx is the alloy denomination according to the EN 573 and EN 1780 standards.
AFM	Atomic Force Microscopy
BRDF	Bidirectional Reflectance Distribution Function
B&O	Bang & Olufsen [DK]
CIE	Commission Internationale de l'Eclairage (International Commission on Illumination)
DFM	Danish Fundamental Metrology [DK]
DTI	Danish Technological Institute [DK]
DTU	Technical University of Denmark [DK]
- Cen	Center for Electron Nanoscopy
- Fotonik	Department of Photonics Engineering
- MEK	Department of Mechanical Engineering
EDS	Energy-Dispersive X-ray Spectroscopy (also abbreviated EDX)
FCC	Face-Centred Cubic
FCT	Face-Centred Tetragonal
FIB	Focused Ion Beam
GDOES	Glow Discharge Optical Emission Spectroscopy
HCP	Hexagonal Close-Packed
LIBS	Laser-Induced Breakdown Spectroscopy
LOM	Light Optical Microscopy
LSA	Laser Surface Alloying
LSC	Laser Surface Cladding
LSM	Laser Surface Melting
OCP	Open Circuit Potential
PVD	Physical Vapour Deposition
SEM	Scanning Electron Microscopy
SKPFM	Scanning Kelvin Probe Force Microscopy

TEM	Transmission Electron Microscopy
UTS	Ultimate Tensile Strength
UV	Ultra Violet
VITO	Vlaamse Instelling voor Technologisch Onderzoek [BE]
XRD	X-Ray Diffraction

---

## List of publications and dissemination at conferences

---

### Appended papers

1.

M. Aggerbeck, S. Canulescu, K. Dirscherl, V. Johansen, S. Engberg, J. Schou, R. Ambat  
*Appearance of anodised aluminium: Effect of alloy composition and prior surface finish*  
Surface and Coatings Technology 254, 28-41, 2014

2.

M. Aggerbeck, A. Junker-Holst, D. Nielsen, V. Gudla, R. Ambat  
*Anodisation of sputter deposited aluminium-titanium coatings: Effect of microstructure on optical characteristics*  
Surface and Coatings Technology 254, 138-144, 2014

3.

M. Aggerbeck, K. Rechendorff, K. Dirscherl, R. Ambat  
*Saline and alkaline corrosion resistance of aluminium-titanium coatings prepared by plasma magnetron sputtering*

4.

M. Aggerbeck, A. Herbreteau, M. Rombouts, J. Verwimp, R. Ambat  
*Alkaline corrosion properties of laser clad aluminium-titanium coatings*  
Anti-Corrosion Methods and Materials, 62/1, 37-47, 2015

### Proceeding articles

M. Aggerbeck, S. Canulescu, J. Schou and R. Ambat

*Optical appearance and corrosion properties of aluminium based plasma coatings*

Proc. of Eurocorr, Stockholm, Sweden, September 2011, p. 2305.

M. Aggerbeck, K. Rechendorff, R. Ambat

*Aluminium based coatings containing titanium for alkaline protection*

Proc. of Aluminium Surface Science and Technology (ASST), Sorrento, Italy, May 2012, p. no. 5

### Posters

M. Aggerbeck, R. Ambat

*Relation between alloy composition, surface finishing and optical properties when anodising aluminium*

Danish Electrochemical Society annual meeting, DTU, Kgs. Lyngby, Denmark, 2010

M. Aggerbeck, S. Canulescu, D. D. Corell, J. Schou, C. Dam-Hansen, R. Ambat

*Optical reflectance of anodised aluminium*

Danish Optical Society annual meeting, 2010

M. Aggerbeck, K. Rechendorff, R. Ambat

*Aluminium coatings on any substrate, with nice appearance and enhanced alkaline protection*

20th annual international anodizing conference and exposition, Aluminium Anodizers Council, Tempe, Arizona, October, 2011

---

## Table of contents

---

<b>1</b>	<b>INTRODUCTION .....</b>	<b>1</b>
1.1	ALUMINIUM IN DESIGN PRODUCTS.....	1
1.2	ALUMINIUM IN THE AUTOMOTIVE INDUSTRY .....	2
1.3	OBJECTIVE OF THE PRESENT STUDY .....	3
1.4	AL-Ti COATINGS.....	4
1.5	OVERALL STRUCTURE OF THE THESIS.....	6
<b>2</b>	<b>ALUMINIUM.....</b>	<b>9</b>
2.1	ALUMINIUM ALLOYS .....	9
2.2	SURFACE TREATMENTS OF ALUMINIUM .....	12
2.3	RECYCLING OF ALUMINIUM ALLOYS .....	19
2.4	OPTICAL APPEARANCE OF ALUMINIUM AND ITS ALLOYS .....	21
2.5	CORROSION PROPERTIES OF ALUMINIUM AND ITS ALLOYS .....	30
<b>3</b>	<b>CREATING ALUMINIUM-TITANIUM COATINGS .....</b>	<b>35</b>
3.1	CORROSION PROPERTIES OF TITANIUM.....	35
3.2	THE AL-Ti SYSTEM.....	37
3.3	PHYSICAL VAPOUR DEPOSITION .....	37
3.4	LASER SURFACE PROCESSES.....	42
<b>4</b>	<b>MATERIALS AND METHODS.....</b>	<b>47</b>
4.1	MATERIALS .....	47
4.2	MICROSTRUCTURAL INVESTIGATIONS .....	51
4.3	OPTICAL INVESTIGATIONS.....	54
4.4	CORROSION EXPERIMENTS .....	58
<b>5</b>	<b>SUMMARY OF PAPERS .....</b>	<b>61</b>
5.1	APPEARANCE OF ANODISED ALUMINIUM: EFFECT OF ALLOY COMPOSITION AND PRIOR SURFACE FINISH (ARTICLE 1) .....	61
5.2	AL-Ti COATINGS PRODUCED BY MAGNETRON SPUTTERING (ARTICLES 2 AND 3) .....	62
5.3	ALKALINE CORROSION PROPERTIES OF LASER CLADDED ALUMINIUM-TITANIUM COATINGS (ARTICLE 4).....	65
<b>6</b>	<b>PAPERS.....</b>	<b>67</b>
<b>7</b>	<b>OVERALL DISCUSSION .....</b>	<b>119</b>
7.1	APPEARANCE OF ANODISED ALUMINIUM .....	119
7.2	MICROSTRUCTURE OF THE PRODUCED ALUMINIUM-TITANIUM COATINGS .....	120
7.3	ALKALINE CORROSION PROPERTIES OF ALUMINIUM-TITANIUM COATINGS.....	121

<b>8</b>	<b>CONCLUSIONS .....</b>	<b>125</b>
8.1	APPEARANCE OF COMMERCIAL ALLOYS .....	125
8.2	MICROSTRUCTURE OF MAGNETRON SPUTTERED ALUMINIUM-TITANIUM COATINGS .....	125
8.3	OPTICAL PROPERTIES OF MAGNETRON SPUTTERED ALUMINIUM-TITANIUM COATINGS.....	126
8.4	CORROSION PROPERTIES OF ALUMINIUM-TITANIUM COATINGS .....	126
<b>9</b>	<b>OUTLOOK .....</b>	<b>129</b>
9.1	APPEARANCE OF ANODISED ALUMINIUM ALLOYS.....	129
9.2	ALKALINE CORROSION PROPERTIES OF ALUMINIUM BASED COATINGS .....	130
<b>10</b>	<b>REFERENCES .....</b>	<b>133</b>

---

# 1 Introduction

---

Aluminium is widely used in applications such as transportation, buildings, heat exchangers, packaging, and design products. This emphasise that the use of aluminium is very versatile, since it can be made into many different semi products and many different production methods can be applied. During the primary production, the aluminium melt is purified; removing impurities such as iron and silicon, and subsequently alloying elements are added to the melt. This is done to achieve the desired properties of the final alloy.

The amount of recycled aluminium is constantly increasing, since the melting process only requires 5 % of the original extraction process [1]. However, the recycling process makes it hard to control the amount of impurities and alloying elements in the final melt and final products. Therefore, increased use of recycled alloys has significant influence on various properties including optical appearance and corrosion properties.

Measured by weight, steel is the most used material in the car industry, where the average car in USA consisted of 1100 kg steel in 2007 [2]. Various types of steels are used in the car industry [3], and with focus on weight reduction and passenger safety, the use of the stronger transformation induced plasticity (TRIP) steels [4] and other light steel structures have been in focus. Aluminium alloys are light and have the same strength-to-weight ratio as that of steel. Therefore, replacing steel with aluminium in a construction can half the weight [1]. This is particularly relevant in the transport industry, where a big part of the fuel consumption is due to transportation of the vehicle itself.

The foci of this study are the visual appearance of anodised aluminium products as a function of alloy composition and surface finish, and using aluminium based model alloy coatings containing titanium to understand the effect of microstructure on the optical appearance and for alkaline corrosion properties for the automotive industry.

## 1.1 Aluminium in design products

The visual appearance of aluminium alloys both bare and after anodisation is an important property for design products such as the ones presented in Fig. 1.1. Repeatability of the optical appearance is extremely important, however, recycled aluminium alloys have resulted in unpredictable surface appearance due to microstructural heterogeneity consisting of intermetallic particles of impurity elements. Controlling colour tinges is therefore important e.g. by alloying additions and microstructural manipulation, based on an optimised method for creating surfaces with predictable appearance. A number of studies have investigated the effect of intermetallics on the optical appearance of anodised specimens, however, these are mostly limited to morphological differences of the interface between the anodised layer and the substrate and the incorporation of various intermetallics in the anodised layer. The exact effect of various steps in the creation process of the anodised layer in terms of optical appearance has been in less focus. Therefore, a deeper understanding of the influence from various factors on the optical appearance is essential for the efficient use



of recycled aluminium alloys in design and structural products, and for designing new easily recyclable alloys and aluminium based coatings.

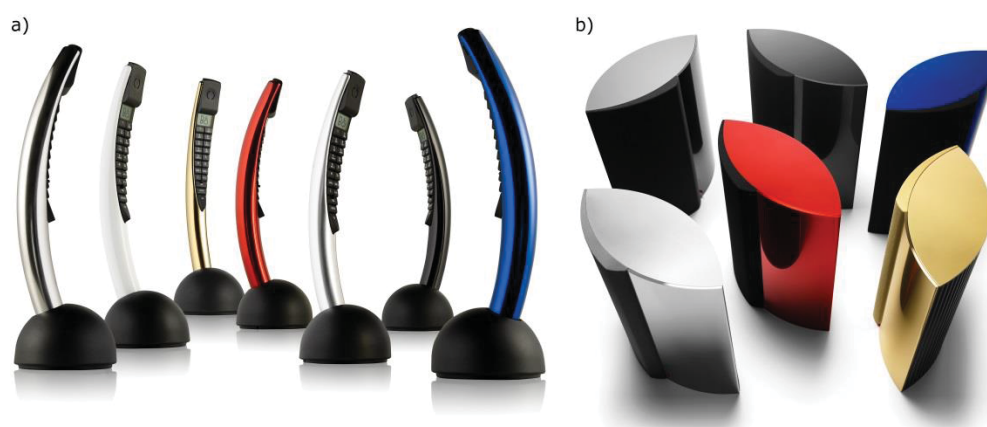


Fig. 1.1 – Bang and Olufsen products, a) BeoCom 2 telephones and b) BeoLab 4000 speakers.

Colouring is normally done by absorption colouring using pigments or dyes to absorb parts of the white light, causing a colour to be perceived. In contrast with this are structural colouring (e.g. known from soap bubbles, rainbows, and the colours in the sky), where the microstructure of the material itself often gives deep, bright, and UV resistant colours. The creation of structural colours requires processes giving control of the microstructure that is not easy by regular production methods. The magnetron sputtering process allows creation of coatings with desired compositions, which cannot be created by the regular casting route used in the primary aluminium production. The technique enables the creation of unique appearances for e.g. high end design products, which can position a design company in a favourable position in the market.

## 1.2 Aluminium in the automotive industry

For weight reductions, the amount of aluminium in the transport industry is continuously increasing as seen in Fig. 1.2a, and Fig. 1.2b shows the distribution of aluminium in the cars today. Calculations from the European Aluminium Association [5] estimates that the weight of the cars today can still be reduced by 36 % by increased use of aluminium. Approximately 80 % of the aluminium used in cars today is made of cast alloys. For the body parts wrought aluminium alloys containing copper was previously used giving high strength but bad corrosion properties. More recently, alloys with magnesium, magnesium + silicon, and zinc + magnesium have been the preferred types of alloys [6,7]. However, only few cars are made with aluminium as the main material, e.g. the Audi A8, which was the first mass-market car with a body of aluminium.

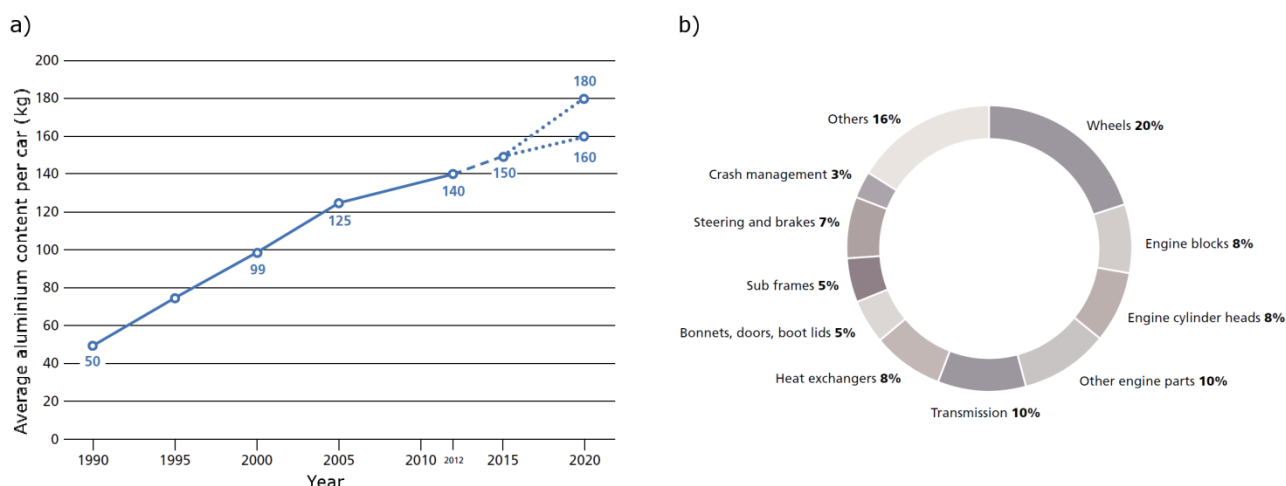


Fig. 1.2 – The use of aluminium in cars produced in Europe [5], a) the average aluminium content in cars since 1990 and b) the distribution of aluminium in European cars.

The use of aluminium is very beneficial in the automotive industry since weight reductions are one of the main factors to reduce fuel or power consumption. However, in the automotive industry all outer surfaces have to withstand the corrosive environments it is exposed to during the use phase, including saline and sulphur containing species. Furthermore, harsh alkaline chemicals are used e.g. in a brushless car wash causing aluminium alloys to corrode heavily. Today nickel salt sealing is used for alkaline protection of e.g. aluminium wheel rims, however, the automotive industry is pursuing a reasonable alternative, due to environmental and health reasons. Furthermore, the nickel salt sealing is not flawless above pH 12.

### 1.3 Objective of the present study

The present study consists of four parts: (i) understanding the optical appearance of anodised commercial aluminium alloys as a function of alloying elements and initial surface finishing, (ii) creating Al-Ti binary coatings by magnetron sputtering to investigate microstructure and appearance after heat treatment and anodisation, and investigation of alkaline corrosion resistance of Al-Ti coatings made using (iii) magnetron sputtering and (iv) laser surface cladding. A brief overview of the four parts is given below:

#### **Appearance of anodised commercial aluminium alloys:**

##### **Effect of alloy composition and prior surface finish**

It was investigated how the optical appearance is affected by the alloy composition, surface morphology, and the microstructure. Four commercial aluminium alloys were studied before and after polishing, etching, anodisation, and hot water sealing, giving an overview on how the alloy composition affects the appearance. It was found that the roughness after etching increases with higher amounts of alloying elements in the alloy (especially iron and silicon). Proper polishing requires some alloy hardness, while alloy purity is required for a glossy appearance after anodisation.

Magnetron sputtered aluminium based coatings containing up to 18 wt. % titanium were investigated. The microstructure of the as-deposited coating had a layered structure, and  $\text{Al}_3\text{Ti}$  phases precipitated during the heat treatment. Furthermore, investigations focused on:

### **Anodisation of sputter deposited aluminium-titanium coatings:**

#### **Effect of microstructure on optical characteristics**

During anodisation, the heat-treated specimens containing  $\text{Al}_3\text{Ti}$  phases turned dark, and the specimens were investigated as a model system on the optical effect of partially oxidised intermetallics and the subsurface morphology after anodisation. It was suggested, that the darkening of the anodised specimens happened due to roughness of the oxide-substrate interface causing light trapping and optical scattering and absorption by the partially anodised intermetallics in the anodised layer.

### **Saline and alkaline corrosion resistance of aluminium-titanium coatings prepared by plasma magnetron sputtering**

Investigations of the magnetron sputtered Al-Ti coatings showed that 13 wt. % titanium and more improved the corrosion resistance at pH 13.5 and this was further improved by heat treatment, especially at 400 °C and more. The improved corrosion properties were ascribed to structural relaxation, decreased galvanic potential differences in the microstructure, and protection from the network of the  $\text{Al}_3\text{Ti}$  phases precipitated during the heat treatment.

### **Alkaline corrosion properties of laser clad aluminium-titanium coatings**

Laser surface cladding of aluminium containing up to 20 wt. % Ti6Al4V were studied focusing on the microstructure and the alkaline corrosion properties. Due to precipitation of large  $\text{Al}_3\text{Ti}$  phases during the cladding process, the microstructure consisted of an almost pure aluminium matrix, which corroded preferentially when exposed to pH 13.5. Additional heat treatment did not break down the solidified microstructure and the corrosion properties were not improved.

## **1.4 Al-Ti coatings**

Creating bulk products of certain chemical compositions can be difficult and expensive, if not impossible. Instead, coatings can be applied to achieve the desired properties. Aluminium based coatings with titanium as the main alloying element was found useful based on two observations:

### **1.4.1 Colouring Al-Ti coatings by scattering**

Titanium dioxide ( $\text{TiO}_2$ ) is the most used white pigment due to its low price, high index of refraction ( $> 2.5$ ), and practically no absorption in the visible spectrum. While common pigment molecules are of sizes up to a few nanometres, regular  $\text{TiO}_2$  pigments are of sizes 200 nm – 300 nm [8]. It is therefore possible to absorb regular pigments into the pores of the anodised aluminium surface (usually 10 nm – 20 nm in diameter,

(described in section 2.2.2.4, page 12), whereas the same is not possible with white pigments. Instead, it might be possible to create an Al-Ti coating and grow titanium-rich particles by heat treatment, followed by anodisation, creating amorphous titanium oxides inside the anodised aluminium layer (Fig. 1.3). The scattering from the titanium oxide inclusions might therefore cause light scattering giving white or other colours depending on the sizes of the inclusions.

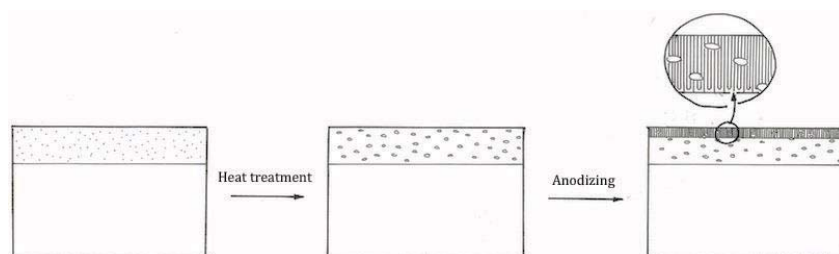


Fig. 1.3 – Schematic showing the evolution of the microstructure and anodized layer for a Al-Ti coating, for the as-deposited coating, after heat treatment, and after anodisation [9].

### 1.4.2 Alkaline resistant Al-Ti coatings

The use of titanium as an alloying element should improve the corrosion resistance due to the high passivity of titanium at all pH values as shown in Fig. 1.4 by the overlapping Pourbaix diagrams for aluminium and titanium. Aluminium is corroding in harsh acidic and alkaline conditions. On the other hand, titanium is stable in both acidic and alkaline conditions and might therefore be usable to protect aluminium from the alkaline chemicals applied in the automotive industry, requiring protection at pH 13.5 in a sodium hydroxide (NaOH) based solution.

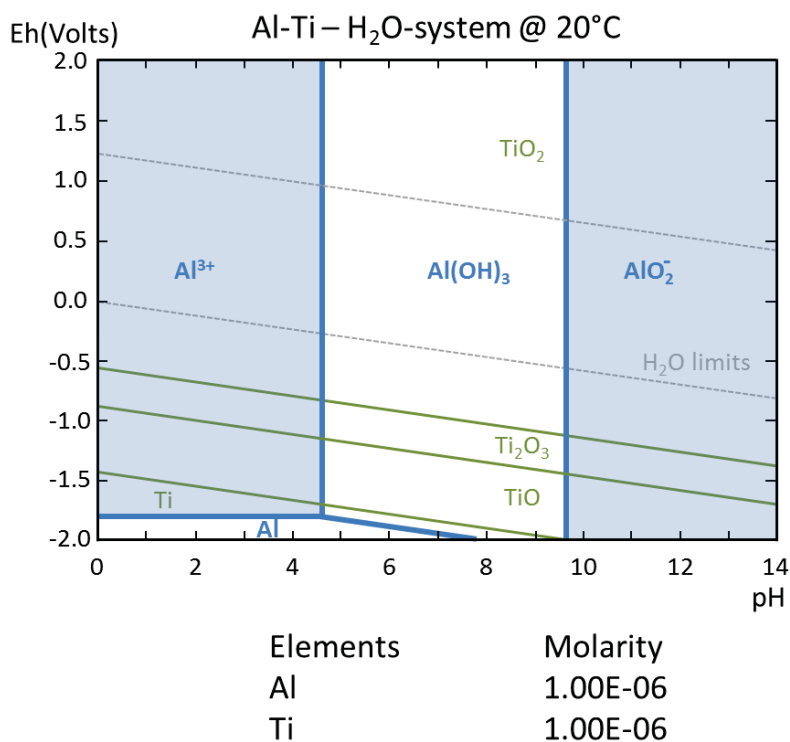


Fig. 1.4 - Overlapping Pourbaix diagrams for aluminium and titanium [10].

### **1.4.3 Techniques for creating Al-Ti coatings**

Physical vapour deposition (PVD) by magnetron sputtering and laser surface cladding (LSC) are both coating processes, where the composition of the coating can be quite freely defined compared to regular casting processes creating wrought aluminium alloys. Creating thick anodisable coatings using the magnetron sputtering process is very expensive, but might be useful for high-end design products. For corrosion protection, the PVD process is useful to create controlled model systems and in some cases applicable, based on product type and cost considerations, while LSC is a rougher but cheaper production method.

## **1.5 Overall structure of the thesis**

Chapter 2 presents a review of literature on aluminium, its alloys, the mechanical surface treatment and anodisation of these, and the recycling process. Additional focus is given to the optical appearance (section 2.4) and the corrosion properties (section 2.5) of aluminium and its alloys. Chapter 3 describes the corrosion properties of titanium and the creation of titanium containing aluminium based coatings with focus on the PVD (section 3.3) and the laser surface processes (section 3.4). All materials and methods used are presented in chapter 4. The four appended papers are summarised briefly in chapter 5 and the entire study is wrapped up with an overall summary (chapter 6) and an outlook (chapter 7). The idea of chapter 5 is to keep the extent of the thesis down, while it is still reasonable to read the whole thesis in one continuous process. Therefore, results and discussions are mainly found within the appended papers.





---

## 2 Aluminium

---

Aluminium is the most common metal in the Earth's crust, with an expected supply of at least 400 years, even though aluminium is the second most used metal (after iron). Most of the aluminium is found in the bauxite rock (containing 30 % - 54 % alumina in different types of minerals), which is usually surface mined (opposite to underground mining), with very little waste at the mining site. The bauxite is refined into alumina ( $\text{Al}_2\text{O}_3$ ) by the Bayer process, which in short includes sodium hydroxide at high pressure and temperature, several filtration and precipitation processes, and by passing the rest products through fluidized calciner at 1100 °C. The subsequent Hall-Héroult process puts a low voltage (3 V – 5 V) direct current of hundreds of thousands of amperes through the solution and liquid aluminium is then deposited at the cathode while carbon dioxide ( $\text{CO}_2$ ) is created at the anode. Since liquid aluminium has a higher density than molten cryolite it is possible to extract the molten aluminium from the bottom of the electrolytic cell while more alumina is added. The Bayer and the Hall-Héroult processes are almost equally energy demanding, requiring about 30 kWh/ton pure aluminium in total. After the Hall-Héroult process, the molten pure aluminium can be further purified and is subsequently added alloying elements and cast as blocks for later semi-product fabrication. Depending on the requirements for the specific semi-product the blocks can be further treated e.g. by heat treatment and for removal of the surface layer. Furthermore, one or more processes can be combined to minimise further secondary processing e.g. by continuous casting and strip casting.

The optical and corrosion properties of aluminium alloys are closely related to the chemical composition and microstructure created during later production steps like casting, extrusion, heat treatment, polishing, etching and anodisation. A general introduction to aluminium alloys and surface treatments, including the anodisation process, are followed by a brief description of recycling of aluminium alloys and sections on the optical and corrosion properties of aluminium and its alloys.

### 2.1 Aluminium alloys

In the EN 573 and EN 1780 standards the aluminium alloys are divided into eight different series depending on the main alloying element(s). In these standards, the nomenclature of wrought alloys contains four digits and the nomenclature of cast alloys contains three digits, a decimal point and one digit. The first digit defines the main alloying element(s), and thereby the series. The other digits define the chemical composition of the alloy in further details. Table 2.1 gives an overview of the eight series, the primary alloying elements and typical applications.



Table 2.1 – Classification of the aluminium alloy series according to the EN 573 and EN 1780 standards.

Primary alloying element	Wrought alloys	Cast alloys	Typical applications
None (commercially pure)	<b>1xxx</b>	<b>1xx.x</b>	<b>Foils, sheets, decorative</b>
Copper	<b>2xxx</b>	<b>2xx.x</b>	<b>Aircraft industry</b>
Manganese	<b>3xxx</b>		<b>Cans, buildings, radiators</b>
Silicon	<b>4xxx</b>	<b>4xx.x</b>	<b>Heat exchangers</b>
Magnesium	<b>5xxx</b>	<b>5xx.x</b>	<b>Cans, transportation, buildings</b>
Magnesium + silicon	<b>6xxx</b>		<b>Transportation, buildings</b>
Zinc (+ copper)	<b>7xxx</b>	<b>7xx.x</b>	<b>Aircraft industry, radiators</b>
Other elements <sup>1</sup>	<b>8xxx</b>	<b>8xx.x</b>	<b>Foil, aircraft industry</b>

<sup>1</sup> The 8xxx series is mainly lithium alloys, but also e.g. iron + silicon alloys.

Grade of purity and the amount of secondary alloying elements vary significantly within each series. The following sections give an overview of the most important alloying elements, focusing on the wrought alloys, divided into work-hardenable and age-hardenable alloys.

### 2.1.1 Work-hardenable wrought alloys

Work-hardenable alloys (1xxx, 3xxx, 4xxx, 5xxx) are primarily strengthened by cold work, solid solution and dispersion strengthening. Therefore, the typical microstructure of these alloys contains an aluminium matrix with intermetallics and if applied, dispersion strengthening particles.

The state of these alloys is normally denoted:

- **F**: As fabricated, with no quality guarantee
- **O**: Soft annealed
- **Hxx**: Strain hardened, where the first digit indicates, whether the product is strain hardened without thermal treatment (H1), partially annealed (H2) or stabilized at a low temperature (H3). Second digit denotes the hardness from ¼ hard (Hx2) to extra hard (Hx9).

The **1xxx** series is commercially pure alloys of minimum 99.0 % purity. These alloys are soft, have high reflectance, and good corrosion properties.

**Manganese** in the **3xxx** series and **Magnesium** in the **5xxx** series are both used for solid-solution strengthening.

**Silicon** is both found as a common impurity and used as an alloying element in the **4xxx** series. High concentrations of silicon is unwanted since more than 0.8 % affect the visual appearance [11] and silicon act cathodic to the aluminium matrix causing roughness during etching [12,13]. Aluminium silicate ((AlO)<sub>2</sub>SiO<sub>3</sub>) has proven to increase the alkaline resistance of silicon-containing alloys.

### 2.1.2 Age-hardenable wrought alloys

In age-hardenable alloys (2xxx, 6xxx and 7xxx), precipitates are grown over time (natural aging) or by heat treatment (artificial aging) to strengthen the alloy. When heat-treated, the alloy is denoted with a **T** followed by one to five digits, indicating the temper process. The typical microstructure of age-hardening alloys contains intermetallics and precipitates.

**2xxx** and **7xxx** alloys contain **copper** and **zinc**, giving high strength alloys e.g. for aircraft applications. The 2xxx alloys are strengthened by  $\text{CuAl}_2$  and  $\text{Al}_2\text{MgCu}$  precipitates. Due to the nobility of copper, the corrosion properties of the 2xxx alloys are bad. The 7xxx series contains zinc and magnesium to form  $\text{MgZn}_2$  precipitates. Many 7xxx alloys contain zinc, magnesium, and copper for creation of  $\text{CuAl}_2$ ,  $\text{Al}_2\text{MgCu}$ , and  $\text{MgZn}_2$  achieving increased strength [14].

In the **6xxx** series, **silicon** and **magnesium** create magnesium silicide ( $\text{Mg}_2\text{Si}$ ) for hardening. The  $\text{Mg}_2\text{Si}$  precipitates act anodic during etching, creating small pits with sizes similar to the original particle [12,13]. Nearly 75 % of aluminium extrusions are made of 6xxx alloys [15].

**Iron** is usually an unwanted but common impurity. Even at low concentrations, iron-rich phases have big effects on the surface microstructure, and might cause miscolouring e.g. in the form of streaks on the surface as known from extrusions. Iron-rich phases react cathodic to the aluminium matrix during etching [12,13] causing pits of sizes up to 10  $\mu\text{m}$  [12,16,17].

**Titanium** is found as an impurity but is also added in low amounts as a grain refiner in age-hardening alloys, forming  $\text{Al}_3\text{Ti}$  precipitates pinning the grain boundaries during grain growth.

### 2.1.3 Choosing wrought alloy series

It can be hard to choose which aluminium alloy to use for at specific purpose, but Vargel [1] has given an overview, where parts of it are presented in Table 2.2. Notice that the evaluation for corrosion resistance is only valid for regular air, freshwater and seawater.

Table 2.2 – Suggested parameters for choosing wrought aluminium alloy series [1].

Criteria	Work-hardenable alloys			Age-hardenable alloys		
	1xxx	3xxx	5xxx	6xxx	2xxx	7xxx
<b>UTS (MPa)</b>	50-100	100-260	100-340	150-310	300-450	320-600
<b>Decorative anodizing</b>	+	-	+	+	-	-
<b>Corrosion resistance</b>	+	+	++	++	-	-
<b>Extrudability</b>	+	+	-	++	-	-

### 2.1.4 Cast alloys

Cast alloys are generally created by recycled aluminium added high amounts of alloying elements e.g. silicon, decreasing the melting temperature. The casting process enables a freer product form than conventional production methods; however, they are not good for anodisation and are therefore often painted, lacquered or used in the unanodised form, making them vulnerable to wear and corrosion.

## 2.2 Surface treatments of aluminium

### 2.2.1 Mechanical surface treatment

Various mechanical surface treatments are used for aluminium products. Blasting techniques like bead blasting (known from Apple products) are used for easy removal of scratches and homogenisation of the surface. The rough surface is subsequently etched before anodisation to remove the largest irregularities and oxides incorporated into the surface during blasting. Treatments like diamond turning and wheel polishing are used for a high gloss surface, which is only degreased before anodisation in order to maintain the glossy surface finish. Wheel polishing use a round cloth wheel fixed on a rotating machine, usually at more than 1200 rpm [18], and a polishing wax is added containing e.g. alumina ( $\text{Al}_2\text{O}_3$ ) as the abrasive agent. Alloying elements and previous mechanical treatments affect the hardness of the specimen and thereby the polishing properties. Harder specimens are in general tougher to polish, while softer specimens are heated more during the process. During wheel polishing, the temperature easily reach 200 °C and may locally rise up to 1000 °C [18]. Beilby [19] found that due to the heat development the peaks of the aluminium morphology are displaced into the valleys, creating an amorphous and/or very fine grained crystalline layer, which is now known as the Beilby layer [19,20]. The structure of the Beilby layer causes an unappealing appearance after anodisation and intense heat development during polishing should be avoided.

### 2.2.2 The anodisation process

A thin passivating oxide layer of alumina is formed on the surface when aluminium is exposed to oxygen. The oxide layer is impenetrable by the atmospheric oxide and is therefore passivating, causing the process to stop at an oxide thickness of 1 nm – 10 nm depending on the alloy and conditions of the surroundings. The alumina layer is transparent, hard, and resistant to wear and corrosion, however, due to the low thickness it is easily worn off. In the 1920's the anodisation process (also called electrolytic oxidation) was invented, and is still today used for most wrought aluminium products, normally creating an oxide layer of 5 µm – 25 µm in thickness. The anodisation process is done in several steps as presented in Fig. 2.1.

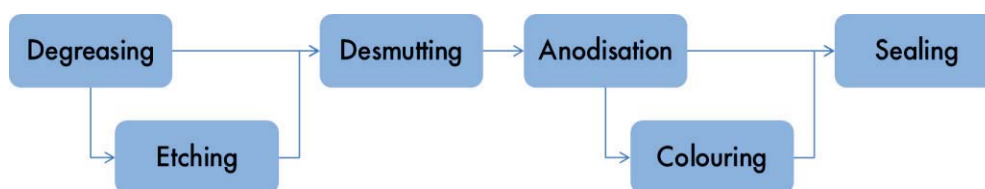


Fig. 2.1 - The steps involved in a normal anodisation process.

### 2.2.2.1 Degreasing

The natural oxide layer as well as oil, lubricants, and other greasing agents on the specimen surface are removed in a degreaser, which can be acidic or alkaline. Since alkaline agents normally stick to the surface, they are often used in order to avoid the specimen from drying in mid-air creating an oxide layer. Even small flaws in the degreasing step can cause the specimen to be discarded since the following process steps can enhance these flaws.

### 2.2.2.2 Etching

Etching is done to level out surface imperfections and gives a matt appearance. The etching step is therefore skipped when creating shiny surfaces as illustrated in Fig. 2.1. NaOH is often used due to its efficiency and the low price. The etching process can be very important for profiles and sheets, since both extrusion and rolling can cause big heterogeneity in the near surface area of the specimen. In these cases, the etching removes the near surface layer containing local composition differences, surface texture differences, and oxide containing particles [21–26]. Several alloying elements will be enriched in the near surface region during etching [21,27], depending on the behaviour of the intermetallics and dissolution of a specific element and etching temperature [21]. Impurities and alloying elements have big influence on the etching (Table 2.3), where cathodic iron rich phases has the largest effect and it has been found that the dissolution rate is proportional to the logarithm of the iron concentration [12]. It has also been found that the weight loss increase linearly with the Fe/Si ratio, which has been ascribed to the passivating properties of silicates.

Table 2.3 - Electrochemical behaviour of intermetallic particles during alkaline etching [12,13].

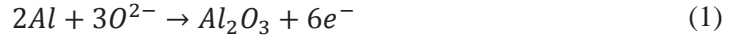
<b>Cathodic</b> (predominant attack of matrix)	~ Electroneutral	<b>Anodic</b> (predominant dissolution of particle)
Al <sub>3</sub> Fe	Al <sub>6</sub> (Mn,Fe)	Al <sub>6</sub> Mn
Al <sub>6</sub> (Fe,Mn)	Al <sub>12</sub> (Mn,Fe) <sub>3</sub> Si	Mg <sub>2</sub> Si
Al <sub>12</sub> (Fe,Mn) <sub>3</sub> Si	Al <sub>7</sub> Cr	Al <sub>2</sub> Cu
Al <sub>9</sub> Fe <sub>2</sub> Si <sub>2</sub>	Al <sub>3</sub> Ni	
Mg <sub>2</sub> Al <sub>3</sub>		
Al <sub>3</sub> Ti		

### 2.2.2.3 Desmutting

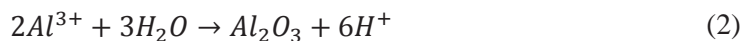
The desmutting step in e.g. nitric acid (HNO<sub>3</sub>) removes smut, consisting of oxides, aluminium hydroxide (Al(OH)<sub>3</sub>), intermetallics, and alloying elements, created during the degreasing and / or etching steps. Since smut is mainly caused by the corrosion products of alloying elements formed during etching, pure alloys will only produce very little smut, whereas highly alloyed specimens will give a visible smut layer on the surface of the specimen depending on the alloying and impurity elements of the alloy.

### 2.2.2.4 Anodisation

The anodisation step is a controlled oxidation of the surface, creating an oxide layer using an electrochemical process, providing the driving force for extended growth of the oxide layer. Anodisation is common and used mainly on aluminium, but can also be performed on e.g. titanium, tantalum, and magnesium, where the specimen is connected as the anode. In the initiation of the anodisation process a uniform oxide layer is formed at the metal-electrolyte interface [28]. This layer will move into the metal while the upper parts will grow a porous structure as later described. The bottom of the anodised layer is therefore a very thin and compact oxide layer, called the barrier layer, which is about 1 nm/V in thickness [29]. There has been a lot of discussions on the creation and the effects of the barrier layer [18,29,30], however, this is not within the scope of this thesis. During the anodisation process oxygen ions will diffuse from the electrolyte through the barrier layer to the metal-oxide interface reacting with the metal (oxidation):



Furthermore, aluminium ions will diffuse in the opposite direction to the oxide-electrolyte interface, reacting with the water:



Aluminium, titanium or steel are often used as cathode with a cathodic reaction producing hydrogen gas in acidic electrolytes (reduction):



Thus the overall reaction can be written as:



The actual chemical composition and structure of the anodised layer is not fully understood. However, it is known that it is amorphous [31] and consists of alumina, aluminium sulphate (Al<sub>2</sub>(SO<sub>4</sub>)<sub>3</sub>) (depending on the anodising bath), and Böhmite (AlOOH). Others have also suggested pseudoböhmite [32], which is Böhmite with excess of water.

After anodisation in e.g. sulphuric acid, the anodised surface consists of pores in hexagonally shaped cells with a central round pore perpendicular to the surface as illustrated in Fig. 2.2. The pores in a standard

anodisation are 10 nm – 20 nm in diameter and 5  $\mu\text{m}$  – 25  $\mu\text{m}$  in depth. The material will expand so that one third of the total anodised layer will be above the original surface.

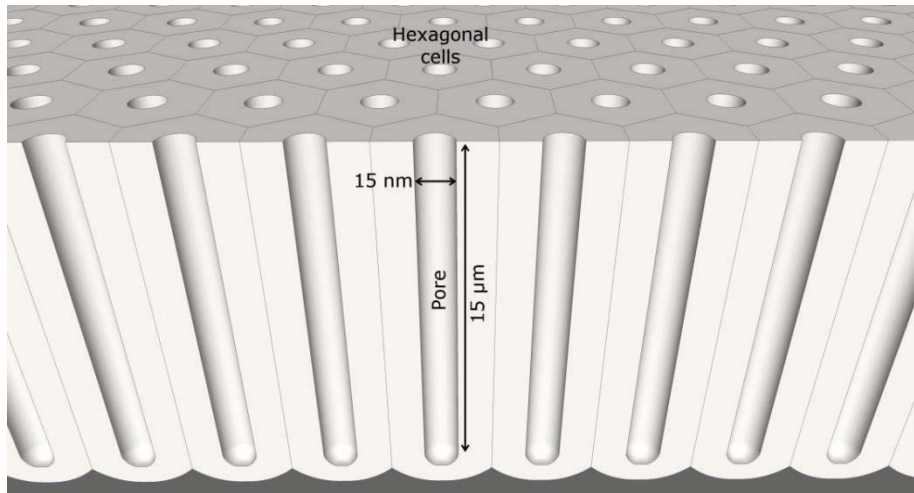


Fig. 2.2 – Ideal structure of an anodized layer (size of the pore is shown as an example).

The anodisation starts at the surface and runs perpendicular into the specimen. Consequently, the upper surface of the anodised layer will be the part that has been exposed to the solution for the longest time. For longer anodisation processes this will create the powdering effect, where the pores do not have parallel walls, but are inclining away from the centre of the pore, moving towards the surface (Fig. 2.3) [11].

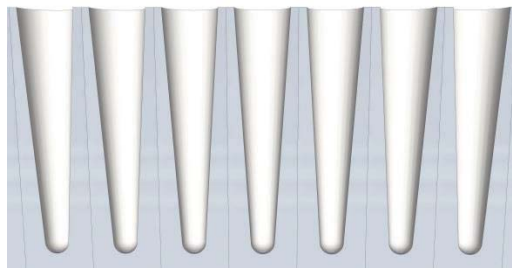


Fig. 2.3 - The powdering effect creating inclining pore walls as the thickness of the anodised layer increases.

The alloy composition has effects on the anodisation behaviour, where intermetallic particles, behave electrochemically differently than the aluminium matrix (Table 2.4). Some phases like  $\text{Mg}_2\text{Si}$  are known to be quickly oxidised, at rates faster than aluminium, whereas others like  $\text{Al}_6\text{Fe}$  are known to oxidise at a lower rate than aluminium [12,13]. Therefore, e.g.  $\text{Al}_6\text{Fe}$  can be found as only partially oxidised in the anodised aluminium layer [33]. Some particles such as  $\text{Al}_3\text{Ti}$  are reported [12,13] to be unaffected by the anodisation and incorporated into the anodised layer.

Table 2.4 – Behaviour of intermetallic particles during anodisation in sulphuric acid [12,13].

Unchanged and incorporated into oxide film	Oxidised and incorporated (or dissolved) at a rate comparable or slower than Al	Oxidised and incorporated (or dissolved) at a rate faster than Al
Si	Al <sub>12</sub> (Mn,Fe) <sub>3</sub> Si*	Al <sub>12</sub> (Mn,Fe) <sub>3</sub> Si*
Al <sub>6</sub> (Mn,Fe)	Al <sub>3</sub> Fe	Mg <sub>2</sub> Al <sub>3</sub>
Al <sub>3</sub> Ti	Al <sub>6</sub> Fe	Mg <sub>5</sub> Al <sub>8</sub>
	Al <sub>6</sub> (Fe,Mn)	Mg <sub>2</sub> Si
	Al <sub>9</sub> Fe <sub>2</sub> Si <sub>2</sub>	Al <sub>7</sub> Cr
		Al <sub>2</sub> Cu

\* Dependent on particle size.

The structure of the anodised layer also depends on the electrolyte, voltage, current density, temperature, and time. These parameters will briefly be described below:

The **electrolyte** ensures oxidation of the dissolved Al<sup>3+</sup> ions. Sulphuric acid (H<sub>2</sub>SO<sub>4</sub>) is often used due to its efficiency and low price. But, other electrolytes like chromic acid (H<sub>2</sub>CrO<sub>4</sub>), boric acid (H<sub>3</sub>BO<sub>3</sub>) and oxalic acid (H<sub>2</sub>C<sub>2</sub>O<sub>4</sub>) are used alone or in combinations of two electrolytes and more [18,34]. With the use of different electrolytes, it is possible to change the properties of the final coating significantly, e.g. to create pores with diameters up to 150 nm – 200 nm. In general the pore characteristics change as follows:

- The pore diameter and growth speed increase with increasing **voltage**, while the density of pores is decreased.
- Low **current densities** produce a soft, thin film with a high density of pores.
- Pore diameter, cell wall thickness, and growth speed increase with **temperature**, whereas the pore density decreases.

The thickness of the coating is often controlled by the anodisation **time**. All processes will have a maximum thickness where the powdering effect removes the outer surface of the anodised layer simultaneously with generation of new oxide at the bottom of the layer.

The approximate total thickness of the layer formed during anodisation (H in µm) can be calculated using the following formula [11]:

$$H = \frac{0.4WTJ}{F} \quad (5)$$

where W is the anodic efficiency, T is the time in minutes, J is the total current in ampere, and F is the surface area in dm<sup>2</sup>. The current is affected by both temperature and voltage, while the anodic efficiency is normally ~ 65 %, but is also affected by temperature and voltage (and current).

### 2.2.2.5 Colouring of the anodised layer

The colouring of aluminium is normally done in one of the following ways:

- **Absorption colouring** is the cheapest, simplest and most common method, where the specimen is exposed to a dye by either dipping or spraying causing the dye to go into the pores. With absorption colouring a wide variety of colours is possible; however, many of these are not resistant to UV light.
- For **electrolytic colouring** a metal or metallic salt is precipitated at the bottom of the pores. The variety of colours possible are less than for absorption colouring, however, the electrolytic colouring compounds are normally more resistant to UV light making the colouring more durable for outdoor use [35]. These colours are created due to light scattering and absorption, and depend on the size of the pores and the metal deposited [35].
- **Integral colouring** is used to colour the transparent anodised layer itself. Integral colouring is done during the anodisation step, where a special alloy is used or the electrolyte contains one or more organic acids that will colour the anodised layer [12]. The largest advantage of integral colouring is that anodisation and colouring are done in the same process step; however, it is expensive and offers only colours of light bronze to black.
- **Interference colouring** is based on the electrolytic colouring process, creating UV resistant interference colours of grey, blue, green [36], and in some cases even yellow, red, and bronze [35,37]. The process runs in three steps: anodisation, electrochemical modification creating pore enlargement at the bottom of the pores, and metal (often tin) deposition in the pores [35–37]. The colours are created due to interference of waves reflected in the top part of the deposited metal and the substrate [35]. Fig. 2.4 illustrates the interference colouring mechanism, where two parallel closely situated rays of light (from the same light source) enter the anodised layer. One ray goes between the deposited volumes of tin and is reflected at the substrate-oxide interface. The other ray hits the top of a deposited volume of tin and is reflected back towards the surface. If the reflecting surfaces are parallel, the rays will still be parallel after the reflection, and therefore the rays will interfere if they are close to each other as illustrated in Fig. 2.4. The type of interference depends on the distance between the two reflecting surfaces and the wavelength of the light. Thus, the colour of the deposition depends on the height of the deposited tin volumes. Furthermore, the type of interference is also dependent on the incoming angle, causing the interference colouring to be iridescent (colour is angle dependent). The technique is not widespread and requires very good control of the process [36,37].

Other non-commercial techniques have been reported to create colours by thin film interference in anodised aluminium products, which are described in section 2.4.7, page 30.



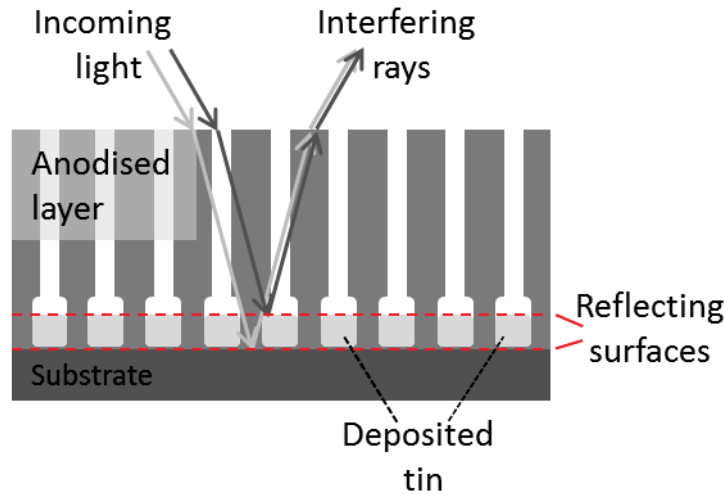


Fig. 2.4 – Principle of interference colouring of anodised specimens.

#### 2.2.2.6 Sealing

In Europe, the most common type of sealing is **hot water sealing**, where the specimen is immersed into water at pH 5.5 – 6.5 at 92 °C – 98 °C, normally for a time span of about 2 min/ $\mu\text{m}$  [38]. During hot water sealing, the hard and brittle alumina is converted:



The anodised layer will expand during the sealing closing the pores. This will avoid capillary forces dragging fingerprints, oil, and dirt into the pores as well as preventing dyes from leaving the pores. Furthermore, small particles can more easily stick to the porous surface compared to the sealed surface. The sealing of the specimen might affect the appearance, which is usually termed as sealing bloom; but this can be avoided by adding commercial sealing agents. In chemical reaction (6) presented above, the compound Böhmite ( $\text{AlO}(\text{OH})$ ) is created, however, the sealed structure is suggested by Bautista et al. [39] to be layered as illustrated in Fig. 2.5. The outer crystalline layer consists of Böhmite or pseudoböhmite, the intermediate layer is pseudoböhmite and the pores are filled with aluminium hydroxide ( $\text{Al}(\text{OH})_3$ ) and pseudoböhmite [32,39].

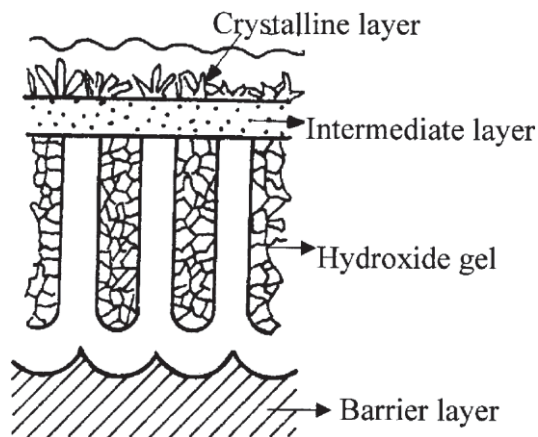


Fig. 2.5 – Surface structure of the anodised layer after hot water sealing [39].

**Steam sealing** is running at 110 °C – 150 °C using a boiler inside a chamber. The growth rate is 2 to 4 times higher than hot water sealing, and the process is less sensitive to pH and impurities.

Sealing is also done with chromates and nickel salts, which are described in 2.5.2, page 32 with focus on the corrosion properties of the different sealing techniques.

## 2.3 Recycling of aluminium alloys

Recycling of aluminium can be done by remelting aluminium scrap. Recycling of aluminium does therefore only require about 5 % of the initial energy consumption used for purifying the bauxite into the primary (initial) aluminium<sup>1</sup>. Apart from remelting the aluminium scrap, solid state recycling [6] has been tested, where the scrap is cleaned chemically and compressed at 200 MPa – 600 MPa, followed by extrusion at 450 °C – 550 °C, creating good bonding of the material [6]. Whereas other materials are worn during the use phase due to wear and corrosion, only little of the aluminium is lost. Furthermore, refiners and recyclers expect 95 % of the incoming aluminium to return to the market again as aluminium ingots [40]. The properties of aluminium are unchanged during remelting, so it is in principle possible to achieve exactly the same properties when using secondary (recycled) aluminium as when using primary aluminium. However, due to alloying elements and impurities, the purity of aluminium alloys is often downgraded during recycling. Secondary aluminium is used e.g. as agent for deoxidation in the steel industry, wrought alloys (e.g. cans), and extruded profiles e.g. in the building industry, however, most secondary aluminium is used for cast products (e.g. for motor blocks) [40,41]. This is mainly due to the high purity requirements for wrought alloys. Cast alloys are alloyed to a much higher degree but do also have restrictions, especially regarding magnesium, which makes 5xxx and 6xxx alloys bad for secondary cast products. Since the need for wrought aluminium alloys is continuously increasing, a cost-effective purification process or more comprehensive alloy sorting is needed [41]. Additional contamination of recycled alloys are very hard to avoid and especially iron contamination are often found due to iron particles within the aluminium scrap and iron contamination during the machining process [42,43]. A good method for removing iron (and nickel), has not yet been developed [42].

As Fig. 2.6 shows, the share of secondary aluminium is continuously increasing and today its share is about one third of the total aluminium production [40]. All secondary aluminium is used right away, and therefore scrap collection is the only way to increase the share of secondary aluminium further. Aluminium beverage cans consume 16 % of the total aluminium consumption. About 70 % of the aluminium beverage cans are recycled worldwide [40], where some of the leading countries are Brazil (97 %), Japan (93 %), and Sweden (91 %) [40]. The cans are easy to recycle due to the use of only two different alloys, which are well defined.

---

<sup>1</sup> It should be noted that a part of the primary aluminium production is done in countries using green energy resources, such as hydropower in Norway and Iceland. The 95 % saved energy is therefore not directly comparable with the burden on the environment, even though it is still significant.

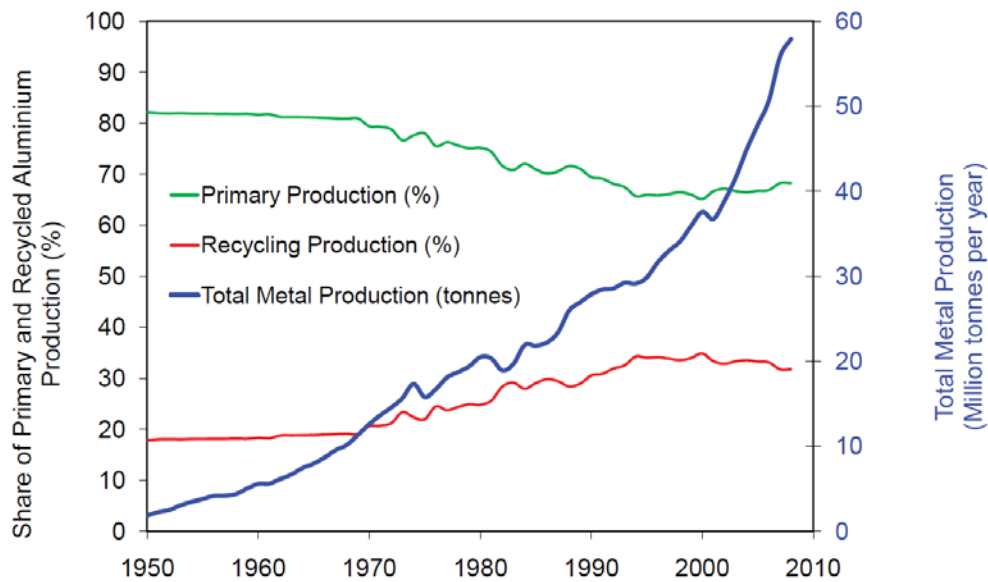


Fig. 2.6 – Global share of primary and recycled aluminium production [40].

In other industries, the recycling process is much more complex due to the use of several different alloys in the same product, and because several products are normally remelted simultaneously. The recycling process of e.g. a car follows several steps such as dismantling, shredding, magnetic removal of iron parts, sink-float, and Eddy current separation [6,40,41]. The aluminium scrap consists of both cast and wrought aluminium alloys. Sorting these from each other is possible by melting the cast parts (melt at a lower temperature), manual sorting by appearance, X-ray scanning, and appearance changes during chemical treatments. However, none of these are both easily applicable and cheap. Using laser-induced breakdown spectroscopy (LIBS), the surface is melted and optical emission spectroscopy is used for identification of the alloying elements [6,44], however, there can be problems when using LIBS on e.g. painted surfaces. Tests have shown that the LIBS technique can sort cast from wrought alloys with a correctness of >96 %, and eight different wrought alloys were sorted with a correctness of >95 % [45].

Now and in the future, secondary wrought aluminium alloys are expected to contain high amounts of alloying elements and impurities, which are hard to control rigorously. The effect of the different alloying elements on mechanical and corrosion properties and appearance is therefore important to understand in order to evaluate the need for sorting and purification during the recycling process for secondary wrought aluminium alloys.

## 2.4 Optical appearance of aluminium and its alloys

The theory behind the optical appearance of aluminium and its alloys encompass several scientific fields of solid state optics. Only the most relevant aspects are in focus here.

### 2.4.1 Electromagnetic waves

The spectrum of electromagnetic waves visible to humans cannot be strictly defined since it varies slightly from person to person [46,47], but it is approximately from 380 nm (violet) to 760 nm (red) as illustrated in Fig. 2.7. Since the perceived colour is dependent on the spectrum of the light, the surrounding light, previous visual impressions among others, the colours in Fig. 2.7 should be understood as a guideline and not necessarily the perceived colours of the actual wavelengths.

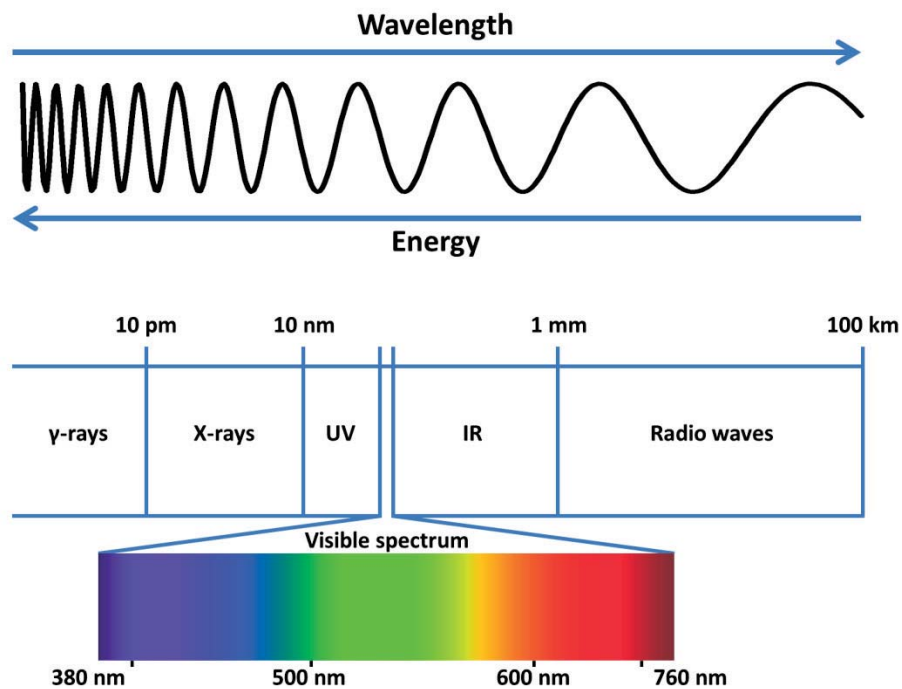


Fig. 2.7 - The electromagnetic spectrum.

The energy and wavelength of an electromagnetic wave correlates as follows:

$$E = \frac{hc}{\lambda} \quad (7)$$

Where,  $h$  is Planck's constant ( $4.136 \times 10^{-15}$  eV·s),  $c$  is the speed of light ( $2.998 \times 10^8$  m/s in vacuum and approximately the same in atmospheric air), and  $\lambda$  is the wavelength of the electromagnetic wave. As a consequence of the denoted relation, blue light with shorter wavelengths is of higher energy than the red light with longer wavelengths.

## 2.4.2 Scattering

Particles of sizes smaller than about  $\lambda/15$  [46] cause so-called Rayleigh scattering, as known from the colours of the human eye and from the blue and red colours of the sky as seen in Fig. 2.8. Scattering caused by particles in the size of the wavelength of the incoming electromagnetic wave and larger, is sometimes called Mie scattering<sup>2</sup>. This type of scattering is known from white objects like milk, snow, clouds, white paints, etc.

### 2.4.2.1 Rayleigh scattering

Rayleigh scattering happens due to electrons excited by absorbing a photon and subsequently reemitting a new photon of the same energy. For transparent materials the photons in the visible regime do not have enough energy to excite an electron; instead the energy is absorbed as vibrations and another photon is emitted. At the resonance frequency of the electrons most of the photons are scattered. The larger the difference between the energies of the incoming photons and the resonance frequency of the electrons in the material is the fewer photons are scattered. For most particles, the resonance frequency for Rayleigh scattering is in the UV regime of the electromagnetic spectrum, causing the waves of the shortest wavelengths of visible light to be scattered the most. Rayleigh scattering in the upper atmosphere scatters light of short wavelengths the most giving blue sky during the day and red light during sunrise and sunset since all the blue light is scattered away from the observing angle. In Fig. 2.8 a sunset over Isefjord is shown, at low angles the sunlight is orange, while at larger angles the sky is blue.

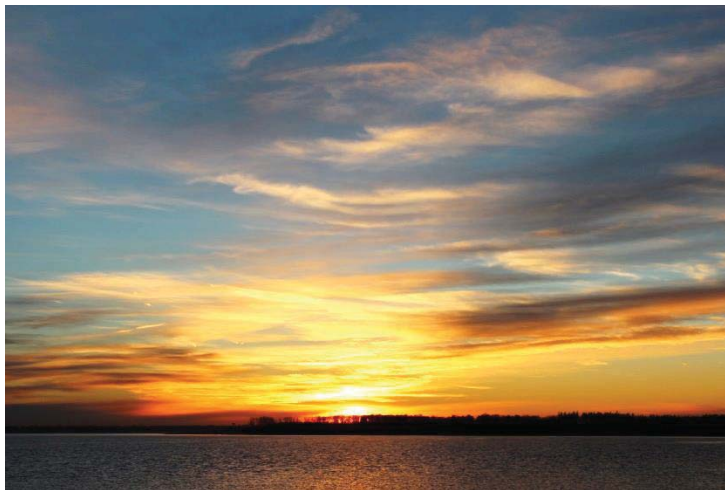


Fig. 2.8 - Rayleigh scattering seen in the sky at a sunset over Isefjord.

Rayleigh scattering is strongest perpendicular to the direction of propagation and does only have an effect when the particles are widely spaced, e.g. in the upper atmosphere. If the particles are packed more closely,

---

<sup>2</sup> Gustav Mie (1869 – 1957) and sometimes others like Ludvig Lorenz (1829 – 1891) are credited for the so called (Lorenz-) Mie solution, describing the solution to Maxwell's equations for scattering of electromagnetic waves when hitting a particle.

the scattering of the individual particles will be cancelled out by scattering from other particles and no effect is perceived.

#### 2.4.2.2 Mie scattering

Larger particles scatter waves of all wavelengths almost equally in all directions and are therefore perceived as white. Most white colours are created in the same way: a transparent matrix of one index of refraction is containing a lot of randomly distributed transparent particles with another index of refraction. The larger the difference of indices, the stronger is the scattering. The most used white pigment is titanium dioxide ( $\text{TiO}_2$ ), since it is cheap and has a very high index of refraction (above 2.5) and practically no absorption in the visible spectrum. For milk the matrix is water and the scattering particles are transparent fat and protein particles [48]. Here the difference in indices of refraction is only up to about 0.1, giving a low-efficient white, which is most distinct in low fat milk, where a tint of blue or red can be experienced when examined near a bright light for scattered and transmitted light respectively.

#### 2.4.3 Reflection on a surface

When a beam of light hits an opaque surface e.g. of a metal, the characteristics of the reflection is dependent on the material and the surface smoothness. At a microscopic level, reflections are defined as incoming angle equals outgoing angle. However, when observed in a more macroscopic manner the surface might not be as flat as it looks. If the surface is flat the reflection will be specular, while rough surfaces reflect in a more diffuse way. Reflections from materials can be described as a combination of these two types of reflections as presented in Fig. 2.9.

In computer graphics a third type of reflection is often included for a better representation of the world. Phong [49] suggested the use of ‘ambient reflection’, i.e. the scattered light from the surroundings. He et al. [50] suggested a ‘directional diffuse’ reflection as seen in Fig. 2.9. This is to take into account that the reflections of many diffuse materials have directionality giving additional reflection intensity near the specular angle.

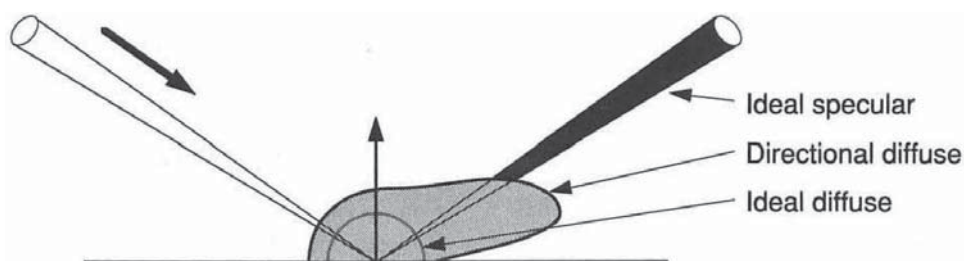


Fig. 2.9 - Reflection from a surface divided into ideal specular, ideal diffuse and directional diffuse reflections [50].

Diffuse reflections in surfaces occur due to surface roughness and subsurface scattering of the light, whereas the directional diffuse reflection is only caused by surface roughness [50]. The diffuse reflection increases with surface roughness until a roughness magnitude comparable to the wavelength of light.



At an atomic scale, a reflection is an effect caused by scattering from all molecules in a media, however, this is in practice different for solid materials; where the atomic spacing is much lower than the wavelength of light. In this case it is only the top  $\lambda/2$  layer that has a significant effect on the reflection, due to interference of scattering events happening deeper in the material [46]. Rays of light can be illustrated as wavefronts, so that a line illustrates several synchronised parallel waves. Fig. 2.10 illustrates the reflection of a wavefront, where only scattering from one atomic layer is included. The incoming wavefront is scattered subsequently in each surface atom (Fig. 2.10a-c), resulting in another wavefront away from the surface (Fig. 2.10d), where the incoming angle equals the outgoing angle.

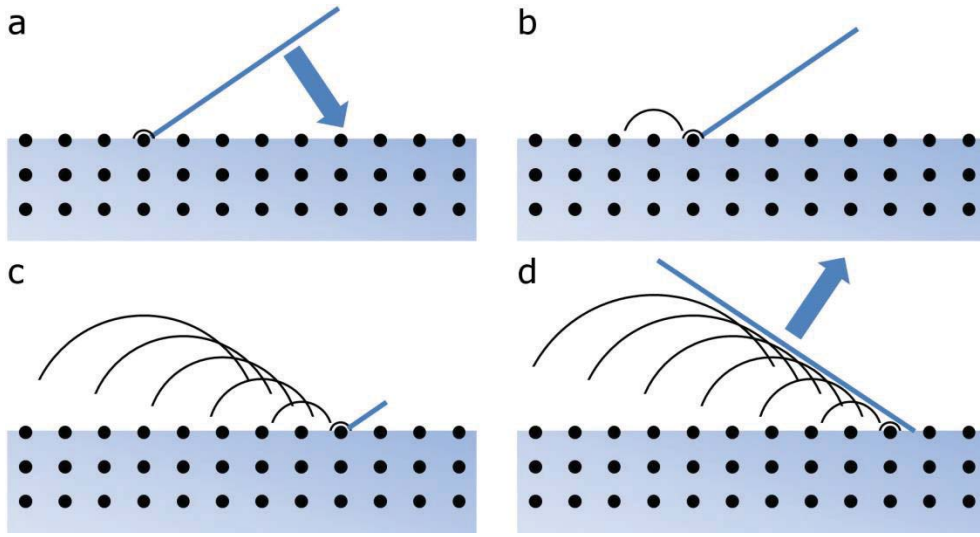


Fig. 2.10 – Reflection on a surface, inspired by [46], a) incoming wavefront hit surface atoms, b-c) subsequent scattering by other atoms, and d) reflected wavefront.

For a transparent medium, the absolute index of refraction refers to the speed of light in the medium:

$$n \equiv \frac{c}{V} \quad (8)$$

where  $c$  is the speed of light in vacuum and  $V$  is the speed of light in the medium. Materials having a larger absolute index of refraction are said to be more optically dense. If light reflects in a more optically dense material it is called an external reflection, and a  $180^\circ$  phase shift occurs for the reflected wave. Fig. 2.11 illustrates the reflectivity of light as a function of the incident angle with respect to the normal of the surface. For an external reflection (dotted line) going from air ( $n=1.00$ ) to anodised and sealed pure aluminium ( $n=1.60$ , this is an approximation explained in section 2.4.5, page 27). The reflectivity is about 5.3 %, for light reflecting perpendicular on the surface, and increase exponentially to 100 % when looking parallel to the surface. If the light reflects in a less optically dense material it is called an internal reflection. In Fig. 2.11 it is found that the reflectivity for an internal reflection (full line) in the same media increases rapidly to 100 % at the critical angle ( $\sim 38.7^\circ$ ), causing total internal reflection to happen with no loss of energy.

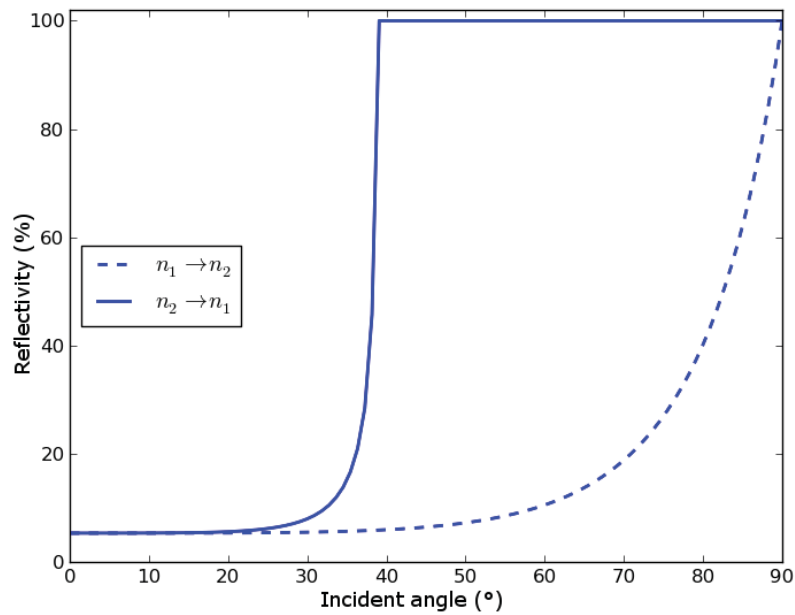


Fig. 2.11 – Reflectivity for external (dotted line) and internal (full line) reflections, where  $n_1 = 1.00$  and  $n_2 = 1.60$ .

#### 2.4.4 Optical properties of metals

The valence band is the uppermost full energy band of the material, while the first partly or totally free energy band is called the conduction band. The energetic distance from the valence band to the conduction band is called the band gap and some of the fundamental optical properties of solids are defined by this. An incoming photon with sufficient energy will cause an electron in the valence band to jump to the conduction band leaving behind an electron hole. There are a lot of free energy levels at the band gap energy and higher, which means that all waves with energy of the band gap energy and more is much more disposed to absorption than waves below the band gap energy. Where all other materials have their uppermost energy band full, metals are defined as materials having the highest energy band only partly filled (Fig. 2.12b). Insulators (Fig. 2.12a) have big band gaps, while metals have very small or even no band gap [46]. Immediately after absorption, the electron can jump back to its original position, emitting a photon with the same energy level as the original one. This absorption and re-emission of new photons gives flat metals its reflective appearance, whereas some metallic powders appear black since reemitted photons are reabsorbed repeatedly causing none or very little light to leave the powder [47].



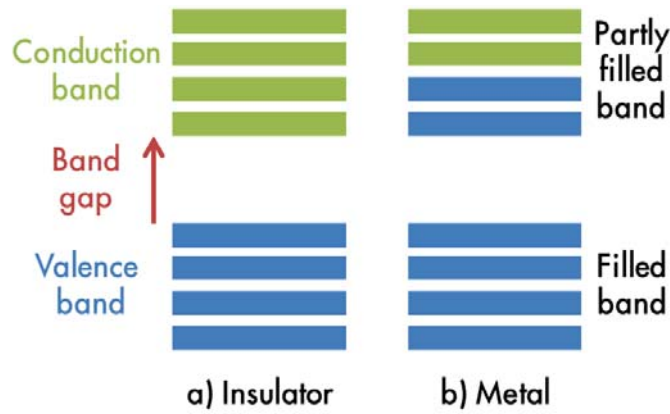


Fig. 2.12 - Valence and conduction band of a) an insulator and b) a metal.

Not all absorbed electrons are re-emitted, and therefore the index of refraction,  $N$ , of metals is defined as:

$$N = n + ik \quad (9)$$

Where  $n$  is the absolute index of refraction (defined in formula (8)),  $i$  is the imaginary unit and  $k$  is called the extinction coefficient or absorption index. An important fact for both  $n$  and  $k$  is that they are wavelength dependent. The reflectivity,  $R$ , defines the fraction of the incoming light reflected in a given material. If the light is falling perpendicular on a metal surface it is independent on polarisation, and the reflectivity can be calculated by:

$$R = \frac{(n - 1)^2 + k^2}{(n + 1)^2 + k^2} \quad (10)$$

The reflectivity spectre of silver, aluminium, titanium, copper and gold are found in Fig. 2.13. For most metals (e.g. silver and aluminium),  $n$  and  $k$  vary only slightly as a function of wavelength within the visual spectrum giving these metals a visually neutral grey appearance. However, the band gap energy of other metals like gold and copper is within the visual spectrum causing low reflectivity for shorter wavelengths (higher energies). The band gap of silver is found in the near visible UV part of the spectrum.

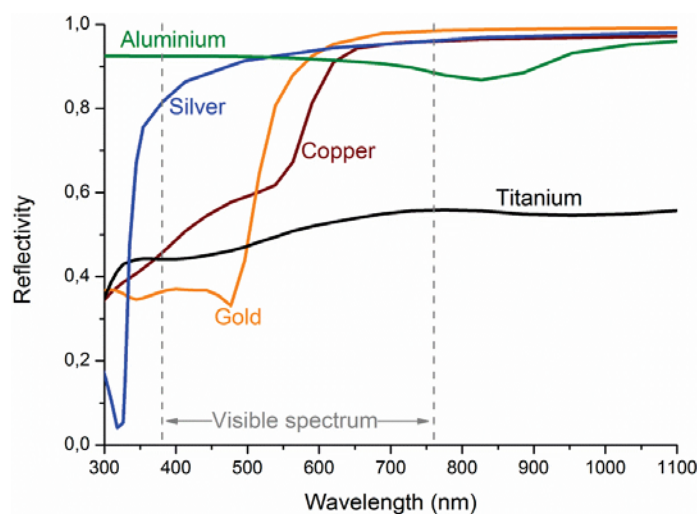


Fig. 2.13 - Reflectivity of silver, aluminium, titanium, copper and gold. Data from [51].

The uniform reflection spectrum of silver has caused it to be used for mirrors in optical parts of scientific products like astronomical telescopes. However, silver is very sensitive to sulphur causing it to corrode in polluted areas impairing the optical properties. Therefore, aluminium is being used more and more in this type of applications due to its good optical properties, and the corrosion resistance of the thin native oxide film [47].

### 2.4.5 Optical appearance of aluminium alloys

As presented in Fig. 2.13, pure aluminium has very high reflectivity. The optical ‘constants’ ( $n$  and  $k$ ) of aluminium has been measured in several conditions, collected by Nyce and Skolnick [52]. At 632.8 nm, they found average values for aluminium evaporated onto sapphire ( $n = 1.60$ ,  $k = 7.53$ ), and electropolished polycrystalline aluminium ( $n = 1.72$ ,  $k = 7.56$ ) [52].

The optical constants of  $\text{Al}_2\text{O}_3$  are  $n = 1.76 - 1.79$  and  $k = 0$  within the visible spectrum [53]. It has been found that the optical constants of porous anodised aluminium, are highly dependent on the porosity of the anodised layer and thereby the anodisation parameters. Shih et al. [54] calculated the effective values of  $n$  and  $k$  based on photospectrometry measurements for layers anodised in 15 % sulphuric acid with different current densities and temperatures. As presented in Fig. 2.14, it was found that when increasing the temperature and/or decreasing the current density, the pore density increased, which caused  $n$  to increase and  $k$  to decrease [54].

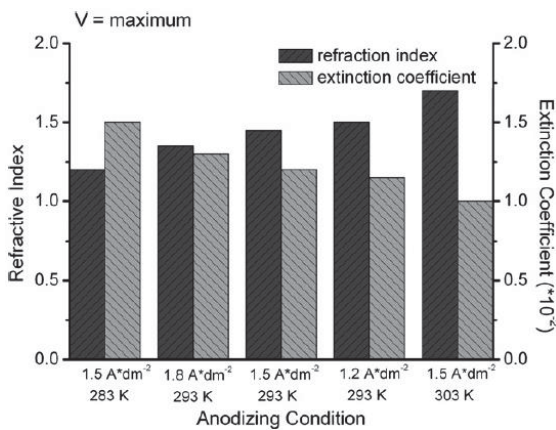


Fig. 2.14 – The  $n$  and  $k$  values as a function of anodisation parameters [54].

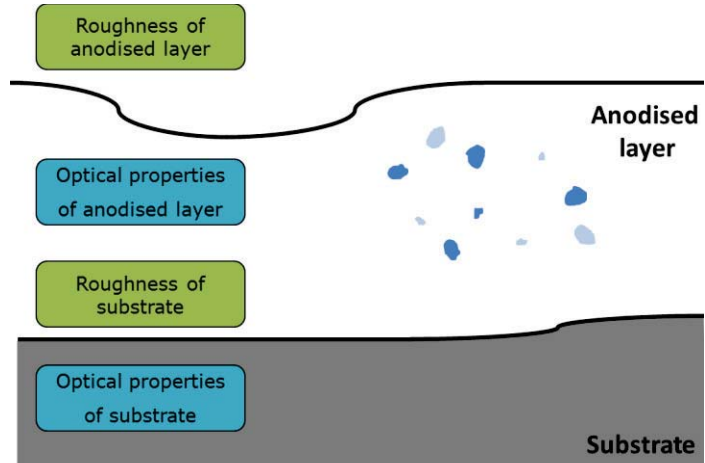


Fig. 2.15 – Features affecting the optical appearance of anodised aluminium.

No literature has been found on the index of refraction for anodised and sealed specimens; however, as described in section 2.2.2.6, page 18, the sealed surface is expected to consist of pseudoböhmite and aluminium hydroxide with absolute refractive indices of  $\sim 1.65$  (Böhmite) and  $\sim 1.57$  respectively. Pseudoböhmite contains some excess of water compared to Böhmite. The absolute refractive index of anodised and sealed aluminium is estimated to be  $\sim 1.6$  and almost constant in the visible spectrum. Furthermore, the absorption index is expected to be very low.

The visual appearance of anodised commercial aluminium alloys are affected by the morphology and optical properties of the anodised layer [12,55–57] and the substrate [12,16,22–24,58–64] as presented in Fig. 2.15. Akeret et al. [12] studied the effect of alkaline etching, brightening, and anodisation. It was found that the degree of cloudiness of the anodised layer depends on the degree of alloying, especially by iron and silicon. On the other hand, sufficiently small intermetallics such as  $\text{Mg}_2\text{Si}$  and  $\text{Mg}_2\text{Al}_3$  have only little effect on the appearance and the highest transparencies of anodised layers are found for high purity alloys and 6xxx ( $\text{AlMgSi}$ ) alloys [12].

Saito et al. [55,56] investigated 50  $\mu\text{m}$  oxide films on pure aluminium (99.99 %) and AA5052 (2.2 - 2.8 % Mg, < 0.5 % Fe, Cr, and Si) created at different current densities. It was found that the oxide film on AA5052 was darker, and that it darkened further with increased current density. The optical loss was ascribed to scattering loss, caused by holes created by dissolved alloying elements (e.g.  $\text{Mg}_2\text{Al}_3$ ), and unoxidised aluminium in the oxide [55,56], which were identified by dissolving the oxide film, and it was thereby not further located in the anodised layer. The unoxidised aluminium was expected to be connected to the undissolved alloy constituents [55,56]. The amount of unoxidised aluminium increased with increasing current density, however, much of it could be oxidised by subsequent heat treatment [55,56]. Irregular cell structures were found around holes in the anodised layer, and were also ascribed to some optical loss. The loss happens mainly in the polarisation direction of the light parallel to the pores [55,56,65].

Tabrizian et al. [57] investigated high gloss diamond turned samples after heat treatment and anodisation. Heat-treated specimens had lower reflection intensity after anodisation compared to non-heated and anodised specimens. It was concluded that the oxide-substrate interface roughness had no effect on the appearance, but instead that inhomogeneity and imperfections in the anodised layer had the largest effect, especially the presence of silicon and  $\text{Mg}_2\text{Si}$  [57]. Whether these particles were unchanged or oxidised during anodisation was not further investigated, however, as presented in Table 2.4,  $\text{Mg}_2\text{Si}$  phases are preferentially oxidised or dissolved in an aluminium matrix during anodisation, while silicon particles are unchanged and incorporated into the anode film [12,13].

Other parts of the literature focus on miscolouring of extruded and rolled specimens with focus on the morphology of the interface between the anodised layer and the substrate. The optical properties of anodised aluminium is affected during mechanical treatments like extrusion, rolling, polishing, etc., and chemical treatments like etching, electropolishing, and anodisation. Fig. 2.16 gives an overview of the common surface structures that affect the optical appearance apart from regular surface roughness.

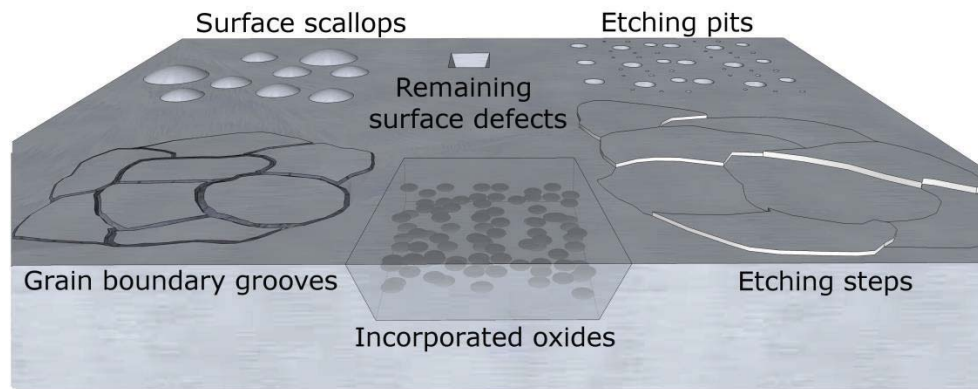


Fig. 2.16 – Surface structures affecting the visual appearance, created before or during etching and anodisation.

Rolling creates a disturbed layer of fine grains, rolled-in oxides and finely distributed intermetallics, where especially **incorporated oxides** [22–24,58] and carbon from lubrications [58] cause absorption of light to a reflectivity level about 10 %-points lower than magnetron sputtered aluminium [24]. **Grain boundary grooves** created during etching increase the diffuse reflection on aluminium extrusions and are created by iron and  $\text{Mg}_2\text{Si}$  intermetallics [16,59], and high angle grain boundaries [59,60]. **Surface scallops** have similar optical effects as grain boundary grooves and are created during etching and anodisation due to alloying elements such as iron and silicon, acting cathodic to the aluminium matrix [61,62]. **Etching pits** are created due to alloying elements, where phases acting anodic to the matrix (e.g.  $\text{Mg}_2\text{Si}$ ) cause pits of sizes similar to the particle [12,16], whereas phases acting cathodic to the aluminium matrix are excavated from the matrix and create pits of sizes up to  $10\text{ }\mu\text{m}$  [12,16,17]. **Etching steps** are created when the etchant or electrochemical dissolution of the surface is grain or subgrain orientation dependant, meaning that different textures will have different densities of etching steps [62,63]. Interference effects occur due to etching steps in a similar way as illustrated for interference colouring in Fig. 2.4, page 18. The largest effect on surface texture for aluminium extrusion profiles is the die design [63], however, also coarse intermetallics affect the surface texture [59,64].

For rolled and extruded specimens, the most important visual factor is a homogeneous appearance, and therefore a homogeneous distribution of the surface structures described above. It is important to control the alloy composition since all the structures mentioned above are affected by alloying elements. Proper etching can often prevent miscolouring of both rolled [21–24] and extruded [17,25] specimens due to removal of near surface heterogeneities.

#### 2.4.6 Visual appearance of recycled wrought aluminium alloys

The demand for secondary wrought aluminium is increasing, and it is expected that recycled aluminium alloys contain higher amounts of impurities and alloying elements. Some elements such as magnesium seem to have much smaller effect on the appearance than others such as iron. Premendra et al. [58] found that rolled AA1050 showed a total reflectance of around 90 %, whereas recycling the same alloy caused higher concentrations of iron, silicon and manganese, and a total reflectance of only 82 % was measured.

### 2.4.7 Structural colouring of aluminium

Structural colours appear due to nano- and/or microstructures in the material itself. These colours do therefore not degenerate when exposed to UV light. Structural colours are known from e.g. soap bubbles (thin film interference), the sky (Rayleigh scattering), rainbows (dispersion), and CD's (diffraction). Previous non-industrial studies [66–72] on structural colours in anodised aluminium have focused on thin film interference.

The colour saturation of the structural colours has been found to be enhanced, when using a dark substrate as background [66,67]. Furthermore, Xu et al. [68] enhanced the colours of a thin barrier type anodised aluminium layer by etching away the substrate, having only the anodised film left. Van Gils et al. [66] studied thin film interference of barrier type anodised layers on aluminium and titanium, where the colours on titanium were more saturated, due to the substrate colour and the higher absolute refractive index of the  $\text{TiO}_2$  compared to  $\text{Al}_2\text{O}_3$  [66].

Some techniques have been tested for creation of thin film interference, with easily tuneable colours. On an aluminium substrate, a thin silver layer was deposited, and subsequently a layer of aluminium, which were anodised making it transparent [69]. Nickel nanowires were grown in the pore bottoms, creating interference colours [70], and thin films of chromium or gold deposited on top of the anodised layer have also shown colourful reflection [71,72]. Liu et al. [67] alternated the current density during anodisation, creating 145 layers of alumina of alternating porosities and therefore of different indices of refraction, giving clear and colourful reflections.

## 2.5 Corrosion properties of aluminium and its alloys

Aluminium is an amphoteric metal, corroding in strong acidic and strong alkaline conditions (as  $\text{Al}^{3+}$  and  $\text{AlO}_2^-$  respectively) [73] as presented in Fig. 2.17. The figure is based on the thermodynamic calculations in the HSC Chemistry software [10], where the stability is calculated to be in the pH interval 4.7 – 9.7 for an Al-molarity of  $10^{-6}$ . Hydrargillite, which is the  $\gamma$ -phase of aluminium hydroxide ( $\text{Al}(\text{OH})_3$ ) is the thermodynamically stable phase in water at room temperature, whereas Böhmite ( $\text{AlOOH}$ ) is the thermodynamically stable phase at temperatures above 80 °C [38].

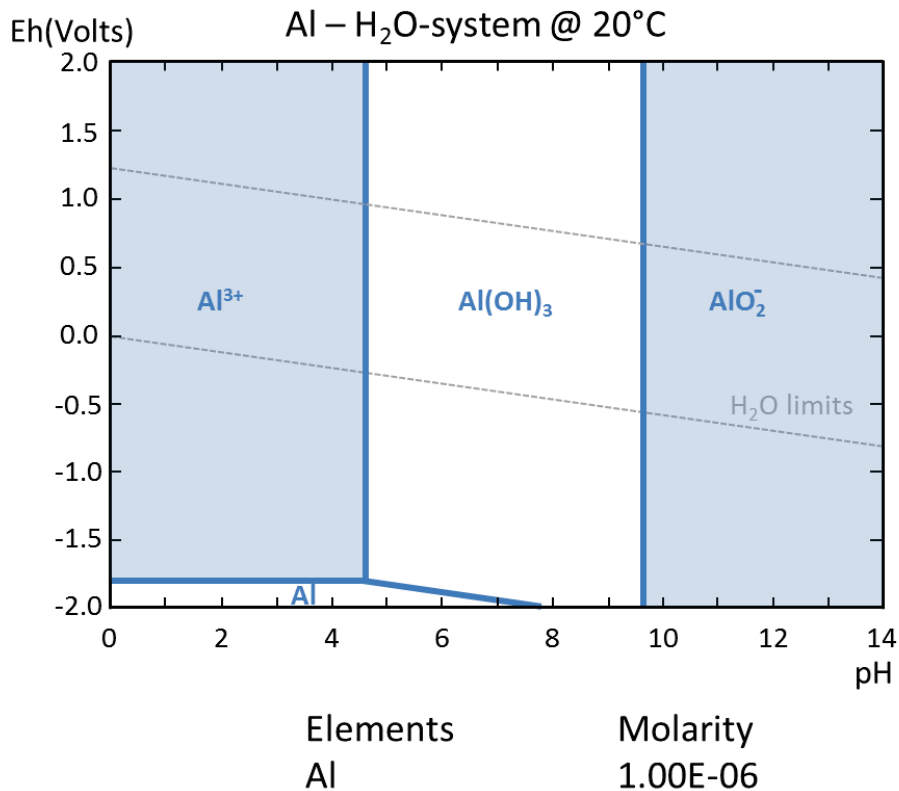


Fig. 2.17 - Pourbaix diagram of aluminium in water [10].

Aluminium and aluminium alloys are in general resistant to uniform corrosion attacks in mild environments due to the naturally formed tenacious oxide film. In environments containing pitting agents such as chloride, pitting might happen due to local breakdown of the oxide film. The corrosion properties of aluminium alloys are mainly affected by the chemical composition and microstructure of the alloy. Work-hardenable alloys have in general good corrosion properties, whereas age-hardenable alloys are more corrosion prone. Intergranular corrosion of aluminium alloys largely depends on the microstructure of the alloys and the second phase particles in the microstructure such as at grain boundaries. Copper containing age-hardenable aluminium alloys can cause intergranular corrosion due to the precipitation of cathodic copper containing phases at the grain boundaries, while the adjacent part of the grain boundary forms a precipitate free zone with less amount of copper. In this case grain boundaries with copper containing precipitates act as cathode causing corrosion along the anodic precipitate free zone. Similar intergranular corrosion is also known from the cathodic iron-rich particles [74], while for 5xxx and 7xxx series, formation of anodic grain boundary precipitates initiate intergranular corrosion along the grain boundaries. Cathodic intermetallics such as iron- and copper-rich precipitates have also been reported to cause filiform corrosion [75].

Aluminium and its alloys corrode normally by pitting in the neutral pH range, and experience uniform corrosion in more acidic and alkaline environments. Aluminium corrodes when exposed to many common acids, including phosphoric (H<sub>3</sub>PO<sub>4</sub>) and chromic (H<sub>2</sub>CrO<sub>4</sub>) acid, however, combining phosphoric and chromic acids stabilise the metallic aluminium surface. The corrosion rate is not necessarily connected to the pH value [1,76], e.g. in acetic acid (C<sub>2</sub>H<sub>4</sub>O<sub>2</sub>) and sodium disilicate (Na<sub>2</sub>O<sub>3</sub>Si) the corrosion rate decrease with



increasing concentration. Additionally, aluminium is inert to strong nitric acid ( $\text{HNO}_3$ ), but corrodes when the nitric acid is diluted. Alloys from the 5xxx series containing more than 4 % magnesium is known to have some resistance to sodium hydroxide ( $\text{NaOH}$ ) and potassium hydroxide ( $\text{KOH}$ ) [76], due to the higher migration rate of  $\text{Mg}^{2+}$  compared to  $\text{Al}^{3+}$  during anodisation, giving a high concentration of magnesium in the upper anodised layer [77].

### 2.5.1 Corrosion properties of recycled aluminium alloys

As previously stated, secondary aluminium alloys are often of lower purity compared to the primary alloys. The problematic sorting and refining processes cause the amount of unwanted alloying elements and impurities (especially iron [42,43]) to increase. Ambat et al. [78] investigated the corrosion properties of the deformed surface layer compared to the bulk of a rolled Al-0.4 Fe-0.3 Si-1.0 Mn alloy in 5 % NaCl at pH 3.0 and 11.5. It was found that the deformed surface layer showed higher cathodic reactivity due to higher concentration of Fe- and Mn-rich phases [78]. Chino et al. [43] investigated extrusions of AA5083, where one was produced by solid state recycling. It was found that the secondary alloy contained almost three times as much iron (0.74 wt. %) as the primary alloy and that the suffered weight loss during immersion testing in 3 wt. % NaCl solution was two times larger than that of the primary alloy [43].

### 2.5.2 Alkaline corrosion protection of aluminium alloys

Regular aluminium alloy surfaces and anodised aluminium surfaces have very little resistance in highly alkaline conditions, such as at pH 12 – 13 due to the amphoteric nature of aluminium. Both **hot water sealed** and **steam sealed** anodised aluminium surfaces consists of aluminium oxides, which are soluble in alkaline conditions, although corrosion properties under normal conditions are excellent [38].

**Chromate sealing** has previously been a popular sealing process together with chromium conversion coatings [79,80] due to the excellent passivating properties of chromium in alkaline media. Chromate sealing use either  $\text{K}_2\text{Cr}_2\text{O}_7$  or  $\text{CrO}_3$  to create aluminium oxydichromate ( $\text{AlOHCrO}_4$ ) or aluminium oxychromate ( $(\text{AlO})_2\text{CrO}_4$ ) in the pores [38]. Chromate sealing has been used as base for paints, where cracks and holes in the paint are less problematic due to the instantaneous passivation of the chromium [81]. Due to environmental issues the chromate sealing is only used in industries with special authorisation e.g. for military use.

**Nickel salt sealing** e.g. combining nickel acetate and nickel fluoride is currently used as sealing method e.g. in the automotive industry where alkaline corrosion protection is needed [38,82,83]. Nickel salt sealing shows good corrosion properties to at least pH 12 in NaOH, however, at higher pH values, the protection is not flawless. Due to environmental and health issues alternatives to the nickel salt sealing are needed.

**Sol-gel** coatings use a colloidal solution (sol) to create an integrated network (gel). E.g. a metal salt can be used as a precursor reacting with an organic compound causing it to solidify on the surface during evaporation, creating a gel. Sol-gel creates an intermediate layer with good adhesion to both the substrate

and the top layer [84]. The main advantages of the sol-gel process is that it create an environmentally friendly coating on complex shaped products at low temperatures [85]. Sol-gel coatings have proven good corrosion protection of aluminium in saline and acidic [81,86–88] and in alkaline conditions [81,89,90]. Zhang et al. [89] used sol-gel to coat aluminium pigments with silica, which showed good results at pH 11 in a NaOH solution. Hirai et al. [90] used zirconium oxide sol-gel on commercially pure aluminium and found that the alkaline corrosion resistance increased by a factor of 24 – 50. However, no studies for pH-values above 11 have been found. It came up at the defence that Si-based sol-gel solutions are used for most German high-end cars [91].

Literature studies on the use of titanium as protecting element using magnetron sputtering and laser surface cladding is given in sections 3.3.4, page 41 and 3.4.5, page 44 respectively.





---

### 3 Creating aluminium-titanium coatings

---

Creating homogeneous bulk aluminium alloys with non-equilibrium composition is very difficult due to the formation of various microstructural phases during the solidification process. However, some surface coating methods can be used to create coatings with desired alloy compositions including non-equilibrium levels of alloying elements. In the current project aluminium coatings with up to 18 wt. % titanium was created as a model system for studying the optical scattering effects after heat treatment and anodisation, and the saline and alkaline corrosion protection in the as-deposited and heat-treated states. Physical vapour deposition (PVD) with focus on magnetron sputtering and laser surface processes with focus on laser surface cladding (LSC) are described in the following sections. The PVD process is expensive and normally used for making thin films and coatings, whereas the LSC process is much cheaper and used for making thicker coatings. Both techniques allow creation of metastable coatings with well-defined chemical compositions. The PVD coatings are applicable for expensive high end design products. Furthermore, it can be used as a test system and in some cases for production method for corrosion protection dependent on product type and cost considerations, whereas the LSC coatings might be usable for corrosion protection of larger products.

#### 3.1 Corrosion properties of titanium

Titanium has a very high strength to weight ratio and is therefore often used for sports equipment such as rackets and golf clubs. Additionally, titanium has extraordinary corrosion properties, due to a tenacious instantaneously forming oxide film, so that it is normally the mechanical rather than corrosion requirements that define the wall thickness of titanium parts [76]. Previously, anodisation of titanium was recommended for corrosion protection, however, the anodised layer does not seem to improve the corrosion resistance of titanium [76,92].

A thermodynamically calculated Pourbaix diagram [10] is presented in Fig. 3.1, showing that titanium is resistant to corrosion for conditions from pH 0 – 14. Normally, it is expected that titanium is stable in an even wider regime. Some references [73,76,93] include regimes of  $\text{Ti}^{2+}$  and  $\text{Ti}^{3+}$  in strong acidic conditions at low potentials [93] and  $\text{HTiO}_3^-$  at pH 12 and more [76]. Pourbaix [73] includes one diagram including anhydrous oxides with only acidic corrosion, and both acidic and alkaline corrosion when including hydroxides and hydrated oxides. Even though these phases are reported, the formation is expected to be very slow due to kinetics, and titanium is expected to be highly resistant at all pH conditions.

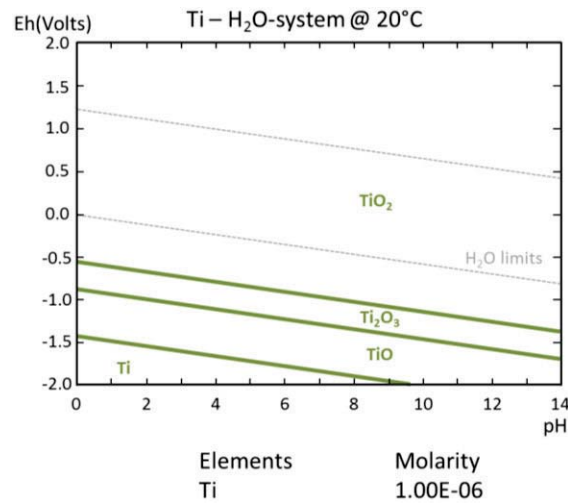


Fig. 3.1 – Calculated Pourbaix diagram for titanium in water with ion activity of 10<sup>-6</sup> at 20 °C [10].

From various sources it can be found that titanium show very good resistance towards saline compounds and many common acids like hydrochloric acid (HCl) and H<sub>2</sub>SO<sub>4</sub>, however, e.g. hydrogen fluoride (HF) cause titanium to corrode heavily [76,92,93]. Titanium is normally protected in alkaline media, showing very low corrosion rates in NaOH, KOH and ammonium hydroxide (NH<sub>4</sub>OH), which increase with temperature and concentration [92,93] as found for NaOH in Table 3.1. It is important to notice that hydrogen evolution during exposure may cause hydrogen embrittlement, especially for pH > 12 and temperatures > 80 °C [92,93].

Table 3.1 - Corrosion rates of unalloyed titanium in NaOH solutions [92].

NaOH conc. (wt. %)	Temperature (°C)	Corrosion rate (mm/y)
5-10	21	0.001
40	66	0.038
40	93	0.064
50	38	0.002
50	66	0.018
50	121	0.033
50-73	188	> 1.09
73	110	0.051
73	116	0.127
73	129	0.178
75	121	0.033

## 3.2 The Al-Ti system

### 3.2.1 Al-Ti phase diagram

The binary Ti-Al phase diagram is presented in Fig. 3.2, where the zone relevant for the coating composition used in the present study is marked in grey. The thermodynamically stable phases for titanium concentrations up to 20 wt. % are  $\alpha$ -Al and  $\text{Al}_3\text{Ti}$ . The  $\text{Al}_3\text{Ti}$  is strictly stoichiometric at 25 at. % titanium (37 wt. %).

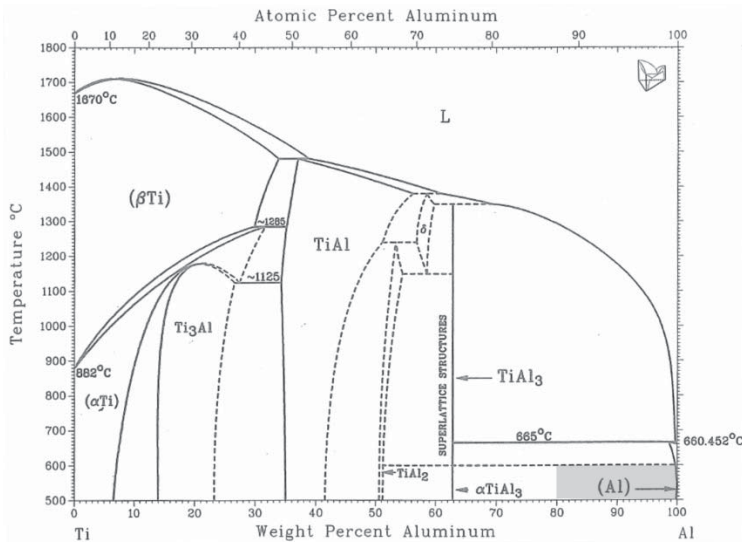


Fig. 3.2 - The binary Ti-Al phase diagram [94].

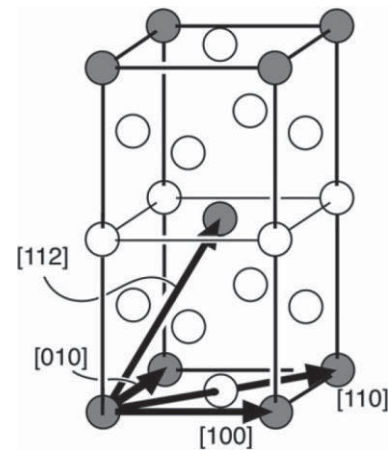


Fig. 3.3 - The  $\text{D0}_{22}$  crystal structure [95]. White atoms: Al, dark atoms: Ti.

The crystal structure of  $\alpha$ -Ti is hexagonal close-packed (HCP), while it is face-centred cubic (FCC) for aluminium. The  $\text{Al}_3\text{Ti}$  phase has the  $\text{D0}_{22}$  crystal structure [95–97] as presented in Fig. 3.3, which is based on two face-centred tetragonal (FCT) cells.

### 3.2.2 The use of titanium in aluminium alloys

Quantities of up to 0.15 wt. % titanium is used as grain refiner in age-hardenable aluminium alloys due to the creation of small  $\text{Al}_3\text{Ti}$  precipitates pinning the grain boundaries counteracting grain growth. Up to 1 wt. % titanium can be obtained in  $\alpha$ -Al near the melting temperature of aluminium, however, with 0.35 wt. % titanium, titanium rich phases will precipitate, even at cooling rates of 100 K/s [98].

## 3.3 Physical Vapour Deposition

The PVD process is running in a vacuum chamber containing the target from which material is sublimated (atomised) to cover everything in the line of sight, including the specimens. Therefore it is the chemical composition of the target(s) that defines the composition of the coating. The coating is mechanically bonded to the substrate and adjustments of the process can be necessary to achieve sufficient bonding. PVD coatings are made in thicknesses from a few nanometres to several microns; however, thicker coatings are time

consuming and cause stresses to build up, which can cause the coating to peel. PVD is a plasma process, and therefore the plasma creation in the chamber is briefly described.

#### 3.3.1 Plasma

By raising the temperature of an atom/molecule the electrons will continuously move faster and above a level of temperature some electrons will be removed from their atom/molecule, creating an ionised gas, also called plasma, a term suggested by Langmuir in 1928 [99]. For PVD processes, a gas is led into a vacuum chamber where the plasma is created. The plasma consists of three types of particles:

- Atoms and molecules (neutral)
- Ions (positively charged)
- Electrons (negatively charged)

Although the degree of ionisation is often less than 0.1 %, the charged particles cause the plasma to be electrically conducting [11]. Plasma can be created both thermally as described above and by electrical discharges, sometimes called electrical ionisation. In electrical ionisation, the plasma is produced in an electric field between a positive anode and a negative cathode. Whenever an electron is removed from a neutrally charged atom/molecule, a negatively charged electron and a positively charged ion is formed. Electrons will be attracted by the anode and is likely to hit more atoms/molecules creating more ions and additional free electrons and thereby maintaining the plasma (Fig. 3.4a). Furthermore, ions will be attracted and collide with the cathode, creating additional free electrons [100]. Fig. 3.4b illustrates the voltage drop between the anode and the cathode. The charged particles are only accelerated when they are subjected to a field change, i.e. near the electrodes. The energy of the electron created when a positively charged ion bumps into the cathode is therefore critical regarding how many of the subsequent hit electrons that will have enough energy to maintain the plasma by hitting other electrons. Apart from hitting other particles, electrons lose energy by excitation of atoms/molecules, subsequently emitting a photon causing the plasma to light up. This energy is wasted in connection to the maintenance of the plasma. Notice that the actual potential in most of the plasma is positive (Fig. 3.4b), which is due to the fact that electrons have higher velocity and will therefore more often leave the plasma than the ions [11,100].

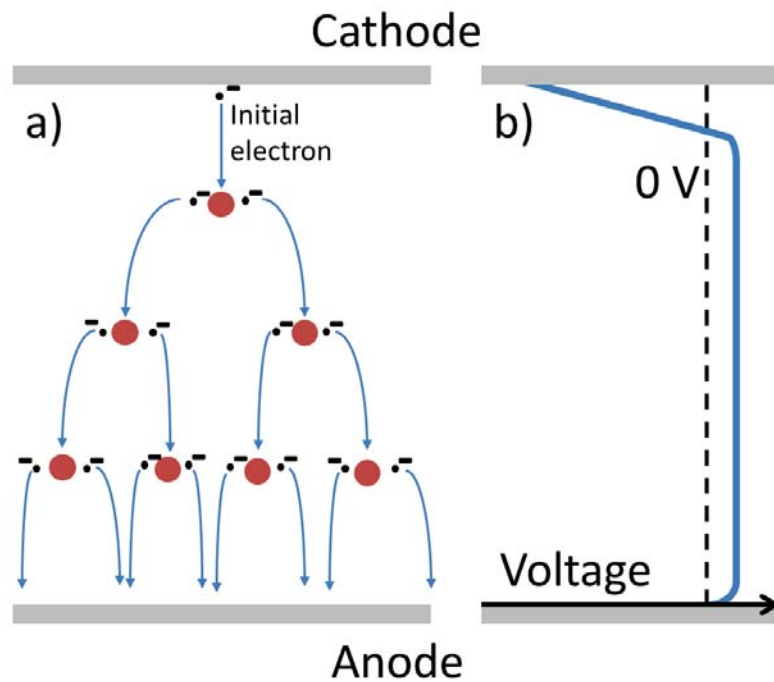


Fig. 3.4 - Anode and cathode for electrical ionisation, inspired by [11].

a) Initial electron causing subsequent electrons to be torn loose.

b) Voltage drop over anode/cathode region.

PVD processes are divided into reactive and non-reactive processes. In reactive processes the chamber is supplied with a gas, reacting with the target-gas atoms. This type of process is used for creation of e.g. titanium nitride (TiN) and titanium dioxide (TiO<sub>2</sub>). In the following part, focus will be on non-reactive magnetron sputtering.

### 3.3.2 Magnetron sputtering

In the magnetron sputtering process (Fig. 3.5) the ionized atoms in the plasma, (usually argon  $\text{Ar}^+$ ) is attracted to collision with a target at high speed sublimating the surface atoms of the target. It is the cathodes situated behind the targets that attract the argon ion, causing the collision with the targets.

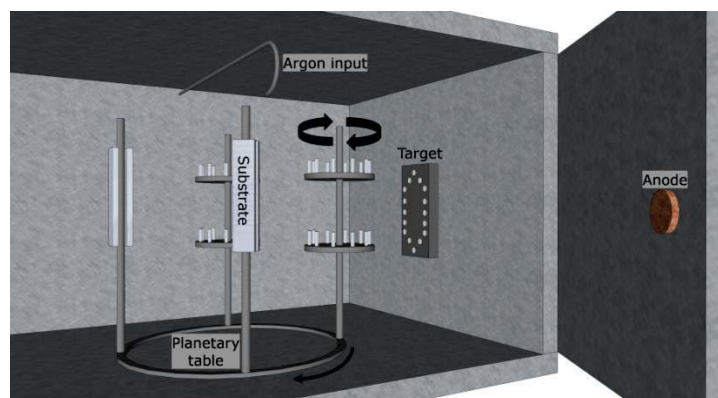


Fig. 3.5 - Illustration of chamber used for magnetron sputtering.

The amount of target atoms that are atomised per incident particle is called the sputtering yield or the sputter coefficient of the target material. The sputtering yield is element dependent and is plotted as a function of atomic number in Fig. 3.6.

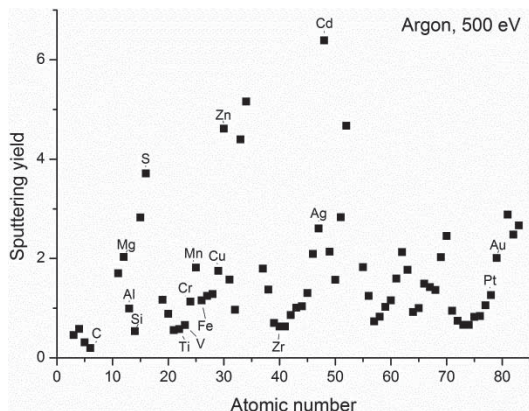


Fig. 3.6 - Sputtering yields when hit by argon ions at 500 eV at an angle of 0°. Data from [101].

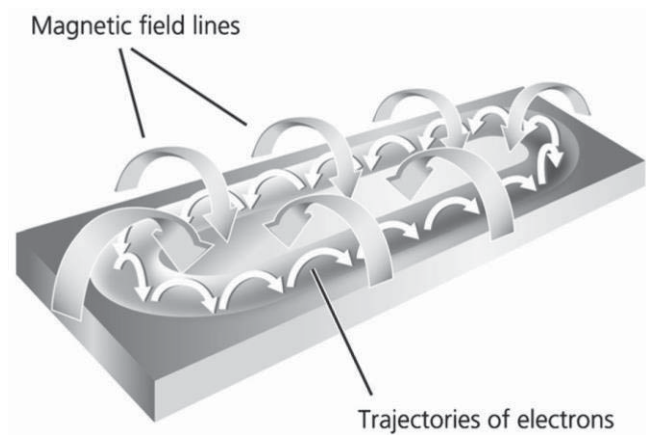


Fig. 3.7 - Magnetic field lines and for magnetron sputtering [102].

Magnetron sputtering is increasing the deposition rate and ionisation efficiency in the plasma, while lowering the substrate heating effects compared to regular sputtering [103]. A magnetic field close to the target (cathode), perpendicular to the electric field is imposed by the electrodes as illustrated in Fig. 3.7 [102]. The magnetic field forces particles to circulate through the magnetic field instead of moving in a straight line to the anode [100]. The number of collisions is raised due to the elongated path and the plasma can therefore be maintained at a lower pressure. A conventional DC-diode sputter operates at 0.5 Pa – 10 Pa whereas magnetron sputtering can operate at 1 mPa – 1 Pa [11]. The reduced pressure leads to less contamination of the process and increases the mean free path of the target particles. This increase the speed and thereby the energy of the target particles when hitting the substrate giving a denser coating.

One disadvantage of magnetron sputtering is low usage of the target, which is in general less than 30 %. However, this can be improved by applying an extra magnet in the centre of the cathode or unbalancing the magnets [102].

A bias voltage on the specimen holder can be applied, changing the charge of the specimens. This is used for sputter cleaning the specimens in the beginning of the process and for changing the energy of the surface layer during the coating process.

#### 3.3.3 Coating structure model

The microstructure of the deposited film is dependent on the process parameters. For an overview, Thornton [104] made a structure model for oxygen free high thermal conductive copper (Fig. 3.8), which has shown to be valid for other systems as well.



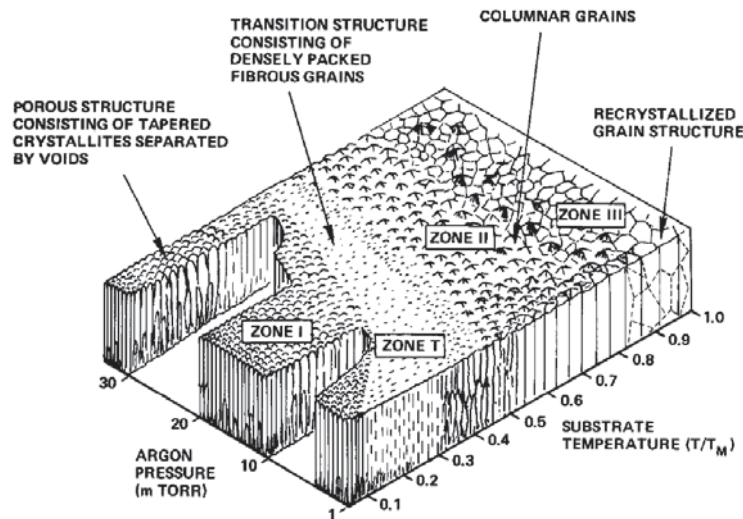


Fig. 3.8 - The Thornton structure model showing microstructure of magnetron sputtered coatings as a function of argon pressure and substrate temperature [104].

The model is divided into three main zones and a transition zone, T, where the structure changes from columnar and porous, to a dense columnar, and to equiaxial as the substrate temperature increases. Later studies have revised and refined the structure model [103,105,106]. The zones are results of shadowing effects (zone 1), surface diffusion (zone 2), and bulk diffusion (zone 3) making them independent of the actual deposition technique [105]. Messier et al. [105] found that the T zone is a subzone of zone 1, however, later references keeps the T zone in their descriptions [11,100] and it is expected to be present since different grain boundaries become mobile at different temperatures [100]. It is known that gas pressure, gas composition, ionization degree, substrate bias and temperature all affect the coating quality [11], and it has therefore been discussed whether the y-axis should describe other or combined parameters and whether more dimensions are necessary for an accurate model [103].

### 3.3.4 Magnetron sputtered Al-Ti coatings

The microstructure and mechanical properties of magnetron sputtered Al-Ti coatings have previously been investigated [107–110]. Sanchette and Billard [107] found that as-deposited Al-Ti coatings contain the  $\alpha$ -Al phase for titanium concentrations up to 40 wt. %. Others [108,110] have supported this finding, however, Oliviera et al. [110] found the change at 57 wt. % titanium. The fact that such large titanium concentrations is possible in supersaturated aluminium in as-deposited coatings were ascribed to that both crystal structures are closed packed (Al: FCC and Ti: HCP) and have similar atomic radii (Al: 0.143 nm and Ti: 0.146 nm). Amorphous structures was found for titanium concentration up to 60 wt. % [107] and 79 wt. % [110], above which supersaturated  $\alpha$ -Ti was found. In Fig. 3.9 is presented the different phases as found in [107], where the white intervals are amorphous phases with some amount of either  $\alpha$ -Al or  $\alpha$ -Ti.



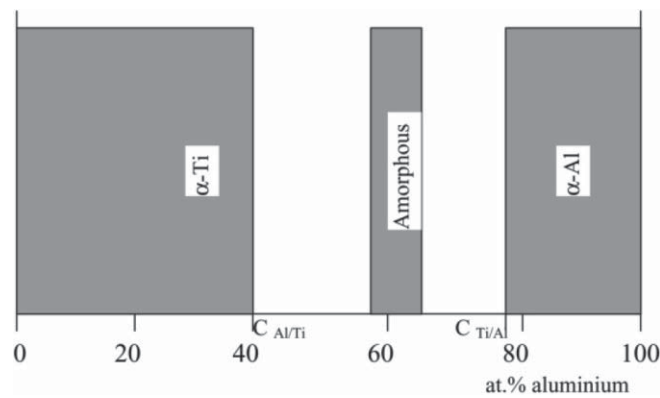


Fig. 3.9 – Phases of magnetron sputtered Al-Ti coatings as a function of aluminium concentration (at. %) [107]

Al-Ti coatings have been investigated after annealing at 600 °C for 1 h [110] and 2 h [108,109]. Hampshire et al. [108] found for titanium concentrations of 32 wt. % that during heat-treatment, the  $\text{Al}_3\text{Ti}$  phase precipitated, as expected from the phase diagram (Fig. 3.2, page 37). Others have used the Al-Ti system to investigate the porous self-organising structures during anodisation varying the titanium concentration and voltage in sulphuric acid with and without hydrogen fluoride [111,112]. It was found that the pore size increases with the titanium concentration and the voltage [111,112].

Addition of titanium in magnetron sputtered aluminium coatings improves corrosion properties in both saline [107,113,114] and in 1 M hydrochloric acid (HCl) [115–118]. Akiyama et al. [117] found additionally that ternary systems of aluminium and titanium combined with especially chromium or nickel improved the results in 1 M HCl even further. No literature has been found on the alkaline corrosion properties of magnetron sputtered Al-Ti coatings.

### 3.4 Laser surface processes

Three basic laser surface treatments are laser surface melting (LSM) [119], laser surface alloying (LSA) [119] and laser surface cladding (LSC) [120]. LSM and LSA will briefly be described; but, the main focus will be on LSC.

During LSM a laser run over the surface line by line to melt the top surface layer of the specimen. The material instantaneously quenches the molten surface due to the large size (thermal mass) of the specimen compared to the size of the molten area. Quenching rates up to  $10^{11}$  K/s [121] creates a nanocrystalline surface, improving mechanical and/or corrosion properties of the surface [119].

LSA is similar to LSM, however in this process one or more alloying elements are added in the form of powder or wire. In this way the top surface layer is alloyed to enhance mechanical or chemical properties [119].

#### 3.4.1 Laser surface cladding

In LSC, the original product is coated with a layer of added material, so that none of the original surface is a part of the final coating surface. LSC is both used for initial coating production and for repairing products at a workshop or on site. Coating by LSC is an efficient way to achieve high quality coatings of thicknesses 0.2 mm – 2.5 mm (typically 0.5 mm – 1.0 mm) with low porosity, few imperfections and very good adhesion by metallurgical bonding. LSC can be done on both flat surfaces and surfaces of more complex shapes. No excess clad material is needed and only the power needed for melting the upper substrate surface and the clad material is used. The clad material is only slightly diluted (1 % - 5 %) by the substrate material [122] and it is possible to incorporate e.g. oxide and carbide particles. The drawbacks of LSC are mainly the large initial investment and the restrictions described below.

#### 3.4.2 Substrate material

All materials that can stand laser melting are in principle usable as substrate, however, high thermal conductivity is needed to ensure a strong bonding to the clad and metals are therefore often used. Most claddings are done on substrates of carbon-manganese and stainless steel, and to some extent alloys based on aluminium, titanium, magnesium, nickel and copper [122]. An unfortunate side effect when using aluminium as substrate material is, that aluminium has a tendency to warp (change shape) when heated above 200 °C. It is therefore important to keep the overall temperature at a minimum when using aluminium substrates, while the near surface temperature increases to the level needed for melting.

#### 3.4.3 Clad material

The clad material is added by wire, foil or powder, where the powder can either be placed on the surface initially (predeposition) or be added through a nozzle during the process (codeposition). For coaxial codeposition [123] as illustrated in Fig. 3.10, the powder nozzle is situated around the laser, which has shown several advantages when cladding aluminium [124]. A shielding gas (e.g. argon) is often used, to ensure that atmospheric air does not react significantly with the clad. The inflow and geometry of the clad material should be adjusted to the specific process. LSC is usually done by codeposition of clad alloys based on cobalt, iron, nickel, titanium and silicon, where the chemical composition of the coating can be altered by mixing different powders. Not all materials can be combined, e.g. a large difference in thermal expansion coefficients might cause cracking during coating and cooling.

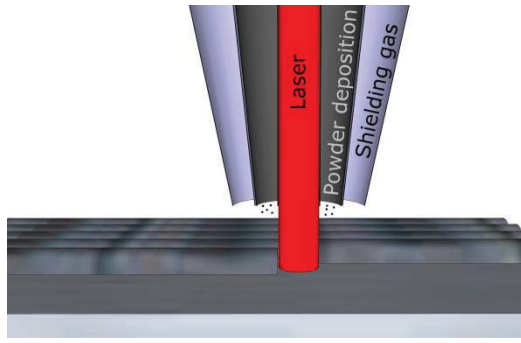


Fig. 3.10 – The laser cladding process with shielding gas and codeposition of powder.

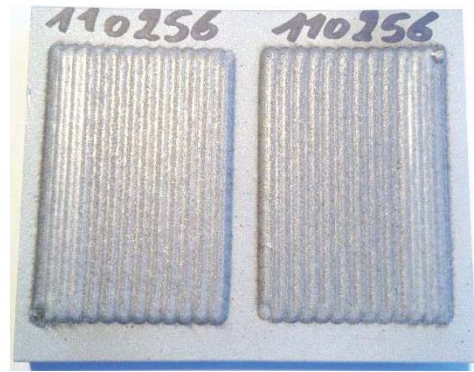


Fig. 3.11 - Laser surface cladded specimen with overlapping tracks.

#### 3.4.4 The laser

The choice of laser is highly dependent on the application. CO<sub>2</sub> lasers are used for large areas and thick coatings on specimens with a regular geometry, whereas diode or Nd:YAG lasers are suitable for precise and thin coatings on products with a complex geometry [122]. The laser power needs to be of a magnitude enabling the clad to melt, however, too high power will cause excess substrate to melt, creating unwanted diffusion and a larger heat affected zone beneath the coating. A laser power of at least 2 kW, with an interaction time of 1 s, and power density of approximately 100 W/mm<sup>2</sup>, is often used [122]. The shape of the laser beam and the heating pattern are also parameters that are necessary to consider. When cladding larger areas sequentially overlapping tracks are used as seen in Fig. 3.11.

#### 3.4.5 Laser cladding of Al-Ti coatings

Some previous studies have investigated the LSC of aluminium and titanium, however, only with focus on titanium coatings containing up to 35 wt. % aluminium [125–127]. Others have used LSA to create aluminium surfaces containing titanium [128–131]. An  $\alpha$ -Al matrix containing Al<sub>3</sub>Ti intermetallics was found in LSA aluminium coatings containing 37 wt. % titanium [128] and when using a titanium wire on an 99.5 % pure aluminium substrate [129]. LSA titanium on AA1200 [130] gave similar structures and additionally the AlTi phase was found, due to a higher titanium concentration as found from the phase diagram of Al-Ti (Fig. 3.2, page 37). Wendt et al. [129] found that the supersaturated  $\alpha$ -Al-phase contained 4 wt. % titanium, whereas other studies [128,130] identified the  $\alpha$ -Al phase by XRD.

LSM gives a fine microstructure with small grains improving the corrosion properties in some cases, whereas for LSA the alloying elements enable improved corrosion properties. However, for both LSM and LSA of aluminium, it has only been possible to find studies on corrosion properties in saline and acidic conditions [119,121,132–136]. LSC studies have only been found for saline and acidic conditions and for oxidation resistance [131,137,138] but none for alkaline corrosion protection. Watkins et al. [136] studied the effect of chromium, tungsten, zirconium, titanium and nickel in aluminium based clads. It was found that the best results were achieved with an Al-Ti-Ni system, where the pitting potential in 1 M NaCl increased by

450 mV compared to as-received AA2014 and 285 mV compared to a AA2014 specimen treated with LSM. Coatings containing Al-0.3TiO<sub>2</sub>-0.3SiO<sub>2</sub> increased the corrosion potential and decreased the corrosion current density in a solution containing 3.5 wt. % NaCl [138].



---

## 4 Materials and methods

---

### 4.1 Materials

#### 4.1.1 Wrought aluminium specimens

Four commercial alloys were studied to investigate the optical and microstructural effects of alloy composition during polishing, etching, anodisation, and hot water sealing. Specimens of 50 mm x 50 mm in size of AA1050, AA5754 and AA6082 of 1 mm sheet and Peraluman706 (P706) of 2 mm sheet were used for investigations reported in article 1. The chemical compositions of the alloys are presented in Table 4.1.

Table 4.1 - Chemical composition of the investigated wrought aluminium alloys.

	Mg	Si	Fe	Cu	Mn	Zn	Ti	Cr	V
AA1050	0.05	0.25	0.4	0.05	0.05	0.05	0.03		0.05
P706	0.3-0.8	0.2	0.2	0.03-0.1	0.05	0.05	0.03	0.02	
AA5754	2.6-3.6	0.4	0.4	0.1	0.5	0.2	0.15	0.3	
AA6082	0.6-1.2	0.7-1.3	0.5	0.1	0.4-1.0	0.2	0.1	0.25	

#### 4.1.2 Polishing

Hard wheel polishing was done with a glinse paste, M8005 from Lea, containing  $\text{Al}_2\text{O}_3$  as abrasive agent. After polishing, a soft disc was used for finishing and removing excess paste. Specimens investigated in the as-polished state were cleaned by ethanol. All polishing was performed using the industrial polishing facilities at B&O.

#### 4.1.3 Magnetron sputtered coatings

Several coatings were created by DC magnetron sputtering using an industrial-scale CemeCon800/8 machine (roughly illustrated in Fig. 3.5, page 39) with two cathodes. The chamber size was 700 mm x 600 mm x 600 mm with the cathodes (targets) placed on each side of a centred planetary rotating table on which the specimens were mounted. The specimens were applied a constant bias voltage of -50 V, and was situated approximately 100 mm from the targets. Evacuation of the deposition chamber was done to a base pressure of 6 mPa. A constant argon flow of 200 SCCM (mL/min) was supplied during the sputtering process, causing a typical argon pressure of 500 mPa. Using a bi-metal thermometer, it was found that the temperature reached maximum temperatures of 150 °C – 200 °C during deposition. The thicknesses of the coatings were calculated and sporadically checked with cross section LOM and SEM investigations. All coating compositions were analysed by Energy-dispersive X-ray spectroscopy (EDS) in the Jeol SEM described in section 4.2.4.

## 4.1.3.1 Coatings with homogenous concentration

For coatings with uniform compositions, substrates of AA465.0 (8 wt. % - 11 wt. % silicon and 2 wt. % - 4 wt. % copper) with dimensions of 70 mm x 25 mm x 4 mm were used. Reference coatings of 25  $\mu\text{m}$  were deposited using two targets of aluminium (AA1050, 99.5 % pure), both running at 1000 W. Binary Al-Ti coatings were deposited using an aluminium target running at 2000 W, and a titanium (grade 1, 99.5 % pure) target with cylindrical aluminium pins of 10 mm in diameter inserted into the target, as illustrated in Fig. 3.5, page 39. The Ti-Al target power, titanium concentrations, and thicknesses of the coatings are presented in Table 4.2.

Table 4.2 – Deposition power of the Ti-Al target and achieved titanium concentration (by EDS) and thickness of the deposited coatings.

<b>Ti-Al target power</b>	<b>Achieved titanium concentration</b>	<b>Coating thickness</b>
<b>100 W</b>	3 wt. %	11 $\mu\text{m}$
<b>200 W</b>	6 wt. %	11 $\mu\text{m}$
<b>400 W</b>	13 wt. %	21 $\mu\text{m}$
<b>600 W</b>	18 wt. %	20 $\mu\text{m}$

These specimens were heat treated according to Table 4.3 and subsequently cooled in air. After heat-treatment blisters were found at the surface of the specimens for specimens heat treated at 400 °C and more, as seen in Fig. 4.1. The specimens were used for photospectrometry measurements as in article 2 and alkaline corrosion tests as in article 3.

Table 4.3 – Heat treatment temperatures for coatings of various titanium concentrations.

<b>Temp. for 2 h</b>	<b>3 wt. % Ti</b>	<b>6 wt. % Ti</b>	<b>13 wt. % Ti</b>	<b>18 wt. % Ti</b>
<b>200 °C</b>			X	
<b>300 °C</b>	X	X	X	X
<b>400 °C</b>			X	
<b>500 °C</b>			X	

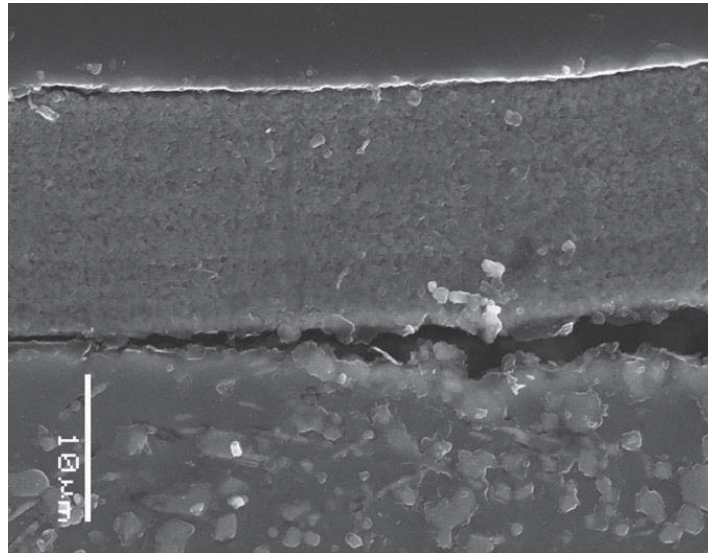


Fig. 4.1 – Cross section SEM image showing delamination of the magnetron sputtered film with 13 wt. % titanium due to outgassing from the cast substrate during heat treatment for 2 h at 500 °C.

#### 4.1.3.2 Gradient coatings

AA6401 (Table 4.4) substrates with dimensions of 220 mm x 40 mm x 5 mm were used for Al-Ti gradient coatings of varying composition along the length of the specimens. The coatings were deposited with the aluminium target running at 2000 W and the Ti-Al target running at 300 W, and the targets were displaced with respect to the centre of the chamber. This was done to achieve a varying deposition flux throughout the chamber, resulting in a coating of varying composition. These types of coatings are practical for screening experiments, since a single deposition creates several compositions.

Table 4.4 - Chemical composition of AA6401.

<b>Mg</b>	<b>Si</b>	<b>Fe</b>	<b>Cu</b>	<b>Mn</b>	<b>Zn</b>	<b>Ti</b>
0.35-0.7	0.35-0.7	0.04	0.05-0.2	0.03	0.04	0.01

Two gradient coatings were produced, and the compositions were measured at a lateral resolution of a centimetre. One specimen had concentrations of 5.0 wt. % - 15.4 wt. % titanium, and the coating thickness was found to increase with the aluminium concentration from 8 μm to 17 μm. This specimen was used for photospectrometry measurements after anodisation of the as-deposited coating (article 2) and saline and alkaline corrosion testing of the as-deposited film (article 3).

The other gradient coating was investigated in detail using EDS, in order to investigate the composition homogeneity across the width of the specimen. Three measurements were done at three different points (nine in total) across the width of the specimen. The mean values were measured to 6.5 wt. % - 16.6 wt. % titanium almost linearly along the length of the specimen as seen in Fig. 4.2a. The deviation from the mean of the nine measurements across the specimen is presented in Fig. 4.2b. The maximum deviation was about  $\pm$  0.4 wt. %-point titanium, with slightly higher concentrations measured in the right side, compared to the left



side of the specimen, when looked at with point 1 positioned downwards. This specimen was cut into four pieces of different concentration spans, which were heat-treated for 4 h at 500 °C and 600 °C and cooled in air followed by anodisation (article 2). Parts from this specimen were also used for detailed SEM, TEM, and scanning Kelvin probe force microscopy (SKPFM) investigations after heat treatment for 4 h at 600 °C and cooled in air (article 2 and 3).

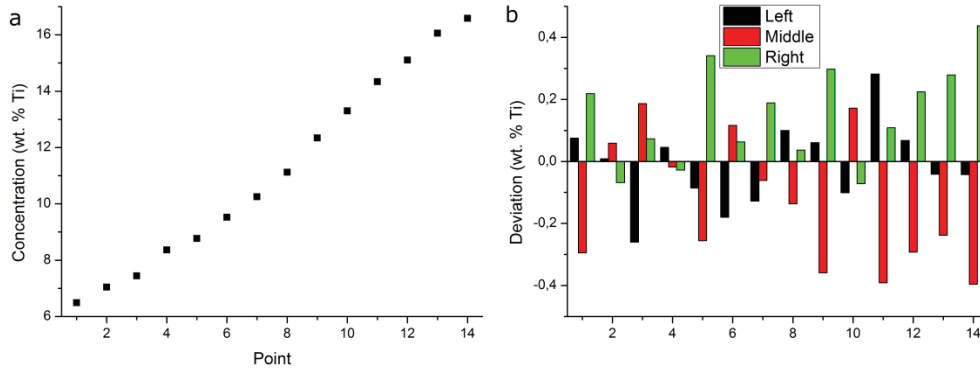


Fig. 4.2 – EDS measurements from Al-Ti gradient coating, a) titanium concentration per cm on gradient specimen, and b) Deviation from mean measurement in point.

#### 4.1.4 Laser surface clad coatings

LSC was done at VITO using substrates of AA6063, which were degreased and sand blasted as preparation for laser cladding. A powder mixture of 99.8 % pure aluminium and 5 wt. %, 10 wt. % and 20 wt. % of Ti6Al4V powder of sizes 45  $\mu\text{m}$  – 100  $\mu\text{m}$ , were fed at 4.8 g/min, 5.1 g/min and 5.2 g/min respectively for the different Ti6Al4V concentrations. The choice of Ti6Al4V was made due to the non-availability of pure titanium powder, and the maximum vanadium concentration of 0.8 wt. % was evaluated as acceptable. A Laserline diode laser with mixed wavelengths of 808 nm and 940 nm at 2.05 kW – 2.2 kW was used for cladding. A circular spot of 3.8 mm in diameter swept over the first six tracks at a speed of 1.0 m/min and afterwards at 1.3 m/min in order to limit dilution. Argon was used as transport and shielding gas.

The laser clad samples had a rough surface with clear tracks (Fig. 3.11), which were removed by milling and the specimens were subsequently polished in sequence until a final polish using a 1  $\mu\text{m}$  diamond suspension. Furthermore, a heat treatment for 10 h at 600 °C was done with the objective of homogenising the microstructure including the unmelted Ti6Al4V particles. The laser clad specimens were subsequently used for microstructural studies and corrosion testing at pH 13.5 (article 4).

#### 4.1.5 Anodisation process

For the wrought aluminium specimens (article 1) and the big as-deposited gradient specimen (article 2), the anodisation was done at B&O in the following industrial setup normally growing an anodised layer of approximately 7  $\mu\text{m}$  in thickness:

- Alkaline cleaning in AlfiClean from AluFinish at 60 °C for 2 min – 6.5 min with rough agitation.
- Cleaning (in demineralised water)
- Etching in 80 g/L NaOH and maximum 50 g/L aluminium at 60 °C for approximately 18.5 min (only for etched specimens).
- Cleaning
- Desmutting in 6 wt. %  $\text{HNO}_3$  at 27.5 °C – 28.0 °C for approximately 4 min.
- Cleaning
- Anodisation in 190 g/L  $\text{H}_2\text{SO}_4$  and 5 g/L – 10 g/L aluminium at 17.9 °C, for about 30 min with mild agitation, at a constant voltage of  $12.6 \text{ V} \pm 0.5 \text{ V}$  and a current density of about  $1 \text{ A/dm}^2$ .
- Cleaning
- Sealing in 2 g/L – 3 g/L AlfiSeal from AluFinish at 96 °C for 25 min.
- Drying at 74 °C – 78 °C for 3 min – 5 min.

Heat-treated magnetron sputtered Al-Ti coatings (article 2), were anodised at the in-house lab set up at DTU:

- Ultrasonic cleaning in ethanol for 5 min.
- Alkaline cleaning in AlfiClean from AluFinish at 60 °C for 2 min with agitation.
- Cleaning
- Desmutting in 69 % nitric acid at room temperature for 4 min.
- Cleaning
- Anodisation in 10 %  $\text{H}_2\text{SO}_4$  at 18 °C for 20 min at  $20 \text{ V} \pm 2 \text{ V}$ .
- Cleaning
- Sealing in demineralised water at 96 °C for 20 min.

## 4.2 Microstructural investigations

### 4.2.1 Oxide thickness measurements

Oxide thickness measurements (article 1) were done on a Nanocalc 2000 Thin film measurement system from Mikropack. The equipment calculates the oxide thickness based on thin film interference of infrared light in 25 points. Each specimen was measured at least two times, depending on consistency, giving a minimum of 50 measurements per specimen.

#### 4.2.2 Deoxidising

A deoxidising process was used to remove the oxide layer of the anodised wrought aluminium alloy specimens (article 1) for post anodisation substrate surface analysis. The specimens were exposed to a solution of 2 g/L  $\text{H}_2\text{CrO}_4$  and 3.5 mL/L  $\text{H}_3\text{PO}_4$  85 % at 60 °C – 70 °C for 40 min.

#### 4.2.3 Light optical microscopy (LOM)

For initial observation of the microstructure as in article 4 and for surface morphology investigation of specimens a LOM Olympus GX41, using an Altra 20 Soft Imaging System was used.

#### 4.2.4 Scanning electron microscopy (SEM) and energy dispersive X-ray spectroscopy (EDS)

Three different SEMs were used in this work depending on the level of resolution needed. An Inspect S from FEI with a tungsten filament was used for many low magnification images and EDS measurements with an Oxford Instruments 50 mm<sup>2</sup> X-Max silicon drift detector (article 1). A JSM-5900 from JEOL with a  $\text{LaB}_6$  filament was used for imaging and EDS measurements using the Oxford link ISIS analyser attached to the microscope (article 2-4). A field emission gun SEM, Quanta 200f from FEI was used for high magnification investigations and EDS measurements with an Oxford Instruments 80 mm<sup>2</sup> X-Max silicon drift detector (article 3+4).

#### 4.2.5 Transmission electron microscopy (TEM)

Detailed cross section TEM investigations were done using a Tecnai T20 G2 from FEI operating at 200 keV (article 2+3). Focused ion beam (FIB) milling and in-situ lift out of a lamella of 2 µm in thickness was carried out using a FEI Quanta 200 3D DualBeam microscope equipped with a micromanipulator. Subsequently, a FEI Helios Nanolab DualBeam was used for lamella thinning.

#### 4.2.6 X-ray diffraction (XRD)

The XRD technique was used for phase identification before and after heat treatment. The equipment used was two different D8 Discover XRD, Bruker AXS. A copper  $\text{K}_{\alpha 1}$  beam (1.54 Å) was used at grazing incidence of 2° and 5° to decrease the penetration depth of the X-rays. On both machines, the step size was 0.03°, however, the step time was 192 s for the old machine (article 4) and 4 s for the new machine (article 2+3). The 2θ range of 20 ° - 85 ° was used for further analysis using the EVA Application software [139].

#### 4.2.7 Glow discharge optical emission spectroscopy (GDOES)

Radio frequency GDOES was done for chemical composition depth profiling on a GD Profiler 2 from Horiba Scientific. The argon pressure was set to 650 Pa and the process ran at a power of 35 W. The module and phase was set to 7.6 V and 3.8 V respectively.

Calibration accuracy of the GDOES process is highly dependent on the use of reference specimens (standards) and with the correct standards; it is possible to measure concentrations of accuracy level within 10 ppm. However, in the present investigations, it was not possible to have correct standards and therefore the Al-Ti coatings were relatively compared using the variation in Voltage input in the spectrometer. The sputter rate of the specimen is dependent on both material and process parameters. For the parameters stated above, a sputter rate of  $\sim 30$  nm/s was found based on profilometer measurements (Fig. 4.3). The bottom of the crater is mostly flat indicating that the process parameters are appropriate for the given material. Similar sputter rates were found for the anodised layer and the metallic magnetron sputtered coating.

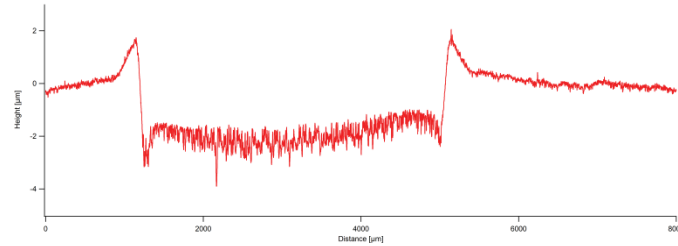


Fig. 4.3 - Profilometer measurements of sputter crater after 70 s of sputtering [9].

#### 4.2.8 Atomic force microscopy (AFM)

The AFM measurements were done for topographical analyses on a Park NX20 AFM from Park Systems (article 1). The equipment enables to program multiple measurements to be done subsequently due to a moving stage beneath the cantilever. Areas of  $30\text{ }\mu\text{m} \times 30\text{ }\mu\text{m}$  was scanned in intermittent and non-contact mode. The SPIP software [140] was subsequently used for first order linewise levelling and calculations of roughness parameters. For AFM measurements, the  $R_q$  (linewise) roughness parameter was used instead of the  $S_q$  (area) roughness parameter due to the line-wise nature of the measurements. The 6.1.0 and later versions of SPIP [140] has a function calculating all  $R_q$  values for all measured lines. Three roughness parameters were chosen for further analysis:

- $R_q$  is the root mean square-value of the deviation from the mean height in a line measurement.
- $S_{dr}$  is the percentage increase of the surface area compared to the ground area of a flat surface.
- $S_{ds}$  is the summit (spike) density per  $\mu\text{m}^2$ . The  $S_{ds}$  gives an indication whether two specimens with equal  $R_q$  and/or  $S_{dr}$  values have similar surface characteristics. A small  $S_{ds}$ -value indicates a few bigger summits compared to many lower summits.

#### 4.2.9 Surface Kelvin probe force microscopy (SKPFM)

Surface potential microscopy or SKPFM [141] is a non-contact scanning microscopy technique. The local surface potential is analysed based on local changes in the work function (energy needed to free an electron) difference between the sample surface and the scanning tip. A voltage is applied to the tip in order to cancel out electric forces related to work function differences. In this way the correction voltage is used to map changes of the surface potential when compared to the topography of the simultaneous AFM measurement.

The correction voltage is measured, so that the lower measured potential represents more noble areas and vice versa. The correction voltage is not directly comparable with the table values of various elements, but can be corrected using electrochemical experiments, however, this was not found necessary for the given purpose.

A Multimode AFM from Bruker was used for combined AFM and SKPFM measurements using the Nanoscope software [142]. Tapping mode was used for a topography scan followed by surface potential difference measurement at a lift height of 35 nm, which were the smallest possible lift height without the tip touching the surface occasionally. The measurements were performed in areas of  $10\ \mu\text{m} \times 10\ \mu\text{m}$  from which areas of  $5\ \mu\text{m} \times 5\ \mu\text{m}$  were used for further analysis in the SPIP software [143].

### 4.3 Optical investigations

#### 4.3.1 Special photographic setup

It is hard to take photographs of both diffusely reflecting and high gloss specimens in the same photographic setup with constant camera settings. The diffusely reflecting specimens require diffuse illumination and the camera should focus on the specimen surface. Whereas a high gloss specimen require something to be reflected in the specimen, and the camera should not focus on the specimen surface but at the reflection in the specimen. To enable visual comparison of specimens of various amounts of diffuse and specular reflection it was necessary to develop a special photographic setup, as presented in Fig. 4.4 (article 1).

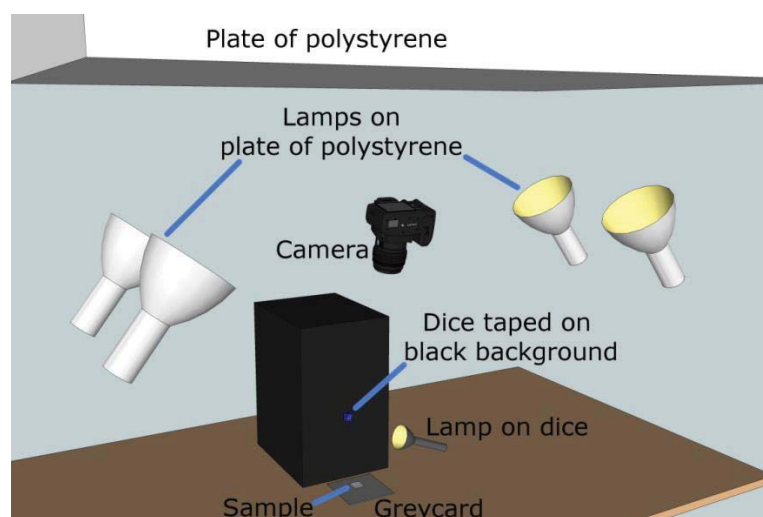


Fig. 4.4 - Special photographic setup.

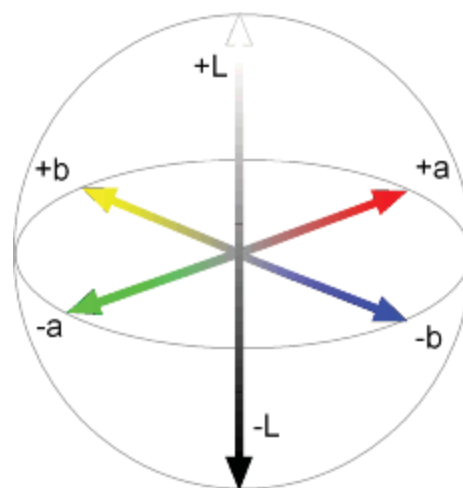


Fig. 4.5 - The CIE-Lab colour space [144].

A big plate of polystyrene was illuminated by four lamps giving diffuse illumination of the specimen, which was placed on a photographers grey card. The grey card was not important for the setup as such however, since this is a new setup, it was applied to enable comparison of brightness and white balance of these pictures with pictures taken at a later point. A blue dice with white pips was taped onto a black box and situated so that it reflected in the specimen from the position of the camera. The dice was illuminated from

below so that it was easy to see the dice in high gloss specimens. The dice should not be too close to the sample, avoiding significant reflections in diffuse specimens, giving the appearance of the specimens a blue tint. The setting, zoom, and focus were maintained for the camera, Pentax K-30, and the white balance was calibrated using a piece of white printing paper. The camera was placed with some distance to the specimen (650 mm) using an aperture of f/40 to gain high depth of focus. The focus point was set at approximately 750 mm from the camera so that both the specimen and the reflection of the dice were within the depth of field. The reflection angle of the dice was about  $14^\circ$  to the normal of the specimens. It is important that this angle is not too big since the specular reflection intensity increases at higher angles (Fig. 2.11, page 25), which might cause the diffusely reflecting specimens to reflect the dice more.

#### **4.3.2 Quantifying colour and brightness (the CIE-Lab colour space)**

Quantifying colours is not a straightforward process, since it is dependent on many different parameters, such as colour hue, saturation, and brightness. This can be done in several ways, where the CIE-Lab colour space [145] is based on the human vision and colour perception and standardised by the International Commission on Illumination (CIE). As illustrated in Fig. 4.5, the three parameters describe lightness,  $L^*$  (0 – 100), green to red colours,  $a^*$ , and blue to yellow colours,  $b^*$ . For  $a^* = b^* = 0$  all neutral colours are achieved from black over grey to white, depending on the  $L^*$ -value.

In this study, the CIE-Lab values were used, as a value for ‘whiteness’ of specimens. RGB values were extracted from the pictures taken in the photographic setup described in section 4.3.1. For each pixel, the CIE-Lab values were calculated and mean values for the whole picture of the specimen was calculated. Since both the  $a^*$  and the  $b^*$  values were close to 0 for all specimens, the  $L^*$ -values were taken as a quantification of the ‘whiteness’ of the specimens.

#### **4.3.3 Photospectrometry**

An integrating sphere coupled with an optical fibre was used for optical reflectance measurements (Fig. 4.6) as in article 1 and 2. A collimated beam from a light source (DH2000, Ocean Optics) was led into the integrating sphere at  $8^\circ$  to vertical. The specimen in the bottom of the sphere reflected the light, which was subsequently reflected multiple times in the highly reflecting white coating of the sphere until it was captured by an optical fibre leading the light to the photospectrometer (QE 65000 from Ocean Optics). The measurement was integrated over 20 s for the wavelength range of 300 nm – 800 nm and referenced against a high reflectivity NIST standard.

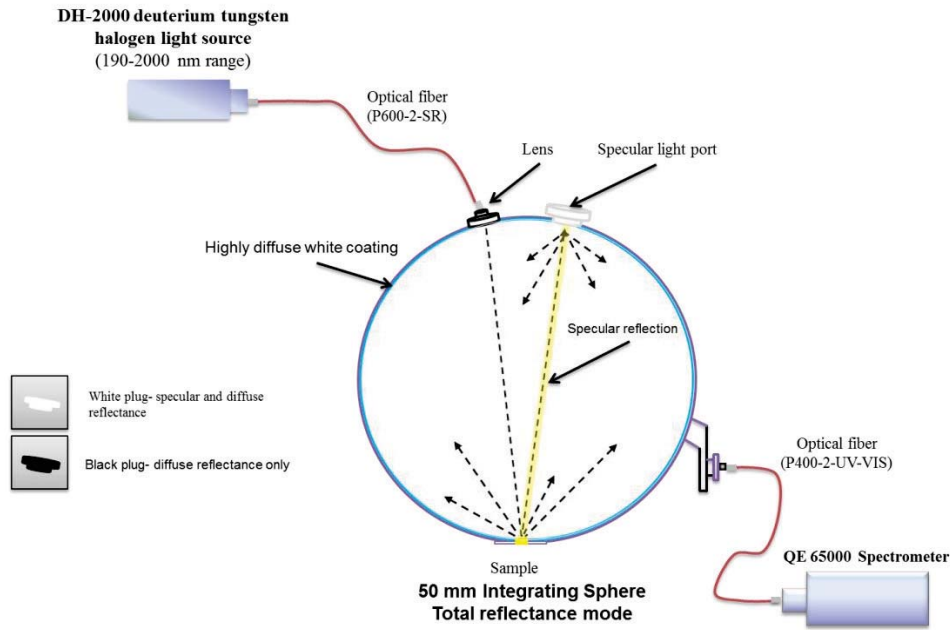


Fig. 4.6 – Integrating sphere photospectrometry setup.

The specular reflection could be absorbed by using a black light trap. It was thereby possible to measure both the total reflectance (diffuse + specular) and only the diffuse reflectance, thus the difference between the two curves indicate the specular reflectance (Fig. 4.7).

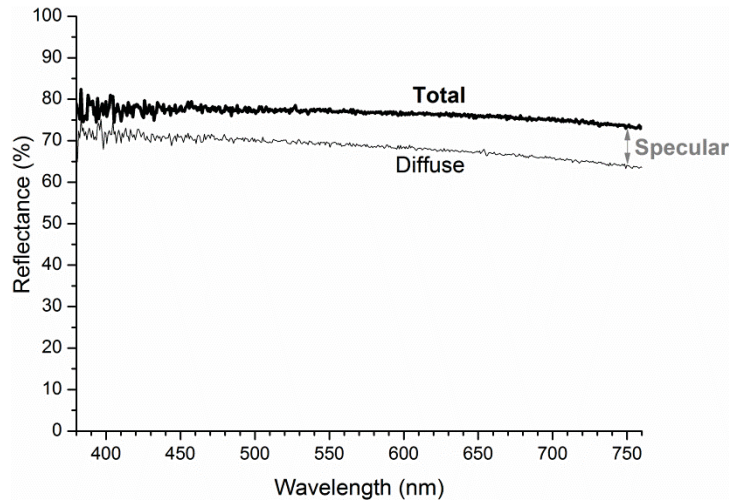


Fig. 4.7 – Photospectrometry measurements of a specimen for the total and the diffuse reflectance.

#### 4.3.4 Bidirectional reflectance distribution function (BRDF)

Angle resolved photospectrometry was done with a BRDF [146] setup (Fig. 4.8), using the same light source, integrating sphere and photospectrometer as described in section 4.3.3. A collimating lens was used to lead the light onto the specimen, which was fixed at a goniometer to control the angle of incidence ( $45^\circ$ ). The scattered light was measured around the specular angle ( $\pm 30^\circ$ ), so that the directional reflectance of the specimen was characterised, instead of the integration of all angles as found for the integrating sphere setup.



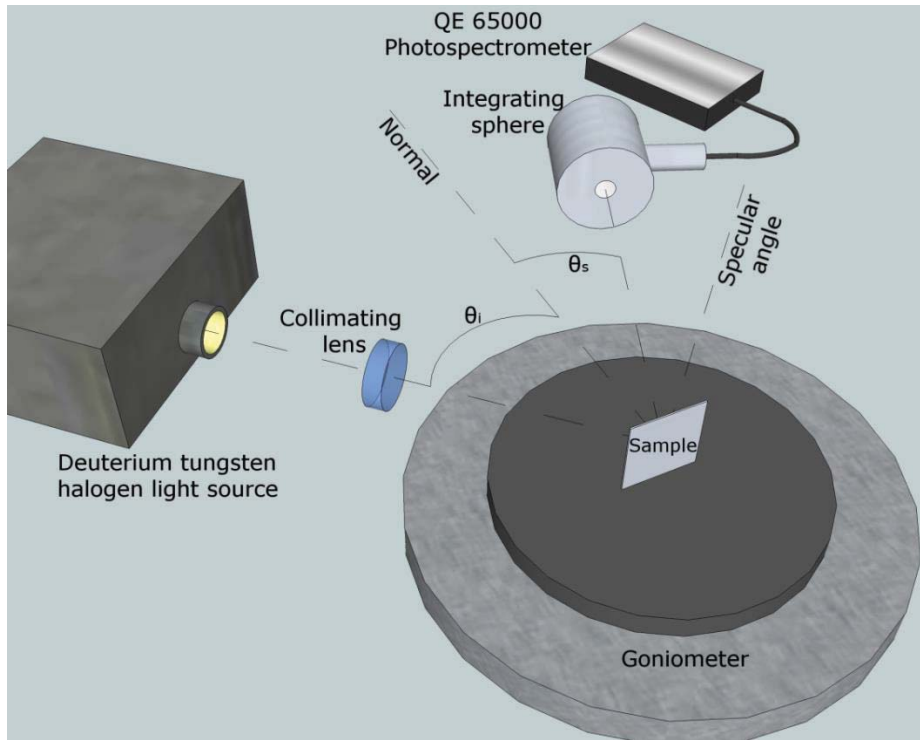


Fig. 4.8 – Illustration of the BRDF setup used for measurements.

The integrating sphere was introduced to the setup to achieve accurate data measurements. The beam of light was approximately 4 mm in diameter on the sample surface, and for a high gloss specimen, it was approximately 7 mm in diameter at the hole in the integrating sphere, which was 10 mm in diameter. Measurements were done for the visible wavelength range (380 nm – 760 nm). Calibration was done by removing the specimen and placing the integrating sphere, so that the light entered directly into it. Diffusely reflecting (etched) specimens gave a lower angular output and the integrating sphere was therefore situated 29 mm from these, whereas for high gloss (polished) specimens the integrating sphere was situated 85 mm from the specimen. The measured intensities from etched and polished specimens were therefore not directly comparable, however, the reflectance characteristics were. Data were plotted in 3D plots with reflectance as a function of wavelength and detector angle  $\theta_s$ . Whereas for easier comparison at 550 nm, the BRDF formula was used and plotted on a logarithmic scale for better visualisation of low intensity signals:

$$BRDF = \frac{P_s / \Omega}{P_i \cos \theta_s} \quad (11)$$

where  $P_i$  and  $P_s$  is the power of the incident and the measured scattered light respectively.  $\Omega$  is the solid angle of the measured reflected light.  $\theta_s$  is the angle between the normal of the specimens and the angle at which the measurement was done, also called the scattered angle.



## 4.4 Corrosion experiments

### 4.4.1 Anodic polarization test at neutral pH

Neutral saline anodic polarisation tests were performed as localised tests using a Dualscope™ EC Microcell [147,148] (Fig. 4.9) for article 3. The setup has a stage for the specimen situated beneath a container with the electrolyte and reference and counter electrodes inside. The working electrode is the specimen connected electrically using a gold pin put on the specimen surface. A drop of the electrolyte can be kept at the tip of the capillary so that the droplet form on the surface and the droplet is connected through the capillary to the reservoir of electrolyte and reference and counter electrodes. The lateral resolution of the measurements depends on the tip diameter. More detailed description of the set up can be found elsewhere [147,148].

For the experiments using this set up, the specimens were polished locally just before the measurements using SiC paper #4000 followed by cleaning using deionised water in order to minimise the thickness of the native film on the surface. The tip diameter was approximately 1 mm and a Ag/AgCl reference electrode was used. An electrolyte of 0.1 M NaCl was used for measurements of an open circuit potential (OCP) for 400 s. Subsequently, anodic polarisation measurements were performed from 100 mV below the corrosion potential ( $E_{\text{corr}}$ ) until reaching a fixed current after pitting occurred.

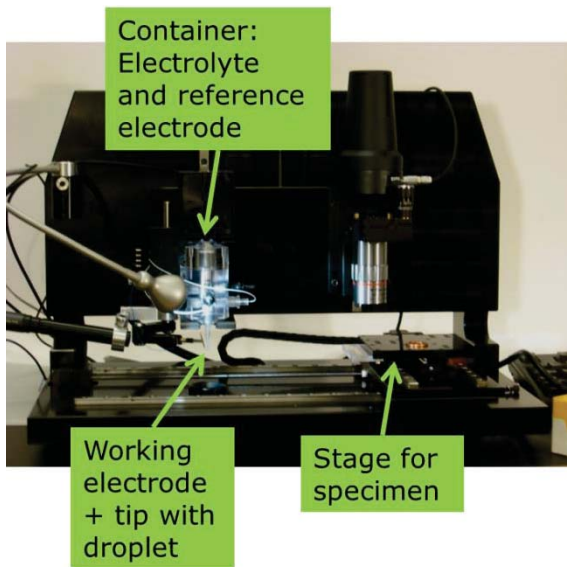


Fig. 4.9 – The microelectrochemical setup.

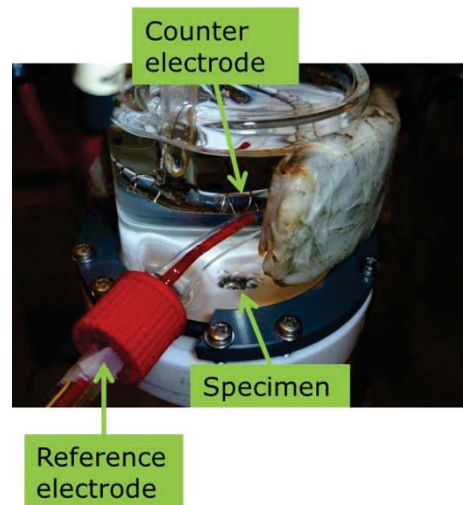


Fig. 4.10 – The flat cell used for alkaline anodic polarization tests.

### 4.4.2 Anodic polarization test at pH 13.5

A flat cell setup (Fig. 4.10) was used for anodic polarisation tests in alkaline conditions (articles 3 and 4). The exposed area of the specimen was approximately  $0.91 \text{ cm}^2$  and the specimen was connected as working electrode. A Ag/AgCl reference electrode was used, while a platinum wire twisted around a glass ring was used as counter electrode. All experiments were performed at pH 13.5 using a solution of 4.6 g/L  $\text{Na}_3\text{PO}_4 \cdot 12\text{H}_2\text{O}$ , 0.131 g/L NaCl, and 12.65 g/L NaOH at room temperature. OCP ran for 3 min followed by

anodic potentiodynamic measurements running from 100 mV below the corrosion potential ( $E_{\text{corr}}$ ) with a sweep rate of 120 mV/min to anodic potentials and the experiments were stopped at +300 mV or +700 mV as no pitting was found even at higher potentials.

### 4.4.3 Alkaline exposure experiment

Alkaline exposure experiments were performed for 10 min exposure at room temperature in the same solution as described in section 4.4.2 (articles 3 and 4). The specimens were lacquered twice to ensure that only the Al-Ti coating was exposed. Subsequently, the specimens were cleaned in demineralised water, desmuted in 70 wt. %  $\text{HNO}_3$  for 4 min and cleaned again. The specimens were then taken to the SEM for further investigations.



---

## 5 Summary of papers

---

The following sections provide summaries of the four papers appended in the form of manuscripts suitable for journal publication.

### 5.1 Appearance of anodised aluminium: Effect of alloy composition and prior surface finish (article 1)

Aluminium is used in many types of products due to its good mechanical properties and appealing appearance. However, the appearance of both etched and polished products can vary significantly for different alloys. The appearance of an anodised specimen depends on the topography and optical properties of the anodised layer, and the substrate surface, which are affected by impurities and alloying elements. This is particularly relevant for recycled alloys, where the uncontrolled chemical composition and increased amount of impurities can have large effects on the appearance.

The effect of alloy chemistry (AA1050, Peraluman 706, AA5754, and AA6082) and surface finish was studied before and after the anodisation and sealing processes. Microstructure and surface topography were investigated using SEM, EDS and AFM. The optical appearance was studied using a special photographic setup, integrating sphere photospectrometry, and a BRDF setup.

From AFM measurements, the  $R_q$ - and  $S_{dr}$ -values showed that the as-etched specimen of AA1050 was flat compared to the other alloys due to its high purity (99.5 %), whereas AA6082 showed the highest roughness after etching, due to high concentrations of iron and silicon. Photospectrometry showed that the specular part of the reflection increased with decreasing roughness of the as-etched specimens. For the as-polished specimens it was found that the AA1050 specimen was much rougher compared to the other specimens due to its softness, whereas AA6082 was flattest.

SEM investigations showed a remarkable correlation between the morphology of the as-etched surface and the oxide-substrate interface after anodisation. Intermetallic particles and pits due to alloying elements were found in the oxide-substrate interface. BRDF measurements (Fig. 5.1) showed that the as-etched specimen had a broad intensity distribution at and near the specular region, whereas the as-polished specimen showed mainly reflectance near the specular region.

No effect on morphology of the oxide and the substrate was found from the sealing process, however, the investigation using the photographic setup showed, that the reflection was more distinct after sealing, likely because the sealed pseudoböhmite is optically more homogeneous than the as-anodised layer.

It was concluded that the intermetallic particles and pits as well as the topography of the oxide-substrate interface had big effects on the appearance. From the literature it was concluded that oxidised, partly oxidised, and unoxidised particles of alloying elements in the anodised layer only have been found to have effects on the appearance of high gloss polished specimens.

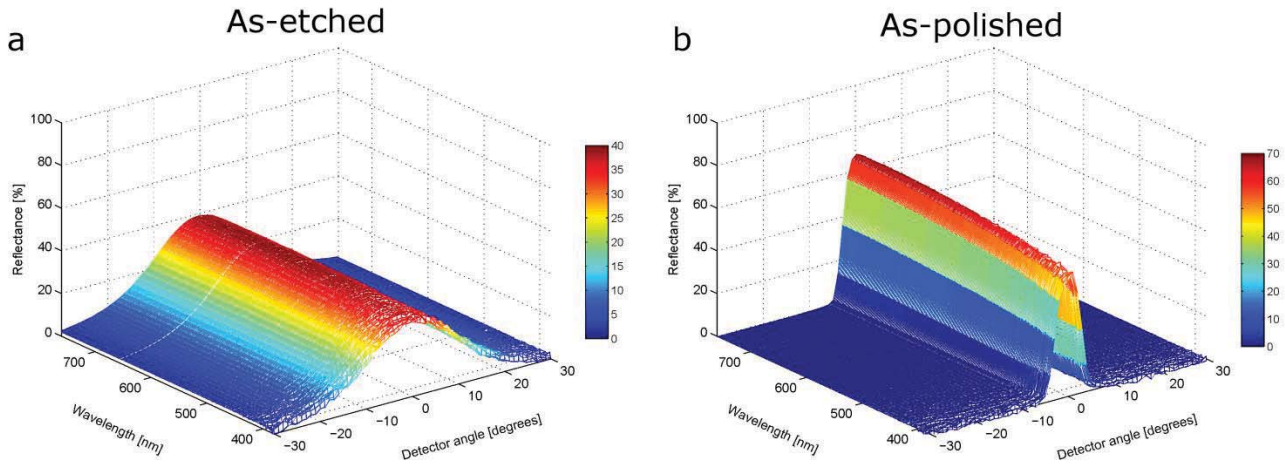


Fig. 5.1 – Angle resolved photospectrometry of P706 specimens with an angle of incidence of  $45^\circ$  of  
a) as-etched and c) as-polished specimens.

## 5.2 Al-Ti coatings produced by magnetron sputtering (articles 2 and 3)

Metastable magnetron sputtered aluminium coatings containing up to 18 wt. % titanium were created, followed by heat treatment at  $200^\circ\text{C}$  –  $600^\circ\text{C}$ . The microstructure was investigated by XRD, SEM, EDS, TEM, and GDOES.

Cross section TEM investigations of the as-deposited film showed a layered structure with a periodicity of  $32\text{ nm} \pm 4\text{ nm}$  (for 13 wt. % titanium) of alternating layers with low and high titanium concentrations due to the geometry in the deposition process. XRD identified only the  $\alpha\text{-Al}$  phase for the as-deposited coatings. After heat treatment at  $400^\circ\text{C}$  and more, the layered structure dissolved and  $\text{Al}_3\text{Ti}$  phases were formed. These coatings were further investigated in articles 2 and 3.

### 5.2.1 Anodisation of sputter deposited aluminium-titanium coatings: Effect of microstructure on optical characteristics (article 2)

The use of coloured aluminium providing a combination of metallic lustre and colours is very popular. However, since white pigments are much bigger than pigments for other colours, it is not possible to incorporate white pigments into the anodised aluminium pores. In the present work, magnetron sputtered Al-Ti coatings were created, followed by heat treatment in order to generate  $\text{Al}_3\text{Ti}$  particles with the intention of forming local oxides of titanium simulating the use of  $\text{TiO}_2$  as pigments for white appearance.

The optical properties were investigated by integrating sphere photospectrometry. The microstructural investigations summarised in section 5.2, were supplemented by additional TEM investigations of the anodised layer.

Photospectrometry measurements of the as-sputtered, heat-treated, and the as-sputtered and anodised specimens showed that the reflectance decreased in all cases with the titanium concentration. For specimens containing 13 wt. % titanium, it was found that the reflectance decreased when increasing the heat treatment temperature. For specimens heat-treated for 4 h at 500 °C and 600 °C followed by anodisation it was found that the specimens turned dark or even black during anodisation. TEM investigations of the 1.2  $\mu\text{m}$  anodised and sealed layer showed fully and partially oxidised  $\text{Al}_3\text{Ti}$  particles (Fig. 5.2) in the anodised layer and at the interface between the substrate and the anodised layer. In the aluminium matrix, the pore sizes were measured to 8 nm – 10 nm and it was found that the pores had collapsed during sealing. Small pores and pores of 25 nm – 35 nm was found in the oxidised  $\text{Al}_3\text{Ti}$  particles, where the pores seemed unaffected by the sealing process. An area of expected unanodised aluminium was found behind a partially oxidised particle. The interface of the substrate and the anodised layer caused some absorption and was found to be very rough. It was expected that much of the light move inclined back towards the top of the anodised layer (Fig. 5.3). Due to total internal reflection at the surface of the anodised layer, light trapping is expected to happen for some of the light. The partially oxidised  $\text{Al}_3\text{Ti}$  particles work as scattering and absorption points, promoting the darkening of the specimen appearance.

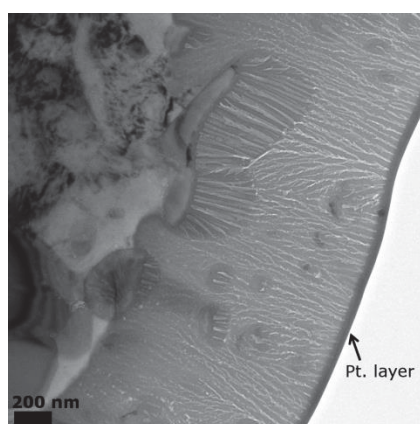


Fig. 5.2 – Cross section TEM image of partially and fully anodised  $\text{Al}_3\text{Ti}$  particles were found in the anodised layer.

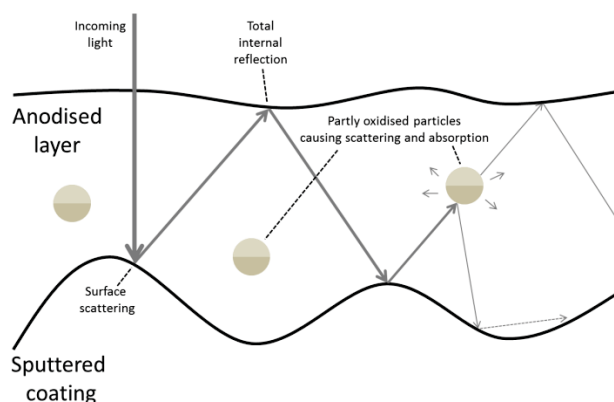


Fig. 5.3 – Schematic showing the possible reasons for darkening after anodisation.



### 5.2.2 Alkaline corrosion resistance of aluminium-titanium coatings prepared by plasma magnetron sputtering (article 3)

Aluminium is a key material for future green technology due to its high strength-to-weight ratio, especially in the transport industry where weight reduction can be directly translated into efficiency and reduction in fuel consumption. However, some of these products have to be able to withstand harsh alkaline conditions at pH 13.5 due to the detergents used in e.g. a brushless car wash. In this study magnetron sputtered Al-Ti coatings were tested in saline and rough alkaline environments.

Microstructural investigations are described in section 5.2. Anodic polarisation experiments, alkaline exposure studies, and SKPFM were used for corrosion analysis.

Anodic polarisation tests in a 0.1 M NaCl solution of the as-deposited specimens showed increased pitting potential with 330 mV for 15 wt. % titanium compared to the pure aluminium coating. For specimens with 8 wt. % titanium and below it was found that the anodic current increased compared to the pure aluminium coating, however, the performance improved in alkaline exposure studies. After heat-treatment, improvement was found for coatings of all concentrations. At 13 wt. % titanium and more, significant improvements were found in the corrosion experiments, especially after 2 h at 500 °C where the anodic current showed a reduction of 95 % compared to the as-deposited pure aluminium coating. Surface potential measurements (Fig. 5.4) showed potential differences for the as-deposited coating, which were slightly decreased after heat treatment for 2 h at 300 °C. After 4 h at 600 °C, the surface potential were homogeneous with precipitates of  $\text{Al}_3\text{Ti}$  having decreased the potential differences even further.

Improvement of the corrosion properties after heat treatment was attributed to the structural relaxation and slight decrease in the surface potential differences. At heat treatments of 400 °C and more, it was found that the homogenised matrix and  $\text{Al}_3\text{Ti}$  precipitates reduced the galvanic potential difference further. Additionally, the network of  $\text{Al}_3\text{Ti}$  phases was expected to provide protection of the surrounding matrix.

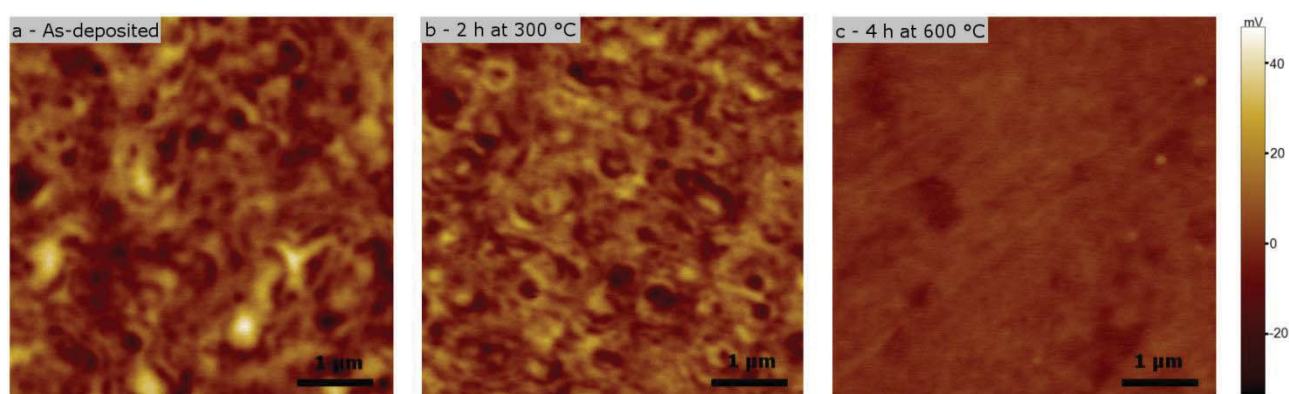


Fig. 5.4 – SKPFM surface potential mapping of polished surfaces in areas of 5 x 5  $\mu\text{m}$ . Specimens containing 13 wt. % titanium for a) an as-deposited coating, and after heat treatment for b) 2 h at 300 °C, and c) 4 h at 600 °C.

### 5.3 Alkaline corrosion properties of laser clad aluminium-titanium coatings (article 4)

The wish for lightweight materials in the transport industry promotes the use of aluminium. However, the requirements for alkaline corrosion resistance are hard to accommodate for regular surface treatments of aluminium alloys. In this study laser surface cladding was used to create Al-Ti coatings, which were heat-treated and investigated for alkaline corrosion resistance at pH 13.5.

Laser surface cladding was used with a combination of pure aluminium powder and 5 wt. %, 10 wt. %, and 20 wt. % of a Ti6Al4V powder. Subsequent heat treatment for 10 h at 600 °C was done to investigate changes in microstructure and corrosion properties. Microstructural analyses were done by LOM, SEM, EDS, and XRD, while corrosion properties at pH 13.5 were investigated by alkaline exposure tests and anodic polarisation measurements.

LOM, SEM, and XRD investigations identified a heterogeneous microstructure of the clad with a supersaturated  $\alpha$ -Al matrix containing up to 1 wt. % titanium.  $\text{Al}_3\text{Ti}$  phases and undissolved Ti6Al4V particles from the cladding process were found (Fig. 5.5). Heat treatment had no significant influence on the microstructure. For 5 wt. % and 10 wt. % Ti6Al4V the  $\text{Al}_3\text{Ti}$  phases were mainly found to be equiaxial, whereas specimens containing 20 wt. % titanium showed a dendritic microstructure. Alkaline exposure tests showed that the matrix preferentially corroded, while the  $\text{Al}_3\text{Ti}$  phases were protected (Fig. 5.6). Anodic polarisation tests at pH 13.5 showed no change in the  $E_{\text{corr}}$ -value and only a slight decrease, when increasing the titanium content from 5 wt. % to 20 wt. %.

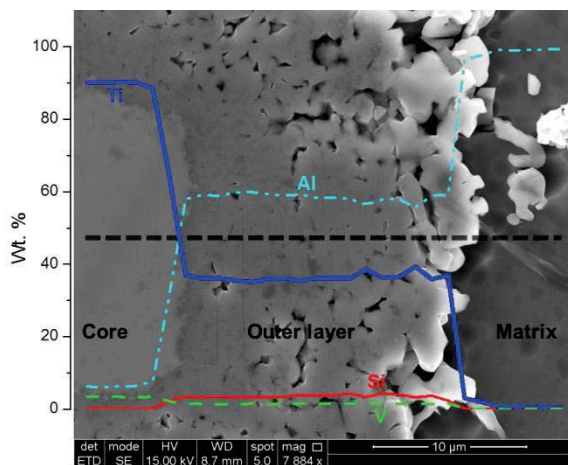


Fig. 5.5 - EDS line scan of a big particle of a heat-treated specimen with 10 wt. % Ti6Al4V. The thick horizontal line follows the line of measurements.

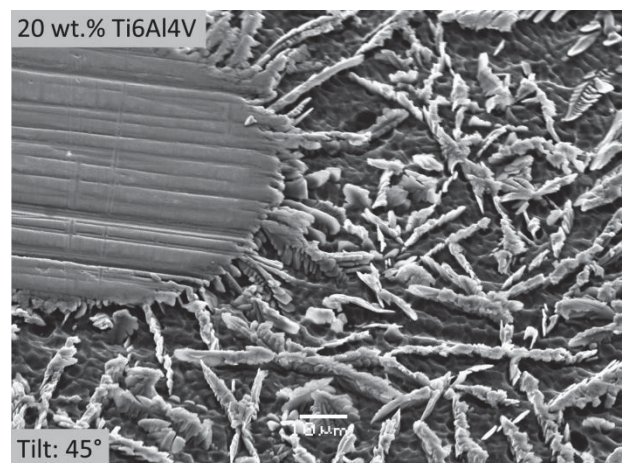


Fig. 5.6 - SEM image of as-cladded specimen with 20 wt. % Ti6Al4V after alkaline exposure test, showing preferential dissolution of the matrix.











# Appearance of anodised aluminium: Effect of alloy composition and prior surface finish

Martin Aggerbeck<sup>a</sup>, Stela Canulescu<sup>b</sup>, Kai Dirscherl<sup>c</sup>, Villads E. Johansen<sup>a</sup>, Sara Engberg<sup>b</sup>, Jørgen Schou<sup>b</sup>, Rajan Ambat<sup>a,\*</sup>

<sup>a</sup> Technical University of Denmark, Department of Mechanical Engineering, Materials and Surface Engineering, Produktionstorvet 425, 2800 Kgs. Lyngby, Denmark

<sup>b</sup> Technical University of Denmark, Department of Photonics Engineering, Optical Microsensors and Micromaterials, Frederiksborgvej 399, 4000 Roskilde, Denmark

<sup>c</sup> Danish Fundamental Metrology, Matematiktorvet 307, 2800 Kgs. Lyngby, Denmark

## ARTICLE INFO

### Article history:

Received 11 January 2014

Accepted in revised form 25 May 2014

Available online 2 June 2014

### Keywords:

Aluminium

Appearance

Etching

Polishing

Alloy composition

BRDF

## ABSTRACT

Effect of alloy composition and prior surface finish on the optical appearance of the anodised layer on aluminium alloys was investigated. Four commercial alloys namely AA1050, Peraluman 706, AA5754, and AA6082 were used for the investigation. Microstructure and surface morphology of the substrate prior to anodising were analysed using scanning electron microscopy and atomic force microscopy. The optical appearance of the anodised surface with and without sealing was investigated using a photography setup, photospectrometry and bidirectional reflectance distribution function. It was found that the roughness of the as-etched surface increases with the degree of alloying due to second phase particles making the reflection more diffused, and that the as-etched surface morphology is similar to the oxide–substrate interface after anodising. Proper polishing is achieved on hard alloys and the glossy appearance was kept for alloys of high purity. Sealing made the specular reflection of the mechanically polished specimens more distinct.

© 2014 Elsevier B.V. All rights reserved.

## 1. Introduction

Aluminium is widely used for decorative appearance, e.g. in the automotive and building industries. Aluminium is easily coloured during the anodisation process, however for a number of applications, anodised aluminium is used without colouring. Before anodising, aluminium products can be etched for a matte finish or polished (chemically or mechanically) for a high gloss finish. However, the appearance can vary significantly when using different alloys even though the same process parameters have been employed. Sulphuric acid anodisation results in a transparent anodised layer, so that the optical appearance depends on the optical properties and morphology of the anodised layer and the subsurface substrate. Therefore, the microstructure of the substrate plays a big role due to differences in the electrochemical behaviour of second phase particles in the anodising bath based on their morphology, size, and composition. Furthermore, differences in the dissolution of microstructural components in the anodising bath can result in unexpected roughening of the subsurface morphology during etching and anodisation. This is particularly important for the recycled alloys due to the presence of higher amounts of intermetallic compounds, which

results in miscolouring of the anodised layer in the form of light or dark streaks and unexpected darkening of the specimens after anodisation. It has been known for many years, that high concentrations of certain alloying elements may lead to miscolouring [1].

Many studies focus on streaks on extruded, etched, and anodised aluminium profiles [2–11]. Zhu et al. [10,11] reported that the morphology of the oxide–substrate interface has the biggest effect on the optical appearance for extruded, etched, and anodised profiles. The streaks appear (lighter or darker) due to inhomogeneity in the surface conditions of the streaked area compared to the non-streaked area. The inhomogeneity introduced during the production of the billet and during the extrusion process may be removed by proper etching [9,11]. Grain boundary grooves, surface scallops, etching pits, and etching steps have a great influence on the visual appearance. All of these effects are created or affected by alloying elements and it can therefore be difficult to control these effects when using recycled aluminium alloys. *Grain boundary grooves* formed during the etching process are reported to have strong effects on the visual appearance of anodised layer. Studies have shown that the amount and depth of the grain boundary grooves are affected by the iron and Mg<sub>2</sub>Si content [3,8] and amount of high angle grain boundaries [6,8] since these are more susceptible to intergranular corrosion than strongly textured low angle grain boundaries. *Surface scallops* decrease the reflectance in a similar way as grain boundary grooves and are created during etching and anodisation due to alloying elements such as iron and silicon, which are cathodic to the matrix [5,12]. *Etching pits* created by particles acting anodic to the

\* Corresponding author. Tel.: +45 45252181; fax: +45 45936213.

E-mail addresses: [mag@plan.aau.dk](mailto:mag@plan.aau.dk) (M. Aggerbeck), [stec@fotonik.dtu.dk](mailto:stec@fotonik.dtu.dk) (S. Canulescu), [kdi@dfm.dk](mailto:kdi@dfm.dk) (K. Dirscherl), [vejo@mek.dtu.dk](mailto:vejo@mek.dtu.dk) (V.E. Johansen), [sleen@fotonik.dtu.dk](mailto:sleen@fotonik.dtu.dk) (S. Engberg), [josc@fotonik.dtu.dk](mailto:josc@fotonik.dtu.dk) (J. Schou), [ram@mek.dtu.dk](mailto:ram@mek.dtu.dk) (R. Ambat).

matrix (e.g.  $Mg_2Si$ ) are in size of the original particle [2,3]. Big pits of sizes up to 10  $\mu m$  are created around e.g. iron rich particles, which act cathodic to the aluminium matrix causing the particles to be excavated during the etching process [2,3,11]. *Etching steps* appear because etchants may attack crystal planes differently, causing interference effects due to height differences of neighbouring grains. Texture differences caused by the extrusion process can therefore cause streaks [4,5]. Karhausen et al. [4] state that the biggest factor on the texture for extruded aluminium profiles is the die design and it is therefore not significantly alloy dependent. However, Zhu et al. [8,13] indicate that coarse intermetallic particles affect the texture. Furthermore, the random orientation of the grains increases with the iron concentration due to a reduced dislocation mobility and restricted grain growth and rotation.

Other studies focus on the appearance of rolled aluminium [14–19]. Van Gils et al. [14] found that the rolled aluminium has approximately 10% lower reflectance compared to magnetron sputtered aluminium. The major reason for reduced reflectance is a deformed layer near the surface created during rolling measured to be between 1.2  $\mu m$  and 2.9  $\mu m$  in thickness on an as-received hot-rolled pure alloy containing 0.5 wt.% magnesium [15]. The absorption in the deformed layer is mainly attributed to the incorporation of the oxides, and increases as well with the amount of alloying elements [15,16,18]. Additionally, Premendra et al. [18] found that the carbon from lubricants works as light absorbing centres. It has been reported that texture differences can cause streaks on rolled specimens [19]. Proper etching removes incorporated particles and the deformed layer [14–17].

The optical properties of the anodised layer have also been studied separately [2,20–23]. Akeret et al. [2] studied the optical effect of alkaline etching, brightening and anodisation. It was found that small anodic intermetallics such as  $Mg_2Si$  and  $Mg_2Al_3$  have little effect on the appearance, whereas cathodic intermetallics, especially the ones rich of iron and silicon have a large effect on the appearance [2]. Saito et al. [20, 21] studied anodised layers of 50  $\mu m$  of thicknesses on pure aluminium (99.99%) [20,21] and AA5052 (2.2–2.8% Mg, <0.5% Fe, Cr, Si) [20]. Extinction (the sum of absorption and scattering) was ascribed to holes in the oxide from e.g.  $Mg_2Al_3$  intermetallics (contradicting [2]), unoxidised aluminium in the anodised layer, and irregular cell structures found near holes and unoxidised aluminium [20,21]. The amount of unoxidised aluminium decreased with subsequent heat treatment [20,21]. The loss happens mainly for the light polarised parallel to the pores [20–22]. The highest transparency of anodised layers was reported for high purity alloys [2,20] and 6xxx alloys (AlMgSi) [2], whereas AA5052 had a significantly higher absorption within the anodised layer compared to the anodised layer of a pure alloy [20]. Tabrizian et al. [23] found that high gloss diamond turned samples that are heat-treated show lower reflectance after anodising compared to non-heated and anodised specimens. Inhomogeneity and imperfections in the anodised layer were reported to be the important factors affecting the optical appearance [23], and that the oxide–substrate interface roughness has no significant influence on the visual appearance on the high gloss specimens. Furthermore, the presence of silicon and  $Mg_2Si$  particles in the anodised layer was reported to have significant influence on the appearance. However, detailed investigations of the particles within the anodised layer were not presented. It has previously been reported that  $Mg_2Si$  phases are preferentially oxidised or dissolved in an aluminium matrix during anodisation [2,24].

The investigations in this paper emphasise the understanding of the combination of alloy chemistry and surface finish, and the effect on optical appearance before and after the anodisation and the sealing process. The microstructure and surface morphology were investigated using scanning electron microscopy and atomic force microscopy. The optical appearance was characterized by using a specially designed photography method, an integrating sphere for spectrally resolved measurements and a bidirectional reflectance distribution function (BRDF) system for measurements of angle-resolved reflectance.

## 2. Materials and methods

### 2.1. Materials

Specimens of 50 mm  $\times$  50 mm in size of four different aluminium alloys (AA1050, AA5754, and AA6082) of 1 mm sheet and the commercial Peraluman 706 (P706) alloy from Alcan of 2 mm thick sheet were used for investigations. The chemical composition of the alloys is presented in Table 1 based on data sheets from the suppliers.

### 2.2. Polishing, etching, anodising, and sealing processes

Mechanical polishing was done by buffing on a hard wheel with a polishing paste, M8005 from Lea, containing  $Al_2O_3$  particles. Subsequently the specimens were polished on a soft disc for finishing and removing excess paste. The specimens investigated in the as-polished state were cleaned with ethanol for removing polishing wax residues. All other specimens were cleaned using a commercial alkaline cleaner, AlfiClean from AluFinish, with rough agitation at 60 °C for 2 min–6.5 min. Etching was done in 80 g/L NaOH and maximum 50 g/L aluminium at about 60 °C for approximately 18.5 min. All specimens were desmutted in 6 wt.%  $HNO_3$  at 27.5 °C–28.0 °C for approximately 4 min. Anodisation of the surface was carried out in a bath containing 190 g/L  $H_2SO_4$  and 5 g/L–10 g/L aluminium at 17.9 °C, for about 30 min with mild agitation, at a constant voltage of 12.6 V and a current density of about 1 A/dm<sup>2</sup>. The series of specimens which were both polished and sealed were anodised 12.1 V. All the specimens are anodised using an industrial scale anodisation setup at Bang & Olufsen, Denmark. Sealing was done in water containing 2 g/L–3 g/L AlfiSeal from AluFinish at 96 °C for 25 min. AlfiSeal was added to remove the smut on the surface during sealing. The sealing was followed by 3 min to 5 min drying at 74 °C–78 °C. All process steps except sealing and drying, were followed by rinsing with demineralised water. The specimens were divided into six series, where e.g. “as-etched” has been etched and cleaned with ethanol, “etched, as-anodised” has been etched, anodised and cleaned with demineralised water, and “etched, sealed” has been etched, anodised and sealed, as presented in Table 2.

### 2.3. Surface appearance by photography

To present the appearance of the specimens in a proper way, a special photographic setup was designed as presented in Fig. 1. The sample was placed on a photographer's grey card used as a standard background. To ensure a homogeneous diffuse light on the specimen, four lamps were placed pointing away from the specimen onto a plate of polystyrene foam. A black box was positioned near the grey card and a blue dice with white pips was taped onto it and illuminated from below. The dice were positioned so that its reflection could be seen in high gloss specimens by the camera.

Pictures were taken with a Pentax K-30, with the white balance calibrated by placing a piece of printing paper in the position of the specimens. All camera settings were identical for all pictures, and the aperture was set to f/40 to gain high depth of focus. The camera was positioned on a tripod about 650 mm above the table top and tilted at an angle of about 14° to vertical. The focus point was set approximately 750 mm from the camera, i.e. between the specimen and the reflection of the dice. Thus, both the reflection of the dice and the specimen are

**Table 1**  
Chemical compositions (in wt.%) of AA1050, Peraluman 706, AA5754, and AA6082.

Alloy	Al	Mg	Si	Fe	Cu	Mn	Zn	Ti	Cr	V
AA1050	Bal.	0.05	0.25	0.4	0.05	0.05	0.05	0.03	–	0.05
P706	Bal.	0.3–0.8	0.2	0.2	0.03–0.1	0.05	0.05	0.03	0.02	–
AA5754	Bal.	2.6–3.6	0.4	0.4	0.1	0.5	0.2	0.15	0.3	–
AA6082	Bal.	0.6–1.2	0.7–1.3	0.5	0.1	0.4–1.0	0.2	0.1	0.25	–

**Table 2**  
Processes used for specimen series.

	Polishing	Cleaning	Etching	Desmutting	Anodising	Hot sealing
As-etched		X	X	X		
Etched, as-anodised		X	X	X	X	
Etched, sealed		X	X	X	X	X
As-polished	X	X <sup>a</sup>				
Polished, as-anodised	X	X		X	X <sup>b</sup>	
Polished, sealed	X	X		X	X	X

<sup>a</sup> As-polished specimens were cleaned with ethanol.

<sup>b</sup> The polished, sealed series were anodised at 12.1 V instead of 12.6 V as the others.

well within the depth of field (DOF) when using a small aperture and both objects consequently appeared in focus.

Each sample was photographed both along and across the rolling direction. As only minor differences were observed, all presented pictures were taken along the rolling direction so that this is in the vertical direction of the pictures. An area of 512 pixels  $\times$  512 pixels (slightly smaller than the specimen) was selected for presentation and CIE-Lab values calculations. The CIE-Lab colour space [25] is based on the human vision and colour perception, represented by lightness,  $L^*$ , and the colour parameters  $a^*$  and  $b^*$ . For  $a^* = b^* = 0$ , the colour is neutral (black/grey/white) depending on the  $L^*$ -value. The CIE-Lab values were calculated from the RGB values for each pixel and a mean value was found for all pixels in each of the photographs of the etched specimens to compare the  $L$ -values (whiteness) of the specimens numerically.

#### 2.4. Microstructural analysis

The thickness of the anodised layer was measured using a thin film analyser (Nanocalc 2000 from Mikropack). Each value is an average of 50 measurements.

For microstructural analysis, a scanning electron microscope (SEM), Inspect S from FEI, was used. This microscope was also used for chemical composition analysis by energy dispersive X-ray spectroscopy (EDS). All EDS measurements agreed well with the expected composition values of the matrix and precipitates described in the literature, and are therefore not presented. The anodised specimens were coated with carbon before SEM analysis. In order to investigate the substrate surface beneath the anodised layer, a deoxidizing process was performed using a solution of 100 mL demineralized water containing 2 g chromic acid and 3.5 mL phosphoric acid 85%. The solution was kept at 60 °C–70 °C and the specimens were deoxidized for about 40 min.

Further topographical analyses of the as-etched and as-polished surfaces were performed using atomic force microscopy (AFM) on a Park

NX20 from Park Systems. An area of 30  $\mu\text{m} \times 30 \mu\text{m}$  was measured in intermittent and non-contact mode. Subsequently, first order line-wise levelling was processed and roughness parameters were calculated using the SPIP software [26]. Three parameters were chosen to illustrate the surface roughness of the specimens: (i)  $R_q$  is the root mean square-value of the absolute deviation from the mean height measured in one line at a time (the presented values are the mean value of the  $R_q$  values of the 512 lines measured, plotted with the standard deviation of the mean), (ii)  $S_{dr}$  is the percentage increase of the surface area compared to a completely flat surface, and (iii)  $S_{ds}$  is the summit density, counting the amount of summits (spikes) per  $\mu\text{m}^2$ .

#### 2.5. Photospectrometry

An integrating sphere coupled with a fibre optic spectrometer was used for optical reflectance measurements. The setup was previously described elsewhere [27]. A collimated beam from a light source (DH 2000 from Ocean Optics) enters the integrating sphere at 8° with respect to vertical. The beam is reflected by the sample and goes subsequently through multiple reflections on the interior of the sphere and is collected with an optical fibre coupled to a spectrometer (QE 65000 from Ocean Optics). Each reflectance spectrum was measured over the wavelength range from 300 nm–800 nm using an average integration time of 20 s. All spectra were referenced against a high-reflectivity standard. The specular reflectance can be excluded using a black light trap. Thereby, both the total reflectance (diffuse + specular) and only the diffuse reflectance can be measured.

#### 2.6. Bidirectional reflectance distribution function

For angle resolved reflectance measurements of etched and polished samples, a bidirectional reflectance distribution function [28] (BRDF) setup (Fig. 2) was used. While the integrating sphere setup quantifies the total amount of light reflected from a surface, it does not provide directional reflectance characteristics information of a surface. In BRDF measurements, the incident angle can be fixed, while the detection angle can vary continuously, allowing the measurements of light scattering as a function of an angle. When the illumination angle equals the detection angle, the specular reflectance dominates the reflectance spectrum. In the current setup, the specimen was illuminated with a collimated white light beam at an angle of incidence of  $\theta_i = 45^\circ$ . The scattered light angle was measured over an angle range ( $\theta_s$ ) from  $-30^\circ$  to  $+30^\circ$  with respect to the specular angle. An integrating sphere coupled with a fibre optic spectrometer was introduced to the setup to achieve an accurate data collection. The size of the collimated beam on the surface of the specimen was about 4 mm and 7 mm when entering the integrating sphere with an entrance hole of 10 mm in diameter, ensuring that all specular light was collected during BRDF measurements.

The BRDF spectra were measured over the visible spectral range (380 nm–760 nm). Calibration was done by setting the direct light incident on the integrating sphere as a baseline for the measurements. The integrating sphere was situated 29 mm from the specimen when measuring the etched specimens and 85 mm from the specimen when

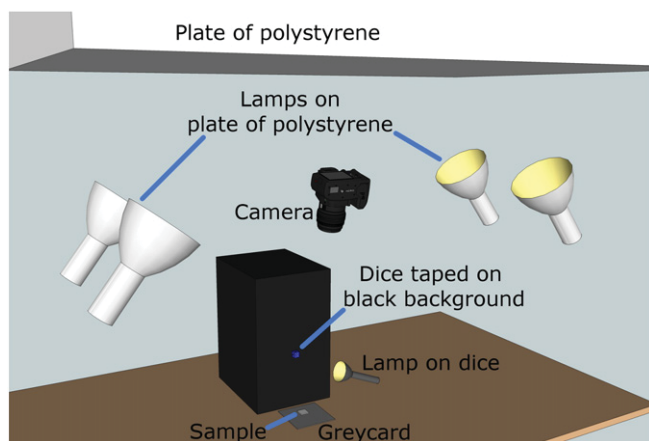


Fig. 1. Special photographic setup.

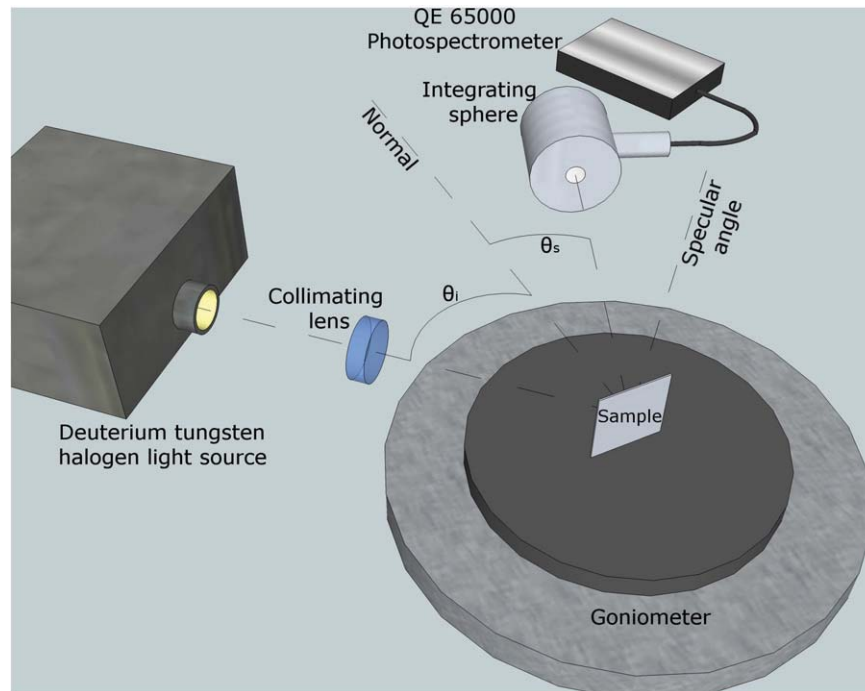


Fig. 2. Illustration of the BRDF setup used for measurements.

measuring the polished specimens. Therefore, the measured intensities from the etched specimens are not comparable with the measurements of the polished specimens, but the reflectance distribution functions are still comparable. The data were plotted in a 3D plot with reflectance as a function of wavelength and the detector angle ( $\theta_s$ ). For easier comparison of the different plots, a two dimensional plot of the data, was plotted using the BRDF formula:

$$\text{BRDF} = \frac{P_s / \Omega}{P_i \cos \theta_s} \quad (1)$$

where  $P_i$  and  $P_s$  is the power of the incident and the measured scattered light, respectively.  $\Omega$  is the solid angle of the measured reflected light and  $\theta_s$  is the scattering angle, i.e. between the normal of the specimen and the angle of detection, as shown in Fig. 2. For a better visualisation of the low intensity signals, the function is plotted on a logarithmic scale.

The BRDF function describes the angular distribution of scattered light from surfaces. If the reflection from the sample surface is perfectly diffused, the scattered light would follow the Lambert's model [28]. On the other hand, a perfect specular surface would reflect light in the specular direction only.

### 3. Results

#### 3.1. Appearance observed using special photography setup

The perceived optical appearance of the specimens photographed using the special setup presented in Fig. 3 are shown as photographs of the **etched** series of AA1050 specimens. Similar pictures were taken for the other alloys, but are not presented as the appearance was quite similar to AA1050. Instead, for numerical comparison the CIE-Lab values [25] were calculated based on the photographs. It was found that all specimens had almost the same colour (not presented) and the L-values (lightness) are presented in Table 3. The as-etched AA1050 specimen had the lowest L-value (76.9) and the as-etched AA5754 specimen had the highest L-value (89.9). All anodised specimens (middle and right-hand column) showed quite similar L-values (80.8–84.9).

Photographs of the polished series of the four different alloys are presented in Fig. 4. All **as-polished** specimens (Fig. 4, left-hand column) showed high gloss, where AA1050 and AA5754 showed slight distortions in the reflection compared to P706 and AA6082. For the polished, as-anodised specimens, the reflection of the dice disappeared almost completely for AA5754 (Fig. 4h) and was blurred out for AA6082 (Fig. 4k), whereas, for AA1050 (Fig. 4b) the pips of the dice were distinguishable and even more for P706 (Fig. 4e). For the polished, sealed

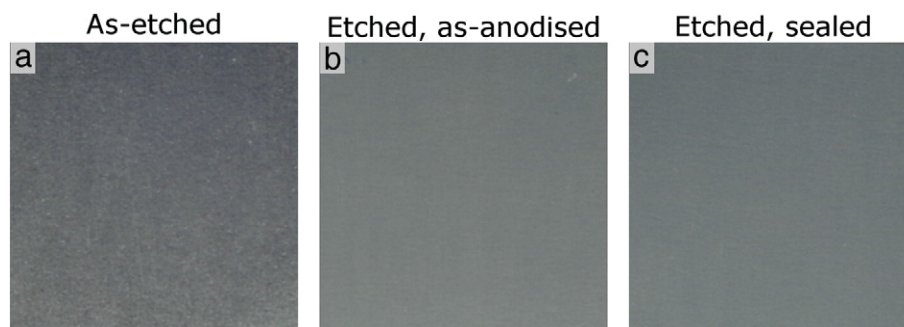


Fig. 3. Photographs of AA1050 specimens, a) as-etched, b) etched, as-anodised, and c) etched, sealed.



**Table 3**

The L-values calculated from photographs.

	As-etched	Etched, as-anodised	Etched, sealed
AA1050	76.9	82.0	80.8
P706	84.0	84.9	83.1
AA5754	89.9	82.2	84.8
AA6082	88.1	81.9	81.0

specimens of AA1050, P706, and AA6082 (Fig. 4c, f, and l), the reflection was more distinct compared to the unsealed samples (Fig. 4b, e and k). For the polished, sealed specimens, P706 showed the most clear and distinct reflection of the dice.

### 3.2. Microstructural and surface morphology analyses

The measured anodised layer thicknesses are presented in Table 4. The anodising process results in oxide thicknesses of 6.1  $\mu\text{m}$ –9.1  $\mu\text{m}$ ,

**Table 4**Thickness ( $\mu\text{m}$ ) of the anodised layer on various specimens.

	Etched, as-anodised	Etched, sealed	Polished, as-anodised	Polished, sealed
AA1050	7.0	7.4	6.6	6.2
P706	6.7	6.9	6.8	6.1
AA5754	8.4	9.1	8.3	7.7
AA6082	7.0	7.6	7.2	6.8

and the thickness varied in general for the alloys from thinnest to thickest in the order of P706, AA1050, AA6082, and AA5754. For the *as-anodised* specimens (left-hand and right-hand column), the thickness of anodised layer was more or less the same for etched and polished specimens. For the **etched** specimens (left-hand and middle column), it was found that a thicker anodised layer was measured after sealing, which is caused by the expansion of the oxide during the process into pseudoböhmite. The **polished** specimen show an opposite

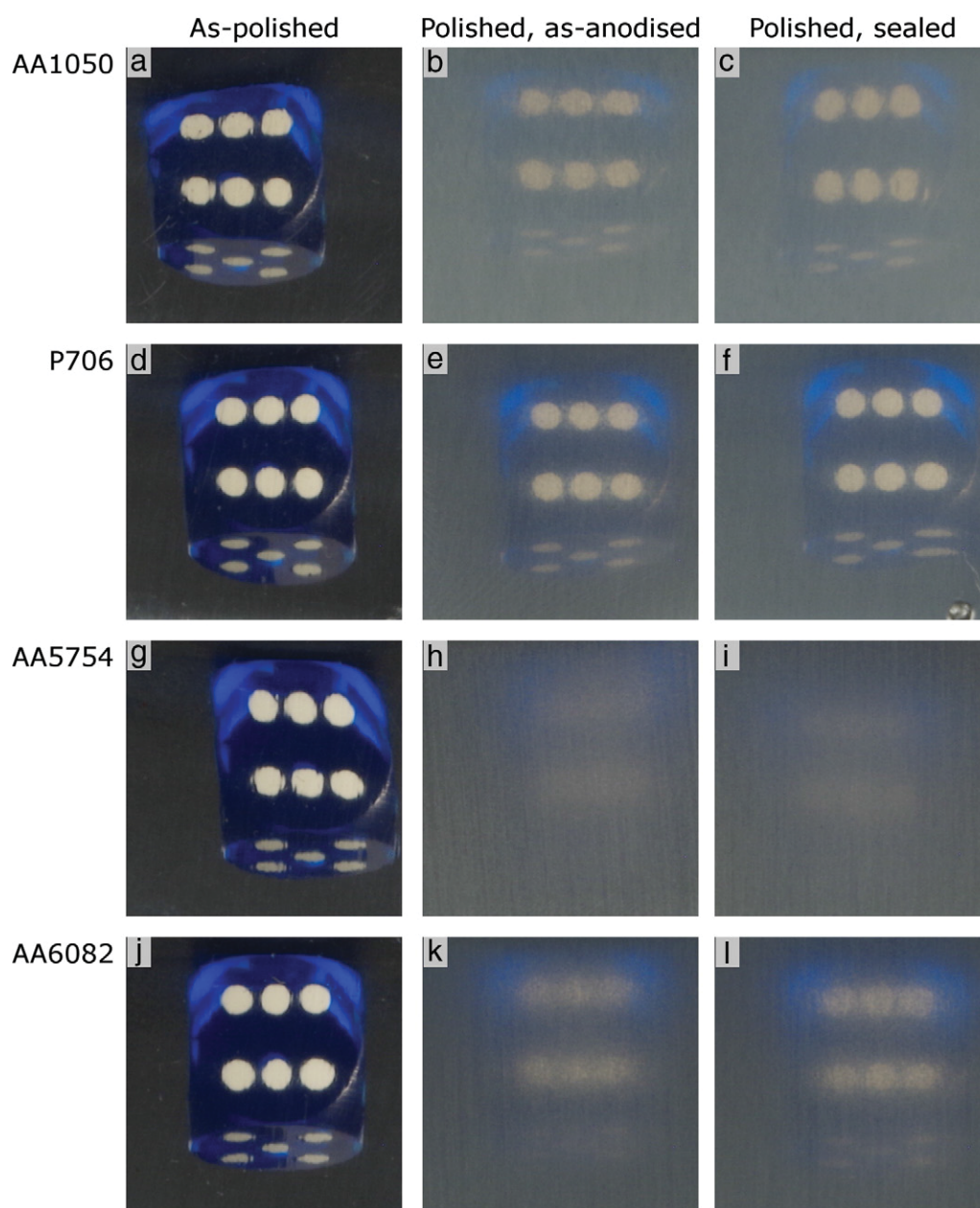


**Fig. 4.** Photographs of polished specimens, a–c) AA1050, d–f) P706, g–i) AA5754, and j–l) AA6082.



effect, which is expected to be due to the lower voltage used for anodisation of the polished and sealed specimens.

For microstructural analysis using SEM, all specimens were investigated. It was found that the sealing did not change the microstructure and therefore the images of the unsealed specimens are not presented. The as-etched/as-polished and the carbon-coated anodised, sealed surfaces were studied as well as the oxide–substrate interfaces after removing the anodised layer. The SEM images of etched and polished specimens are presented in Figs. 5 and 6, respectively.

As expected, the AA1050, **as-etched** specimen (Fig. 5a) had the smoothest surface due to the high purity of the alloy, whereas the AA6082, as-etched specimen (Fig. 5j) showed the roughest surface. When comparing the as-etched surface (Fig. 5, left-hand column) and the oxide–substrate interface (Fig. 5, right-hand column) it was found that the morphology was rather similar. The surface of the anodised layer (Fig. 5, middle column) showed that the structures were somewhat

smoother compared to the as-etched surface and the oxide–substrate interface. Many surface scallops are found especially for the highly alloyed AA5754 (Fig. 5g–i) and AA6082 (Fig. 5j–l), where iron and silicon rich particles induce the creation of scallops [5,12].

For the **as-polished** specimens, it was found that the intermetallic particles were easily seen in the surface of P706, AA5754 and AA6082 (Fig. 6d, g and j), where only few were found in the surface of AA1050 (Fig. 6a). The scratches from the polishing process were clearly seen for the as-polished specimens (Fig. 6, left-hand column). However, at the oxide–substrate interface (Fig. 6, right-hand column), the polishing tracks diminished and intermetallic particles were sticking out of the surface and pits were found. The surfaces of the anodised layers (Fig. 6, middle column) showed the presence of particles and shallow marks from the polishing process.

For a detailed roughness characterization of the specimens after surface treatment, AFM measurements were performed. In Fig. 7 the

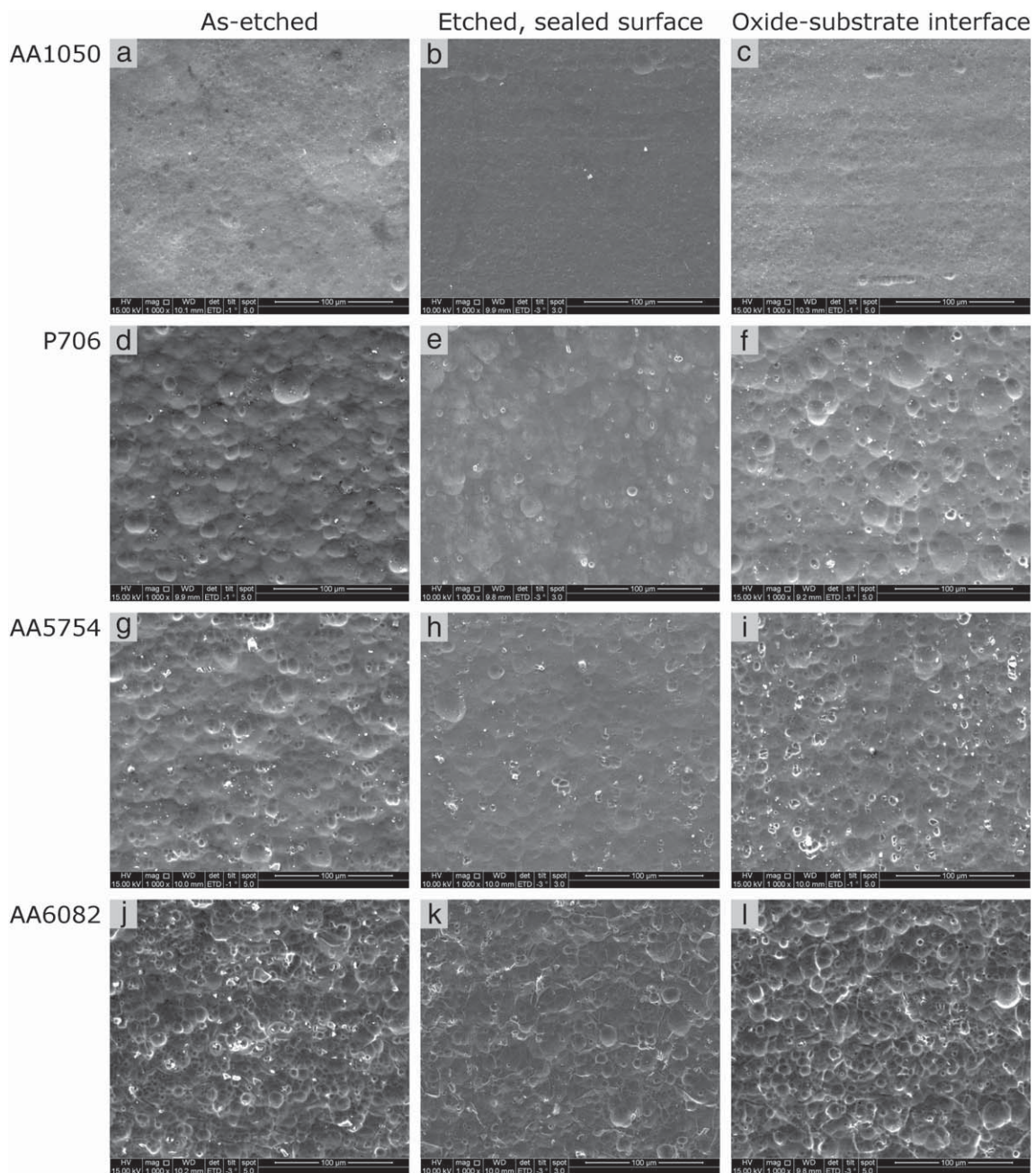


Fig. 5. SEM micrographs of etched specimens, a–c) AA1050, d–f) P706, g–i) AA5754, and j–l) AA6082.

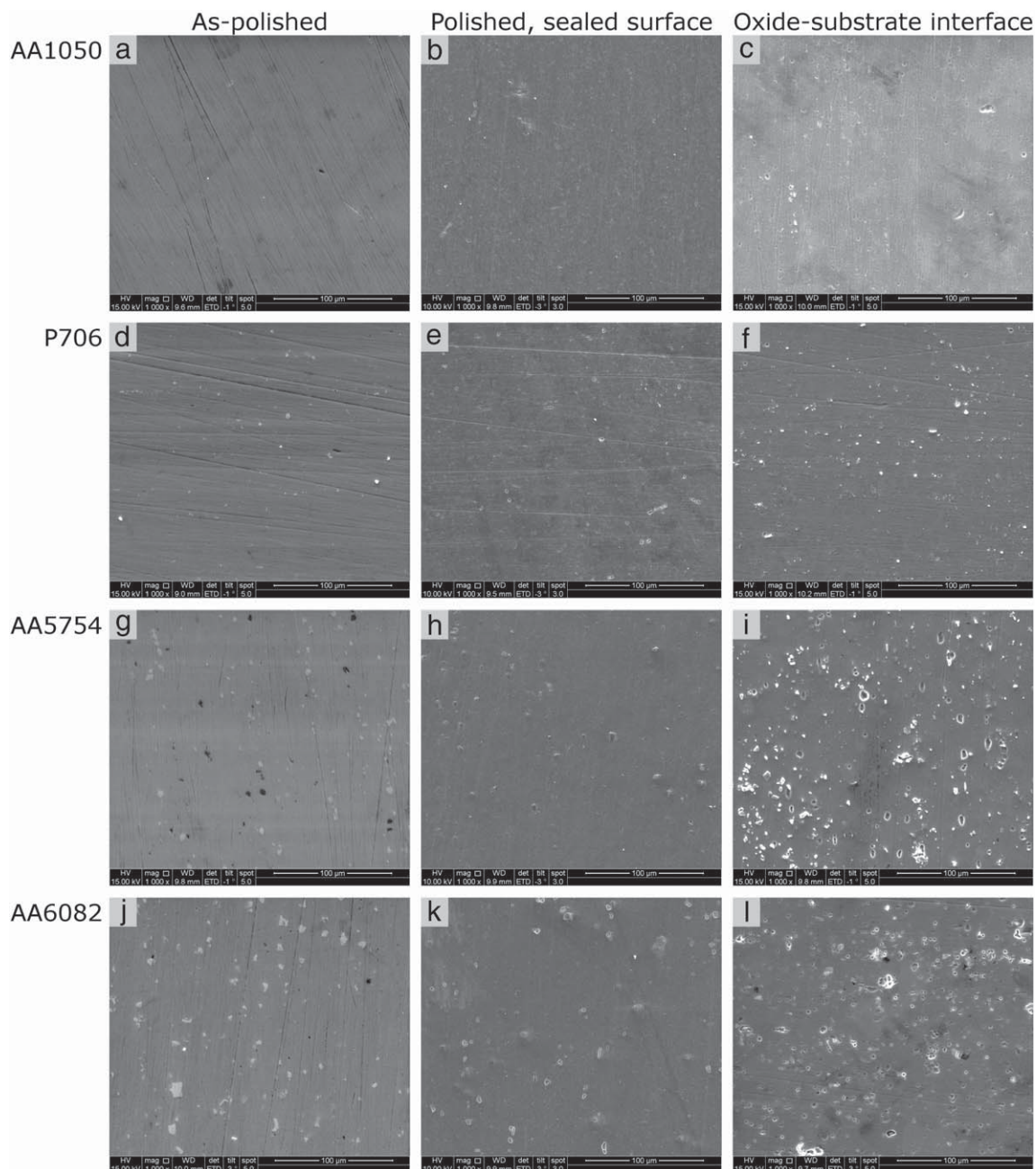


Fig. 6. SEM micrographs of polished specimens, a–c) AA1050, d–f) P706, g–i) AA5754, and j–l) AA6082.

surface morphology of the **as-etched** specimens is presented. It was found that the roughness was the lowest for pure AA1050 (Fig. 7a) and roughest for AA6082 (Fig. 7d). Fig. 8 shows the AFM surface morphology of the **as-polished** specimens. For all specimens, clear polishing tracks were found and P706, AA5754, and AA6082 (Fig. 8b–d) showed quite smooth surfaces, whereas AA1050 (Fig. 8a) was significantly rougher due to the softness of the alloy. For AA6082 (Fig. 8d), the surface showed a lot of small particles in sizes of 60 nm to 160 nm in diameter sticking up to 40 nm above the base. These particles were also found in SEM investigations (not presented) and are expected to be  $Mg_2Si$  particles as reported in the literature [29,30]. Similar but smaller particles were found for AA5754 of sizes about 1 µm in diameter and 25 nm in height.

Roughness parameters were calculated (Fig. 9) based on the measurements presented in Figs. 7 and 8. For the **as-etched** specimens (Fig. 9a), it was found that the AA1050 had the lowest and AA6082 had the highest  $R_q$  and  $S_{dr}$  values as expected from Fig. 7. Additionally,

AA6082 had a low  $S_{ds}$ -value as it had high roughness giving only few local peaks. For P706 and AA5754 the values of  $R_q$  are almost similar, but the  $S_{dr}$  value was clearly lower for P706 than AA5754. When closely investigated it was found that the P706 (Fig. 7b) showed many small spikes giving it a high  $S_{ds}$  value, whereas e.g. AA5754 had a zigzag structure with fewer spikes. For the **as-polished** specimens (Fig. 9b), it was found that the AA1050 had by far the highest  $R_q$  value, as expected when investigating Fig. 8, whereas, AA6082 showed the lowest  $R_q$  and  $S_{dr}$  values. Both AA5754 and AA6082 had high amounts of particles in the surface giving high  $S_{ds}$ -values. The high  $S_{ds}$ -value of P706 is caused by the polishing tracks creating many local maxima.

### 3.3. Photospectrometry

Photospectrometry measurements were used to study the visual appearance of the specimens. Solid curves in Figs. 10 and 11 represent



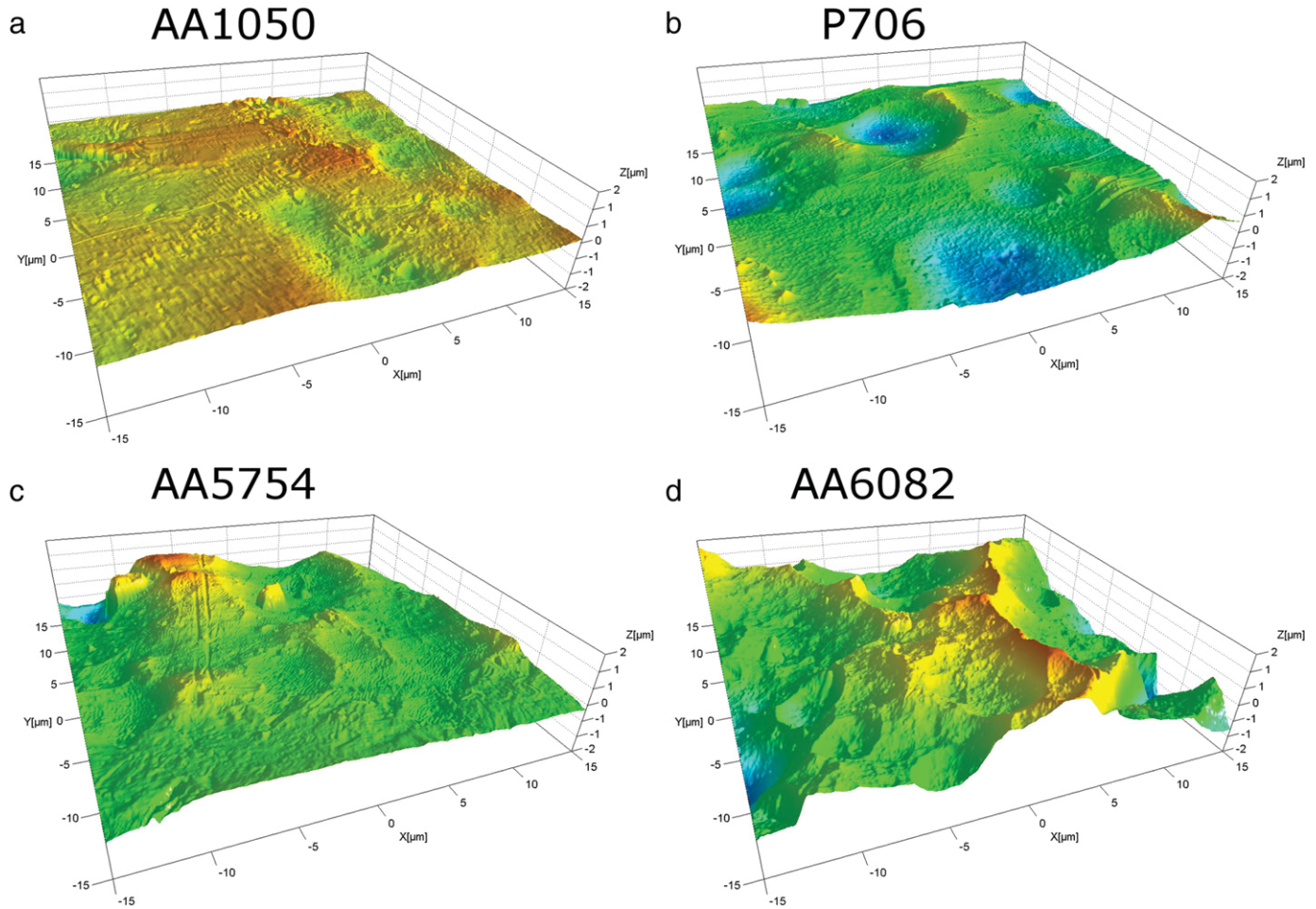


Fig. 7. Surface topography using AFM ( $30\ \mu\text{m} \times 30\ \mu\text{m}$ ) of as-etched specimens, a) AA1050, b) P706, c) AA5754 and d) AA6082.

the spectrum of the total reflectance including both specular and diffuse reflectance, while the dotted curves are only the diffuse reflectance, measured with a gloss trap in the specular light port. The difference between the total (solid) and the diffuse (dotted) curves is therefore an indication of the level of specular reflectance.

The photospectrometry results for the **etched** specimens are presented in Fig. 10. For AA1050 (Fig. 10a) and P706 (Fig. 10b) there were some specular reflectance, which decreased after anodisation. Negligible difference was observed between the total and the diffuse reflectance for AA5754 (Fig. 10c) and AA6082 (Fig. 10d), meaning that there was no measurable specular reflectance from these specimens. For all as-etched specimens, the total reflectance decreased, whereas the diffuse/total reflectance ratio slightly increased. No effect was registered from the sealing process in the visible spectrum; however, there was a registered decrease in the reflectance around 340 nm for the sealed specimens, which is expected to be due to absorption by the pseudoböhmite layer. AA5754 had the flattest (most horizontal) curve among the specimens and therefore the most neutral colour (white/grey) both before and after anodisation and sealing.

Fig. 11 presents the photospectrometry measurements of the **polished** specimens, where a much larger difference between total (solid lines) and diffuse (dotted lines) measurements was found (as expected) compared with the etched specimens (Fig. 10). In general it was found that the total reflectance was similar for all as-polished specimens and it was more or less retained after anodisation. However, the diffuse reflectance was clearly larger for anodised specimens, meaning that the specular reflectance decreased when the specimens were anodised. For AA1050 (Fig. 11a) and AA6082 (Fig. 11d), the sealing

process increased the specular reflectance compared to the as-anodised specimens. Although only slightly, the AA5754 (Fig. 11c) showed lower specular reflectance when sealed. The P706 alloy (Fig. 11b) showed no significant change in the reflectance characteristics when sealed and showed the highest specular reflectance when sealed compared to the other alloys. Fringes due to the thin film interference were found in the reflectance spectra for some specimens.

### 3.4. Bidirectional reflectance distribution function

The angle resolved spectral reflectance of P706 specimens, which were etched and polished both before and after anodisation are shown in Fig. 12. It was found that the reflectance of the **etched** specimens (Fig. 12a and b) had broad peaks with an intensity peak at the specular angle. Large peaks at the specular direction and narrow scattering characteristics can be seen for the **polished** specimens (Fig. 12c and d). It was found that the reflectance peak values decreased at the specular angle for the anodised specimens compared to the as-etched (Fig. 12a vs. b) and as-polished (Fig. 12c vs. d) specimens. The spectra of the polished, as-anodised specimen showed interference fringes similar to those found in the photospectrometry (Fig. 11b).

A line profile at 550 nm was extracted from the BRDF images and is shown in Fig. 13. The reflectance spectrum of the polished, as-anodised specimen (Fig. 12d) has interference fringes, and at 550 nm the reflectance of the polished, as-anodised specimen was in a trough, 5% points below the nearby crests. The as-etched specimen reflected light in a broad area over the measured angle range  $-30^\circ$  to  $+30^\circ$  from the specular angle and a peak value of  $4.1\ \text{sr}^{-1}$ . The etched, as-anodised

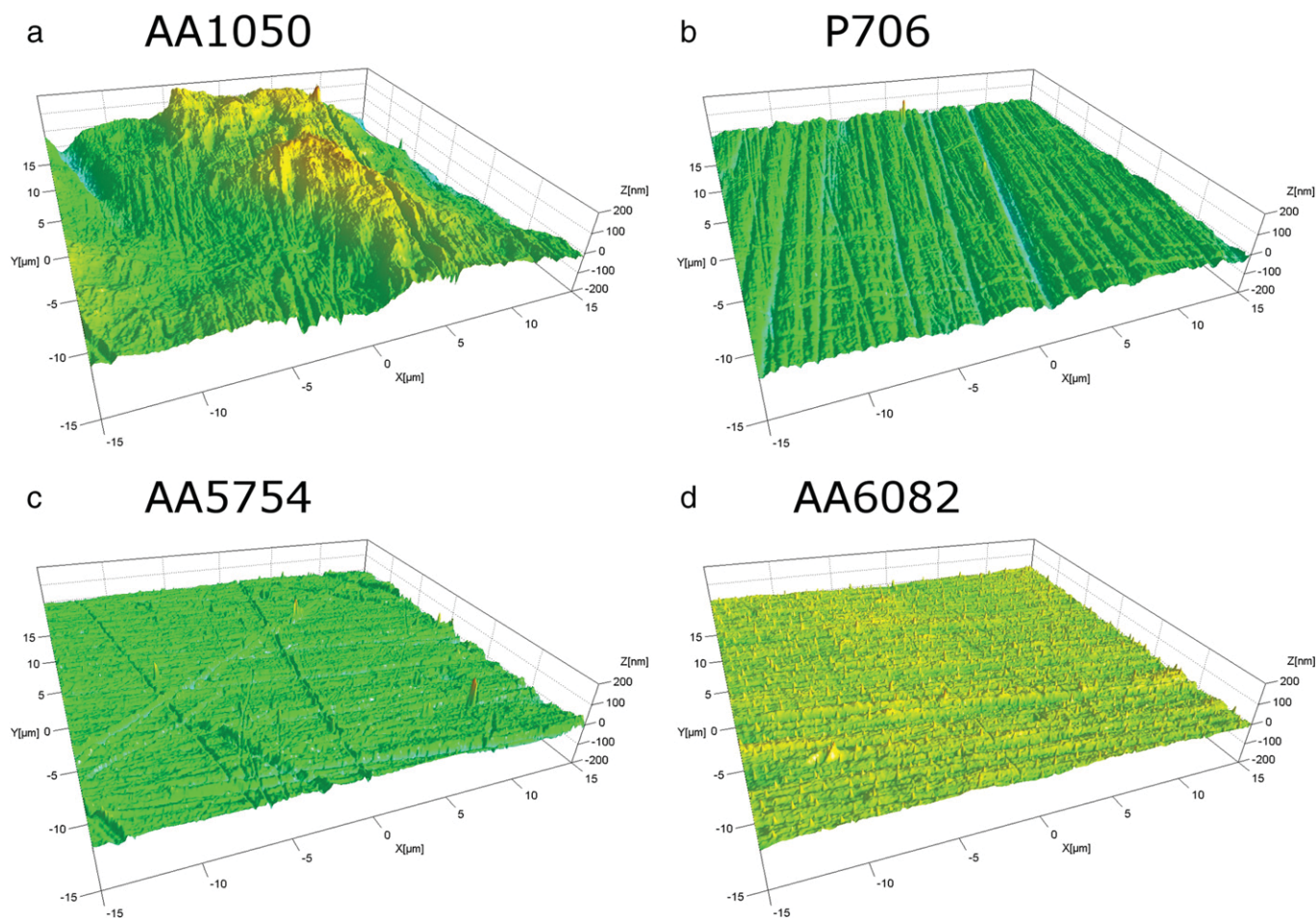


Fig. 8. Surface topography using AFM ( $30\ \mu\text{m} \times 30\ \mu\text{m}$ ) of as-polished specimens, a) AA1050, b) P706, c) AA5754 and d) AA6082.

specimen showed a lower peak value ( $1.8\ \text{sr}^{-1}$ ). However, the reflection distribution function broadens after anodisation. The as-polished specimen showed measurable reflectance at approximately  $\pm 10^\circ$  from the specular angle with a peak value of  $90.8\ \text{sr}^{-1}$ . At larger angles, no signal was detected. The polished, as-anodised specimen showed a narrow distribution with a specular peak value of  $43.1\ \text{sr}^{-1}$ , but the scattering of light at larger angles became more dominant after anodising suggesting that the oxide layer introduces diffuse scattering.

#### 4. Discussion

The difference in appearance of anodised aluminium specimens due to prior surface finish such as polishing and etching is well-known and is used commercially for various applications. On the other hand, the less known synergistic effects of alloy composition and prior surface finish are important for the decorative applications, where a reliable finish and reproducible appearance are critical. The increased use of

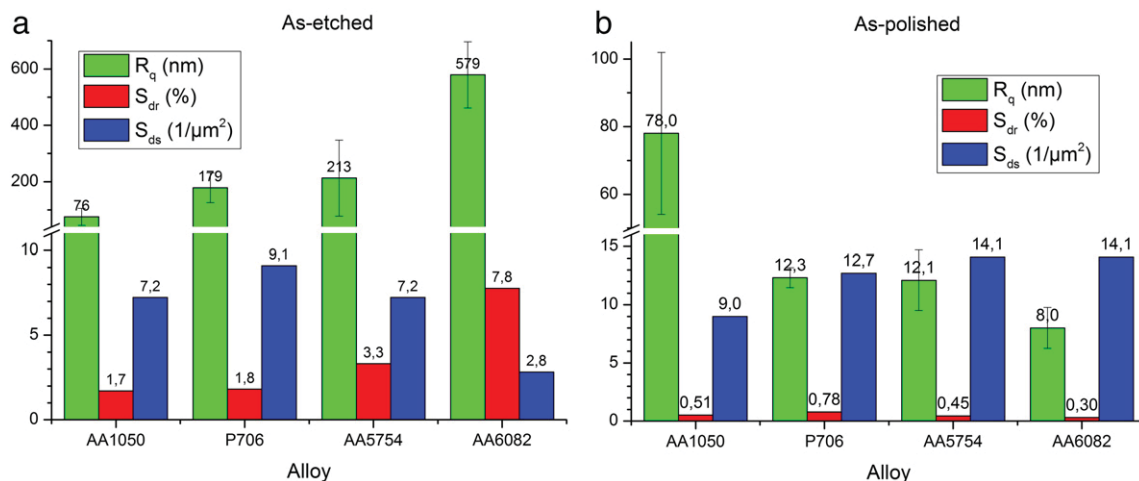
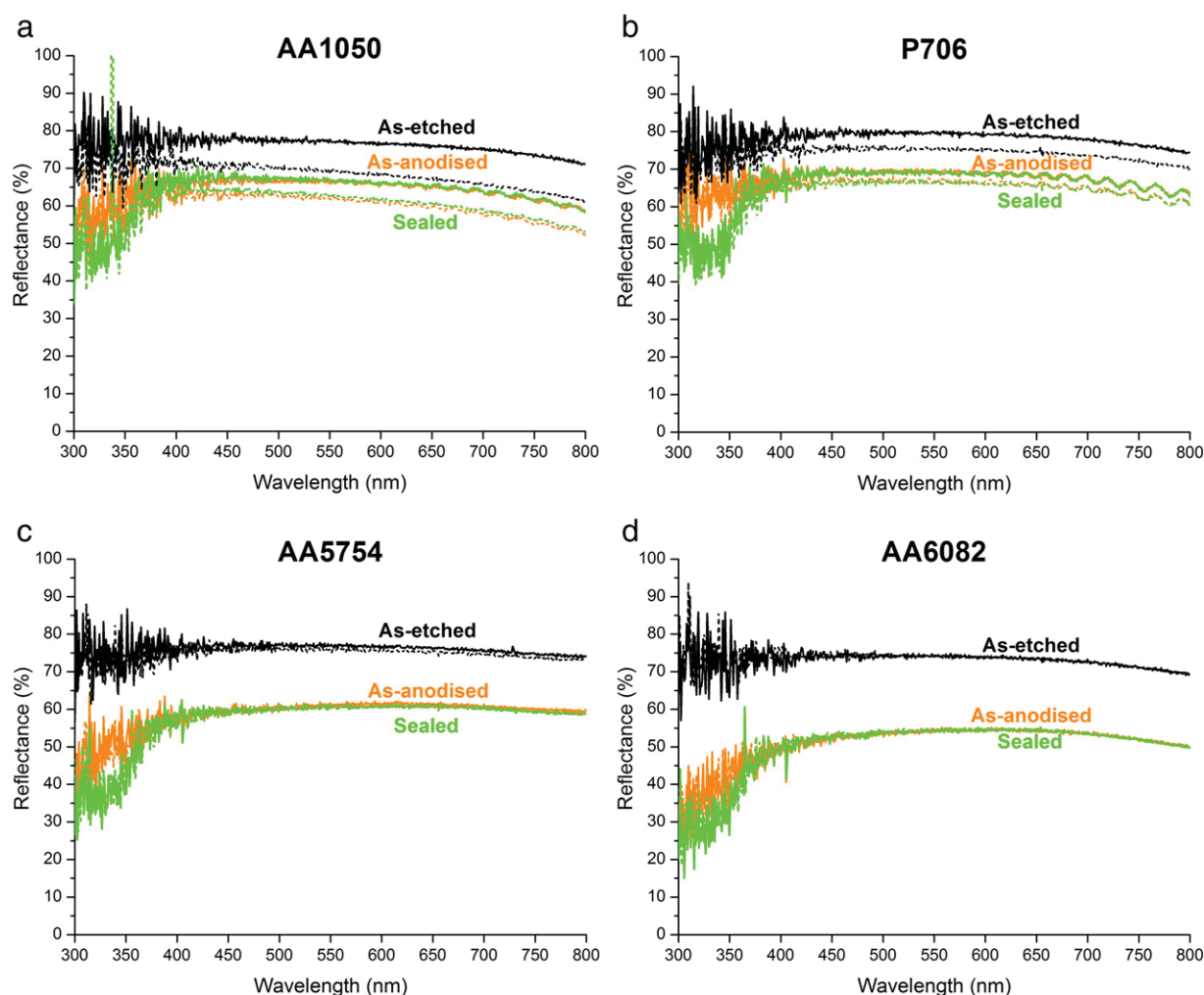


Fig. 9. Roughness parameters for a) as-etched specimens, and b) as-polished specimens.



**Fig. 10.** Photo spectrometry measurements of etched specimens, showing total reflectance (solid curves) and only diffuse reflectance (dotted curves), a) AA1050, b) P706, c) AA5754 and d) AA6082.

recycled aluminium alloys boost these effects due to the increased amount of alloying elements. The results presented in this paper show that the alloying elements have a big influence on the appearance of the anodised surface due to the creation of certain surface structures. Additionally, results show that the prior surface finish topography is more or less maintained at the oxide–substrate interface after anodisation. For a totally pure aluminium specimen, maintenance of surface morphology after anodising is expected to result in only negligible changes in the reflectance behaviour of the substrate before and after anodisation. However, the reflectance is much more diffuse for regular aluminium alloys after anodisation due to second phase particles of the alloying elements creating pits or sticking out of the substrate into the oxide as unchanged phases or partially oxidised. More detailed discussions of the effects of various parameters are presented below.

#### 4.1. Effect of prior surface finish

It is well-known that etching is performed to roughen the surface of the specimen, giving a matt finish. The results presented in Figs. 5, 7 and 10 show that the effect of etching on the microstructure and appearance after anodisation are alloy dependant. For the as-etched specimens, there is a direct connection between the measured roughness parameters,  $R_q$  and  $S_{dr}$  (Fig. 9a) and the degree of specular reflectance (Fig. 10). The as-etched specimen of the 99.5% pure AA1050 is flat (Fig. 7a) and shows the most specular reflectance (Fig. 10a) followed by P706

(Fig. 10b) and AA5754 (Fig. 10c) with very little specular reflectance, while the roughest alloy, AA6082, shows no specular reflectance (Fig. 10d). Looking at the effect of alloy compositions (Table 1), it is found that the AA5754 is alloyed to the highest degree with magnesium as the main alloying element. The AA6082 has higher silicon content and slightly higher iron concentration limit and might also contain more manganese compared to AA5754, supporting that iron and silicon rich phases create rougher surfaces than magnesium containing phases since magnesium is more reactive with NaOH than e.g. silicon and iron [2].

The photograph of the AA1050, **as-etched** specimen (Fig. 3a) is quite dark compared to all other specimens, as found in the calculated L-values, (Table 3). The L-values calculated based on the photographs of the etched specimens were compared to L-values calculated based on the photospectrometry measurements of the etched specimens seen in Fig. 10 (not presented). It was found that the values are directly comparable for totally matte specimens (Fig. 10c and d). Whereas, some deviations were found for P706 with some specular reflectance and especially for AA1050 showing more specular reflectance, probably due to reflection of the black background (Fig. 10b and a respectively).

Polishing is done to achieve a high gloss surface finish. However, the AA1050 is pure and therefore very soft, making it very hard to polish without causing grooves during the polishing process (Fig. 8a), compared to the harder P706, AA5754, and AA6082 (Fig. 8b–d). AA6082 was expected to have the hardest surface due to age hardening creating  $Mg_2Si$  phases [31], and shows the lowest  $R_q$  and  $S_{dr}$  values (Fig. 9b), and



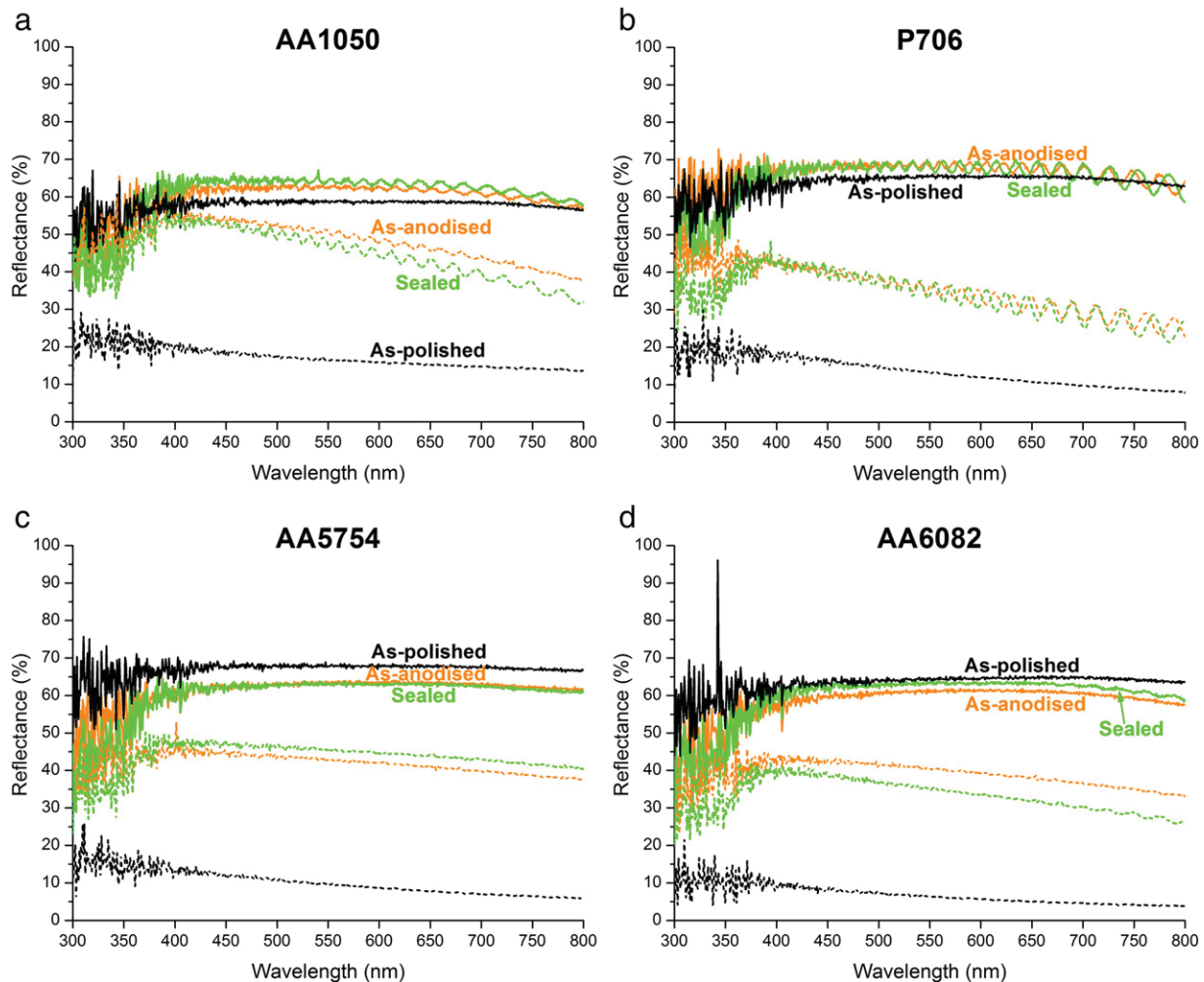


**Fig. 11.** Photo spectrometry measurements of polished specimens, showing total reflectance (solid curves) and only diffuse reflectance (dotted curves), a) AA1050, b) P706, c) AA5754 and d) AA6082.

the lowest diffuse reflectance for the as-polished specimens (Fig. 11d). Even though the specular reflectance of AA5754 (Fig. 11c) is as high as for AA6082 (Fig. 11d), the reflection is found to be slightly distorted (Fig. 4g) compared to P706 and AA6082 (Fig. 4a and d), but this has not been investigated further.

The roughness measurements show  $R_q$  values above 175 nm for the etched specimens (Fig. 9a) and below 13 nm for polished specimens (Fig. 9b) for P706, AA5754, and AA6082. As expected, the etched specimens have a dominant diffuse reflectance (Figs. 3 and 10), whereas the polished specimens have a large specular reflectance (Figs. 4 and 11). This is in agreement with reported literature [11] that the gloss of an aluminium surface decreases as the roughness increases until a roughness of about 200 nm.

The purity of AA1050 leads to a clear, relatively flat etched surface (Fig. 7a) and the softness of the alloys causes an uneven polishing (Fig. 8a). Comparing the roughness parameters of the as-etched and as-polished AA1050 specimens (Fig. 9); it is found that the  $R_q$  value is slightly higher for the as-polished specimen, and that the  $S_{dr}$  value is bigger for the as-etched specimen.

From the photospectrometry measurements it is found that the total reflectance of the as-etched specimens (Fig. 10) is higher than that for the as-polished specimens (Fig. 11). It is expected that etching removes oxides in the subsurface layer occurring during rolling [15,16], which will not be completely removed during polishing, but the surface material will be smeared out. Additionally, it is found that the reflectance is the highest for the pure alloys (Fig. 10a and b). However, the reflectance

of P706 is higher than that of AA1050, and the reflectance is higher for AA5754 than for AA6082. In both cases, the higher reflectance alloy has a higher concentration of magnesium but lower concentration of iron and silicon.

#### 4.2. Effect of anodisation

The SEM investigations of the etched specimens (Fig. 5) show that there is a remarkable correlation between the topography of the as-etched surface (left-hand column) and the oxide-substrate interface after anodisation (right-hand column), as previously indicated by Fratila-Apachitei et al. [12]. Thus, the original morphology has a significant impact on the morphology of the oxide-substrate interface and thereby the final appearance of the anodised aluminium specimen. The SEM investigations of the **as-polished** specimens (Fig. 6, left-hand column) show that the surfaces are flat with polishing grooves, which are to some extent smoothed out in the oxide-substrate interface (right-hand column). Furthermore, the oxide-substrate interface showed pits and intermetallic particles sticking out from the substrate into the oxide due to the difference in oxidation behaviour of the second phases compared to the aluminium matrix. It is reported that the iron and silicon rich particles are usually unaffected, while  $Mg_2Si$  and other active particles are partially or fully oxidised or dissolved during anodisation [24]. The particles sticking out from the substrate into the oxide are expected to have a large influence on the appearance of the specimens, as described in previous studies [10,11]. The particles in

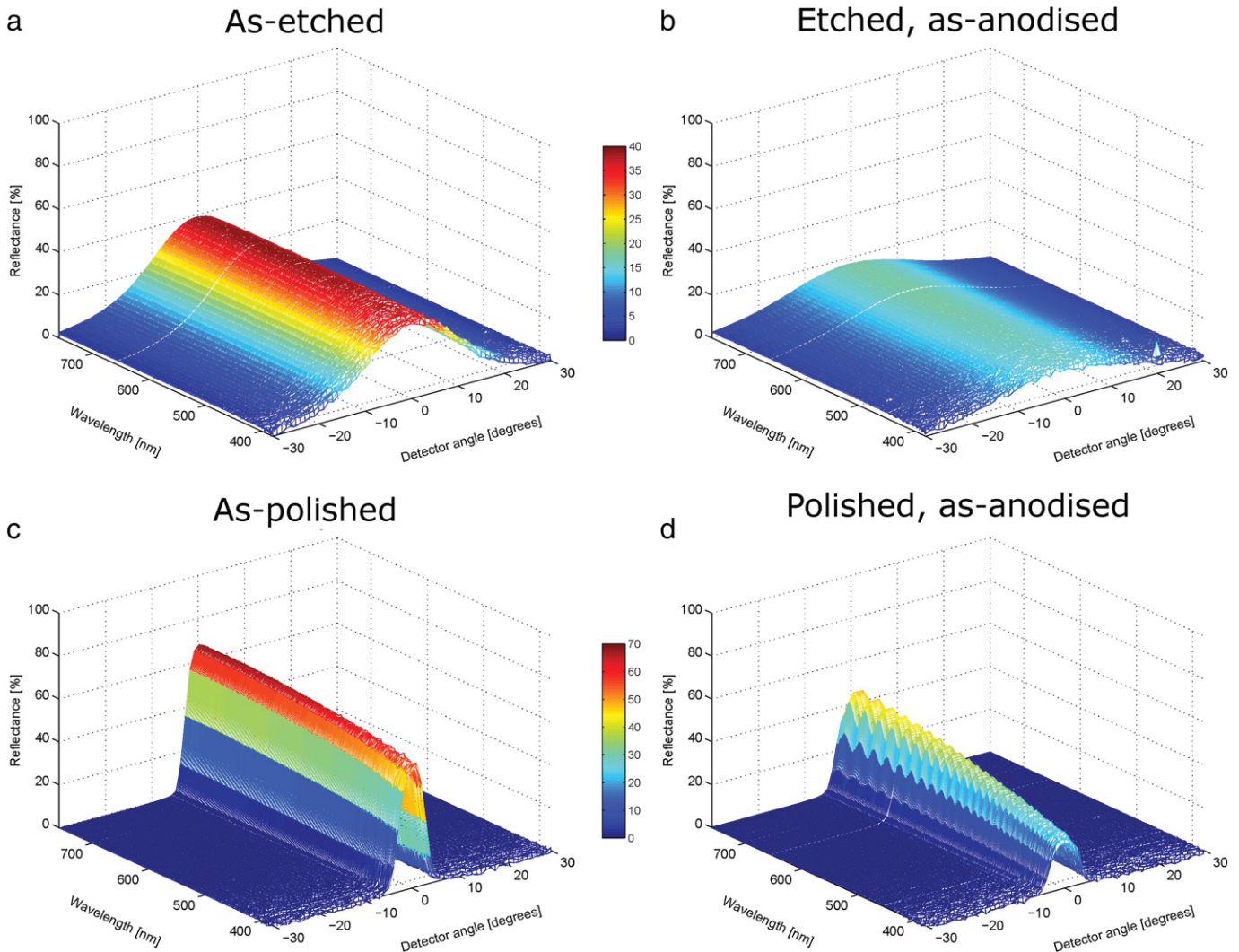


Fig. 12. Angle resolved photospectrometry on P706 specimens with an angle of incidence of  $45^\circ$ . a) as-etched, b) etched, as-anodised, c) as-polished, and d) polished, as-anodised.

the interface will cause diffuse scattering of light and therefore lower the amount of specular reflectance for the anodised AA5754 and AA6082 specimens compared to the purer AA1050 and P706, as seen in the photographs (Fig. 4) and the photospectrometry measurements (Fig. 11).

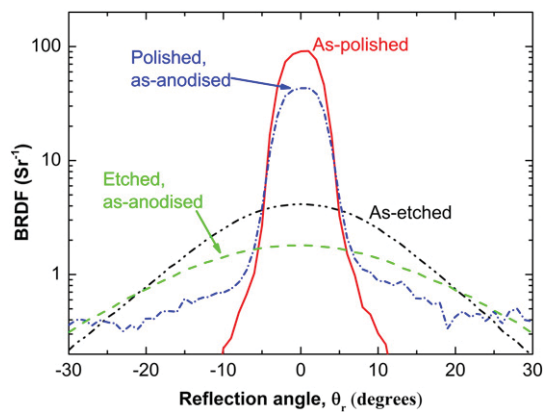


Fig. 13. BRDF measurements of alloy P706 measured at an incident angle of  $\theta_i = 45^\circ$  at 550 nm at angles of  $\pm 30^\circ$  from the specular angle.

The BRDF results of the P706 specimens (Fig. 13) show that the rough as-etched specimen reflects light over a wide angular range to about  $\pm 30^\circ$ . On the other hand the polished, as-anodised specimen reflects still at low measurable reflectance intensities at higher angles. Since a smoother surface is found for the polished and anodised specimens (Fig. 6e and f) compared to the as-etched specimen (Fig. 5d), it is expected that the scattering of light occurring in the anodised layer might be the reason for the broad reflectance characteristics of the polished, as-anodised specimen.

Fringes are found in the photospectrometry measurements for the **polished** and anodised specimens (Fig. 11) for specimens with anodised layers up to  $6.8 \mu\text{m}$  in thickness (Table 4), and are not seen for anodised layers of  $7.2 \mu\text{m}$  and more. This pattern is previously found by Shih et al. [32], however they found that the fringes disappeared for AA1050 specimens at thicknesses of  $2.5 \mu\text{m}$  and more [32]. Additionally, it is found that the polished, as-anodised, P706 specimen (Fig. 11b) with  $6.8 \mu\text{m}$  oxide shows much bigger fringes than the polished, sealed, AA6082 specimen (Fig. 11d) with same oxide thickness. It is expected that the impurities in the AA6082 oxide obstruct the thin film interference due to scattering effects. Furthermore, the morphology of the oxide–substrate interface has an effect on the interference fringes, as found for the etched and anodised specimens of P706 (Fig. 10b) of similar thickness ( $6.7 \mu\text{m}$  and  $6.9 \mu\text{m}$  (Table 4)) showing much smaller fringes.

For the **etched** P706 specimens, both the integrating sphere (Fig. 10b) and the BRDF measurements (Fig. 12a and b) show that the total reflectance decreases after anodisation. For the **polished** P706 specimens, the integrating sphere measurements (Fig. 11b) the total reflectance is almost similar for the as-polished and the polished, as-anodised specimen, while the diffuse reflectance is lower for the as-polished specimen. Thus, it has the highest specular reflectance. This is supported by the BRDF measurements (Fig. 13), where the as-polished specimen shows a higher BRDF peak at and near the specular region compared to the polished, as-anodised specimen. The BRDF of the polished, as-anodised specimen shows broad reflectance characteristics in the near specular region, supporting that the oxide layer induces diffuse scattering of the light [20,21]. A larger diffuse reflectance of the anodised specimens is also observed in the photographs of the polished specimens (Fig. 4, middle and right-hand column), where the bright light reflected by the plate of polystyrene is reflected in the specimens. Less illumination of the plate of polystyrene had probably reduced the diffuse reflectance seen in the photographs and thereby enhanced the appearance of the specular reflection for the polished specimens.

#### 4.3. Effect of sealing

Sealing of the anodised layer after anodisation did not create major changes in the optical appearance of the **etched** specimens (Table 3 and Figs. 3 and 10). Additionally, the results of the SEM investigations of the etched, as-anodised specimens are not presented, but the specimens look identical to the images presented of the etched, sealed specimens in Figs. 5 and 6. The photospectrometry measurements (Fig. 10) of the etched, sealed specimens compared to the etched, as-anodised (and polished, as-anodised) specimens show no difference in the visible spectrum, but the presence of pseudoböhmite causes a dip in the reflectance spectra at around 350 nm due to light absorption in the sealed layer.

Looking at the photographs of the **polished** specimens it is found that the sealing actually has an effect on the appearance of the specimens. The polished, sealed specimens of AA1050 and P706 (Fig. 4c and f) have a more distinct reflection, than the polished, as-anodised specimens (Fig. 4b and e). It is expected that during the sealing, the porous anodised layer is transformed into a much more optically uniform layer of pseudoböhmite and aluminium hydroxide ( $\text{Al}(\text{OH})_3$ ) [33,34] giving a more undisturbed and distinct reflection compared to the unsealed specimens. It is noticed that the anodised layer of the sealed specimens are thinner (Table 4) due to the lower anodisation voltage of 12.1 V instead of 12.6 V as for the polished, as-anodised specimens. However, the difference is considered insignificant as the photospectrometry measurements (Fig. 11) show an almost identical reflectance spectrum for the polished, as-anodised and the polished, sealed specimens. The anodised layer has an effect on the appearance, which is in agreement with other studies [2,20–23]. Zhu et al. [11] found very little optical effect of the anodised layer but it is important to notice that their studies were made on etched specimens. It is expected that the appearance of high gloss specimens is much more sensitive to smaller variations in the appearance compared to those of the etched specimens. Furthermore, it is hard to determine whether the reflection of an etched specimen is distinct, due to the nature of the diffuse reflection. Tabrizian et al. [23] studying high gloss specimens found that the inhomogeneity and imperfections in the anodised layer have a large effect on the optical appearance of anodised aluminium specimens.

All **polished** specimens have almost the same total reflectance, however the specular reflectance is higher for P706 and AA6082 after anodisation and sealing (Figs. 4c, f and 11b, d) compared to AA1050 and AA5754 (Figs. 4i, l and 11a, c). The SEM images show big amounts of particles and pits in the oxide–substrate interface for the AA5754 and AA6082 specimens (Fig. 5i and l), which cause

the anodised specimens to show more diffused reflections (Fig. 4i and l).

Comparing **etched**, sealed specimens, it is found that the degree of alloying (Table 1) is correlated with the roughness after etching (Fig. 7). As expected, an increase in the surface roughness results in an enhanced diffuse scattering of light (Fig. 10a and d).

Comparing **polished**, sealed specimens, it is notable that some alloying is necessary for gaining a proper polished flatness (Fig. 8). In addition, a high alloy purity ensures a more specular reflection, since only few particles and pits are present at the oxide–substrate interface (Fig. 6f) [10,11], and only little absorption and scattering will occur in the anodised layer [23]. It is found that for P706 the uniform pseudoböhmite layer after sealing gives a distinct (Fig. 4f) and highly specular reflectance (Fig. 11d).

The results presented in this paper show that alloying elements, especially iron and silicon, have significant influence on the appearance of both etched and polished, anodised aluminium specimens. The alloying elements affect the optical properties of the anodised layer making it less transparent, and change the surface and oxide–substrate morphology during etching and anodisation. The knowledge achieved here on the commercial alloys is particularly important when using recycled aluminium alloys containing higher amounts of impurities and alloying elements.

#### 5. Conclusion

The appearance of commercial alloys AA1050, Peraluman 706 (P706), AA5754, and AA6082 were investigated with focus on the effect of etching, polishing, anodisation, and sealing. It was found that:

- The roughness and percentage of diffuse reflectance caused by etching increased with the degree of alloying. For pure and soft alloys, the polishing was hard and resulted in a rougher surface compared to specimens with a higher amount of alloying elements.
- BRDF measurements showed that the as-etched specimens show a broad intensity distribution function of the scattered light at and near the specular region, whereas the as-polished specimen exhibit high reflectance near the specular angle. After anodisation, for both etched and polished specimens, the fraction of diffuse light scattering increases and this could be explained by the light scattering within the anodised layer.
- A clear correlation was found between the topography of the original surface and the topography of the oxide–substrate interface beneath the anodised layer after anodising.
- Polished specimens alloyed to a higher degree lost their high gloss appearance after anodisation due to particles and pits in the oxide–substrate interface and heterogeneities in the oxide due to alloying elements. The high purity alloy P706 with 0.3 wt.%–0.8 wt.% magnesium showed high gloss after polishing, anodisation and sealing due to the high purity and the flat polished surface.
- Sealing made the reflection of the polished specimens more distinct since the pseudoböhmite layer is optically more homogenous than the porous as-anodised layer. Absorption was observed in the reflectance for sealed specimens at 350 nm due to absorption in the pseudoböhmite layer.

#### Acknowledgements

The authors thank the Danish Agency for Science, Technology and Innovation for their financial support of the IdeAl project. Thanks to all partners in the IdeAl innovation consortium. This project was additionally supported by the Danish National Technology Foundation through the ODAAS project. Also thanks to Ib Kongstad and Flemming Jensen and colleagues at Bang & Olufsen for the help with producing the specimens.



## References

- [1] S. Wernick, R. Pinner, P.G. Sheasby, *The Surface Treatment and Finishing of Aluminium and its Alloys*, 5th ed. Finishing Publications Ltd & ASM International, Teddington, UK, 1987.
- [2] R. Akeret, H. Bichsel, E. Schwall, E. Simon, M. Textor, *Trans. Inst. Met. Finish.* 68 (1990) 20–28.
- [3] T. Hauge, K.F. Karhausen, *Alum. Extrus.* (1998) 32–37.
- [4] K.F. Karhausen, A.L. Dons, T. Aukrust, *Mater. Sci. Forum* 217–222 (1996) 403–408.
- [5] Y. Ma, X. Zhou, G.E. Thompson, J.-O. Nilsson, M. Gustavsson, A. Crispin, *Trans. Inst. Met. Finish.* 91 (2013) 11–16.
- [6] T. Minoda, H. Yoshida, *Metall. Mater. Trans. A* 33A (2002) 2891–2898.
- [7] M. Torkar, M. Godec, M. Lamut, *Eng. Fail. Anal.* 16 (2009) 909–913.
- [8] H. Zhu, X. Zhang, M. Couper, A.K. Dahle, *Mater. Chem. Phys.* 113 (2009) 401–406.
- [9] H. Zhu, M.J. Couper, A.K. Dahle, *High Temp. Mater. Process.* 31 (2012) 105–111.
- [10] H. Zhu, X. Zhang, M.J. Couper, A.K. Dahle, *Metall. Mater. Trans. A* 40 (2009) 3264–3275.
- [11] H. Zhu, X. Zhang, M.J. Couper, A.K. Dahle, *JOM* 62 (2010) 46–51.
- [12] L.E. Fratila-Apachitei, H. Terryn, P. Skeldon, G.E. Thompson, J. Duszczuk, L. Katgerman, *Electrochim. Acta* 49 (2004) 1127–1140.
- [13] H. Zhu, T. Wei, M.J. Couper, A.K. Dahle, *JOM* 65 (2013) 618–624.
- [14] S. Van Gils, T. Dimogerontakis, G. Buytaert, E. Stijns, H. Terryn, P. Skeldon, G.E. Thompson, M.R. Alexander, *J. Appl. Phys.* 98 (2005) (083505–1–9).
- [15] G. Buytaert, H. Terryn, S. Van Gils, B. Kernig, B. Grzempa, M. Mertens, *Surf. Interface Anal.* 37 (2005) 534–543.
- [16] G. Buytaert, H. Terryn, S. Van Gils, B. Kernig, B. Grzempa, M. Mertens, *Surf. Interface Anal.* 38 (2006) 272–276.
- [17] G. Buytaert, B. Kernig, H. Brinkman, H. Terryn, *Surf. Coat. Technol.* 201 (2006) 2587–2598.
- [18] Premendra, J.H. Chen, F.D. Tichelaar, H. Terryn, J.H.W. DeWit, L. Katgerman, *Surf. Coat. Technol.* 201 (2007) 4561–4570.
- [19] P. Ratchev, R. Labie, B. Verlinden, R. Van Den Broeck, *Z. Met.* 91 (2000) 510–515.
- [20] M. Saito, S. Yasunori, M. Miyagi, K. Wada, O. Sachiko, *J. Appl. Phys.* 34 (1995) 3134–3138.
- [21] M. Saito, Y. Shiga, M. Miyagi, *J. Electrochem. Soc.* 140 (1993) 1907–1911.
- [22] L.-F. Huang, M. Saito, M. Miyagi, *Jpn. J. Appl. Phys.* 32 (1993) 3169–3174.
- [23] N. Tabrizian, H.N. Hansen, P.E. Hansen, R. Ambat, P. Møller, *Surf. Coat. Technol.* 204 (2010) 2632–2638.
- [24] J. Timm, *Key Eng. Mater.* 44–45 (1990) 219–232.
- [25] S.M. Luke, P. Vukusic, B. Hallam, *Opt. Express* 17 (2009) 14729–14743.
- [26] Image Metrology A/S, Software: SPIP 6.1.1, 2013.
- [27] S. Davíðsdóttir, S. Canulescu, K. Dirscherl, J. Schou, R. Ambat, *Surf. Coat. Technol.* 216 (2013) 35–45.
- [28] P. Dutre, P. Bekaert, K. Bala, *Advanced Global Illumination*, 2nd ed. A K Peters/CRC Press, Wellesley, USA, 2006.
- [29] C. Vargel, *Corrosion of Aluminium*, Elsevier Science, Oxford, UK, 2004.
- [30] G.A. Edwards, K. Stiller, G.L. Dunlop, M.J. Couper, *Acta Mater.* 46 (1998) 3893–3904.
- [31] J.R. Davis, *ASM Speciality Handbook: Aluminium and Aluminium Alloys*, ASM International, 1996.
- [32] T.-S. Shih, P.-S. Wei, Y.-S. Huang, *Surf. Coat. Technol.* 202 (2008) 3298–3305.
- [33] A. Bautista, J.A. González, V. Lopez, *Surf. Coat. Technol.* 154 (2002) 49–54.
- [34] S.J. Feliu, M.J. Bartolomé, J.A. González, S. Feliu, *J. Electrochem. Soc.* 154 (2007) C241–C248.







# Anodisation of sputter deposited aluminium–titanium coatings: Effect of microstructure on optical characteristics

Martin Aggerbeck, Andreas Junker-Holst, Daniel Vestergaard Nielsen, Visweswara Chakravarthy Gudla, Rajan Ambat \*

Technical University of Denmark, Department of Mechanical Engineering, Materials and Surface Engineering, Produktionstorvet 425, 2800 Kgs. Lyngby, Denmark

## ARTICLE INFO

### Article history:

Received 11 January 2014

Accepted in revised form 25 May 2014

Available online 10 June 2014

### Keywords:

Aluminium

Titanium

Anodisation

Microstructure

Appearance

TEM

## ABSTRACT

Magnetron sputtered coatings of aluminium containing up to 18 wt.% titanium were deposited on aluminium substrates to study the effect of microstructure on the optical appearance of the anodised layer. The microstructure and morphology were studied using transmission electron microscopy (TEM), X-ray diffraction (XRD), and glow discharge optical emission spectroscopy (GDOES), while the optical appearance was investigated using photospectrometry. The microstructure of the coatings was varied by heat treatment, resulting in the precipitation of  $\text{Al}_3\text{Ti}$  phases. The reflectance of the anodised surfaces decreased with titanium content in the as-deposited, and heat-treated states, and after anodisation of the as-deposited coatings. Specimens turned grey or black when anodising after heat treatment. Partially anodised  $\text{Al}_3\text{Ti}$  phases were found in the anodised layer, and the interface between substrate and anodised layer was rough, causing light trapping. Progressive darkening of the anodised layer is assumed to be due to the synergetic effect of morphology of incorporated intermetallics and substrate interface.

© 2014 Elsevier B.V. All rights reserved.

## 1. Introduction

Anodised aluminium surfaces are widely used for decorative applications, often without colouring. The increased use of recycled aluminium alloys makes it difficult to predict the appearance of the anodised surface due to the presence of higher amounts of impurity elements and second phase particles in the aluminium matrix. Therefore it is of great interest to understand the optical effect of various elements and second phase particles in the aluminium matrix, including those which are not highly soluble in aluminium.

Magnetron sputtering is a process which can be used for synthesising non-equilibrium coating compositions, where the amount of various elements can be precisely controlled. Therefore sputter coatings can be used as a model system for studying the effect of alloying elements and the resulting microstructure on various properties such as corrosion and wear resistance, and optical appearance. Both crystalline and amorphous  $\text{TiO}_2$  are known to have high refractive indices, and therefore titanium has been deposited to create anodised aluminium layers containing  $\text{TiO}_2$  constituents.

For as-deposited coatings containing up to 40 wt.% titanium it has been reported that the microstructure is comprised of a supersaturated  $\alpha\text{-Al}$  [1–3]. Hampshire et al. [4,5] investigated the microstructure and

mechanical properties of Al–Ti sputtered coatings in the as-deposited form and after heat treatment for 2 h at 600 °C. Additionally, many authors have studied the corrosion properties of Al–Ti coatings in saline [2, 6,7], acidic [8–11] and alkaline environments [12].

Studies on the optical properties of a sputtered aluminium film show that both the index of refraction,  $n$ , and the extinction coefficient,  $k$ , are found to be affected by the sputtering parameters [13]. Wöltgens et al. [14] investigated optical properties of magnetron sputtered Al–Ti films of 80 nm thickness containing up to 13 wt.% titanium and found that the reflectance decreases with the titanium concentration both for the as-deposited film and after heat treatment.

Anodisation of Al–Ti coatings have been done in several studies [3, 15–18], finding the anodised layer to be amorphous with few inclusions of crystalline  $\text{Al}_2\text{O}_3$  and  $\text{TiO}_2$  [3,15,17]. The oxide layer has approximately the same Al–Ti ratio as the coating [3,15,17,18], and  $\text{Ti}^{4+}$  migrates at rates, which are maximum 10% lower than that of  $\text{Al}^{3+}$  [15]. Anodisation of Al–Ti coatings showed that the pore diameters and pore distance for fixed potential [16,18] and the pore diameter for fixed current [3] increase with the titanium concentration both with and without hydrogen fluoride in the sulphuric acid electrolyte. The thickness of the anodised layer was found to decrease significantly with increasing titanium content when the anodisation potential was kept constant [16,18].

The investigations in this paper use magnetron sputtered Al–Ti coatings containing up to 18 wt.% titanium as a model system to investigate the microstructural and optical effects of electrochemically stable titanium rich second phase particles. The as-deposited microstructure was altered by heat treatment and the coatings were anodised in sulphuric

\* Corresponding author. Tel.: +45 45252181; fax: +45 45936213.

E-mail addresses: [mag@plan.aau.dk](mailto:mag@plan.aau.dk) (M. Aggerbeck), [s093221@student.dtu.dk](mailto:s093221@student.dtu.dk) (A. Junker-Holst), [daniel.v.nielsen@gmail.com](mailto:daniel.v.nielsen@gmail.com) (D.V. Nielsen), [vichg@mek.dtu.dk](mailto:vichg@mek.dtu.dk) (V.C. Gudla), [ram@mek.dtu.dk](mailto:ram@mek.dtu.dk) (R. Ambat).

acid. Microstructural investigations were performed using transmission electron microscopy, X-ray diffraction and glow discharge optical emission spectroscopy, while optical investigations were performed with reflectance analysis using an integrating sphere spectrometer setup.

## 2. Materials and methods

### 2.1. Materials and heat treatments

Coatings were deposited by DC magnetron sputtering using an industrial-scale CemeCon CC800/8 machine with a chamber volume of 70 cm × 60 cm × 60 cm, and two cathodes. The opposite placed cathodes faced the substrates which were mounted on a planetary rotating table in the middle of the chamber to ensure a homogeneous deposition. The deposition chamber was initially evacuated to a base pressure of 6 mPa. During sputtering constant argon flow of 200 SCCM (mL/min) was used, leading to a typical argon pressure of 500 mPa. The distance between the targets and sample was about 100 mm, and the bias voltage on the substrates was fixed at −50 V. The maximum temperature during deposition was between 150 °C and 200 °C, as measured by a bi-metal thermometer during the deposition.

Specimens of homogenous composition were produced on substrates of AA465.0 (8 wt.%–11 wt.% silicon and 2 wt.%–4 wt.% copper) with dimensions of 70 mm × 25 mm × 4 mm. For comparison, AA1050 coatings were produced using two AA1050 targets. Binary Al–Ti coatings were produced using an AA1050 target and a titanium target (grade 1, 99.5% purity) with cylindrical pins of 1 cm in diameter of AA1050. The aluminium target was sputtered at a power of 2000 W, while the titanium–aluminium target was sputtered at 100 W, 200 W, 400 W, and 600 W achieving titanium concentrations of 3 wt.%, 6 wt.%, 13 wt.%, and 18 wt.% (measured with energy dispersive X-ray spectroscopy (EDS)). The coatings were 11 µm–25 µm in thickness. These coated specimens were heat-treated for 2 h at 200 °C, 300 °C, 400 °C and 500 °C and subsequently cooled in air.

Al–Ti gradient coatings were produced on substrates of AA6401 (0.35 wt.%–0.7 wt.% magnesium and 0.25 wt.%–0.7 wt.% silicon) with dimensions of 220 mm × 40 mm × 5 mm. The targets were displaced with respect to the centre of the sputter coating chamber. The aluminium target was sputtered at a power of 2000 W, while the Ti–Al target was sputtered at a power of 300 W giving a gradually varying composition along the length of the specimen. One specimen with titanium concentrations of 6.5 wt.%–16.6 wt.% was obtained and cut into pieces, giving three specimens for each of four different concentration spans. The specimens were analysed in the as-deposited state and after heat treatment for 4 h at 500 °C and 4 h at 600 °C and subsequent air cooling. Another specimen was measured to contain 5.0 wt.%–15.4 wt.% titanium and was anodised in the as-deposited state and subsequently analysed by photospectrometry.

### 2.2. Anodisation

The specimens were rinsed with ethanol in an ultrasonic bath for 5 min before 2 min cleaning in 60 g/L AlfiClean from AluFinish at 60 °C. Desmutting was performed for 4 min in 69% nitric acid at room temperature. Anodisation was carried out for 20 min in 10% sulphuric acid at 13 °C–17 °C and a constant voltage of 18 V–19 V (the specimen containing 8.4 wt.%–10.5 wt.% titanium, heat treated at 500 °C was instead unintentionally anodised at 20 V–23 V, but gave the same appearance). Subsequent sealing of the anodised specimens was carried out in demineralised water at 96 °C. All steps except sealing were followed by recurring rinsing in demineralised water.

The as-deposited 5.0 wt.%–15.4 wt.% gradient sample was anodised for 30 min in sulphuric acid at 12.6 V and hot water sealed in one piece in an industrial setup described elsewhere [19].

### 2.3. Microstructural analysis

Phase identification was done by X-ray diffraction (XRD) measurements on a Bruker D8 Discover diffractometer with a copper K $\alpha$ 1 beam (1.54 Å) with grazing incidence at 2°. The measurements were performed in a 2 $\theta$  range from 20° to 100° (only 20° to 85° is presented) with a step size of 0.03° and a step time of 4 s. Obtained diffraction patterns were indexed using the EVA Application software [20].

For detailed microstructural analysis, transmission electron microscopy (TEM) was performed using a Tecnai T20 G2 from FEI operated at 200 keV. A Quanta 200 3D DualBeam microscope from FEI equipped with a micromanipulator was used for focused ion beam milling and in-situ lift out of a lamella of 2 µm thickness, followed by thinning in a Helios Nanolab DualBeam from FEI. The thickness of the TEM lamella made from the as-deposited coating was 175 nm, whereas the heat-treated and anodised specimen was milled to a thickness of 450 nm in the thickest area, while the oxide layer was milled away faster than the rest of the specimen and was therefore thinner. The final finishing of the lamella was performed by ion milling (2 kV) with low energy to avoid unintended damage from the beam.

Composition depth profiling was done using radio frequency glow discharge optical emission spectrometry (GDOES) on a GD Profiler 2 from Horiba Scientific. The argon pressure was set to 650 Pa and the process ran at a power of 35 W. The module and phase was set to 7.6 V and 3.8 V respectively.

### 2.4. Photospectrometry

For optical reflectance measurements, an integrating sphere setup (described in details in Ref. [21]) with light from DH 2000 from Ocean Optics using an optical fibre entering at 8° with respect to vertical was used. Reflections from the sample surface were integrated within the highly reflecting coated sphere and collected by an optical fibre connected to a photospectrometer (QE 65000 from Ocean Optics). Measurements were performed across a wavelength range of 380 nm–760 nm over an integration period of 3 s. All spectra were referenced against a NIST high reflectivity standard.

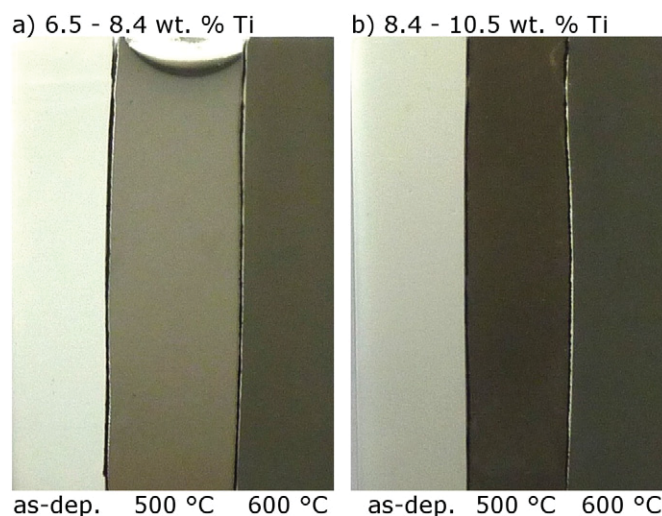


**Fig. 1.** Photographs of anodised specimens for, left: as-deposited, middle: 500 °C, and right: 600 °C for specimens with a titanium concentrations of a) 6.5 wt.%–8.4 wt.%, and b) 8.4 wt.%–10.5 wt.%.



### 3. Results

#### 3.1. Photographs

Fig. 1 shows the appearance of the anodised specimens of the lowest titanium concentrations for the as-deposited specimens and after heat treatment. For all titanium concentrations, anodisation after heat treatment at 500 °C and 600 °C gave a homogenous dark grey, brown or even black appearance. The as-deposited specimens showed a more regular light appearance after anodisation, and in some cases with colour bands due to thin film interference [22,23]. The concentrations shown in Fig. 1 are the measured titanium content on the as-deposited specimens. Similar appearance was found for the other titanium concentrations.

#### 3.2. Microstructural investigation

The TEM image of the as-deposited specimen containing 13 wt.% titanium (Fig. 2a) showed a layered structure with a general periodicity of  $32 \text{ nm} \pm 4 \text{ nm}$  due to the use of two different targets placed on opposite sides of the rotating specimen. Layers with bright appearance were mainly deposited from the AA1050 target with lower amounts of titanium, while the dark layers were rich in titanium. The bright layers of low titanium concentration were measured to be 22 nm–30 nm and the dark titanium rich layers were measured to 2.5 nm–9.5 nm depending on which layer was measured and how the layer boundaries were defined. Fig. 2b gives an overview of a specimen containing 10 wt.% titanium that was heat-treated for 4 h at 600 °C followed by anodisation. After heat treatment the layered structure was dissolved and a homogeneously appearing matrix containing precipitates with an average size of approximately  $250 \text{ nm} \times 550 \text{ nm}$  was formed. All precipitates were of the same composition, and the difference in contrast is due to the orientation with respect to the electron beam. The average thickness of the anodised layer was approximately 1.2  $\mu\text{m}$ . The encircled part of Fig. 2b shows an area with no particles, where the anodisation continued between two particles. The dark layer appearing at the oxide surface in

Fig. 2c is the platinum layer deposited for protection during the milling and lift out process. Particles in the anodised layer were found to be partly or fully oxidised as presented in Fig. 2c and d. The pores originated from the anodising process and were measured to be 8 nm–10 nm in diameter in the aluminium matrix. The titanium-containing phases featured both narrow and wider pores with diameters of the wider pores of 25 nm–35 nm. Furthermore, the pores in the aluminium collapsed during sealing, whereas both the narrow and the wide pores in the titanium-rich particles seemed unaffected by the sealing process. A bright region behind a particle (Fig. 2e) was expected to be unanodised metallic aluminium [24–26], where Walmsley et al. [26] found similar areas behind partly oxidised particles and identified these as unoxidised aluminium. Fig. 2f shows a partly anodised particle in the oxide–substrate interface.

XRD measurements (Fig. 3) were used for phase identification of the as-deposited film containing 12 wt.% titanium, after heat treatment for 4 h at 500 °C and 600 °C, and for a heat-treated and anodised specimen. For the as-deposited specimen, only peaks for the  $\alpha\text{-Al}$  phase were found, whereas for the specimens heat-treated at 500 °C and 600 °C, additional peaks corresponding to the  $\text{Al}_3\text{Ti}$  phase were found. No oxide containing phases were identified for the anodised specimen.

The GDOES measurements of an anodised specimen containing 7 wt.% titanium are presented with an overview and magnified view of the lower intensity values (Fig. 4a and b respectively). From crater depth measurements (not presented) the sputter rate was calculated to be  $\sim 30 \text{ nm/s}$ . In Fig. 4a and b, dotted lines indicate the interface between the anodised layer and the sputtered coating and the coating–substrate interface. The oxide–coating interface was at about 1.9  $\mu\text{m}$  ( $\sim 63 \text{ s}$ ) from the surface, and the coating–substrate interface was at about 10.5  $\mu\text{m}$  ( $\sim 350 \text{ s}$ ) from the surface. It is found that the aluminium and oxygen signals stabilised briefly within the oxide layer. This was followed by increasing signal for aluminium and decreasing signal for oxygen when closing in on the interface between the anodised layer and the sputtered coating. Presence of sulphur was attributed to the use of sulphuric acid in the anodisation process and hydrogen containing species were expected to be incorporated into the film both during anodisation and especially

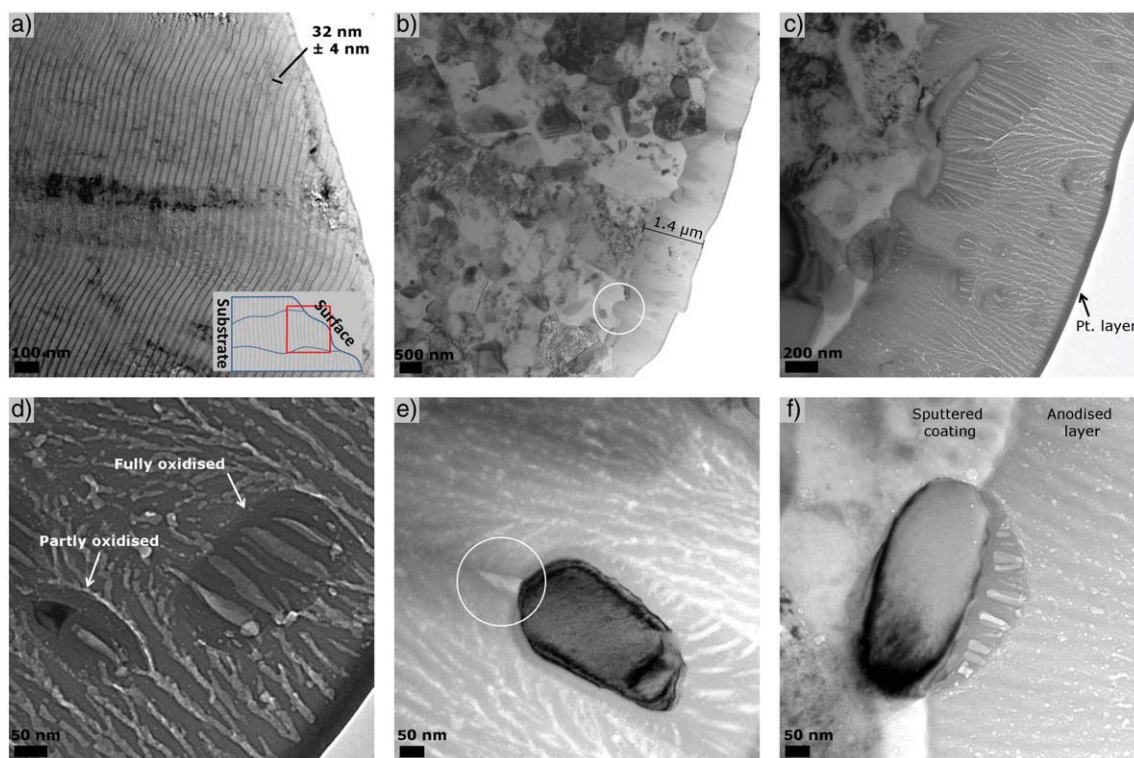
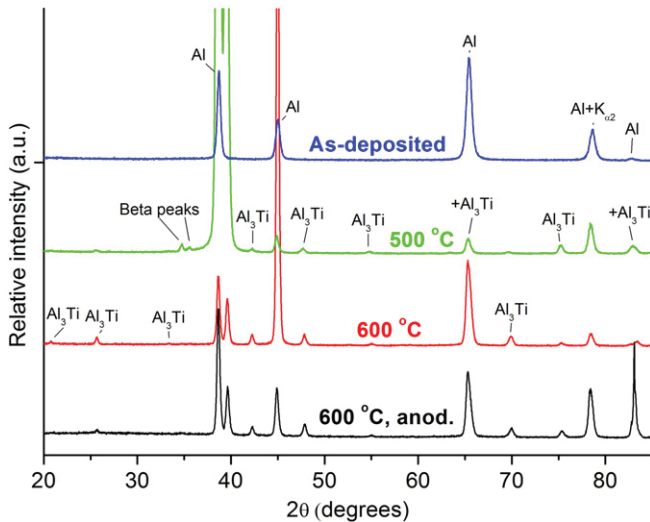


Fig. 2. Cross section transmission electron microscopy images of a) as-deposited coating containing 13 wt.% titanium, and b–f) heat-treated and anodised specimen containing approximately 10 wt.% titanium.



**Fig. 3.** X-ray diffraction measurements for coatings containing approximately 12 wt.% titanium in the as-deposited and heat-treated condition.

during sealing. The carbon peak at the surface was due to ethanol cleaning just before the measurement. Mainly aluminium and titanium were found in the sputtered coating. The oxygen concentration decreased and the magnesium concentration increased throughout the sputtered coating, due to diffusion from the AA6401 substrate during heat treatment.

### 3.3. Photospectrometry measurements

Photospectrometry measurements of the as-deposited coatings (Fig. 5a) showed that the total reflectance decreased with increasing titanium concentration. Additionally, it was found that the fraction of longer wavelengths increased with the titanium concentration i.e. the pure aluminium coating had a slight blue tint, whereas the coatings containing 13 wt.% and 18 wt.% titanium had a red tint. In Fig. 5d the reflectance of the as-deposited coatings is plotted at 600 nm as a function of titanium concentration (squares). Additionally, similar values for specimens heat-treated for 2 h at 300 °C are plotted (circles). In both cases the reflectance decreased with increasing titanium concentration. A series of specimens containing 13 wt.% titanium was heat-treated at different temperatures and the reflectance characteristics are presented in Fig. 5b and the reflectance at 600 nm in Fig. 5e. The reflectance in general

remains constant for specimens heat treated for 2 h at 400 °C, while the reflectance decreased after heat treatment at 500 °C (Fig. 5e). Furthermore, as seen in Fig. 5b, the reflectance of the anodised specimen heat treated at 500 °C was constant over the range of wavelengths, whereas for other specimens, reflectance has increased towards red. The as-deposited and anodised specimen showed large interference fringes, making the plot harder to evaluate. Therefore, Fig. 5c presents curves, which are smoothed by adjacent averaging in Origin, enabling comparison of the reflectance. A decrease in the reflectance was found from 450 nm towards lower wavelengths. The plot of reflectance at 600 nm (Fig. 5f) shows that the reflectance decreased with increasing titanium concentration from 8 wt.% titanium and more. The oxide thickness was measured by cross section SEM images (not presented) to be 3.8 μm for 5.0 wt.% titanium to 1.1 μm for 15.4 wt.% titanium.

## 4. Discussion

### 4.1. Microstructure and appearance of as-deposited coatings before and after anodisation

The microstructure of the as-deposited coating was found to be alternating layers of low and high content of titanium (Fig. 5a), which is similar to the structure of magnetron sputtered coatings reported in the literature with similar configuration of targets and rotation of specimens [14,15]. Since no titanium-containing phases were formed during deposition (Fig. 3), the coating is expected to be supersaturated  $\alpha$ -Al, at least in the aluminium-rich layers [1–3]. The reflectance of the specimens is well correlated with the titanium concentration (Fig. 5b), which is not expected, as the layered structure should negate the effect of the titanium concentration. The penetration depth of light at 500 nm (the depth where the radiation intensity is ~37% of the original incoming intensity) is calculated to be approximately 6.6 nm for pure aluminium and 16.5 nm for titanium. Furthermore, reflected light needs to return to the surface, doubling the optical path. Since the alternating layers had a period of 32 nm (Fig. 5a) for the specimen containing 13 wt.% titanium, it is not expected, that the light necessarily would be affected by both aluminium- and titanium-rich layers for all of the specimens. Furthermore, the measured layers are from different coatings produced in different processes, so that it is not expected that the same type of layer is at the surface for all specimens. The observed correlation between titanium concentration and the reflectance has not been explained. However, previous studies on Al–Ti coatings with a layered structure with a periodicity of only 1.6 nm [14] showed similar

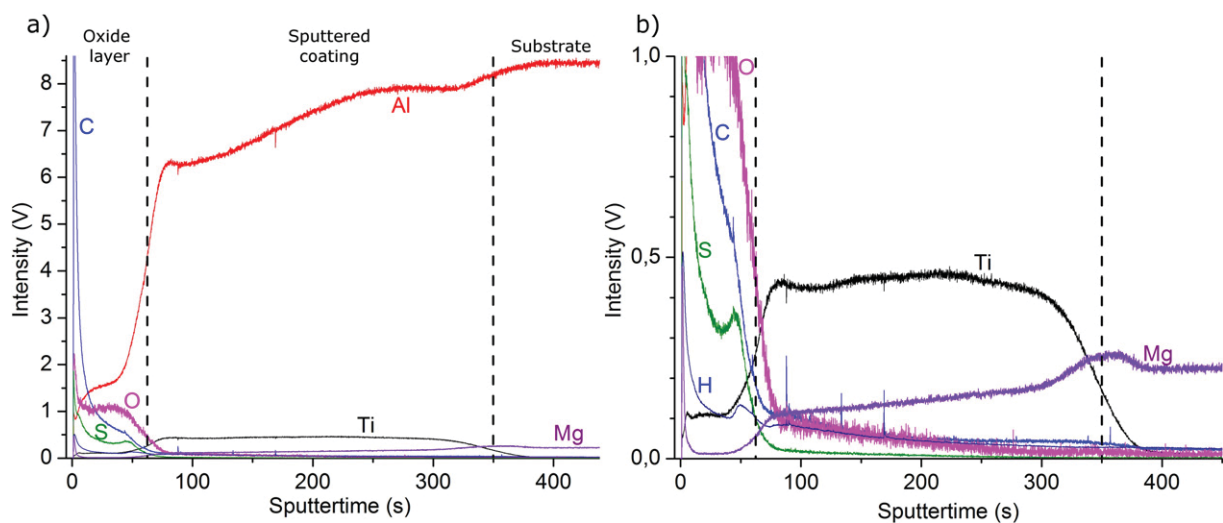


**Fig. 4.** Glow discharge optical emission spectroscopy measurements of an anodised coating containing about 7 wt.% titanium on an AA6401 substrate, a) overview, b) same measurement with expanded intensity-scale.

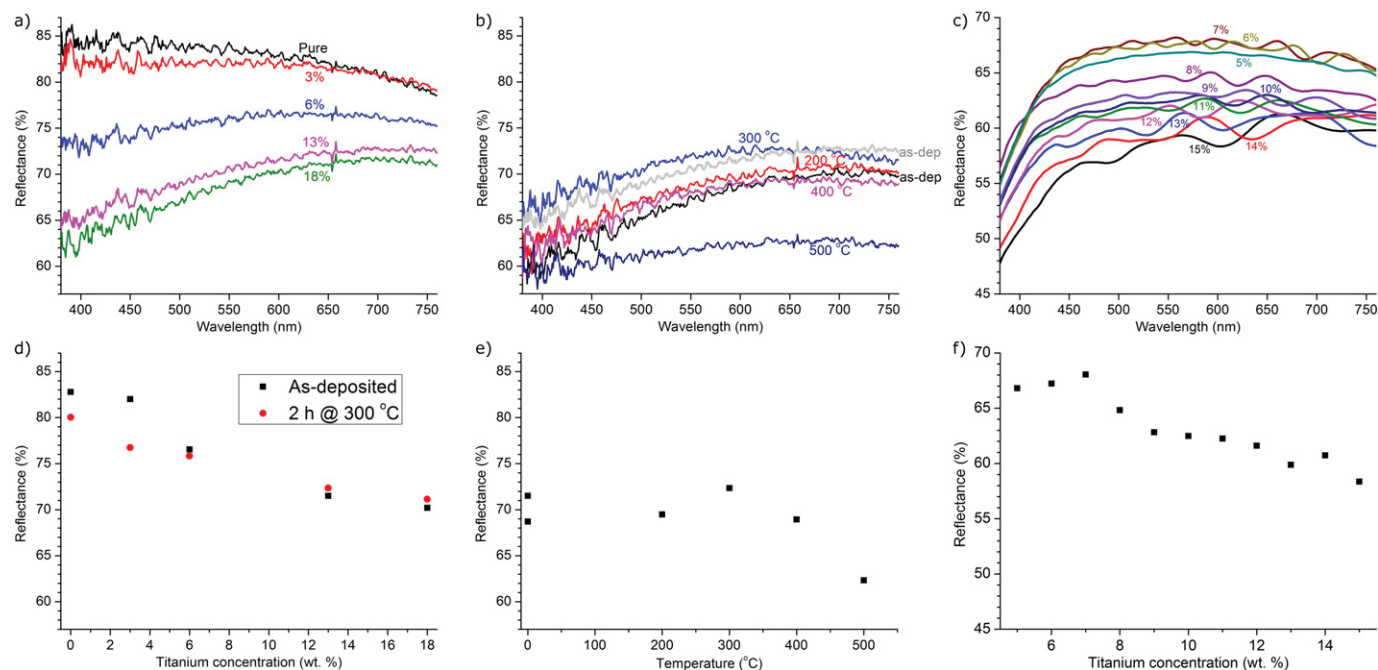


**Fig. 5.** Photospectrometry measurements of a) as-deposited coatings, b) reflectance as a function of heat-treatment temperature for specimens containing 13 wt.% titanium, c) intensities measured on as-deposited, anodised specimen, smoothed by adjacent averaging in Origin. Reflectance values corresponding to 600 nm wavelength from a, b, and c are extracted and plotted in d, e and f respectively.

behaviour, where the reflectance also decreased with the titanium concentration.

After anodisation of the as-deposited coating, wide colour fringes due to thin film interference [22,23] were observed (Fig. 5c). The oxide thickness was found to decrease with titanium concentration as previously reported [16,18]. The reflectance of the anodised specimen decreased with the titanium concentration (Fig. 5c), whereas for a regular aluminium alloy it is generally expected that the reflectance decreases with the thickness of the anodised layer [23].

#### 4.2. Microstructure and appearance of heat-treated coatings before and after anodisation

Heat treatment of the specimens modified the layered structure and resulted in the formation of  $\text{Al}_3\text{Ti}$  phases (Figs. 2b and 3). Previous work identified  $\text{Al}_3\text{Ti}$  phases to form for heat treatment at 350 °C and more [5, 14], which corresponds well with the XRD results presented in Fig. 3. From the GDOES measurement it was found that the magnesium diffused from the substrate into the sputtered coating (Fig. 4b); however no magnesium containing phases were found in the XRD measurements (Fig. 3), which might be due to the low concentration. Wöltgens et al. [14] found that the reflectance and the resistivity of the film decreased with the titanium concentration after heat treatments, as found in Fig. 5d (circles). In Fig. 5b and e it is found that the reflectance increases with heat treatment up to 300 °C followed by a decrease in the reflectance at higher heat treatment temperatures. The same trend was found for thin Al–Ti films [14], where the reflectance decrease from around 210 °C, due to the much lower thickness (80 nm) of the investigated films. It is therefore expected that the precipitation and growth of  $\text{Al}_3\text{Ti}$  phases, caused by the heat treatment, cause the resistivity and the reflectance to decrease.

Due to the passivating nature of titanium,  $\text{Al}_3\text{Ti}$  particles are in most cases only partially oxidised during anodisation. This creates a structure with an oxidised upper part and a lower metallic core (Fig. 2c and f). It is known that anodised aluminium is amorphous [27] and that the anodised Al–Ti coatings are amorphous with low amounts of crystalline  $\text{Al}_2\text{O}_3$  and  $\text{TiO}_2$  phases [3,15,17]. This is well supported by the lack of

oxide-containing phases in the XRD measurement of the anodised specimen (Fig. 3). In general it is expected that the presence of intermetallic particles in the anodised layer causes darkening [24,25,28–30]. Furthermore, previous studies have shown that similar darkening effects can be created by holes within the oxide [31,32] and by very high substrate roughness before anodisation [33]. Therefore, the darkening effect might be due to various effects for different specimens.

#### 4.3. The darkening mechanism

The surface structure consists of a matrix of anodised and sealed aluminium. The matrix contains partially oxidised  $\text{Al}_3\text{Ti}$  particles with an oxide and an unoxidised part. Furthermore, there is an interface between the anodised layer and the sputtered coating.

For the darkening effect to happen, some absorbing constituents are expected within the anodised layer. It has previously been reported that metallic parts such as the aluminium substrate [13], unoxidised aluminium [24–26] and the unoxidised part of intermetallic particles [34] all absorb light. The anodised and sealed aluminium matrix, and the oxidised part of the  $\text{Al}_3\text{Ti}$  particles are expected to have only little absorption.

Due to the low thickness of the oxide film (1.2  $\mu\text{m}$ ), additional effects are expected, causing the light to travel longer in the medium and thereby increasing the absorption of light. This can happen due to scattering, causing light to move inclined and more parallel to the surface. Scattering is expected to happen as surface scattering at the interface between the anodised layer and the sputtered coating and in the metallic part of the particles. Furthermore, changes in refractive indices of the oxides will cause additional scattering. The interface between the anodised layer and the sputtered coating was quite rough as observed in Fig. 2b and c. In comparison to a rough surface in air, the subsurface morphology appears optically larger when the background medium (the anodised layer) has a refractive index larger than air. Since we can expect a refractive index around 1.6 (the refractive index of the main constituents are  $n_{\text{Bohmite}} \sim 1.65$  and  $n_{\text{Gibbsite}} \sim 1.57$ ), the scattering effects at the interface are comparable to the same structure enlarged by 1.6 in air.



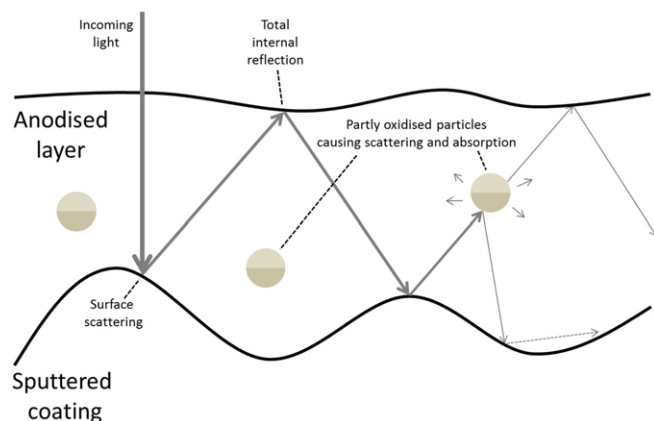


Fig. 6. Schematic showing the possible reasons for oxide film darkening during anodisation.

A preliminary suggestion to the darkening mechanism is presented in Fig. 6, where incoming light hits the subsurface interface and is partly absorbed during surface scattering (reflection). For light returning to the surface at angles larger than the critical angle,  $\sim 38.7^\circ$  to the surface normal ( $n_{\text{anodised layer}} = 1.60$ ), the light is experiencing total internal reflection in the interface of the anodised layer and the air without any loss. Subsequently, the light will again be reflected by the subsurface interface causing additional absorption. Most of the incoming light is therefore expected to reflect back and forth between the top surface of the anodised layer and the subsurface, denoted light trapping. Only light returning to the surface at an angle smaller than the critical angle will leave the oxide. Furthermore, the presented specimens contain absorbing particles inside the oxide causing the mean free path of a light wave to be even smaller, and thereby causing both more absorption and scattering.

The darkening effect is therefore expected to be caused by absorbing and scattering constituents in the oxide layer and the roughness of the interface between the anodised layer and the metallic sputtered coating. The described mechanism is yet to be verified, but all these factors seem to contribute in a significant way.

The cross section TEM images (Fig. 2) show evidence of the presence of local changes in oxide structures, metallic cores or shadow regions, which all support the mechanisms explained above. Similar partially oxidised intermetallics are found previously for silicon- [35,36], iron-rich [37,38], and unidentified particles in AA6060 [26]. Presence of impurities and alloying elements has been reported to darken the anodised layer [24,25,28,30], and the effect might be due to an undissolved part of the particles absorbing and scattering the light [34]. Electrochemical oxidation of intermetallics in the anodisation bath depends on its electrochemical behaviour, and a number of intermetallics in commercial aluminium alloys are oxidised slower (e.g.  $\text{Al}_3\text{Fe}$  and  $\text{Al}_9\text{Fe}_2\text{Si}_2$ ) or faster (e.g.  $\text{Mg}_2\text{Al}_3$  and  $\text{Mg}_2\text{Si}$ ) than the aluminium matrix [28,39]. It has been reported that  $\text{Al}_3\text{Ti}$  particles are cathodic during etching and remain unchanged and incorporated into the oxide film during anodisation [28,39]. The parameters of the sulphuric anodisation are not specified in Refs. [28,39] and therefore the rather high anodisation voltage in this study might have caused the  $\text{Al}_3\text{Ti}$  particles to partly oxidise. Furthermore, it has been reported that the electrochemical behaviour of some intermetallic particles is highly dependent on the particle size [28,39]. Similarly, both fully and partly oxidised intermetallics are found in Fig. 2, where the biggest particles are not fully oxidised. The pores are wider in the  $\text{Al}_3\text{Ti}$  particles as previously reported [3,16,18]. Habazaki et al. [15] found that the migration rate of  $\text{Ti}^{4+}$  are up to 10% slower than the rate of  $\text{Al}^{3+}$ , which does not directly correlate with this picture, where there seems to be a bigger difference in the oxidation rate; however, this can be correlated to both particle size and the fact that this is  $\text{Al}_3\text{Ti}$  particles instead of metallic Ti as in [15].

It is known that surface structures such as grain boundary grooves [40–42] and surface scallops [36,43] are formed due to alloying elements and impurities, and that these cause a decrease in the reflectance of aluminium alloys. Since these surface structures are expected to cause a more diffuse reflection from the interface between the anodised layer and the sputtered substrate, it could also be caused by light trapping. Results presented elsewhere [19] show that the total reflectance of polished alloys is not decreased by anodisation, whereas the total reflectance of etched specimens decreased with relation to the previous etching roughness [19]. This is in line with the proposed darkening mechanism.

The results presented in this paper show that the addition of titanium into aluminium based magnetron sputtered coatings decreases the reflectance of the specimen. After heat-treatment and anodisation the specimens turned dark. It is suggested that the darkening mechanism is caused by partially oxidised  $\text{Al}_3\text{Ti}$  particles and a rough interface between the anodised layer and the sputtered coating. Controlling the subsurface roughness and the amount of partially oxidised particles in anodised layer of e.g. recycled aluminium alloys, might therefore be a way to achieve the desired appearance in spite of high amounts of impurities and alloying elements.

## 5. Conclusions

Magnetron sputtered coatings containing up to 18 wt.% titanium were investigated in the as-deposited form and after heat-treatment before and after anodisation. It was found that:

- A structure of alternating layers containing low and high amounts of titanium was found, with  $\alpha\text{-Al}$  as the only identified phase in the as-deposited coatings. After heat treatment for 4 h at  $600^\circ\text{C}$ , a homogeneous aluminium matrix and high concentrations of elongated  $\text{Al}_3\text{Ti}$  precipitates, with an average length of approximately  $0.5\ \mu\text{m}$  and an aspect ratio of about 1:2, appeared.
- Photospectrometry measurements showed that the reflectance decreases with increasing titanium concentration for the as-deposited specimens, for the specimens heat-treated for 2 h at  $300^\circ\text{C}$ , and for the as-deposited and anodised specimens.
- Coatings containing 6 wt.%–16 wt.% titanium that were heat-treated for 4 h at  $500^\circ\text{C}$  and  $600^\circ\text{C}$  all turned dark grey, brown or black during anodisation.
- Transmission electron microscopy of a specimen containing 10 wt.% titanium showed an oxide film of  $1.2\ \mu\text{m}$ , containing many partially oxidised  $\text{Al}_3\text{Ti}$  particles with a metallic core. In some cases, expected unoxidised aluminium was found behind the particles. Pores of  $8\ \text{nm}$ – $10\ \text{nm}$  in diameter were found both in the aluminium matrix and in the  $\text{Al}_3\text{Ti}$  particles, where additional pores of  $25\ \text{nm}$ – $35\ \text{nm}$  in diameter were also found.

## Conflict of interest

There is no conflict of interest.

## Acknowledgements

The authors would like to thank the Danish Agency for Science, Technology and Innovation for their financial support of the IdeAl project and all partners of the consortium. Kristian Rechendorff, Danish Technological Institute, is acknowledged for coating deposition and Rolf Jensen, DTU MEK, for his help with GDOES measurements. Acknowledgements to Villads Egede Johansen, DTU MEK, for discussions on the darkening effect and for calculating the penetration depth of light, and Jørgen Schou and Stela Canulescu, DTU Department of Photonics Engineering, for their help on photospectrometry measurements. Ib Kongstad, Bang & Olufsen, is acknowledged for anodisation of the as-deposited gradient specimen.

## References

- [1] J.C. Oliveira, A. Manaia, J.P. Dias, A. Cavaleiro, D. Teer, S. Taylor, *Surf. Coat. Technol.* 200 (2005) 395–398.
- [2] F. Sanchette, A. Billard, *Surf. Coat. Technol.* 142–144 (2001) 218–224.
- [3] V.C. Nettikaden, H. Liu, P. Skeldon, G.E. Thompson, *Corros. Sci.* 57 (2012) 49–55.
- [4] J. Hampshire, P.J. Kelly, D.G. Teer, *Thin Solid Films* 447–448 (2004) 392–398.
- [5] J. Hampshire, P.J. Kelly, D.G. Teer, *Thin Solid Films* 447–448 (2004) 418–424.
- [6] Q. Yan, H. Yoshioka, H. Habazaki, A. Kawashima, K. Asami, K. Hashimoto, *Corros. Sci.* 31 (1990) 401–406.
- [7] H. Yoshioka, Q. Yan, K. Asami, K. Hashimoto, *Mater. Sci. Eng. A* 134 (1991) 1054–1057.
- [8] K. Hashimoto, N. Kumagai, H. Yoshioka, J.H. Kim, E. Akiyama, H. Habazaki, S. Mrowec, A. Kawashima, K. Asami, *Corros. Sci.* 35 (1993) 363–370.
- [9] Q. Yan, H. Yoshioka, H. Habazaki, A. Kawashima, K. Asami, K. Hashimoto, *Corros. Sci.* 32 (1991) 327–335.
- [10] E. Akiyama, H. Habazaki, A. Kawashima, K. Asami, I.L. Hashimoto, K. Hashimoto, *Mater. Sci. Eng. A* 226–228 (1997) 920–924.
- [11] H. Yoshioka, Q. Yan, H. Habazaki, A. Kawashima, K. Asami, K. Hashimoto, *Corros. Sci.* 31 (1990) 349–354.
- [12] M. Aggerbeck, K. Rechendorff, R. Ambat, Aluminium based coatings containing titanium for alkaline protection, in: *Proc. Alum. Surf. Sci. Technol. (ASST)*, Sorrento, Italy (May 2005) p. no. 5.
- [13] S. Van Gils, T. Dimogerontakis, G. Buytaert, E. Stijns, H. Terryn, P. Skeldon, G.E. Thompson, M.R. Alexander, *J. Appl. Phys.* 98 (2005) (083505–1–9).
- [14] H. Wöltgens, I. Friedrich, W.K. Njoroge, W. Theiß, M. Wuttig, *Thin Solid Films* 388 (2001) 237–244.
- [15] H. Habazaki, K. Shimizu, P. Skeldon, G.E. Thompson, G.C. Wood, *Thin Solid Films* 300 (1997) 131–137.
- [16] S. Berger, H. Tsuchiya, P. Schmuki, *Chem. Mater.* 20 (2008) 3245–3247.
- [17] A.N. Kamkin, L.A. Fishgoit, A.D. Davydov, *Russ. J. Electrochem.* 39 (2003) 738–743.
- [18] H. Tsuchiya, S. Berger, J.M. Macak, A. Ghicov, P. Schmuki, *Electrochem. Commun.* 9 (2007) 2397–2402.
- [19] M. Aggerbeck, et al., *Surf. Coat. Technol.* (2014), <http://dx.doi.org/10.1016/j.surfcoat.2014.05.047>.
- [20] SOCABIM, Software: EVA Application 6.0.0.1, 2000.
- [21] S. Davíðsdóttir, S. Canulescu, K. Dirscherl, J. Schou, R. Ambat, *Surf. Coat. Technol.* 216 (2013) 35–45.
- [22] S. Van Gils, P. Mast, E. Stijns, H. Terryn, *Surf. Coat. Technol.* 185 (2004) 303–310.
- [23] T.-S. Shih, P.-S. Wei, Y.-S. Huang, *Surf. Coat. Technol.* 202 (2008) 3298–3305.
- [24] M. Saito, Y. Shiga, M. Miyagi, *J. Electrochem. Soc.* 140 (1993) 1907–1911.
- [25] M. Saito, S. Yasunori, M. Miyagi, K. Wada, O. Sachiko, *J. Appl. Phys.* 34 (1995) 3134–3138.
- [26] J.C. Walmsley, C.J. Simensen, A. Bjørgum, F. Lapique, K. Redford, *J. Adhes.* 84 (2008) 543–561.
- [27] J.D. Edwards, F. Keller, *Trans. Am. Inst. Min. Metall. Eng.* 156 (1944) 288–299.
- [28] R. Akeret, H. Bichsel, E. Schwall, E. Simon, M. Textor, *Trans. Inst. Met. Finish.* 68 (1990) 20–28.
- [29] L.-F. Huang, M. Saito, M. Miyagi, *Jpn. J. Appl. Phys.* 32 (1993) 3169–3174.
- [30] N. Tabrizian, H.N. Hansen, P.E. Hansen, R. Ambat, P. Møller, *Surf. Coat. Technol.* 204 (2010) 2632–2638.
- [31] A. Junker-Holst, D.V. Nielsen, Effect of microstructure of plasma sputtered coatings on optical appearance, (Bachelor thesis) Technical University of Denmark, 2012.
- [32] Y. Ma, X. Zhou, G.E. Thompson, J.-O. Nilsson, M. Gustavsson, A. Crispin, *Surf. Interface Anal.* 45 (2013) 1479–1484.
- [33] M. Aggerbeck, Optical appearance of aluminium, (Master thesis) Technical University of Denmark, 2010.
- [34] V.C. Gudla, S. Canulescu, R. Shabadi, K. Rechendorff, J. Schou, R. Ambat, *Accept. Light Met. 2014 Alum. Alloy. Dev. Charact. Appl.*, 2014.
- [35] L. Fratila-Apachitei, F. Tichelaar, G. Thompson, H. Terryn, P. Skeldon, J. Duszczyk, L. Katgerman, *Electrochim. Acta* 49 (2004) 3169–3177.
- [36] L.E. Fratila-Apachitei, H. Terryn, P. Skeldon, G.E. Thompson, J. Duszczyk, L. Katgerman, *Electrochim. Acta* 49 (2004) 1127–1140.
- [37] K. Shimizu, G.M. Brown, K. Kobayashi, P. Skeldon, G.E. Thompson, G.C. Wood, *Corros. Sci.* 40 (1998) 1049–1072.
- [38] M. Jariyaboon, P. Møller, R.E. Dunin-Borkowski, R. Ambat, *Anti Corros. Method Mater.* 58 (2011) 173–178.
- [39] J. Timm, *Key Eng. Mater.* 44–45 (1990) 219–232.
- [40] H. Zhu, X. Zhang, M. Couper, A.K. Dahle, *Mater. Chem. Phys.* 113 (2009) 401–406.
- [41] T. Hauge, K.F. Karhausen, *Alum. Extrus.* (1998) 32–37.
- [42] T. Minoda, H. Yoshida, *Metall. Mater. Trans. A* 33A (2002) 2891–2898.
- [43] Y. Ma, X. Zhou, G.E. Thompson, J.-O. Nilsson, M. Gustavsson, A. Crispin, *Trans. Inst. Met. Finish.* 91 (2013) 11–16.



# Saline and alkaline corrosion resistance of aluminium-titanium coatings prepared by plasma magnetron sputtering

M. Aggerbeck<sup>a</sup>, K. Rechendorff<sup>b</sup>, K. Dirscherl<sup>c</sup>, R. Ambat<sup>a</sup>

<sup>a</sup> Technical University of Denmark, Department of Mechanical Engineering, Materials and Surface Engineering, Produktionstorvet 425, 2800 Kgs. Lyngby, Denmark

<sup>b</sup> Danish Technological Institute, Kongsvang Allé 29, 8000 Aarhus C, Denmark

<sup>c</sup> Danish Fundamental Metrology, Matematiktorvet 307, 2800 Kgs. Lyngby, Denmark

## Abstract

The effect of microstructural changes by heat treatment up to 500°C on the corrosion properties of magnetron sputtered aluminium coatings containing up to 18 wt.% titanium was investigated in saline conditions and at pH 13.5. The coating microstructure was investigated using XRD, SEM, and TEM; while anodic polarization experiments, alkaline exposure studies, and scanning kelvin probe force microscopy were used for corrosion analysis. The alkaline corrosion resistance was significantly improved with 13 wt.% titanium and additionally improved by heat treatment. The improved corrosion resistance after heat treatment were ascribed formation of Al<sub>3</sub>Ti precipitates, homogenization of titanium concentration, and structural relaxation.

**Keywords:** A. Aluminium, A. Sputtered films, A. Titanium, B. Polarization, B. XRD, C. Alkaline corrosion

## 1. Introduction

Aluminium is a key material of future green technology due to its high strength-to-weight ratio. In a number of technological applications replacing steel with aluminium will result in significant weight reductions, which can be directly translated into efficiency and reduction in fuel consumption in the transportation sector. However, any material used in the automotive industry needs considerable corrosion resistance not only in usual mild to harsh corrosive conditions, but it also necessitates some level of corrosion resistance in highly alkaline conditions (up to pH 13.5) due to the alkalinity of the detergents used for automatic car wash. Today nickel salt sealing [1] is often used in the automotive industry, but since nickel is an allergen, an alternative surface treatment needs to be found. Also the level of corrosion resistance provided by the nickel sealing is not faultless beyond pH 12. Therefore several alternative techniques have been tested for enhancing the corrosion resistance of aluminium, especially the sol-gel and the magnetron sputtering techniques.

Sol-gel coatings on aluminium have shown to be protective in saline and acidic conditions [2–5], while others studied the improvement of the alkaline corrosion resistance [5–7]. Akid et al. [5] studied the properties of combined polyanilin/sol-gel coatings in 3.5 % NaCl in neutral (pH 6.8), acidic (pH 3.5) and alkaline (pH 9.2)

conditions. Significant improvement in neutral and acidic conditions was found; however, less promising results were achieved in alkaline conditions. Zhang et al. [6] coated aluminium pigments with silica and found a corrosion protection factor of 99.3 % in a NaOH solution at pH 11. Hirai et al. [7] found that zirconium oxide sol-gel coatings improved the corrosion properties of commercially pure aluminium significantly in a 10 wt. % NaOH solution.

The magnetron sputtering technique enables the formation of aluminium coatings with desired compositions of other alloying elements. Although, the process is not feasible for all applications due to cost and the limitation of the size and shape of the object that can be coated, the method can be effectively used for understanding the behaviour of various alloy compositions. Unlike conventional processes such as casting, magnetron sputtering allows preparation of non-equilibrium coating compositions and homogenous distribution of the alloying elements throughout the coating.

Magnetron sputtered coatings of binary Al-Ti alloys have previously shown good corrosion resistance in saline conditions [8–10]. Additionally, many different transition metals have been studied for protection in 1 M HCl [11] including several studies on Al-Ti coatings [12–14]. Yan et al. [12] found that the time to natural oxide breakdown in 1 M HCl increased with the titanium con-

centration. However, after oxide breakdown the anodic current was higher for coatings containing up to 70 wt. % titanium compared to pure aluminium coatings. Akiyama et al. [13] found that ternary sputter coatings containing aluminium and titanium plus chromium, nickel or magnesium gave good results in 1 M HCl.

In other studies, the mechanical properties of binary Al-Ti coatings have been investigated after annealing at 600 °C for 1 h [15] and 2 h [16,17] followed by investigations of the microstructure and mechanical properties. It was found that the microstructure, hardness, and surface friction varied with the alloy composition. Sun [18] annealed thin titanium coatings on aluminium substrates and investigated the corrosion properties in the neutral salty conditions. These investigations showed that the heat treatment for 2 h at 550 °C enhanced the corrosion properties significantly. No literature has been found on the use of coatings containing aluminium and titanium for alkaline protection. However, previous tests in our laboratory where excessive amounts of titanium and zirconium was used [19], showed good alkaline corrosion protection.

Investigations carried out in this paper are aimed at: (i) understanding the role of titanium content (3 wt. % to 18 wt. %) on the neutral saline and the alkaline corrosion behaviour of aluminium and (ii) understanding how the microstructure of the coating including the precipitation of intermetallic phases during heat treatment affects the electrochemical and corrosion behaviour. Microstructural analyses were performed by X-ray diffraction (XRD), scanning electron microscopy (SEM), and transmission electron microscopy (TEM) whereas corrosion properties were studied by alkaline immersion exposure testing and potentiodynamic polarization testing both at pH 13.5. Surface topography and surface potential profiling was done by scanning kelvin probe force microscopy (SKPFM) measurements.

## 2. Materials and methods

### 2.1 Coating preparation using plasma magnetron sputtering

Coatings were deposited by DC magnetron sputtering using an industrial-scale CemeCon CC800/8 machine with a chamber volume of 70 cm x 60 cm x 60 cm, and two cathodes. The opposite placed cathodes faced the substrates which were mounted on a planetary rotating table in the middle of the chamber to ensure a homogeneous deposition. The deposition chamber was initially evacuated to a base pressure of 6 mPa. During sputtering constant argon flow of 200 SCCM (mL/min) was used,

leading to a typical argon pressure of 500 mPa. The distance between the targets and sample was about 100 mm, and the bias voltage on the substrates was fixed at -50 V. The maximum temperature during deposition was between 150 °C and 200 °C, as measured by a bi-metal thermometer during the deposition.

Deposition of reference coatings of aluminium (AA1050, 99.5 % pure) used two targets with 1000 W on each. Binary Al-Ti coatings were produced using one target of aluminium and one of titanium (grade 1, 99.5 % pure) with cylindrical aluminium inserts of 1 cm in diameter. The aluminium target ran at 2000 W, while the titanium target ran at 100 W, 200 W, 400 W and 600 W, giving titanium concentrations of 3 wt. %, 6 wt. %, 13 wt. % and 18 wt. % in the coatings. These coatings were deposited on cast aluminium samples (EN AC-46500, 8 wt. % – 11 wt. % silicon and 2 wt. % – 4 wt. % copper) with dimensions 70 mm x 25 mm x 4 mm. Coating thickness was between 11 and 25 µm.

An AA6401 substrate with dimensions 220 mm x 40 mm x 5 mm was coated with an Al-Ti gradient of varying composition along the length of the specimen. An aluminium target running at 2000 W and the Ti-Al target previously described running at 300 W were displaced with respect to the centre of the chamber. Thereby the titanium content in the deposition flux varies throughout the chamber and the resulting coating on the relatively long substrate has a varying composition. This method is very practical for screening purposes, as a single deposition will give different compositions. The titanium content of the coating varied from 5 wt. % titanium in one end to 15 wt. % titanium in the other, with thicknesses of the coating varying from 17 µm to 8 µm.

### 2.2 Heat treatment

In order to alter the microstructure of the coatings, three series of heat treatments were performed: (i) 2 h at 300 °C for coatings with compositions of pure AA1050, 3 wt. %, 6 wt. %, 13 wt. % and 18 wt. % titanium, and coatings containing 13 wt. % was heat-treated for (ii) 2 h at 200 °C, 300 °C, 400 °C, and 500 °C, and (iii) 4 h at 600 °C from the gradient coating for high resolution SEM and SKPFM measurements.

### 2.3 Microstructural analysis

To identify phases formed during deposition and heat treatment, X-ray diffraction measurements were done on a Bruker D8 Discover diffractometer using a copper  $K_{\alpha 1}$  beam (1.54 Å) running with grazing incidence of 5 °. The measurements ran from 20 ° to 100 °, however, only results from 20 ° to 85 ° are presented. The step size was 0.03 ° with a step time of 192 s. The EVA Application



software [20] was used for analysing the results.

For microstructural analysis, a SEM JSM-5900 from JEOL was used. Also EDS measurements for composition analyses were done using the Oxford link ISIS analyser attached to the SEM. The microscope is equipped with a LaB<sub>6</sub> filament which operated at 13 kV for both imaging and EDS analyses. High resolution back scattered electron images were produced on a field emission gun SEM, Quanta 200f from FEI.

TEM was used for detailed investigations of cross sections on a FEI Tecnai T20 G2 at 200 keV. A focussed ion beam on a FEI Quanta 200 3D DualBeam microscope was used for cutting and lifting out a specimen followed by milling in a FEI Helios Nanolab DualBeam. An as-deposited film (13 wt. % titanium) was milled to a thickness of about 175 nm and a film (10 wt. % titanium) heat-treated 4 h at 600 °C was milled to a thickness of 450 nm in the thickest area, however, the oxide layer was milled at a higher rate and has therefore been thinner.

#### 2.4 Anodic polarization test at neutral pH

To test the corrosion properties of the as-deposited specimens in neutral pH conditions, a series of localised electrochemical polarization tests were performed. A Dualscope<sup>TM</sup> EC Microcell [21,22] was used with a 0.1 M NaCl electrolyte at neutral pH conditions. The measurements were performed on the as-deposited surface, which were polished locally using SiC paper #4000 and cleaned using deionized water prior to the experiment to remove the native oxide film. An Open Circuit Potential (OCP) monitoring for 400 s was followed by measurements from 100 mV below the corrosion potential ( $E_{\text{corr}}$ ) until reaching a fixed current value after the pitting occurred. The lateral resolution of the experiments is dependent on the tip diameter. The results reported in this paper were carried out with a tip diameter of approximately 1 mm. The reference electrode used was Ag/AgCl. Two to six measurements were performed on each sample depending on the consistency of the results.

#### 2.5 Anodic polarization test at pH 13.5

For studies of the corrosion properties in harsh alkaline conditions, an electrochemical flat cell was used for the potentiodynamic polarization measurements. The anodic polarization tests were performed using a solution containing 4.6 g/L Na<sub>3</sub>PO<sub>4</sub>·12H<sub>2</sub>O, 0.131 g/L NaCl and 12.65 g/L NaOH in deionized water (pH of the solution was 13.5). The exposed area of the specimen was approximately 0.91 cm<sup>2</sup>. A Ag/AgCl electrode was used

as reference electrode and the counter electrode was a twisted platinum wire ring. The OCP measurements were carried out for 180 s followed by anodic potentiodynamic polarization measurements starting at 100 mV below the  $E_{\text{corr}}$ -value to +300 mV vs. the Ag/AgCl reference electrode.

#### 2.6 Alkaline exposure test

For additional corrosion testing, an alkaline immersion test was done for 10 min at room temperature in the alkaline solution described for the anodic polarization test at pH 13.5. The rest of the specimen was lacquered before the test in order to expose only the coated area and to avoid galvanic coupling of the coating and the substrate. After alkaline exposure, the specimens were rinsed with deionized water and immersed into 70 wt. % nitric acid for 4 min to desmut the surface. The lacquer was removed mechanically and the samples were investigated for corrosion surface morphology using SEM.

#### 2.7 Topography and surface potential

Topography and surface potential measurement using AFM/SKPFM were carried out on samples polished with diamonds of ¼ µm in size. The SKPFM or surface potential microscopy [23] is a scanning probe microscopy technique running in non-contact mode. Monitoring local changes in the work function difference between the sample surface and the scanning tip provides information about the local surface potential. For this purpose, a voltage signal is applied to the tip in order to cancel out the electric forces related to the work function differences. This correction voltage signal is recorded and provides a local mapping of changes in the surface potential when superimposed on the topography data of the simultaneous AFM scan.

A Multimode AFM from Bruker with Nanoscope software v. 8.15 was used for combined AFM and SKPFM. The Multimode ran in tapping mode for the topographic scan, and was set to a lift height of 35 nm when measuring the surface potential differences. This was the closest lift height possible without the tip touching the surface occasionally. Areas of 10 µm x 10 µm were scanned and a suitable area of 5 µm x 5 µm was chosen for further analysis in the SPIP software [24]. In the reported results, the correction voltage is measured, so that the lower measured potential represents more noble areas and vice versa.

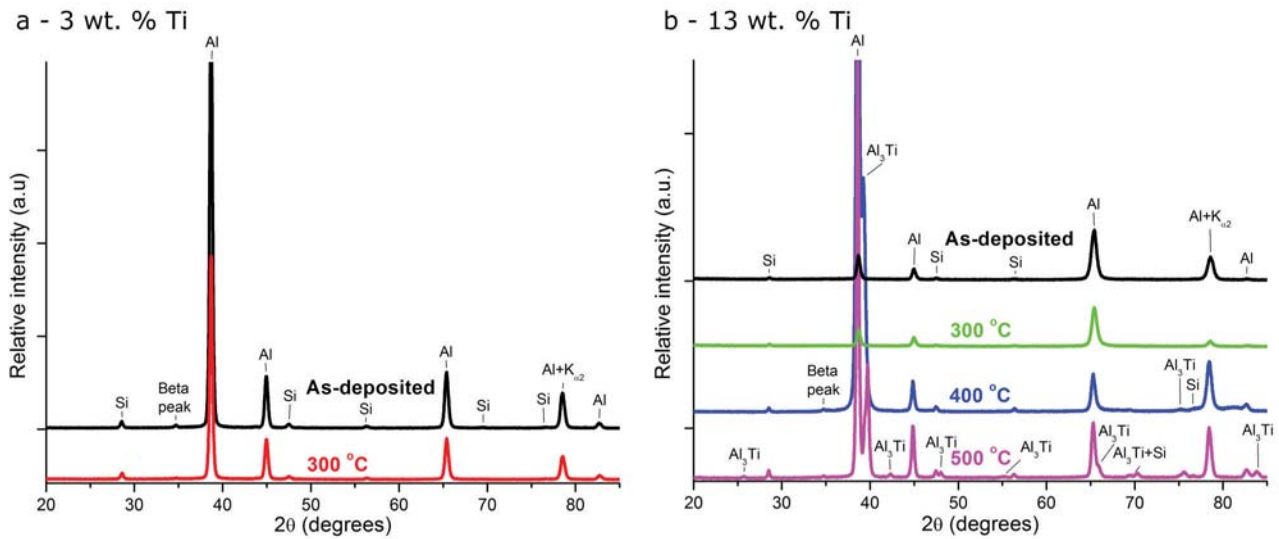


Fig. 1 - XRD measurements of specimens with a) 3 wt. % titanium, as-deposited and heat-treated for 2 h at 300 °C and b) 13 wt. % titanium, as-deposited, heat-treated for 2 h at 300 °C, 400 °C and 500 °C.

### 3. Results

#### 3.1 Microstructural investigation

##### 3.1.1 X-ray diffraction

The results from XRD measurements used for phase identification are presented in Fig. 1. For both 3 wt. % titanium (Fig. 1a) and 13 wt. % titanium (Fig. 1b), the as-deposited specimens showed only peaks corresponding to FCC aluminium and a silicon phase due to the silicon in the cast substrate alloy. After heat treatment of both specimens containing 3 wt. % and 13 wt. % titanium for 2 h at 300 °C, the intensity of the peaks for aluminium was slightly decreased, and no additional peaks were found compared to the as-deposited specimens. For specimens containing 13 wt. % titanium, after heat treatment at 400 °C, the aluminium and the silicon signals have strengthened, while the diffractogram showed additional peaks corresponding to  $\text{Al}_3\text{Ti}$ . Heat treatment at 500 °C caused the signals for all the phases to increase showing relative volumetric increase of the phases.

##### 3.1.2 High resolution scanning electron microscopy

Backscatter images showing the elemental distribution of the microstructure are presented in Fig. 2. The coating with 13 wt. % titanium, heat treatment for 2 h at 300 °C (Fig. 2a) did not show significant change in compositional distribution. After heat treatment for 2 h at 500 °C (Fig. 2b), microstructure showed phases of higher atomic number of sizes up to 0.5  $\mu\text{m}$ . When heat-treated for 4 h at 600 °C (Fig. 2c), these phases of sizes up to 1.3  $\mu\text{m}$  were precipitated. The EDS measurements and EDS mapping of the microstructure after 600 °C heat treatment (not presented here) showed that the phase had higher titanium content in its composition pointing to  $\text{Al}_3\text{Ti}$  as found from the XRD results.

##### 3.1.3 Transmission electron microscopy

TEM investigations of the sputtered coating showed a columnar structure growing vertically upward from the substrate as presented in Fig. 3a, while Fig. 3b is a high magnification image of the interface between two columns. The structure of the coating was made of two

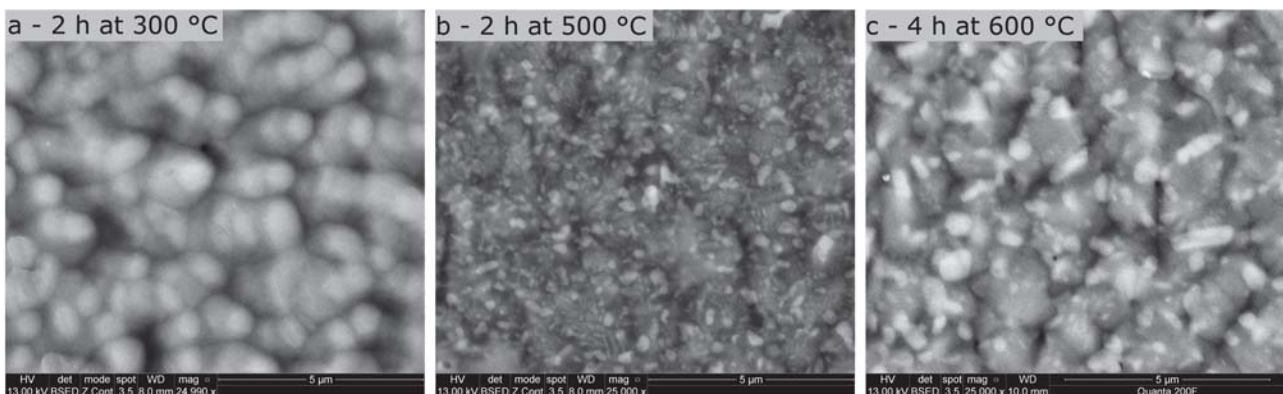


Fig. 2 - Top view SEM images of backscatter electrons of 13 wt. % titanium heat-treated for a) 2 h at 300 °C. b) 2 h at 500 °C and c) 4 h at 600 °C.

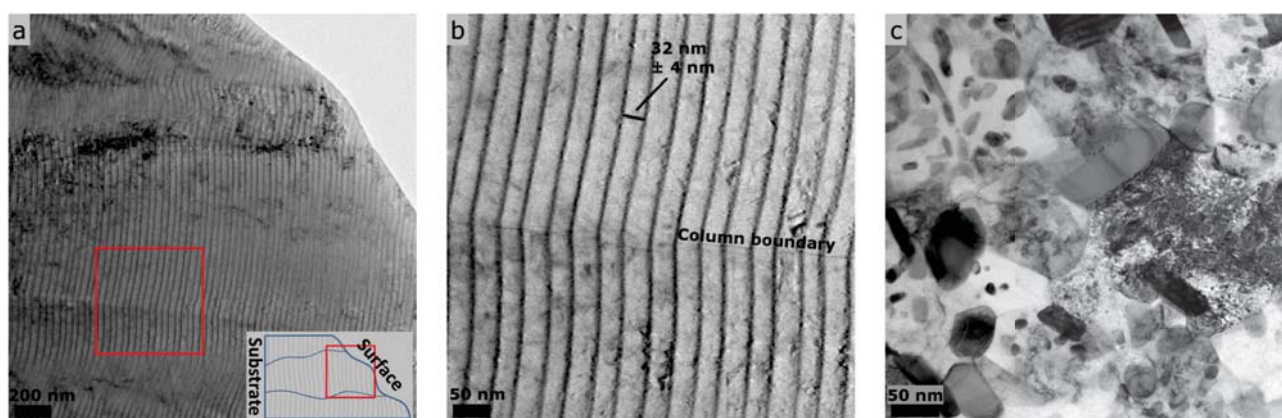


Fig. 3 - TEM micrographs of as-deposited coating containing 13 wt. % titanium of, a) an overview showing the columnar structure and b) zoom showing interface of two columns and layers of titanium and aluminium, and c) specimen containing 10 wt. % titanium after heat treatment for 4 h at 600 °C.

alternating layers at a period of approximately  $32 \pm 4$  nm and the directionality following the specific growth direction of the column. The bright layers showed widths of 22.0 nm – 30.0 nm and the dark layers were 2.5 nm – 9.5 nm in width, both dependent on how the layer boundaries are defined. The bright layers were aluminium with lower amounts of titanium, whereas the dark layers were highly rich in titanium. Fig. 3c presents the microstructure of a specimen heat-treated for 4 h at 600 °C, where a homogeneous matrix is found containing precipitates of sizes from 150 nm x 50 nm up to 1.3  $\mu\text{m}$  x 0.7  $\mu\text{m}$ .

## 3.2 Corrosion investigation

### 3.2.1 Anodic polarization test at neutral pH

Fig. 4a shows the anodic polarization curves in a 0.1 M NaCl solution at neutral pH for different titanium concentrations. The  $E_{\text{corr}}$  value did not show any specific trend with varying titanium concentration, but overall varied within a range of 150 mV. Addition of titanium reduced the corrosion current ( $i_{\text{corr}}$ ) value compared to pure aluminium, however no significant effect on the  $i_{\text{corr}}$  value was found with increase in titanium concentration. All the specimens showed an initial increase of the anodic current followed by a plateau region, where the

height of the plateau region increased with the titanium concentration. The plateau current density also showed a general decrease (approximately half a decade) with increased titanium content. The breakdown potential shifted towards more positive values with increased titanium concentration in the coating. Fig. 4b shows the breakdown potential as a function of titanium content. A clear trend was seen where the increased amount of titanium in the coating increased the breakdown potential of the coating. The coating with 15 wt. % titanium had an  $E_{\text{pit}}$  value approximately 330 mV higher than the pure AA1050 coating.

### 3.2.2 Anodic polarization test at pH 13.5

Fig. 5a shows the anodic polarization curves in alkaline solution at pH 13.5 for the as-deposited specimens. None of the curves showed any break down at potential values up to 300 mV vs. Ag/AgCl. Instead a long plateau region was observed for all the specimens indicating passivation. Overall, a decrease in anodic current was seen with increasing titanium concentration. Similar measurements were performed for the specimens with varying titanium concentration heat-treated at 300 °C and the specimens with 13 wt. % titanium heat-treated at varying temperatures. Although not shown, nature of the polarization curves were similar to Fig. 5a, therefore

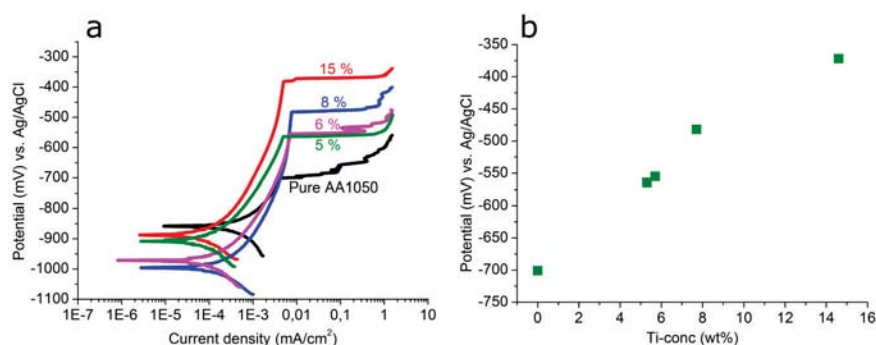


Fig. 4 – Localised anodic polarization measurements on as-deposited specimens in a 0.1 M NaCl solution at neutral pH. a) Anodic polarization curves and b) Pitting potential as a function of titanium-concentration.



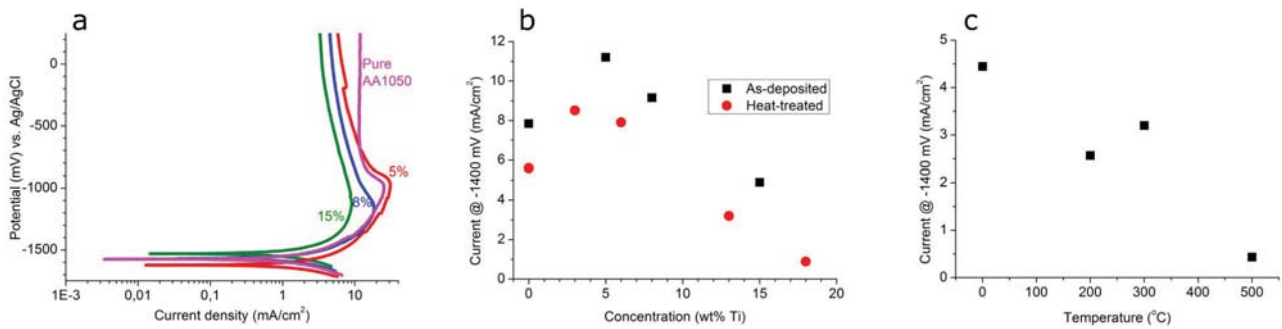


Fig. 5 – Anodic polarization measurements at pH 13.5. a) Measured curves for as-deposited specimens. Anodic current at -1400 mV as a function of b) titanium-concentration for as-deposited coating and specimens heat-treated for 2 h at 300 °C and c) Temperature for 2 h heat treatment of specimens containing 13 wt. % titanium.

summary of the data extracted from the polarization curves are presented in Fig. 5b and c.

Fig. 5b shows a comparison of the anodic dissolution current just above the  $E_{\text{corr}}$  value (-1400 mV vs. Ag/AgCl). For the as-deposited specimens (points marked as squares), the anodic current showed a decrease with increasing titanium concentration. Additionally, heat treatment (points marked as circles) decreased the anodic current for all titanium concentrations. The anodic current was slightly lower for the pure aluminium coating than for the specimens containing 3 wt. % to 8 wt. % titanium, while increased titanium concentration reduced the anodic current by almost one order of magnitude after heat treatment. The anodic current for the as-deposited pure aluminium coating (7.8 mA/cm²) compared to the current found for the heat-treated specimen with 18 wt. % titanium (0.88 mA/cm²) corresponded to a decrease of about 88 %.

Fig. 5c presents the anodic current at -1400 mV vs. Ag/AgCl for specimens containing 13 wt. % titanium, as-deposited and heat-treated for 2 h at 200 °C, 300 °C and 500 °C. It was found that the heat treatment reduced the anodic current especially for samples heat-treated at higher temperatures. The as-deposited coating showed an anodic current of 4.4 mA/cm², whereas the specimen heat-treated at 500 °C an anodic current of 0.43 mA/cm². This corresponds to a decrease of about 91 %.

### 3.2.3 Alkaline exposure test

Fig. 6 presents SEM images of the as-deposited surfaces with varying titanium concentration after the alkaline exposure test at pH 13.5. The surface of the AA1050 coating (Fig. 6a) corroded significantly more than that found on titanium containing surfaces (Fig. 6b-d). Higher levels of alkaline corrosion and hemispherical pits were found all over the surface of the AA1050 coating compared to the titanium containing coatings. All the titanium containing surfaces showed fine etch pits, with the lowest density of pits for the 15 wt. % titanium specimen. The pit diameters were similar for 5 wt. %

and 10 wt. % titanium, but smaller for 15 wt. % titanium and the pit depths decreased with increasing titanium content.

Fig. 7 shows the effect of the alkaline test after heat treatment for 2 h at 300 °C on coatings with various titanium concentrations. For comparison, Fig. 8b shows the specimen containing 13 wt. % titanium with the same heat treatment. For pure AA1050 (Fig. 7a) the behaviour was similar to the as-deposited specimen (Fig. 6a). On the contrary for coatings containing titanium, corrosion was significantly decreased with both heat treatment and increased titanium content. While the specimen with 3 wt. % titanium showed localized concentration of pits, increased titanium content caused more uniform distribution of smaller pits.

Fig. 8 presents SEM images of specimens containing 13 wt. % titanium, heat-treated for 2 h at 200 °C, 300 °C, 400 °C, and 500 °C. A significant improvement was found even for heat treatment at 200 °C (Fig. 8a) compared to the as-deposited specimen in Fig. 6d. This was further improved after heat treatment at 300 °C, 400 °C, and 500 °C as seen in Fig. 8b, c and d respectively. For specimens heat-treated at 400 °C and 500 °C, an outgassing from the cast substrates caused blisters to appear on the surface.

### 3.2.4 Scanning kelvin probe force microscopy

Fig. 9 and 10 respectively present the topography and SKPFM surface potential measurements of specimens containing 13 wt. % titanium. The measurements were done in a combined process and the topography for the areas represented in Fig. 9a-c therefore respectively corresponds to the surface potential for the areas presented in Fig. 10a-c. For the as-deposited specimen it was found that the specimen was smoothly polished (Fig. 9a) and that the potential differences (Fig. 10a) of the surface was very inhomogeneous and with measured potential differences up to about 80 mV. Also the specimen heat-treated for 2 h at 300 °C was smoothly polished (Fig. 9b), but showed an inhomogeneous surface poten-

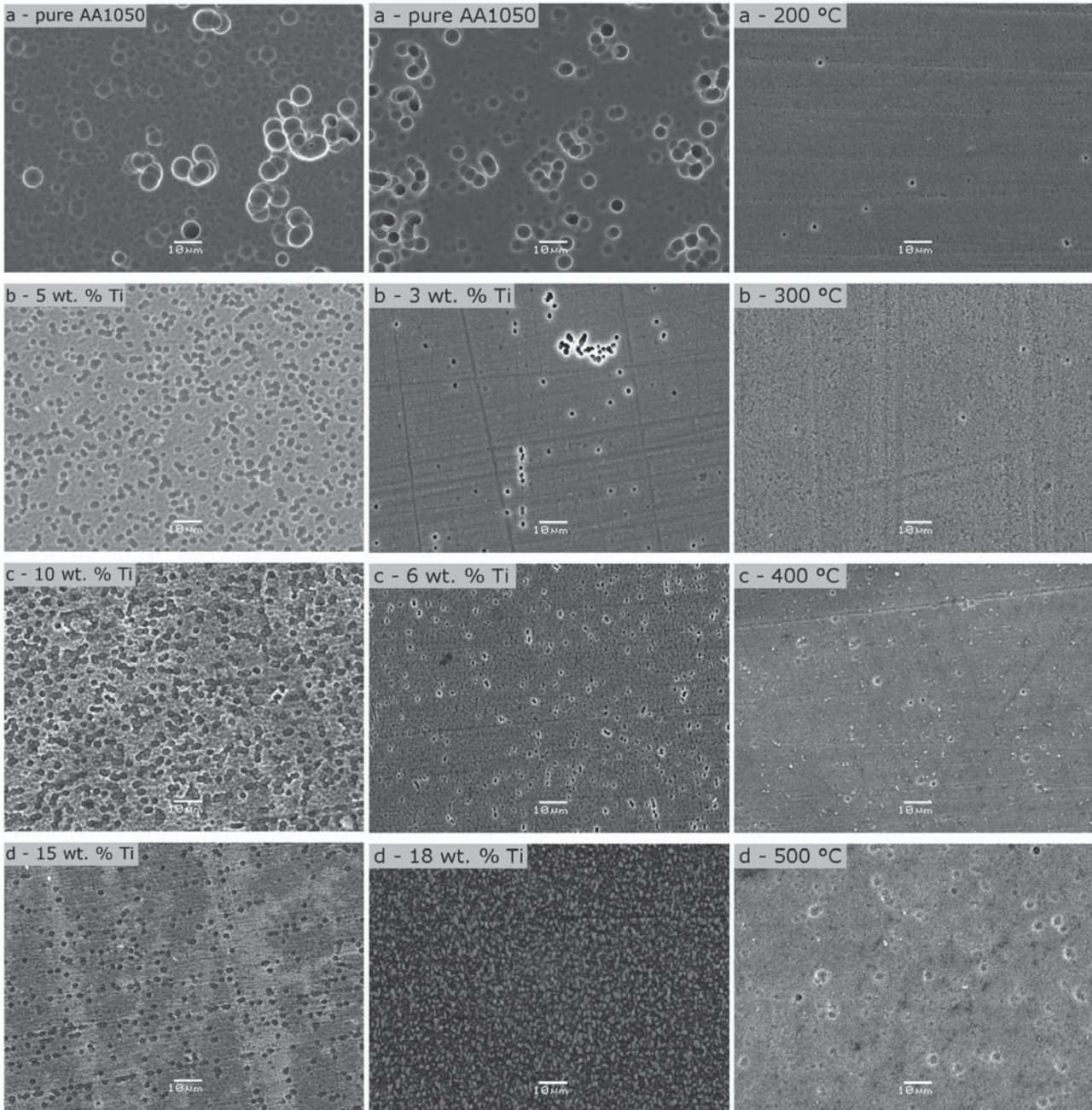


Fig. 6 - SEM images after pH 13.5 exposure of as-deposited coatings with titanium-concentrations of a) 0 % b) 5 wt. % c) 10 wt. % and d) 15 wt. %.

Fig. 7 - SEM images after pH 13.5 exposure of aluminium coatings heated 2 h at 300 °C with titanium concentrations of a) 0 % b) 3 wt. % c) 6 wt. % and d) 18 wt. %.

Fig. 8 - SEM images after pH 13.5 exposures of aluminium coatings containing 13 wt. % titanium, heat-treated for 2 h at a) 200 °C b) 300 °C c) 400 °C and d) 500 °C.

tial distribution (Fig. 10b). A finer structure was found and the potential differences in general were decreased for the specimen heat-treated to 300 °C (Fig. 10b) compared to the as-deposited specimen (Fig. 10a), with maximum difference in the potential of 64 mV. The specimen heat-treated for 4 h at 600 °C was also smoothly polished, however, with features of up to about  $\pm 40$  nm in height (Fig. 9c) with respect to the base. The surface potential was dramatically homogenised (Fig. 10c) compared to the other measurements and dark features were found being cathodic to the matrix with a potential difference of about 30 mV.

#### 4. Discussion

It is well-known that pure aluminium has good corrosion properties in neutral conditions due to the native  $\text{Al}_2\text{O}_3$  layer on the aluminium surface. The oxide layer retains its passivity when subjected to environments within a pH range of about 4 to 9 [25]. Aluminium is an amphoteric metal, and will therefore dissolve in highly acidic and alkaline conditions. In the acidic conditions, aluminium dissolves as  $\text{Al}^{3+}$  ions, while dissolving species in the alkaline condition is aluminate ions ( $\text{AlO}_2^-$ ) [25].



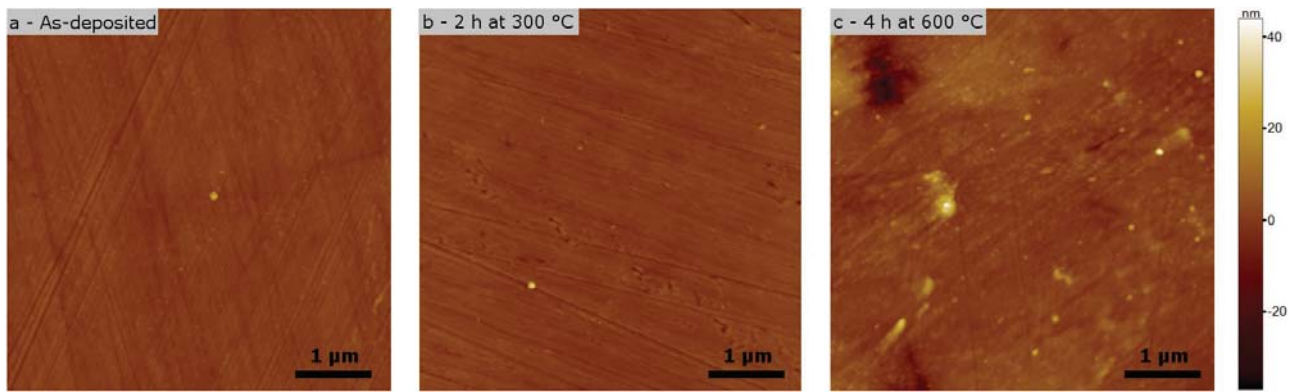


Fig. 9 – Topography measurements of polished surfaces in areas of  $5 \times 5 \mu\text{m}$ . Specimens containing 13 wt. % titanium. a) as-deposited, b) heat-treated for 2 h at 300 °C and c) heat-treated for 4 h at 600 °C.

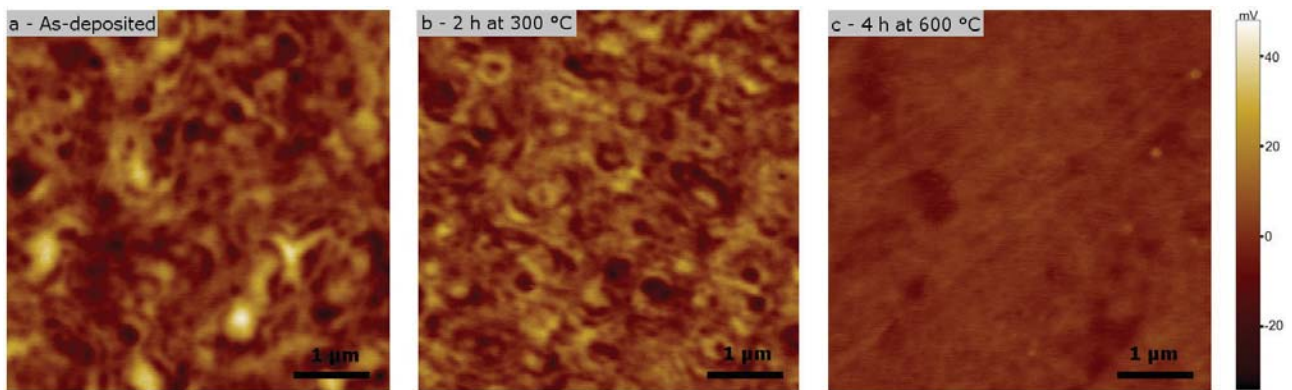


Fig. 10 – SKPFM surface potential mapping of polished surfaces in areas of  $5 \times 5 \mu\text{m}$ . Specimens containing 13 wt. % titanium. a) as-deposited, b) heat-treated for 2 h at 300 °C and c) heat-treated for 4 h at 600 °C.

Titanium has very good corrosion stability at high pH values [25] due to a tenacious and stable oxide film formed on the surface. However, conventional casting processing allows only 0.15 wt. % titanium to be introduced into aluminium [26,27]. The magnetron sputtering process on the other hand can be used for creation of aluminium coatings with higher titanium concentrations as shown in the present investigation with titanium concentrations up to 18 wt. %. Overall the results show significant improvement of the corrosion properties when increasing the titanium content and that altering the microstructure by heat treatment improved the corrosion resistance even further. The corrosion stability of the microstructure depends upon the local potential difference based on the relative distribution of titanium in the aluminium matrix either as elemental titanium or as precipitated second phase particles.

#### 4.1 Microstructure of as-deposited coatings, effect of heat treatment and surface potential changes

The cross section of the sputter coated layer (Fig. 3a) show a columnar structure with a directional growth of the film from the substrate with increasing width of the column towards the surface [28]. The XRD measurements (Fig. 1) show that in the as-deposited samples (both 3 wt. % and 13 wt. % titanium), titanium is distri-

buted in the elemental form as no crystalline peak corresponding to titanium or titanium containing phases is found. This is expected since the sputter deposition process was carried out at low temperatures (below 200 °C) and therefore no short range diffusion creating intermetallic phases is expected within the process time. The lack of one or more titanium-containing phases fits well with previous studies [10,15,16]. Sanchette and Billard [10] concluded that the as-deposited magnetron sputtered Al-Ti coatings are in the form of supersaturated  $\alpha$ -Al for titanium-concentrations up to about 40 wt. % and they found a quasi-amorphous phase up to 60 wt. % titanium. At higher titanium contents, a supersaturated HCP titanium phase was found. They concluded that similar packing structures (Al: FCC and Ti: HCP) and similar atomic radii (Al: 0.143 nm and Ti: 0.146 nm) are the reasons for such a high content of titanium is possible in  $\alpha$ -Al. Oliveira et al. [15] found similar results, however here the boundaries were found to be 57 wt. % and 79 wt. % titanium respectively. The TEM images of the as-deposited coating (Fig. 3a and b), show a microstructure consisting of alternating layers of low and high levels of titanium. The layers develop during the sputtering process due to the planetary rotation table causing alternating flux from the aluminium target at high power and the titanium target with aluminium pins at a lower power. Additionally, the sputter yield (average number

of atoms ejected per incident ion) of titanium is about half that of aluminium. The local titanium concentration is therefore expected to be quite high in the dark aluminium-titanium layers. However, since no titanium containing phases are found (Fig. 1) in the dark layers (Fig. 3a), it is expected that the local titanium concentration must be lower than 79 wt. % titanium [15]. The surface potential of the as-deposited specimen (Fig. 10a) showed significant heterogeneity attributed to the layered structure (Fig. 3a and b), while the random distribution of the higher and lower potential might be due to the fact that the preceding polishing reveals different parts of the layers. Therefore, the dark regions in the SKPFM potential map (Fig. 10) are expected to be due to partial appearance of dark layers shown by the TEM (Fig. 3), while the bright regions corresponds to bright layers.

Heat treatment up to 300 °C only slightly change the microstructure, since no new phases are found by XRD (Fig. 1) or SEM (Fig. 2a). The only change in microstructure expected in this case is the short range movement of titanium atoms giving rise to some level of homogenization (Fig. 10b). The decrease of the  $\alpha$ -Al phase peak for specimens heat-treated at 300 °C (Fig. 1a and b) implies that the as-deposited films are under stress and that the microstructural changes happening during heat treatment to some extent are attributed to recovery. This is supported by the SKPFM measurements, where the heterogeneity in the surface potential distribution is somewhat reduced (Fig. 10b) compared to the as-deposited specimen (Fig. 10a).

For specimens containing 13 wt. % titanium, the  $\text{Al}_3\text{Ti}$  phase precipitates during heat treatments at 400 °C and 500 °C (Fig. 1b), which fits well with the phase diagram of the binary Al-Ti system [27] and a previous study on Al-Ti coatings [16]. Use of titanium rich layers for the precipitation of the intermetallics have resulted in more uniformly distributed composition in the microstructure. In the SEM backscatter images, no particles are identified when heat-treated at 300 °C (Fig. 2a), but several appear after heat treatment at 500 °C (Fig. 2b), and the size has increased further after heat treatment at 600 °C (Fig. 2c and 3c). The XRD results (Fig. 1) supplemented with EDS and EDS mapping (not presented) support that these are in fact  $\text{Al}_3\text{Ti}$  phases. In the SKPFM measurement, for the specimen heat-treated at 600 °C (Fig. 10c) the dark more noble areas are in the same size range as the  $\text{Al}_3\text{Ti}$  particles in the SEM image (Fig. 2c), making it reasonable to conclude that these are the  $\text{Al}_3\text{Ti}$  particles. The reason for the lower amount of particles found in the SKPFM measurement compared to the SEM and TEM images (Fig. 2c and 3c) is due to the much smaller interaction volume of the scanning probe

compared to the SEM (about 1.5  $\mu\text{m}$  penetration depth at an acceleration voltage of 13 kV in aluminium containing 13 wt. % equally distributed titanium) and the thickness of the specimen used for TEM investigation.

## 4.2 Variation of corrosion properties with change in microstructure

Overall the corrosion properties of the coating improved with increasing concentration of titanium and with the microstructural changes due to heat treatment. Under saline conditions, although the corrosion current density did not show significant change, the effect of increased titanium concentration in the coating on corrosion performance is evident from the reduced passive current density and significant shift in the pitting potential towards more positive values (Fig. 4). For the as-deposited coatings, it is expected that the elemental titanium in the coating participates in the oxide formation, and the mixed oxide provide higher corrosion resistance than the oxide on the pure AA1050 coating. In general a similar behaviour is observed at pH 13.5; however, a slightly higher anodic current was measured for coatings containing 3 wt. % to 8 wt. % titanium compared to the pure AA1050 coatings both for as-deposited and heat-treated specimens (Fig. 5b). However, the TEM images (Fig. 3a and b) and SKPFM measurements (Fig. 10a) show an inhomogeneous microstructure indicating regions of higher titanium concentration in the matrix, which is expected to act as cathodic regions, increasing the anodic current of the aluminium matrix. Heat treatment at 300 °C decreases the anodic current for all titanium concentrations and even for the pure AA1050 coating (Fig. 5b), which is expected to be due to the release of the residual stresses built up during the sputter coating process. During heat treatment, crystallisation and structural relaxation, can lead to reduced surface activity and thereby decreased corrosion rate [14,29]. Polarization curves in the alkaline solution further shows a long plateau region, however the breakdown was not reached until a high potential value of 300 mV. The alkaline exposure studies (Fig. 6 and 7) of the titanium containing coatings show corrosion by pitting, whereas the pure AA1050 coating is affected by both general corrosion and pitting corrosion. In the alkaline exposure studies, it is found that for both as-deposited coatings (Fig. 6) and coatings heat-treated at 300 °C (Fig. 7) the corrosion resistance is improved with increased titanium concentration. This is in contradiction with the anodic polarization tests (Fig. 5b) where the AA1050 specimen show lower anodic current than the specimens of low titanium content (3 wt. % - 8 wt. %). The difference in the anodic polarization test is within the uncertainty of the measurements, however, the behaviour might be

attributed to the fact that the anodic current of the lower titanium containing specimens might be concentrated at a few very deep pits instead of corroding the overall surface like general corrosion as found for the pure AA1050 coating (Fig. 6a and 7a).

Fig. 5b shows that there is an initial increase in corrosion rate with increased titanium until a threshold concentration of ~8 wt. %, from where the corrosion rate drastically decreases with increase in titanium content. Comparing with the TEM observations (Fig. 3) of the as-received coatings and microstructure of the heat-treated specimens and SKPFM results (Fig. 10); the behaviour might be due to the balance between the amount of titanium, distribution, and precipitation in decreasing the heterogeneity in the surface potential.

As previously described, heat treatments at temperatures higher than 400 °C cause  $\text{Al}_3\text{Ti}$  phases of considerable sizes to precipitate as seen in the XRD measurements (Fig. 1b), SEM images (Fig. 2b and c), TEM image (Fig. 3c) and SKPFM measurements (Fig. 10c). The  $\text{Al}_3\text{Ti}$  phases are quite uniformly distributed as seen in the SEM image (Fig. 2b), enabling the creation of a network of  $\text{Al}_3\text{Ti}$  helping to reduce corrosion of the aluminium matrix when exposed to alkaline environments. Additionally, the SKPFM measurement (Fig. 10c) shows that heat treatment at 600 °C cause the microstructure to homogenize and EDS measurements (not presented) show that the matrix still contains some titanium. It has previously been found that heat treatment improves the corrosion properties in neutral salt conditions for other Al-Ti coatings [18], and for sputtered Al-Cr coatings [29] in 0.1 M HCl, where it was found that the corrosion properties were improved for coatings containing 27 wt. % chromium, but that the corrosion rate increased when heat treating coatings containing 51 wt. % chromium.

Structural relaxation decreasing the surface reactivity and a small decrease in potential differences in the structure are expected to be the main reasons for improvement of the corrosion properties for specimens heat-treated at 300 °C. A titanium concentration threshold between 8 wt. % and 13 wt. % titanium was established where the corrosion properties are improved compared to the pure AA1050 coating. For specimens containing 13 wt. % titanium heat-treated at 400 °C and more it was found that homogenization of the matrix and exhaustion of the preferentially distributed cathodic titanium rich areas into nucleation of the weaker cathodic  $\text{Al}_3\text{Ti}$  phases along with structural relaxation caused a significant improvement in the corrosion properties.

The results presented in this paper show that titanium might be usable for harsh alkaline corrosion protection of aluminium specimens using the magnetron sputtering technique. This technique has been used as a model system, where the necessary titanium concentration and microstructure has been indicated, however, optimisation is needed if using the magnetron sputtering technique.

## 5. Conclusions

- Microstructural investigation of the as-sputtered aluminium coatings containing up to 18 wt. % titanium showed alternating layers of lower and higher titanium content attributed to the deposition process. Heat treatments at 400 °C and more enabled the precipitation of  $\text{Al}_3\text{Ti}$  phases well distributed in a homogenised matrix.
- TEM images and surface potential measurements showed an inhomogeneous distribution of titanium and corresponding heterogeneity in surface potential for the as-deposited coating. Heat treatment for 4 h at 600 °C homogenized the surface potential distribution due to the precipitation of  $\text{Al}_3\text{Ti}$  reducing the galvanic potential with the matrix.
- Anodic polarization tests of as-deposited films in a neutral salt solution showed an increase in pitting potential with increase in titanium content. Overall a shift of 330 mV in pitting potential was found for the increase of titanium content from 0 – 15 wt. %.
- Corrosion tests at pH 13.5 showed that the anodic current increased with increase in titanium concentration from 3 wt. % - 8 wt. % titanium, but decreased significantly above this concentration. Heat-treatment for 2 h at 500 °C of a coating with 13 wt. % titanium showed an anodic current reduction of 95 % compared to as-deposited AA1050 coating.

## 6. Acknowledgements

The authors thank the Danish Agency for Science, Technology and Innovation for their financial support of the project and all partners of the IdeAl innovation consortium. Help of Visweswara Gudla, DTU-MEK for FIB and TEM work is acknowledged. The students Cathrine P. Larsen, David K. K. Hansen and Jacob B. Chortsen are acknowledged for running some of the experiments.



## 7. References

- [1] S. Wernick, R. Pinner, P.G. Sheasby, *The Surface Treatment and Finishing of Aluminum and Its Alloys*, 5th ed., Finishing Publications Ltd & ASM International, 1987.
- [2] P.C.R. Varma, J. Colreavy, J. Cassidy, M. Oubaha, C. McDonagh, B. Duffy, Corrosion protection of AA 2024-T3 aluminium alloys using 3, 4-diaminobenzoic acid chelated zirconium-silane hybrid sol-gels, *Thin Solid Films*. 518 (2010) 5753–5761.
- [3] N.N. Voevodin, N.T. Grebasch, W.S. Soto, L.S. Kasten, J.T. Grant, F.E. Arnold, et al., An organically modified zirconate film as a corrosion-resistant treatment for aluminum 2024-T3, *Org. Coat*. 41 (2001) 287–293.
- [4] M. Sheffer, A. Groysman, D. Mandler, Electrodeposition of sol-gel films on Al for corrosion protection, *Corros. Sci.* 45 (2003) 2893–2904.
- [5] R. Akid, M. Gobara, H. Wang, Corrosion protection performance of novel hybrid polyaniline/sol-gel coatings on an aluminium 2024 alloy in neutral, alkaline and acidic solutions, *Electrochim. Acta*. 56 (2011) 2483–2492.
- [6] Y. Zhang, H. Ye, H. Liu, K. Han, Preparation and characterisation of aluminium pigments coated with silica for corrosion protection, *Corros. Sci.* 53 (2011) 1694–1699.
- [7] S. Hirai, K. Shimakage, S. Aizawa, K. Wada, Alkaline Corrosion Resistance of Anodized Aluminum Coated with Zirconium Oxide by a Sol-Gel Process, *J. Am. Ceram. Soc.* 81 (1998) 3087–3092.
- [8] Q. Yan, H. Yoshioka, H. Habazaki, A. Kawashima, K. Asami, K. Hashimoto, Passivity and its breakdown on sputter-deposited amorphous Al-Ti alloys in a neutral aqueous solution with Cl<sup>-</sup>, *Corros. Sci.* 31 (1990) 401–406.
- [9] H. Yoshioka, Q. Yan, K. Asami, K. Hashimoto, Pitting potential and structure of sputter-deposited Al-Ti alloys, *Mater. Sci. Eng. A*. 134 (1991) 1054–1057.
- [10] F. Sanchette, A. Billard, Main features of magnetron sputtered aluminium-transition metal alloy coatings, *Surf. Coat. Technol.* 142-144 (2001) 218–224.
- [11] K. Hashimoto, N. Kumagai, H. Yoshioka, J.H. Kim, E. Akiyama, H. Habazaki, et al., Corrosion-resistant amorphous surface alloys, *Corros. Sci.* 35 (1993) 363–370.
- [12] Q. Yan, H. Yoshioka, H. Habazaki, A. Kawashima, K. Asami, K. Hashimoto, The corrosion behavior of sputter-deposited Al-Ti alloys in 1 N HCl, *Corros. Sci.* 32 (1991) 327–335.
- [13] E. Akiyama, H. Habazaki, A. Kawashima, K. Asami, I.L. Hashimoto, K. Hashimoto, Corrosion-resistant amorphous aluminum alloys and structure of passive films, *Mater. Sci. Eng. A*. 226-228 (1997) 920–924.
- [14] H. Yoshioka, Q. Yan, H. Habazaki, A. Kawashima, K. Asami, K. Hashimoto, Passivity and its breakdown on sputter-deposited amorphous Al-early transition metal alloys in 1 M HCl at 30 °C, *Corros. Sci.* 31 (1990) 349–354.
- [15] J.C. Oliveira, A. Manaia, J.P. Dias, A. Cavaleiro, D. Teer, S. Taylor, Structure and mechanical properties of Ti-Al films deposited by magnetron sputtering, *Surf. Coat. Technol.* 200 (2005) 395–398.
- [16] J. Hampshire, P.J. Kelly, D.G. Teer, The structure of co-deposited aluminium-titanium alloy coatings, *Thin Solid Films*. 447-448 (2004) 418–424.
- [17] J. Hampshire, P.J. Kelly, D.G. Teer, The tribological properties of co-deposited aluminium – titanium alloy coatings, *Thin Solid Films*. 447-448 (2004) 392–398.
- [18] Y. Sun, Thermally oxidised titanium coating on aluminium alloy for enhanced corrosion resistance, *Mater. Lett.* 58 (2004) 2635–2639.
- [19] H.T. Holt, R.H. Møller, Master thesis: Anodising of aluminium med optimerede egenskaber, DTU, 2008.
- [20] EVA Application 6.0.0.1, SOCABIM, (2000).
- [21] R. Ambat, P. Møller, Corrosion investigation of material combinations in a mobile phone dome –key pad system, *Corros. Sci.* 49 (2007) 2866–2879.
- [22] M. Jariyaboon, A.J. Davenport, R. Ambat, B.J. Connolly, S.W. Williams, D.A. Price, The effect of welding parameters on the corrosion behaviour of friction stir welded AA2024–T351, *Corros. Sci.* 49 (2007) 877–909.
- [23] M. Nonnenmacher, M.P. O’Boyle, H.K. Wickramasinghe, Kelvin probe force microscopy, *Appl. Phys. Lett.* 58 (1991) 2921–2923.

- [24] SPIP 6.0.4, Image Metrology A/S, (2012).
- [25] M. Pourbaix, Atlas of electrochemical equilibria in aqueous solutions, NACE, Houston, Texas, 1974.
- [26] [26] J. Cissé, H.W. Kerr, G.F. Bolling, The nucleation and solidification of Al-Ti alloys, Metall. Trans. 5 (1974) 633–641.
- [27] T.B. Massalski, J.L. Murray, L.H. Bennet, H. Baker, Binary phase diagrams vol. 1, 1st ed., ASM, Ohio, 1986.
- [28] J.A. Thornton, Influence of substrate temperature and deposition rate on structure of thick sputtered Cu coatings, J. Vac. Sci. Technol. 12 (1975) 830–835.
- [29] M. Mehmood, E. Akiyama, H. Habazaki, A. Kawashima, K. Asami, K. Hashimoto, The effect of heat treatment on the corrosion behavior of sputter-deposited aluminum-chromium alloys, Corros. Sci. 41 (1999) 477–499.







# Alkaline corrosion properties of laser-clad aluminum/titanium coatings

*Martin Aggerbeck and Alexis Herbreteau*

Department of Mechanical Engineering, Materials and Surface Engineering,  
Technical University of Denmark, Kgs. Lyngby, Denmark

*Marleen Rombouts and Jo Verwimp*

VITO – Laser Centre Flanders, MOL, Belgium, and

*Rajan Ambat*

Department of Mechanical Engineering, Materials and Surface Engineering,  
Technical University of Denmark, Kgs. Lyngby, Denmark

## Abstract

**Purpose** – The purpose of this paper is to study the use of titanium as a protecting element for aluminum in alkaline conditions.

**Design/methodology/approach** – Aluminum coatings containing up to 20 weight per cent Ti6Al4V were produced using laser cladding and were investigated using light optical microscope, scanning electron microscope – energy-dispersive X-ray spectroscopy and X-Ray Diffraction, together with alkaline exposure tests and potentiodynamic measurements at pH 13.5.

**Findings** – Cladding resulted in a heterogeneous solidification microstructure containing an aluminum matrix with supersaturated titanium (<1 weight per cent), Al<sub>3</sub>Ti intermetallics and large partially undissolved Ti6Al4V particles. Heat treatment lowered the titanium concentration in the aluminum matrix, changed the shape of the Al<sub>3</sub>Ti precipitates and increased the degree of dissolution of the Ti6Al4V particles. Corrosion testing showed significant localized dissolution of the aluminum matrix.

**Research limitations/implications** – Increased titanium concentration and heat treatment gave improved alkaline corrosion properties. At pH 13.5, the Al<sub>3</sub>Ti phases were protected, while the aluminum matrix corroded.

**Practical implications** – For alkaline corrosion-protection of aluminum in the automobile industry, titanium might be useful at pH values below 13.5 or by using other coating techniques.

**Originality/value** – This is the first study testing the use of titanium as a protective element of aluminum in stringent alkaline conditions.

**Keywords** Aluminum, Titanium, Laser cladding, Microstructure, Alkaline corrosion

**Paper type** Research paper

## 1. Introduction

Aluminum alloys are important for current and future lightweight structural applications. In the automotive industry, weight reduction can be translated into energy efficiency, and the use of aluminum alloys is growing rapidly because of their high strength-to-weight ratio and reduced cost caused by increased use of recycled materials. However, both saline and highly alkaline corrosion resistance is an important requirement for the automotive industry because of the use of caustic compounds in automatic brushless washing. Therefore, the short-term exposure (10 min) resistance of aluminum alloys in saline pH 13.5 conditions is a prerequisite for some applications.

Aluminum is an amphoteric metal, as the Pourbaix diagram (Pourbaix, 1974) indicates, and as commercial aluminum

alloys usually have low concentrations of alloying elements, these alloys are susceptible to corrosion in both acidic and alkaline conditions. However, surface modification methods such as laser cladding and laser alloying can produce metastable surface layers with significantly higher proportions of (for example) corrosion-resistant alloying elements.

For several years, surface properties have been improved using laser surface treatments, including laser surface melting (LSM) (Watkins *et al.*, 1997), laser surface alloying (LSA) (Watkins *et al.*, 1997) and laser surface cladding (LSC) (Pawlowski, 1999). Using LSM, fine non-equilibrium surface microstructures are created by surface melting and fast quenching. Using LSA, thin surface alloyed layers can be created where the degree of alloying and coating thickness is controlled by the laser treatment parameters. LSC is a method for producing thicker surface layers (typically in the range of

The current issue and full text archive of this journal is available on Emerald Insight at: [www.emeraldinsight.com/0003-5599.htm](http://www.emeraldinsight.com/0003-5599.htm)



Anti-Corrosion Methods and Materials  
62/1 (2015) 37–47  
© Emerald Group Publishing Limited [ISSN 0003-5599]  
[DOI 10.1108/ACMM-07-2013-1290]

The authors thank the Danish Agency for Science, Technology and Innovation for their financial support of the IdeAl project. Thanks to all partners in the IDEAL innovation consortium. Thanks to all employees at DTU MEK, Materials and Surface Engineering who have helped with experiments.

Received 30 July 2013  
Revised 12 June 2014  
Accepted 30 June 2014

0.5–1.0 mm), where the original surface is not a part of the surface of the final coating. The coatings have a good metallurgical bonding and small dilution with the substrate. Thanks to low and local heat input, LSC is very well suited for the treatment of heat-sensitive materials and components, as deformation is limited and the heat affected zone is small. Various feeding techniques can be used. However, the coaxial deposition method (de Oliveira *et al.*, 2005), situating the powder nozzle supplying metallic-based powder around the laser, has shown several advantages when cladding aluminum (da Silva *et al.*, 2012).

Aluminum coatings for corrosion protection using laser surface treatments are reported in a number of publications, focusing mainly on LSM and LSA, and mostly in connection with acidic and saline conditions (Almeida *et al.*, 1995; Bonora *et al.*, 1980; Ferreira *et al.*, 1996; Hannour *et al.*, 2001; Li *et al.*, 1996; McCafferty *et al.*, 1982; Watkins *et al.*, 1997, 1998, 1994). McCafferty *et al.* (1982) found that LSM of an AA3003 (1.2 weight per cent Mn) improved the corrosion resistance in both hydrochloric and sodium citrate solutions. Moore *et al.* (1977) did not find any improvement in pitting resistance using LSM of AA2024 with a CO<sub>2</sub> laser. The behavior was attributed to the presence of cracks and pores in the laser-treated surface, (Bonora *et al.*, 1980) studied a pure aluminum alloy LSM-treated with a Q-switched ruby laser with an energy density between 1 and 5 J/cm<sup>2</sup> at an estimated cooling rate up to about 10<sup>11</sup> K/s. They found increased corrosion potential, lower passive current density and an unchanged pitting potential, although with a lower pitting corrosion rate. Similar behavior has been reported by Hagans and Yates (1989) using a Q-switched Nd:YAG laser with 5 ns pulses at 4 mJ/pulse. The beneficial effect was attributed to the amorphous aluminum surface created during the surface treatment. McMahon (1994) reported a 100 mV increase in pitting potential for laser-treated AA2014 (Al-4.6Cu-0.5Mg). Li *et al.* (1996) showed that for LSM-treated AA2024-T351 in 3 weight per cent NaCl solution, the as-received surface showed intergranular and pitting corrosion, while laser-treated regions showed only pitting attack. The use of an excimer-type laser enables increased surface absorption and shorter pulse durations and has also shown promising results for aluminum (Autric *et al.*, 2000; Barnikel *et al.*, 1996, 1997). Excimer lasers have been used for improving corrosion properties of AA2050 (Viejo *et al.*, 2010) and for changing microstructures, thereby modifying the cathodic reactivity of friction stir welded AA7449 (Padovani *et al.*, 2011).

Aluminum surface layers with alloyed transition metals using LSA have been tested for corrosion protection (Watkins *et al.*, 1997) where systems containing molybdenum (Watkins *et al.*, 1994) and chromium (Almeida *et al.*, 1995) increased the pitting potential. Ferreira *et al.* (1996) added chromium to AA7175 using LSA preventing crevice corrosion. Watkins *et al.* (1998) studied the properties of LSA-treated aluminum systems containing chromium, tungsten, zirconium, titanium and nickel. It was found that the pitting potential in 1 M NaCl was improved by 450 mV for an Al-Ti-Ni system compared to as-received AA2014.

A number of investigations that are reported in the literature on LSC (Ocylok *et al.*, 2011; Xu *et al.*, 2006) were related to the effect on wear or high temperature oxidation resistance.

Yue *et al.* (2006) studied LSC coatings on AA7075 substrates with powders containing Al-0.3TiO<sub>2</sub>-0.3SiO<sub>2</sub>, Al-0.17Cr<sub>2</sub>O<sub>3</sub>-0.5SiO<sub>2</sub> and Al-0.375CuO-0.375SiO<sub>2</sub>. It was found that the coating with Al-0.375CuO-0.375SiO<sub>2</sub> impaired the corrosion properties, while the other two – especially the addition of Al-0.3TiO<sub>2</sub>-0.3SiO<sub>2</sub> – decreased the corrosion current density and increased the corrosion potential in a 3.5 weight per cent NaCl solution. The differences in corrosion properties were attributed mainly to the lower potential differences between the matrix and the titanium and chromium phases. Abboud *et al.* (1994a), 1994b) have characterized the microstructure and composition of clad Al/Ti systems, although only up to 35 weight per cent aluminum. In both studies, dendritic structures of AlTi-intermetallics were found. No studies have been found focusing on the alkaline corrosion resistance, irrespective of the surface processing method.

The study presented here focused on the microstructure and alkaline corrosion properties of LSC coatings of aluminum, with titanium as a major alloying element, using a combination of aluminum powder mixed with 5, 10 and 20 weight per cent of a Ti6Al4V powder for both as-clad and heat-treated specimens. The aim of alloying with titanium was to investigate the effect on the alkaline corrosion properties of the resulting microstructure arising from the alkaline corrosion stability of titanium. The microstructure of the coatings was studied using light optical microscopy (LOM), scanning electron microscopy (SEM), energy-dispersive X-ray spectroscopy (EDS) and X-ray Diffraction. The alkaline corrosion performance of the laser-clad layers was investigated by exposure tests and using potential dynamic polarization experiments, both at pH 13.5.

## 2. Materials and methods

### 2.1 Materials and laser cladding process

Commercial AA6063 substrates were degreased and sand blasted and, subsequently, laser-clad using a powder mixture of commercially pure aluminum of 99.8 per cent purity and a powder of Ti6Al4V (45–100 μm particle size) at concentrations of 5, 10, and 20 weight per cent. The cladding was done with a Laserline diode laser with mixed wavelengths of 808 and 940 nm at 2050 and 2200 W, respectively. The spot diameter was 3.8 mm, and the cladding was performed at a speed of 1,000 mm/min for the first six tracks and thereafter 1,300 mm/min to limit dilution. The powder containing 5, 10 and 20 weight per cent Ti6Al4V was fed at 4.8, 5.1 and 5.2 g/min, respectively. Argon was used as a transport and shielding gas.

Heat treatment was carried out at 600°C in air for 10 hours. The samples were ground and polished to a diamond polishing level of 1 μm.

### 2.2 Microstructural analysis

Microstructural analysis of the as-clad and heat-treated specimens was performed using an LOM Olympus GX41, using an Altra 20 Soft Imaging System.

For further microstructural investigations, an SEM, JSM-5900 from JEOL at 13 kV was used for imaging and EDS measurements for compositional analysis. An EDS line-scan was done on a field emission gun SEM, Quanta 200f from FEI, at 15 kV.

Phase identification was done using XRD measurements on a D8 Discover from Bruker AXS with a copper  $K_{\alpha 1}$  beam at grazing incidence of  $5^\circ$ . The measurements were done from  $20$  to  $160^\circ$ ; however, only results from  $20$  to  $85^\circ$  are presented. The step size was  $0.03^\circ$  with a step time of  $4$  s. The results were analyzed using the EVA Application 6.0.0.1 software from SOcABIM.

### 2.3 Alkaline exposure tests at pH 13.5

Before alkaline exposure, the specimens were lacquered on all sides apart from the laser-clad surface. This was done to ensure that only the clad area was exposed to the solution and no galvanic coupling to the substrate would influence the results.

The alkaline resistance was tested in a solution containing  $4.6$  g/L  $\text{Na}_3\text{PO}_4 \cdot 12\text{H}_2\text{O}$ ,  $0.131$  g/L  $\text{NaCl}$  and  $12.65$  g/L  $\text{NaOH}$  in demineralized  $\text{H}_2\text{O}$ , causing a pH of around  $13.5$ . After  $10$  min of exposure at room temperature, the specimens were cleaned with demineralized water, de-smutted in  $70$  weight per cent nitric acid for  $4$  min and cleaned again with demineralized water. After the test, the lacquer was removed, and the specimens were investigated using the SEM.

### 2.4 Anodic polarization tests at pH 13.5

Potentiodynamic polarization experiments were done using a flat cell for further studies of the corrosion properties in harsh alkaline conditions. This was performed at pH  $13.5$  using the same solution as for the alkaline exposure tests. The cell had an exposed area of approximately  $0.91$  cm<sup>2</sup> of the specimen, which was connected as the working electrode. A twisted platinum wire ring was used as counter electrode, and an Ag/AgCl electrode was used as the reference electrode. Initially, the Open Circuit Potential (OCP) of the specimen was monitored for  $3$  min, followed by a potentiodynamic scan starting at  $100$  mV below the OCP to  $+700$  mV vs the Ag/AgCl reference electrode, at a sweep rate of  $120$  mV/min.

## 3. Results

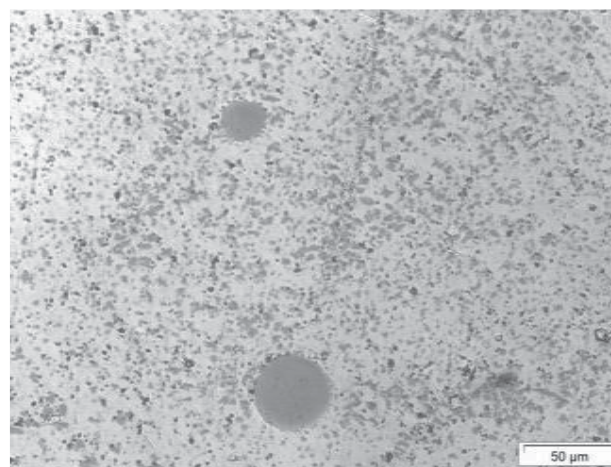
### 3.1 Microstructure analysis

The LOM images in Figure 1 present the microstructure of the as-clad specimens, and Figure 2 shows the microstructure after heat treatment. As-clad specimens with  $5$  weight per cent Ti6Al4V (Figure 1a) had a microstructure with a matrix containing small precipitates of up to  $3$   $\mu\text{m}$  in diameter. Additionally, large particles of about  $20$ – $50$   $\mu\text{m}$  in diameter were observed. No excessive impact on the microstructure was observed due to heat treatment of the  $5$  weight per cent Ti6Al4V specimens (Figure 2a) when studied under the LOM. However, SEM investigations presented later show that the particles were changed into a more spherical form.

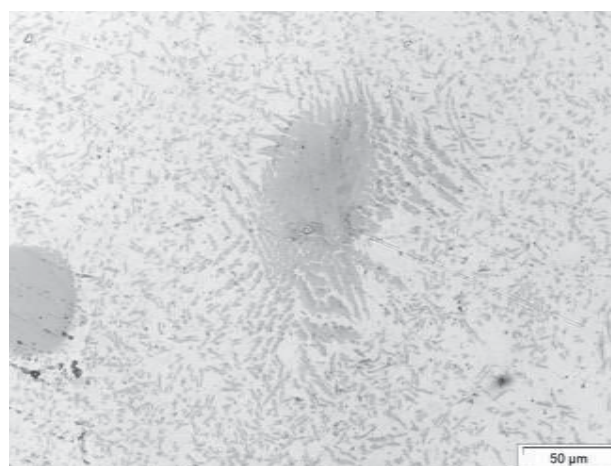
Specimens with  $10$  weight per cent Ti6Al4V (Figures 1b and 2b) had a microstructure similar to the specimens containing  $5$  weight per cent Ti6Al4V (Figure 1a). Additionally, some precipitates had an elongated shape.

The microstructure of as-clad specimens with  $20$  weight per cent Ti6Al4V (Figure 1c) had a structure with elongated dendrites extending up to about  $5$   $\mu\text{m}$  in thickness. The large particles were, in general, up to  $100$   $\mu\text{m}$  in size. However, in

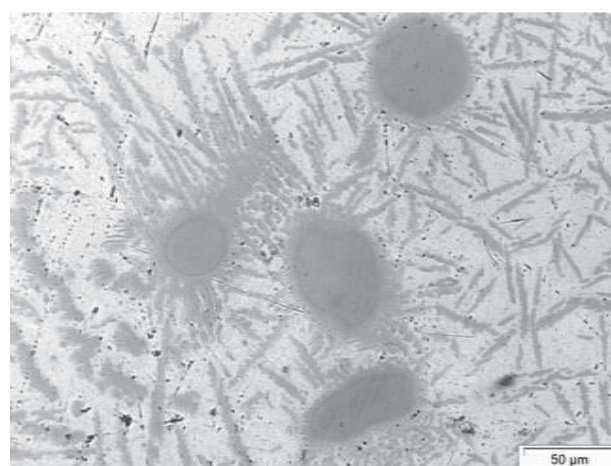
**Figure 1** Optical micrographs of as-clad specimens



(a)



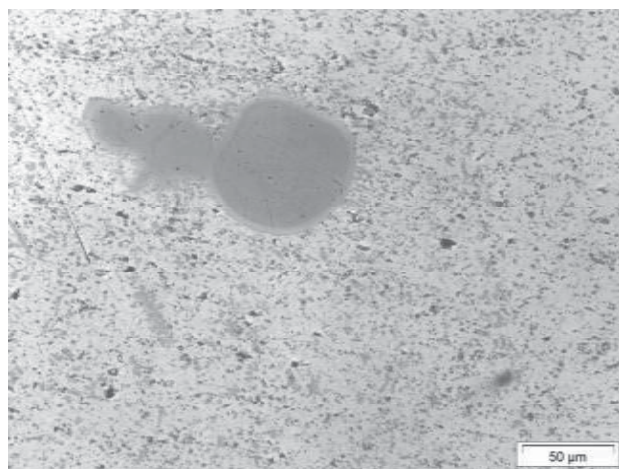
(b)



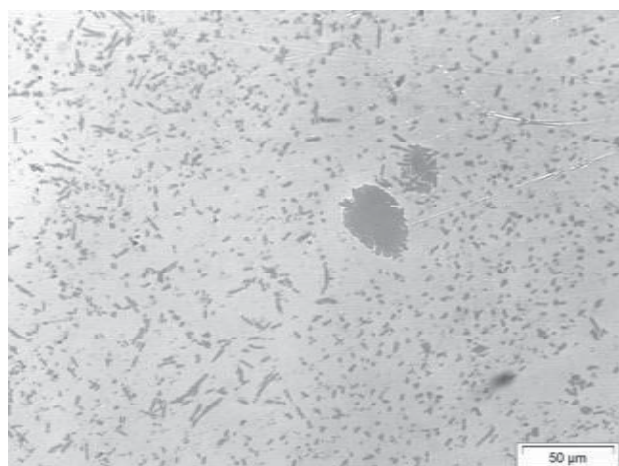
(c)

**Notes:** (a)  $5$  wt.% Ti6Al4V; (b)  $10$  wt.% Ti6Al4V; (c)  $20$  wt.% Ti6Al4V

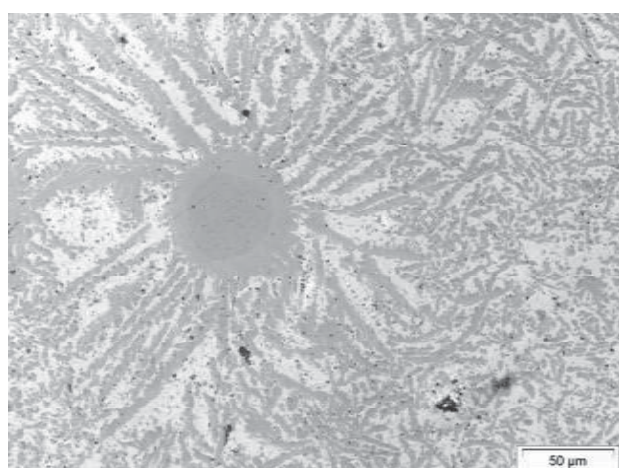


**Figure 2** Optical micrographs of heat-treated specimens

(a)



(b)



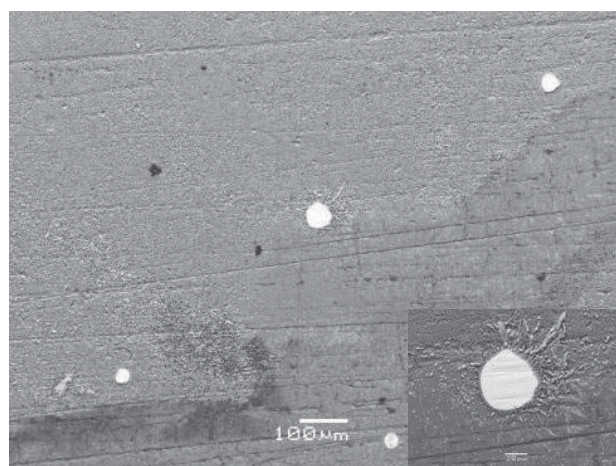
(c)

**Notes:** (a) 5 wt.%Ti6Al4V; (b) 10 wt.%Ti6Al4V;  
(c) 20 wt.%Ti6Al4V

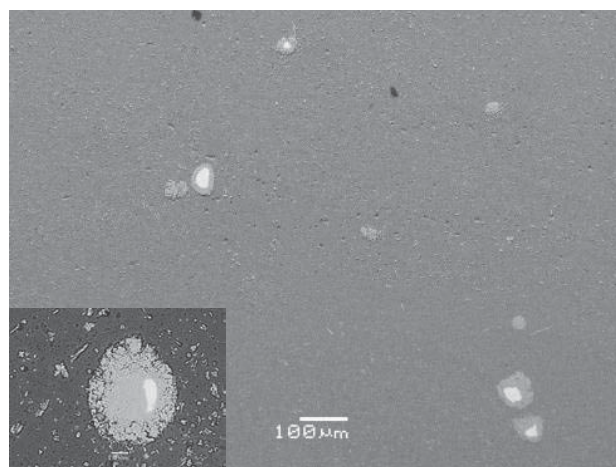
some areas, particles had grown together covering a larger area. Heat treatment (Figure 2c) caused the growth of new precipitates and growth of the dendrites, both in length and thickness.

A backscatter image of an as-clad specimen is presented in Figure 3a, showing the elemental distribution of the microstructure. The small precipitates appear brighter than the matrix, indicating that they have a higher atomic density. Additionally, the core of the large particles has a significantly higher atomic density than the small precipitates and, in some cases, the outer layer of the larger particles. Figure 3b presents a backscatter image of a heat-treated specimen. Here it was observed that the size of the bright core was diminished, leaving a thicker, less bright, outer layer around the core.

The EDS analysis results from the various areas of the microstructure are presented in Table I. The compositions of the different phases were in the same range for specimens of different Ti6Al4V concentrations, both before and after heat treatment. However, after heat treatment, silicon was detected

**Figure 3** SEM backscatter image showing undissolved particles in LSC specimens with 5 weight per cent Ti6Al4V. The bright cores show undissolved Ti6Al4V

(a)



(b)

**Notes:** (a) As-clad; (b) heat-treated



Table I Summary of EDS result from all specimens

Concentration (weight %)	Al	Ti	V
Matrix	99-100	0-1*	—
Intermetallic precipitates	60-80	20-40	0-1.5
Undissolved particles, outer layer	40-60	35-60	1-2
Undissolved particles, core	6	90	4

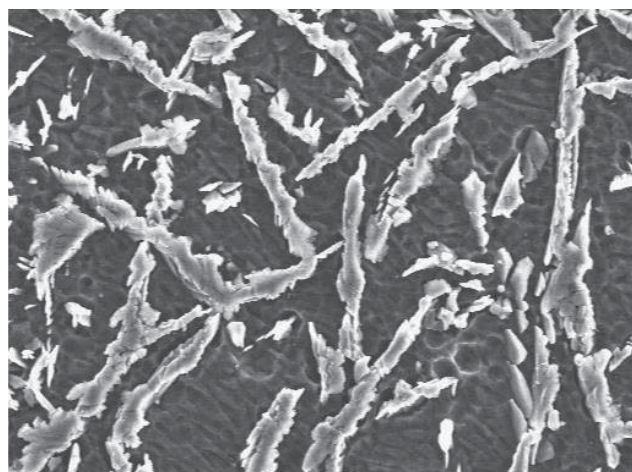
Notes: \*Ti in the matrix was mainly found in as-cladded specimens; in addition, 3-4 weight per cent Si was identified after heat treatment

at concentrations up to 3 weight per cent. This is expected to be caused by diffusion from the substrate material as silicon diffuses rapidly in the aluminum matrix. EDS mapping (Figure 4) was done to support these measurements. From the binary Al/Ti phase diagram (Massalski *et al.*, 1986),  $\alpha$ -Al and  $\text{Al}_3\text{Ti}$  (63 weight per cent Al) phases are expected after solidification. The EDS results showed that the matrix was

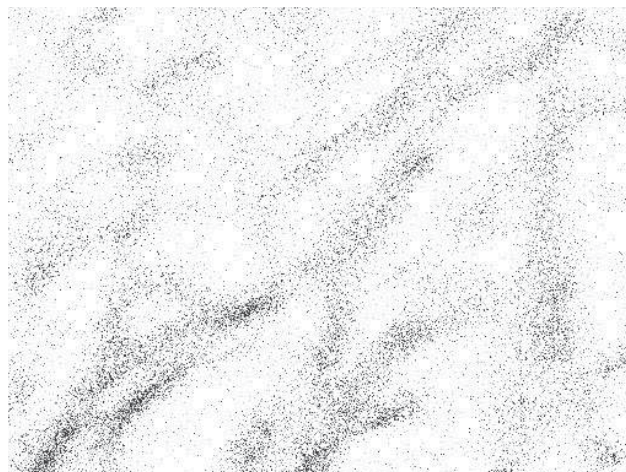
pure aluminum (Figure 4b), with sporadic titanium concentrations up to 1 weight per cent, especially in the as-clad specimens. The intermetallic precipitates (the small equiaxed phases and the elongated dendrites) consisted mainly of aluminum, containing 20-40 weight per cent titanium (Figure 4c) and up to 1.5 weight per cent vanadium (Figure 4d).

The core of the large particles had the same composition as the Ti6Al4V feedstock powder. The outer layer of these particles contained 35-60 weight per cent titanium and 1-2 weight per cent vanadium. An EDS line scan of such a particle is presented in Figure 5. Here, it was observed that the chemical composition of the investigated particle was very stable throughout the particle. The core had the Ti6Al4V-composition, and the outer layer of the particle had about 36 weight per cent titanium, 3 weight per cent to 4 weight per cent silicon and about 1.5 weight per cent vanadium.

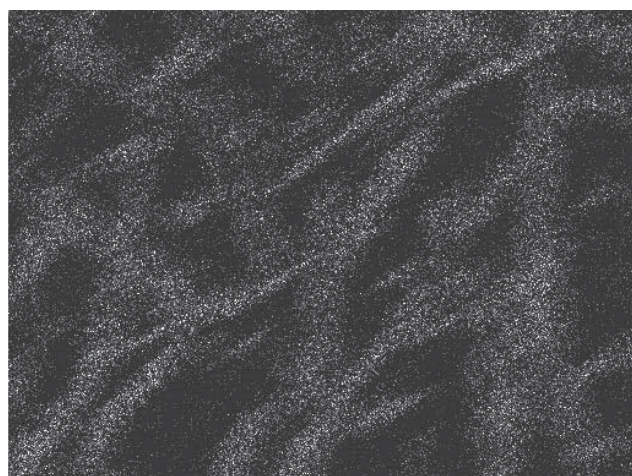
Figure 4 EDS mapping of as-clad specimen with 20 weight per cent Ti6Al4V after alkaline exposure test



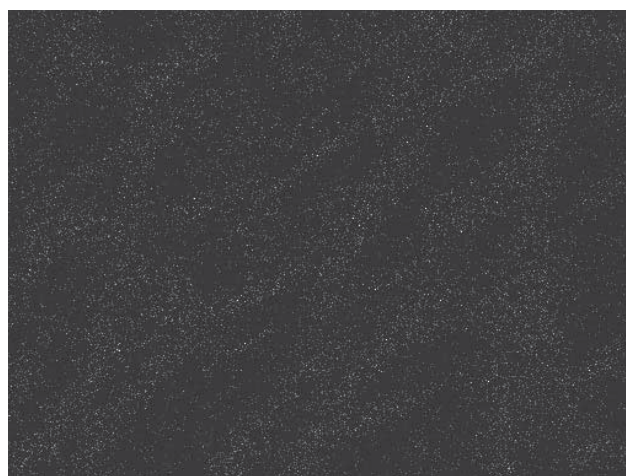
(a)



(b)



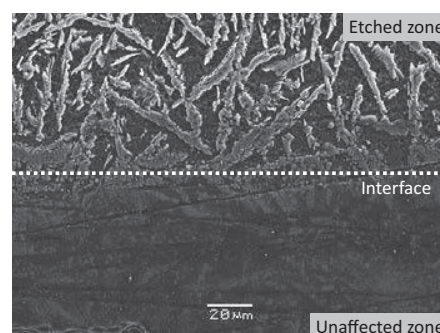
(c)



(d)

Notes: (a) SEM image; (b) Al  $K_{\alpha}$ ; (c) Ti  $K_{\alpha}$ ; (d) V  $K_{\alpha}$

**Figure 7** SEM images of as-clad specimen with 20 weight per cent Ti6Al4V after alkaline exposure test



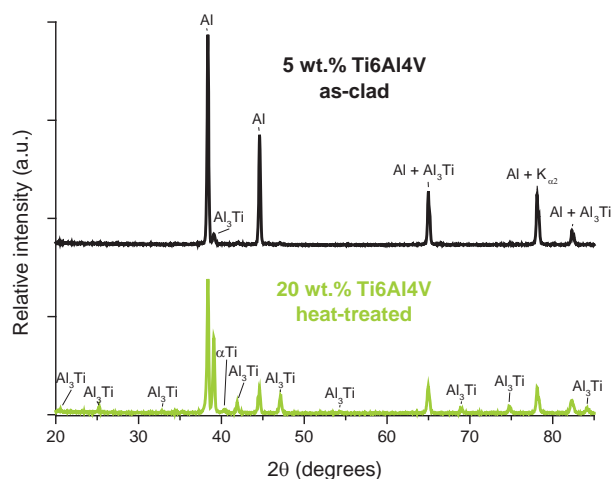
(b)

**Notes:** (a) Interface between exposed and unexposed zone; (b) Image taken at a tilted angle showing matrix dissolution around the particles and dendrites

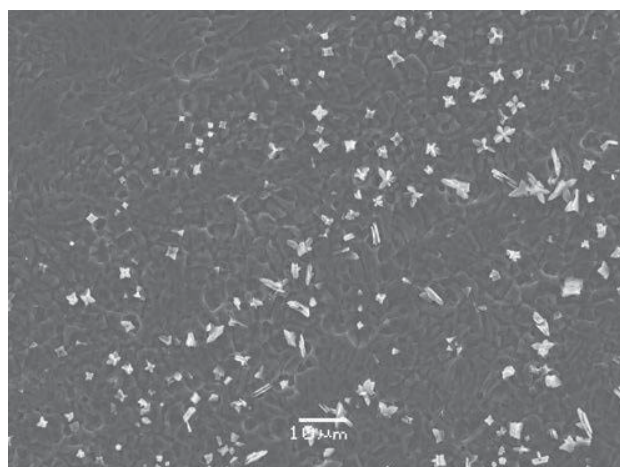
Figure 8 presents SEM images of as-clad specimens after the alkaline exposure test. Figure 9 presents SEM images of the clad specimens after heat treatment followed by the alkaline exposure test. The as-clad specimens with 5 and 10 weight per cent Ti6Al4V (Figure 8a and 8b) showed that the precipitates were equiaxed flake-structures or dendrites, which changed into more spherical shapes during heat treatment (Figure 9a and 9b). As-clad specimens were etched in the matrix area, showing features ranging from 2 to 4  $\mu\text{m}$ . After the heat treatment, corrosion of the matrix was more uniform. All micrographs in Figures 8 and 9 show preferential dissolution of the matrix around the  $\text{Al}_3\text{Ti}$  intermetallics. However, this was more pronounced for the heat-treated specimens. For specimens with 5 and 10 weight per cent Ti6Al4V, the preferential dissolution caused undermining and release of the smaller intermetallics during the exposure. The growth of intermetallic phases and the undermining of the intermetallics during exposure to the alkaline solution are considered to be the probable reasons for fewer particles being evident after heat treatment.

### 3.3 Anodic polarization tests at pH 13.5

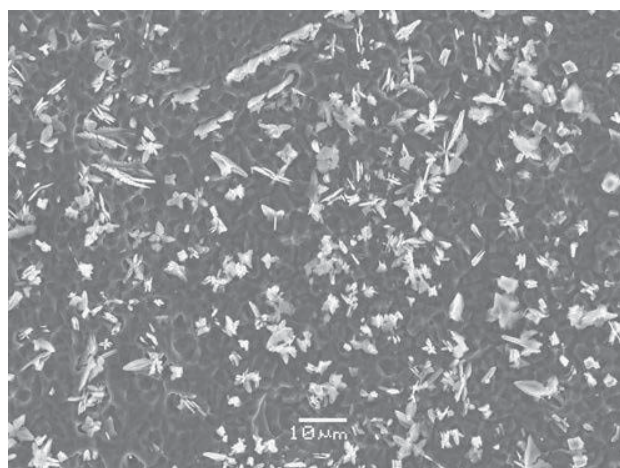
**Figure 6** XRD measurements from 20° to 85° on LSC samples



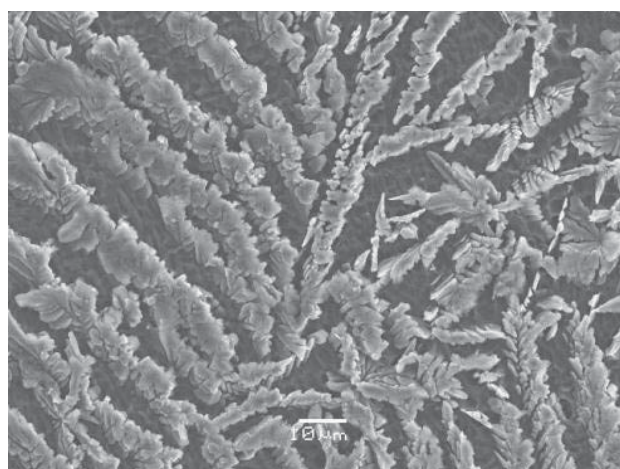


**Figure 8** SEM images of as-clad specimens after alkaline exposure test

(a)

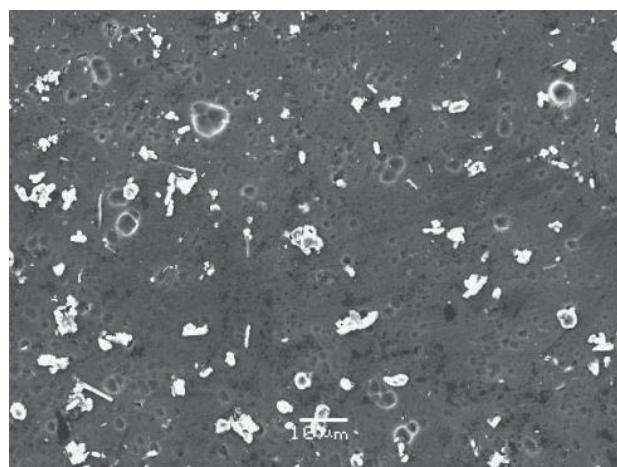


(b)

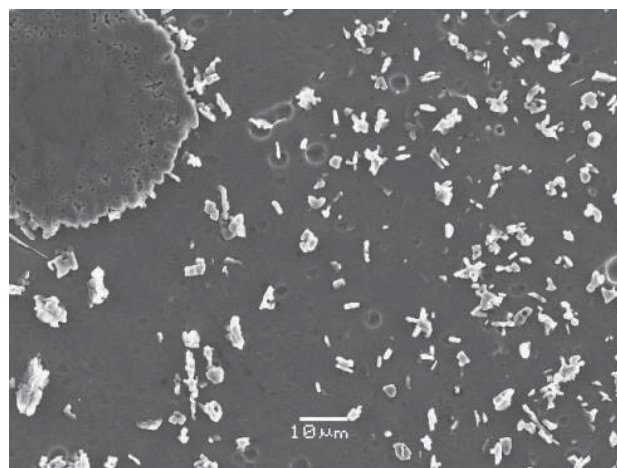


(c)

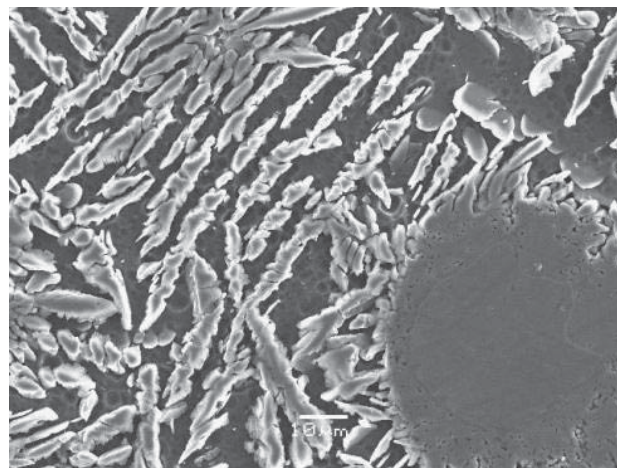
**Notes:** (a) 5 wt.% Ti6Al4V; (b) 10 wt.% Ti6Al4V; (c) 20 wt.% Ti6Al4V

**Figure 9** SEM images of heat-treated specimens after alkaline exposure test

(a)

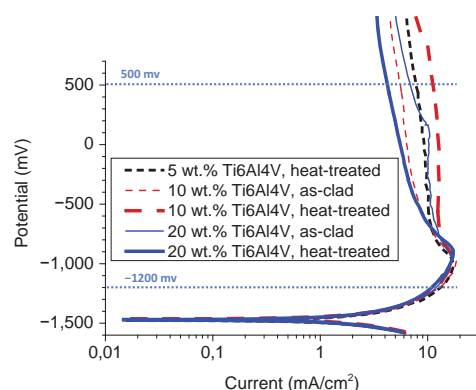


(b)

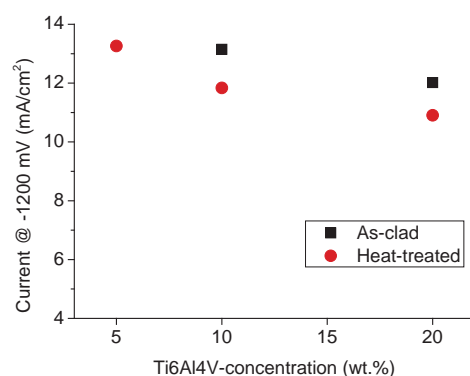


(c)

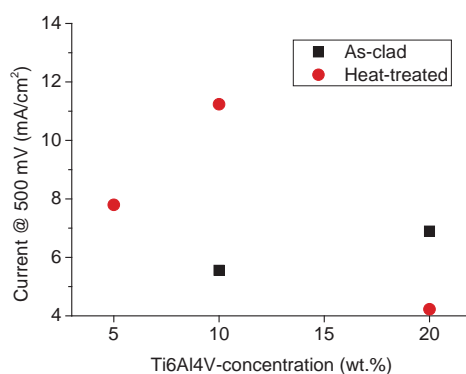
**Notes:** (a) 5 wt.% Ti6Al4V; (b) 10 wt.% Ti6Al4V; (c) 20 wt.% Ti6Al4V

**Figure 10** Polarization curves of LSC treated samples

(a)



(b)



(c)

**Notes:** (a) Polarization curves; (b) Anodic current @ 21200 mV; (c) Anodic current @ 1500 mV

conditions. It was observed that the  $E_{\text{corr}}$ -value was approximately 1475 mV vs the Ag/AgCl reference electrode for all the specimens. The anodic corrosion current just after the  $E_{\text{corr}}$ -value (at -1200 mV vs the Ag/AgCl reference electrode) and the plateau current (at +500 mV vs the Ag/AgCl reference electrode) deduced from the polarization curves are presented in Figure 10b and 10c, respectively.

At -1200 mV (Figure 10b), it was found that the current decreased when the concentration of Ti6Al4V increased for both the as-clad specimens (squares) and the heat-treated

specimens (circles). Additionally, heat treatment decreased the corrosion current for the specimens with 10 and 20 weight per cent Ti6Al4V. Comparing the highest current (5 weight per cent Ti6Al4V, heat-treated) and the lowest current (20 weight per cent Ti6Al4V, heat-treated), the anodic current decreased from 13.3 to 10.9 mA/cm<sup>2</sup>, which is a reduction of about 18 per cent.

Figure 10c illustrates the corrosion current at +500 mV vs the Ag/AgCl reference electrode for the as-clad specimens (squares) and the heat-treated specimens (circles). The plateau current density did not show any clear trend. However, a comparison of the lowest and highest concentrations shows a decrease in the current density from 7.8 to 4.2 mA/cm<sup>2</sup>, which is a reduction of about 46 per cent.

#### 4. Discussion

High purity aluminum has good corrosion properties in neutral environments because of the natural oxide layer of Al<sub>2</sub>O<sub>3</sub> created on the surface when exposed. The passivity of the surface is quickly rebuilt when damaged and can be retained at pH-values of about 4–9. However, when aluminum is exposed to a harsh alkaline environment, the passive oxide layer is dissolved and re-passivation is slower, causing aluminum alloys to corrode with the creation of AlO<sub>2</sub><sup>-</sup> ions (Pourbaix, 1974). In contrast to this, titanium has high stability at pH values from 0 to 14 as depicted by the Pourbaix diagram (Pourbaix, 1974) because of its tenacious oxide film. Therefore, the addition of titanium was proposed to improve the alkaline corrosion resistance of aluminum alloys. The maximum titanium concentration in an aluminum matrix in equilibrium conditions at room temperature is only up to 0.2 weight per cent, as the binary Al-Ti phase diagram (Massalski et al., 1986) indicates. Higher titanium concentrations in solid solution in aluminum can be encountered after rapid cooling from elevated temperature, such as after LSC with Al-Ti powder.

After LSC, microstructural investigations revealed an aluminum matrix with up to about 1 weight per cent titanium. The solidification of the melted powders resulted in the precipitation of Al<sub>3</sub>Ti intermetallics. The intermetallics were equiaxed for specimens containing 5 and 10 weight per cent Ti6Al4V and elongated dendritic for the specimens containing 20 weight per cent Ti6Al4V. Additionally, some of the particles from the Ti6Al4V powder were not completely molten during the laser-cladding process and were trapped in the partly undissolved condition in the matrix.

No information was found from literature about the microstructure of laser-clad Al-Ti coatings. However, reported results on LSA of Al-Ti systems are consistent with the present investigation (García et al., 2002; Mabhali et al., 2012; Wendt et al., 2003; Xu et al., 2006). García et al. (2002) treated titanium substrates with the aim of producing titanium aluminides reinforced with hard titanium nitrides. When the laser speed was kept at 300 mm/min, no nitride was found at the surface of the alloying zone, giving 37 weight per cent titanium and 63 weight per cent aluminum. Here a matrix of pure aluminum was identified with dendrites of Al<sub>3</sub>Ti. Mabhali et al. (2012)



studied AA1200 with mixtures of nickel, titanium and SiC powders. When using only titanium powder, a matrix of pure aluminum and dendrites of  $\text{Al}_3\text{Ti}$  was evident. Wendt *et al.* (2003) treated aluminum using a titanium wire. A supersaturated aluminum phase containing up to 4 weight per cent titanium was identified, as well as dendrites of  $\text{Al}_3\text{Ti}$ . The reported results on the titanium concentration in the  $\alpha\text{-Al}$  matrix are based on only EDS measurements (Wendt *et al.*, 2003) or XRD measurements (García *et al.*, 2002; Mabhali *et al.*, 2012). The EDS measurements performed during this study (Table I) showed rather pure  $\alpha\text{-Al}$  with sporadic traces of titanium up to 1 weight per cent, especially before heat treatment. Wendt *et al.* (2003) did not provide many details on the experimental setup, but the high titanium concentration of 4 weight per cent in the aluminum matrix could be attributed to the processing conditions (e.g. due to pulsed laser processing), leading to a cooling rate that was higher than the one achieved during the present experiments.

In the present investigation, heat treatment caused the intermetallic phases of the 5 and 10 weight per cent Ti6Al4V specimens to turn into more spherical shapes and the dendrites of the 20 weight per cent Ti6Al4V specimens to grow, smoothing their edges (Figure 8 and Figure 9). The mechanism behind the growth of the dendrites was expected to be the diffusion of titanium and vanadium from the matrix and the partially undissolved particles during the heat treatment procedure. Additionally, aluminum was expected to diffuse into the large, partially undissolved particles of Ti6Al4V.

The microstructures presented in this study were very similar to the microstructures observed by Xu *et al.* (2006), investigating the microstructure and wear properties of laser cladding with Ti-Al-Fe-B coatings on AA2024. For titanium concentrations of 19 and 28.5 weight per cent, Xu *et al.* (2006) identified a matrix–dendritic microstructure of  $\alpha\text{-Al}$  and  $\text{Al}_3\text{Ti}$  and larger particles with a core of almost pure titanium.

In the present study, XRD measurements (Figure 6) identified  $\alpha\text{-Al}$ ,  $\text{Al}_3\text{Ti}$ , and an  $\alpha\text{-Ti}$  phase. Additionally, the EDS measurements (Table I and Figure 4) show a matrix of almost pure aluminum and large particles with cores of undissolved Ti6Al4V (Figure 3). The  $\text{Al}_3\text{Ti}$  phase corresponds to about 63 weight per cent aluminum and about 37 weight per cent titanium. EDS measurements on the small  $\text{Al}_3\text{Ti}$  intermetallic precipitates probably show higher proportions of aluminum (60–80 weight per cent) because the interaction volume of the electron beam of the EDS analysis extended into the matrix. The lower concentration of aluminum measured in the outer layer of large particles (40–60 weight per cent aluminum) may result from various factors. The outer layer is not always pure  $\text{Al}_3\text{Ti}$ , but it is mixed with other intermetallic Al-Ti-phases (such as  $\text{AlTi}$  and  $\text{AlTi}_3$ ) or, at some locations, even small volumes of metallic titanium. Alternatively, the underlying structures contain more titanium than is visible as the undissolved core may spread out beneath the surface. However, the line scan (Figure 5) shows a very stable titanium concentration close to the composition of  $\text{Al}_3\text{Ti}$ , with small increases at two areas.

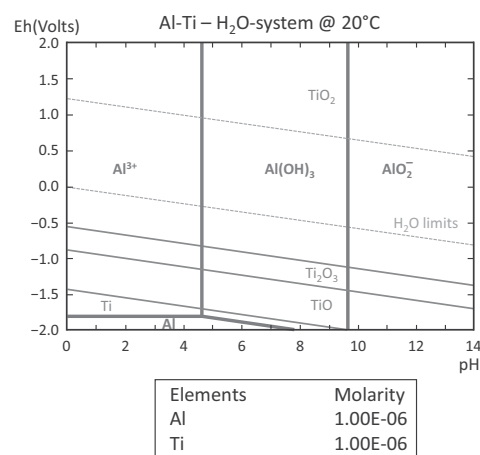
After the exposure test of the as-clad specimens (Figure 8), it was found that the  $\alpha\text{-Al}$  phase corroded, whereas the  $\text{Al}_3\text{Ti}$  phase and other higher titanium-concentrated phases were much more stable. This result is in agreement with the Pourbaix diagram presented in Figure 11, combining the diagrams of aluminum and titanium (Roine, 2002). The microstructure of the material was highly heterogeneous, resulting in preferential dissolution of the aluminum matrix, as would be expected because of the low degree of supersaturation of titanium. On the other hand, if titanium was distributed uniformly at atomic level or as Al-Ti intermetallic phases, corrosion resistance is expected to be higher, as found in the case of Al-Ti magnetron sputtered coatings (Aggerbeck *et al.*, 2012). Magnetron-sputtered coatings produced a uniform distribution, and the heat treatment generated a network of intermetallic phases, helping to reduce the corrosion of the aluminum matrix under alkaline conditions.

The results presented in this paper have illustrated the microstructural evolution during the LSC process and the resulting corrosion behavior of the rapidly solidified coating. The results of the polarization experiments were in agreement with the exposure tests; the specimens were corroding heavily at pH 13.5, even at the highest titanium concentration and after heat treatment. Aluminum/titanium coatings might be useful in the automotive industry for protection, e.g. in less alkaline conditions (pH <13.5) or if applied using other coating techniques causing a different microstructure than the one presented.

## 5. Conclusions

- Laser surface cladding of aluminum and 5 to 20 weight per cent Ti6Al4V powders resulted in a microstructure containing  $\alpha\text{-Al}$ ,  $\text{Al}_3\text{Ti}$  intermetallic equiaxed or elongated dendrites and undissolved Ti6Al4V particles.
- Heat treatment made the intermetallic  $\text{Al}_3\text{Ti}$  phases exhibit more spherical shapes in the specimens containing 5 and 10 weight per cent Ti6Al4V. For specimens containing 20 weight per cent Ti6Al4V, heat treatment caused thickening of the elongated dendrites.

**Figure 11** Combined Pourbaix diagram for Al (thick lines) and Ti (thin lines). Calculated by software (Roine, 2002)



- Exposure tests in a pH 13.5 solution showed heavy preferential dissolution of the  $\alpha$ -Al matrix, while phases of higher titanium concentrations were protected. After 10 hours at 600°C, corrosion around the Ti-rich phases was more pronounced because of a lower degree of titanium supersaturation in the aluminum matrix.
- Anodic polarization tests at pH 13.5 showed no change of the  $E_{\text{corr}}$  value, while slight decrease in the overall current density was observed with increased titanium concentration and heat treatment.

## References

- Abboud, J.H., Rawlings, R.D. and West, D.R.F. (1994a), "Functionally gradient layers of Ti-Al based alloys produced by laser alloying and cladding", *Materials Science and Technology*, Vol. 10 No. 5, pp. 414-420.
- Abboud, J.H., West, D.R.F. and Rawlings, R.D. (1994b), "Functionally gradient titanium-aluminide composites produced by laser cladding", *Journal of Materials Science*, Vol. 29 No. 13, pp. 3393-3398.
- Aggerbeck, M., Rechendorff, K. and Ambat, R. (2012), "Aluminium based coatings containing titanium for alkaline protection", *Proceeding of Aluminium Surface Science and Technology (ASST)*, Sorrento, p. 5.
- Almeida, A., Anjos, M., Vilar, R., Li, R., Ferreira, M.G.S., Steen, W.M. and Watkins, K.G. (1995), "Laser alloying of aluminium alloys with chromium", *Surface and Coatings Technology*, Vol. 70 Nos 2/3, pp. 221-229.
- Autric, M., Perrais, J. and Barreau, G. (2000), "Corrosion resistance improvement of metals by excimer laser surface treatment", *Proceeding of SPIE*, Vol. 3888, pp. 742-749.
- Barnikel, J., Seefeld, T., Emmel, A., Schubert, E. and Bergmann, H.W. (1996), "Enhancing the corrosion resistance of metals by laser processing", *JOM*, Vol. 48 No. 5, pp. 29-32.
- Barnikel, J., Seefeld, T., Scutte, K. and Bergmann, H.W. (1997), "Erhöhung der korrosionsbeständigkeit von aluminiumlegierungen durch excimerlaserstrahlung", *HTM Haerterei Technische Mitteilungen*, Vol. 52 No. 2, pp. 94-96.
- Bonora, P.L., Bassoli, M., De Anna, P.L., Battaglin, G., Della Mea, G., Mazzoldi, P. and Miotello, A. (1980), "Electrochemical and corrosion behaviour of laser modified aluminium surfaces", *Electrochimica Acta*, Vol. 25 No. 11, pp. 1497-1499.
- Da Silva, M.D., Partes, K., Seefeld, T. and Vollertsen, F. (2012), "Comparison of coaxial and off-axis nozzle configurations in one step process laser cladding on aluminum substrate", in Elsevier, B.V. (Ed.), *Journal of Materials Processing Technology*, Vol. 212 No. 11, pp. 2514-2519.
- De Oliveira, U., Ocelik, V. and De Hosson, J.T.M. (2005), "Analysis of coaxial laser cladding processing conditions", *Surface and Coatings Technology*, Vol. 197 Nos 2/3, pp. 127-136.
- Ferreira, M.G.S., Li, R. and Vilar, R. (1996), "Avoiding crevice corrosion by laser surface treatment", *Corrosion Science*, Vol. 38 No. 12, pp. 2091-2094.
- García, I., de la Fuente, J., de Damborenea, J.J., Fuente, J., De and Damborenea, J.J.De. (2002), "(Ti,Al)/(Ti,Al)N coatings produced by laser surface alloying", *Materials Letters*, Vol. 53 Nos 1/2, pp. 44-51.
- Hagans, P.L. and Yates, R.L. (1989), "Environmental degradation of ion and laser beam treated surfaces", in Was, G.S. and Grabowski, K.S. (Eds), *Minerals Metals and Materials Society*, Warrendale, PA, p. 215.
- Hannour, F., Davenport, A.J., Williams, S.W., Morgan, P.C. and Figgures, C.C. (2001), "Corrosion behaviour of laser treated friction stir welds in high strength aluminium alloys", *Proceeding of the 3rd International Symposium of Friction Stir Welding*, Kobe.
- Li, R., Ferreira, M.G.S., Almeida, A., Vilar, R., Watkins, K.G., McMahon, M.A. and Steen, W.M. (1996), "Localized corrosion of laser surface melted 2024-T351 aluminium alloy", *Surface and Coatings Technology*, Vol. 81 Nos 2/3, pp. 290-296.
- McCafferty, E., Moore, P.G. and Peace, G.T. (1982), "Effect of laser-surface melting on the electrochemical behavior of an Al-1% Mn alloy", *Journal of The Electrochemical Society*, Vol. 129 No. 1, pp. 9-17.
- McMahon, M.A. (1994), PhD thesis, University of Liverpool.
- Mabhalli, L.A.B., Pityana, S.L. and Sacks, N. (2012), "Laser surface alloying of aluminium AA1200", *Molecular Crystals and Liquid Crystals*, Vol. 555 No. 1, pp. 138-148.
- Massalski, T.B., Murray, J.L., Bennet, L.H. and Baker, H. (1986), *Binary Phase Diagrams*, Vol. 1, 1st ed., ASM International, OH.
- Moore, P.G., McCafferty, E. and Weinman, L.S. (1977), *Report NRL Progress*, p. 9.
- Ocylok, S., Weisheit, A. and Kelbassa, I. (2011), "Increased wear and oxidation resistance of titanium aluminide alloys by laser cladding", *Advanced Materials Research*, Vol. 278, pp. 515-520.
- Padovani, C., Davenport, A.J., Connolly, B.J., Williams, S.W., Siggs, E., Groso, A. and Stampanoni, M. (2011), "Corrosion protection of AA7449-T7951 friction stir welds by laser surface melting with an excimer laser", *Corrosion Science*, Elsevier Ltd, Vol. 53 No. 12, pp. 3956-3969.
- Pawlowski, L. (1999), "Thick laser coatings: a review", *Journal of Thermal Spray Technology*, Vol. 8 No. 2, pp. 279-295.
- Pourbaix, M. (1974), *Atlas of Electrochemical Equilibria in Aqueous Solutions*, NACE, Houston, TX.
- Roine, A. (2002), "Software: HSC Chemistry 5.11", Outotec, Finland.
- Viejo, F., Coy, A.E., Garcia-Garcia, F.J., Liu, Z., Skeldon, P. and Thompson, G.E. (2010), "Relationship between microstructure and corrosion performance of AA2050-T8 aluminium alloy after excimer laser surface melting", *Corrosion Science*, Elsevier Ltd, Vol. 52 No. 6, pp. 2179-2187.
- Watkins, K.G., Ferreira, M.G.S., Vilar, R., Steen, W.M., McMahon, M.A. and Liu, Z. (1994), "Laser surface alloying of 2014 aluminum alloy for enhanced corrosion resistance alloys", *Proceeding of the International Congress on Applications of Lasers and Electro-optics (ICALEO)*, Laser Institute of America 79, Orlando, FL, pp. 135-144.

- Watkins, K., Liu, Z., McMahon, M., Vilar, R. and Ferreira, M.G. (1998), "Influence of the overlapped area on the corrosion behaviour of laser treated aluminium alloys", *Materials Science and Engineering: A*, Vol. 252 No. 2, pp. 292-300.
- Watkins, K., McMahon, M. and Steen, W. (1997), "Microstructure and corrosion properties of laser surface processed aluminium alloys: a review", *Materials Science and Engineering: A*, Vol. 231 Nos 1/2, pp. 55-61.
- Wendt, U., Settegast, S. and Grodrian, I.U. (2003), "Laser alloying of aluminum with titanium wire", *Journal of Materials Science Letters*, Vol. 22 No. 19, pp. 1319-1322.

- Xu, J., Liu, W., Kan, Y. and Zhong, M. (2006), "Microstructure and wear properties of laser cladding Ti-Al-Fe-B coatings on AA2024 aluminum alloy", *Materials & Design*, Vol. 27 No. 5, pp. 405-410.
- Yue, T.M., Huang, K.J. and Man, H.C. (2006), "In-situ laser cladding of Al<sub>2</sub>O<sub>3</sub> reaction coating on aluminium alloy 7075 for corrosion resistance improvement", *Materials Transactions*, Vol. 47 No. 3, pp. 948-951.

### **Corresponding author**

**Rajan Ambat** can be contacted at: ram@mek.dtu.dk





---

## 7 Overall discussion

---

This section provides overall discussions supplementing the work presented in the appended papers. It is divided into three parts focusing on the appearance of anodised aluminium (articles 1 and 2), microstructure of the produced aluminium-titanium coatings (articles 2-4), and alkaline corrosion properties of aluminium-titanium coatings (articles 3 and 4).

### 7.1 Appearance of anodised aluminium

The increasing use of recycled aluminium alloys requires comprehensive knowledge on how various alloying elements, microstructure, and surface treatments affect the appearance of anodised aluminium. The work presented was conducted in order to understand the optical appearance of anodised commercial aluminium alloys (article 1) and sputtered coatings (article 2). This has given new insights especially on how the appearance of anodised aluminium is affected by the oxide-substrate interface, which is again determined by the alloy composition and surface treatment processes. This finding was supplemented by the suggested light trapping mechanism described in article 2 (Fig. 6).

Studies in article 1 investigated the appearance of commercial alloys as a function of alloy composition and pre-treatments such as etching, polishing, anodisation, and hot water sealing. After removal of the oxide layer, it was possible to investigate the oxide-substrate interface. There was found clear correlation between the oxide-substrate interface roughness and the visual appearance of the specimen. For etched specimens with a higher degree of alloying, the roughness increased and therefore the specular reflection decreased. The total reflectance after anodisation of etched specimens seemed to depend on alloy purity. The appearance after anodisation of the polished specimens was affected by intermetallic particles and pits in the oxide-substrate interface, which was created due to impurities and alloying elements. Furthermore, it was found that the total reflectance of the polished specimens was more or less the same before and after anodisation, whereas the total reflectance of the etched specimens decreased after anodisation.

In article 2 the visual appearance of sputtered coatings of aluminium-titanium were investigated as a function of titanium concentration, heat treatment, and anodisation. After heat treatment and anodisation partly oxidised particles were found in the oxide layer. These partly oxidised particles are expected to have a significant effect on the appearance after anodisation of high gloss specimens. In article 2 an anodised layer of 1.2  $\mu\text{m}$  containing partially oxidised  $\text{Al}_3\text{Ti}$  particles caused the specimen to turn black. Additionally, the interface between the anodised layer and the substrate was very rough. This caused the reflection of light to move inclined towards the specimen surface and light trapping was expected to happen.

As presented in Fig. 2.13 on page 26, it is known that pure aluminium has a total reflectivity of more than 90 %. Thus, for commercial aluminium alloys, the substrate is expected to absorb at least 10 % - 15 % of the incoming light due to alloying elements, surface structures, and defects. Additionally, it was found in article 1 that the polished specimens had a higher total reflectance than the etched specimens after anodisation. Since the investigations after polishing and etching of the same alloys gave different reflectance

measurements, the increased absorption has to be caused by surface structures created during the etching process. As stated in article 2 both surface roughness and partially oxidised alloying elements can have big influence on the optical appearance. However, the amount of partially oxidised particles is expected to be approximately the same for etched and polished specimens of the same alloy. This indicates that light trapping caused by surface structures like grain boundary grooves and surface scallops are significant reasons for the decreased total reflectance after etching and anodisation in article 1.

The suggested mechanism is that light enters the oxide layer and is partly absorbed and scattered by oxidised, partly oxidised, and unaffected alloying element phases (see Table 2.4 on page 16). A part of the light will go through the oxide layer and will be reflected in the substrate surface containing e.g. grain boundary grooves and surface scallops causing the reflected light to move inclined back towards to oxide surface. So even if the grain boundary grooves and the surface scallops do not absorb additional light compared to a pure aluminium substrate, the inclined reflection has a significant effect on the total reflectance due to the light trapping mechanism. The inclined light (of a certain inclination and flatter) will experience at least one internal reflection, however, more is possible. For each total internal reflection (which is loss-less) the light will be reflected at the substrate interface once more with a loss of at least about 10 % for each reflection.

The use of titanium dioxide as scattering particles in anodised aluminium products can neither be approved nor denied based on the data presented in article 2. Thus, anodisation of coatings or specimens containing aluminium and metallic titanium require additional focus on the anodisation process in order to ensure appropriate oxidation of the embodied titanium-containing phases. These phases should be fully instead of partly oxidised as found in article 2, Fig. 2. Other possibilities should be considered e.g. the incorporation of titanium dioxide particles into metallic aluminium or already anodised aluminium surfaces. Again this would require focus on the anodisation process in order to ensure proper oxidation all around the titanium dioxide particles, avoiding volumes of metallic aluminium absorbing and scattering the light [55,56].

## **7.2 Microstructure of the produced aluminium-titanium coatings**

The use of aluminium based alloys and coatings are highly interesting due to the use of aluminium for many commercial products with high requirements for both appearance and corrosion properties. Additionally, the coatings are also interesting when combining e.g. cast aluminium or polymer substrates with coatings. The microstructure of sputtered aluminium-titanium coatings was presented in articles 2 and 3, while the microstructure of LSC coatings was presented in article 4.

Aluminium based coatings containing up to 18 wt. % titanium were produced by magnetron sputtering. The as-sputtered coatings had alternating layers of high and low titanium concentrations. From the XRD-measurements (article 2, Fig. 3 and article 3, Fig. 1) it was found that the as-deposited layers only had the  $\alpha$ -Al phase, which supported the existing literature [107,110]. During heat treatment, the microstructure aged into an inhomogeneous structure of an  $\alpha$ -Al phase and  $\text{Al}_3\text{Ti}$  precipitates with sizes up to 1  $\mu\text{m}$  in diameter.

In the LSC process the self-quenching mechanism can cause amorphous and nano-crystalline microstructures. However, as presented in article 4 the microstructure of the aluminium-titanium coatings produced by LSC produced a cast structure with an  $\alpha$ -Al matrix containing  $\text{Al}_3\text{Ti}$  phases (article 4, Fig.1 and 2). The  $\text{Al}_3\text{Ti}$  phases were of sizes of 3  $\mu\text{m}$  for the 5 wt. % Ti6Al4V specimens and were found to be larger for the specimens of higher Ti6Al4V-concentrations.

It was found that the microstructures of the created aluminium-titanium coatings were highly different when comparing the sputtered and LSC specimens. Where the sputtered coatings precipitated during heat treatment from a basis of a nano-crystalline structure, the LSC coatings had a much coarser cast structure. For the aluminium-titanium system this was quite an important difference causing the corrosion properties (and probably also the optical properties) to be highly different in the two cases as described in section 7.3 below. Since the microstructure of the LSC specimens was rougher than expected, supplementary coatings were created using different parameters. However, due to time pressure, these were not investigated further. It might be possible to achieve a finer structure e.g. by causing a pulsed laser causing a higher quenching rate and thereby creating a finer microstructure. Additionally, a pulsed laser might reduce the heating of the specimen avoiding the specimen to warp as described in section 3.4.2 on page 43.

### **7.3 Alkaline corrosion properties of aluminium-titanium coatings**

Nickel salt sealing is still used in the automotive industry in order to gain alkaline corrosion protection in NaOH solutions used e.g. in a brushless carwash. However, due to environmental and health issues, one or more alternatives are needed. The analysis of the alkaline corrosion resistance of aluminium-titanium coatings were analysed in articles 3 and 4. It was found that magnetron sputtered coatings might be applicable for alkaline corrosion protection, whereas the LSC specimens corroded heavily.

Specimens coated by sputtering (article 3) showed quite good corrosion properties in saline solution in the as-deposited state where the pitting potential increased with the titanium concentration (article 3, Fig. 4). Additionally, the specimens were heat-treated and tested in rough alkaline conditions giving the best results with specimens containing 13 wt. % titanium and more. Heat treatment caused structural relaxation of the sputtered coatings, causing the corrosion properties of all coatings to improve by heat treatment at 300 °C. For specimens containing 13 wt. % titanium heat treated for 2 h at 500 °C, the corrosion properties were found to improve significantly both for alkaline exposure tests and anodic polarisation tests, both at pH 13.5. The improvement was scribed to structural relaxation, decrease in potential differences in the microstructure, and the protection of the aluminium matrix from the network of  $\text{Al}_3\text{Ti}$  particles.

Article 4 presents the investigations of the alkaline corrosion properties of aluminium-Ti6Al4V coatings created by LSC. It was found that the structure was very coarse and that this caused the  $\alpha$ -Al matrix to corrode preferentially in alkaline exposure test at pH 13.5 while the  $\text{Al}_3\text{Ti}$  phases were anodically protected (article 4, Figs. 7 – 9). Thus, the used parameters did not provide sufficient cooling rate to achieve a uniform distribution of supersaturated titanium in  $\alpha$ -Al is hoped, instead  $\text{Al}_3\text{Ti}$  phases precipitated.

As stated in section 7.2, the structure of the sputtered coatings was much more promising than the coatings produced by the LSC process. However, the sputtering process is quite expensive for larger specimens and therefore it will not always be a beneficial process. The results in article 3 indicate that a threshold between 8 wt. % and 13 wt. % titanium could be sufficient to achieve satisfactory corrosion resistance. This could be used for developing new methods using other coating techniques or wet chemistry where titanium can be implemented e.g. during anodisation and/or sealing.

Based on these observations the following requirements are proposed for aluminium-titanium specimens and coatings to create corrosion resistant coatings in rough NaOH-based alkaline conditions at pH 13.5:

- The aluminium-titanium specimen or coating should have a titanium-concentration of at least 8 wt. %.
- The process has to enable creation or growth of e.g.  $\text{Al}_3\text{Ti}$  phases with sizes of maximum 1  $\mu\text{m}$  – 3  $\mu\text{m}$  (the optimal size might be smaller than 1  $\mu\text{m}$ ).
- Stresses in the specimen/coating should be avoided (e.g. by stress relaxation during heat treatment).
- Coatings require full coverage with no holes and good adhesion to the substrate.

The use of titanium as a protective element in aluminium specimens and coatings has shown to have quite good perspectives in both saline and rough alkaline conditions. For alkaline corrosion protection at pH 13.5 it was found that the corrosion properties are significantly changed by titanium concentration and by changes in the microstructure. Therefore, more work could develop into an industrial production line creating a satisfactory protecting coating.







---

## 8 Conclusions

---

### 8.1 Appearance of commercial alloys

The appearance of commercial alloys AA1050, Peraluman 706 (P706), AA5754, and AA6082 were investigated with focus on the effect of etching, polishing, anodisation, and sealing. It was found that:

- The roughness and percentage of diffuse reflectance caused by etching increased with the degree of alloying. For pure and soft alloys, the polishing was hard and resulted in a rougher surface compared to specimens with a higher amount of alloying elements.
- As-etched specimens show a broad intensity distribution function of the scattered light at and near the specular region, whereas the as-polished specimen exhibit high reflectance near the specular angle.
- A clear correlation was found between the topography of the original surface and the topography of the oxide–substrate interface beneath the anodised layer after anodising.
- Polished specimens alloyed to a higher degree lost their high gloss appearance after anodisation due to particles and pits in the oxide–substrate interface and heterogeneities in the oxide due to alloying elements.

### 8.2 Microstructure of magnetron sputtered aluminium-titanium coatings

Magnetron sputtered coatings containing up to 18 wt. % titanium were investigated in the as-deposited form and after heat-treatment before and after anodisation. It was found that:

- A structure of alternating layers containing low and high amounts of titanium was found, with  $\alpha$ -Al as the only identified phase in the as-deposited coatings with inhomogeneous distribution of titanium.
- After heat treatment for 4 h at 600 °C, a homogenous aluminium matrix and high concentrations of elongated  $\text{Al}_3\text{Ti}$  precipitates appeared.
- Anodisation of the heat-treated specimens created an oxide film of approx. 1.2  $\mu\text{m}$  containing many partially oxidised  $\text{Al}_3\text{Ti}$  particles with a metallic core. In some cases, unoxidised aluminium was found behind the particles.

Laser surface clad coatings containing up to 20 wt. % Ti6Al4V were investigated in the as-deposited form and after heat-treatment. It was found that:

- Coatings of aluminum and 5 wt.% to 20 wt.% Ti6Al4V powders resulted in a microstructure containing  $\alpha$ -Al,  $\text{Al}_3\text{Ti}$  intermetallic equiaxed or elongated dendrites and undissolved Ti6Al4V particles.
- Heat treatment made the intermetallic  $\text{Al}_3\text{Ti}$  phases exhibit more spherical shapes in the specimens containing 5 wt.% and 10 wt.% Ti6Al4V. For specimens containing 20 wt.% Ti6Al4V, heat treatment caused thickening of the elongated dendrites.

### 8.3 Optical properties of magnetron sputtered aluminium-titanium coatings

- The reflectance decreases with increasing titanium concentration for the as-deposited specimens, for the specimens heat-treated for 2 h at 300 °C, and for the as-deposited and anodised specimens.
- Coatings containing 6 wt.%–16 wt.% titanium that were heat-treated for 4 h at 500 °C and 600 °C all turned dark grey, brown or black during anodisation.

### 8.4 Corrosion properties of aluminium-titanium coatings

Magnetron sputtered coatings:

- Surface potential measurements showed heterogeneity in surface potential for the as-deposited coating due to the inhomogeneous distribution of titanium. Heat treatment for 4 h at 600 °C homogenized the surface potential distribution due to the precipitation of  $\text{Al}_3\text{Ti}$  reducing the galvanic potential with the matrix.
- Anodic polarization tests of as-deposited films in a neutral salt solution showed an increase in pitting potential with increase in titanium content.
- Corrosion tests at pH 13.5 showed that the anodic current increased with increase in titanium concentration from 3 wt. % - 8 wt. % titanium, but decreased significantly above this concentration. Heat-treatment for 2 h at 500 °C of a coating with 13 wt. % titanium showed an anodic current reduction of 95 % compared to as-deposited AA1050 coating.

Laser surface clad coatings

- Exposure tests in a pH 13.5 solution showed heavy preferential dissolution of the  $\alpha$ -Al matrix, while phases of higher titanium concentrations were protected.
- Anodic polarization tests at pH 13.5 showed no change of the  $E_{\text{corr}}$  value, while slight decrease in the overall current density was observed with increased titanium concentration and heat treatment.
- Both percentage and distribution of titanium have big influence on the corrosion properties, where the magnetron sputtering process seems more appropriate than laser surface cladding, at least with the tested process parameters.





---

## 9 Outlook

---

The presented work could initiate new studies such as:

### 9.1 Appearance of anodised aluminium alloys

- A more detailed investigation of the structure of intermetallics incorporated in the oxide film and their effect on the appearance of the anodised layer. This could be with focus on the size and composition of phases based on alloying elements and impurities. These phases should be investigated after anodisation regarding partial and full oxidation and the interaction with the incoming light.
- The effect of changing anodisation parameters to change the level of oxidation of the aluminium matrix and intermetallic particles. This work is quite extensive regarding both size and composition as stated above.
- The suggested reason for the darkening of the specimens should be investigated further. This could be done by a series of experiments where separate oxide removal and substrate removal experiments are performed. Thereby, the optical properties of the anodised layer and the substrate can be investigated separately. The deoxidised specimen can be immersed into a liquid of the same refractive index as the anodised layer, in order to test the idea of light trapping without the partially oxidised particles. In this way the impact of both the partially oxidised particles and the light trapping mechanism can be explored further.
- The incorporation of various types of intermetallics and oxide particles (such as  $\text{TiO}_2$ ,  $\text{ZrO}_2$ , and  $\text{CeO}_2$ ) into metallic and subsequently anodised or post-anodised specimens should be investigated. This could be used for obtaining various appearances by modifying the structure of these particles in the anodised layer, which will influence the optical scattering effects.
- Magnetron sputtering can be used to create alternating layers of  $\text{Al}_2\text{O}_3$  and  $\text{TiO}_2$  to create strong colours with a protective layer on top for high-end design products. However, such a stack of layers is vulnerable to wear and an anodised aluminium layer on top of such a stack will be both protecting and transparent without affecting the colour of the stack. Initial tests have been made covering the stack with a thick metallic layer which was subsequently anodised. These specimens turned grey and dull after anodisation, however by calibration of the process parameters in both the sputtering and the anodisation process might make it work.

## 9.2 Alkaline corrosion properties of aluminium based coatings

- Optimisation of the current magnetron sputtering process is necessary in order to find the titanium concentration and heat treatment and thereby microstructure to achieve satisfactory corrosion protection. The magnetron sputtering process is not relevant for e.g. the body of a car, due to the size limitations and cost of the sputtering process. However, for smaller consumer products and industrial products this process might be interesting. This could e.g. be for hood ornaments of high-end cars and other products of small sizes, which are exposed to rough environments.
- The presented laser surface cladding coatings were much too coarse and unsatisfactory with regards to corrosion properties. However it is expected to be possible to tweak the cladding parameters in order to create finer microstructures by laser surface cladding. This could e.g. be by using a pulsed laser process.
- Other coating processes should be considered. The following requirements are proposed for aluminium-titanium specimens and coatings to create corrosion resistant coatings in rough NaOH-based alkaline conditions at pH 13.5:
  - The aluminium-titanium specimen or coating should have a titanium-concentration of at least 8 wt. %.
  - The process has to enable creation or growth of e.g.  $\text{Al}_3\text{Ti}$  phases with sizes of maximum  $1\text{ }\mu\text{m}$  –  $3\text{ }\mu\text{m}$  (the optimal size might be smaller than  $1\text{ }\mu\text{m}$ ).
  - Stresses in the specimen/coating should be avoided (e.g. by stress relaxation during heat treatment).
  - Coatings require full coverage with no holes and good adhesion to the substrate.
- Sealing processes using titanium and zirconium acetates and fluorides have been tested without satisfactory results at pH 13.5; however, results were well at pH 12.5 and might therefore be used for replacing nickel salt sealing in some cases. Further studies and optimisation of these sealing processes are required.
- A cheap wet process is still needed to achieve satisfactory alkaline protection in the automotive industry. This project can therefore be used to set up some requirements for the results of such a process.







---

## 10 References

---

- [1] C. Vargel, Corrosion of aluminium, Elsevier Science, Oxford, UK, 2004.
- [2] R. Sherefkin, Surging steel prices galvanize auto industry, *Financ. Week.* (2008).
- [3] S. Keeler, Report: Advanced High Strength Steel (AHSS) Application Guidelines v. 4.1, Brussels, Belgium, 2009.
- [4] T.N. Lomholt, PhD Thesis: Microstructure Evolution during Friction Stir Spot Welding of TRIP steel, Technical University of Denmark, 2011.
- [5] European Aluminium Association, Report: Aluminium in cars - Unlocking the light-weighting potential, Brussels, Belgium, 2012.
- [6] J. Cui, H.J. Roven, Recycling of automotive aluminum, *Trans. Nonferrous Met. Soc. China.* 20 (2010) 2057–2063. doi:10.1016/S1003-6326(09)60417-9.
- [7] E. Romhanji, M. Popović, D. Glišić, M. Stefanović, M. Milovanović, On the Al-Mg alloy sheets for automotive application: Problems and solutions, *MJom.* 10 (2004) 205–216.
- [8] Dupont, Report: DuPont<sup>TM</sup> Ti-Pure titanium dioxide, USA, 2007.
- [9] A. Junker-Holst, D. V Nielsen, Bachelor thesis: Effect of microstructure of plasma sputtered coatings on optical appearance, Technical University of Denmark, 2012.
- [10] A. Roine, Software: HSC Chemistry 5.11, Outotec, Finland, (2002).
- [11] P. Møller, L.P. Nielsen, Advanced surface technology, vol. 1, 5th ed., Møller & Nielsen, Denmark, 2012.
- [12] R. Akeret, H. Bichsel, E. Schwall, E. Simon, M. Textor, The influence of chemical composition and fabrication procedures on the properties of anodised aluminium surfaces, *Trans. Inst. Met. Finish.* 68 (1990) 20–28.
- [13] J. Timm, Influence of Fe and Si containing phases on the anodisation behaviour, *Key Eng. Mater.* 44-45 (1990) 219–232. doi:10.4028/www.scientific.net/KEM.44-45.219.
- [14] J. Buha, R.N. Lumley, a. G. Crosky, Secondary ageing in an aluminium alloy 7050, *Mater. Sci. Eng. A.* 492 (2008) 1–10. doi:10.1016/j.msea.2008.02.039.
- [15] S.K. Das, W. Yin, The worldwide aluminum economy: The current state of the industry, *Jom.* 59 (2007) 57–63. doi:10.1007/s11837-007-0142-0.
- [16] T. Hauge, K.F. Karhausen, Extrusion parameters influencing the anodising quality, *Alum. Extrus.* (1998) 32–37.
- [17] H. Zhu, X. Zhang, M.J. Couper, A.K. Dahle, The formation of streak defects on anodized aluminum extrusions, *JOM.* 62 (2010) 46–51.

- 
- [18] S. Wernick, R. Pinner, P.G. Sheasby, *The surface treatment and finishing of aluminum and its alloys*, 5th ed., Finishing Publications Ltd & ASM International, Teddington, UK, 1987.
- [19] G. Beilby, *Aggregation and flow of solids*, Macmillan, London, 1921.
- [20] G.M. Scamans, M.F. Frolish, W.M. Rainforth, Z. Zhou, Y. Liu, X. Zhou, et al., The ubiquitous Beilby layer on aluminium surfaces, *Surf. Interface Anal.* 42 (2010) 175–179. doi:10.1002/sia.3204.
- [21] G. Buytaert, B. Kernig, H. Brinkman, H. Terryn, Influence of surface pre-treatments on disturbed rolled-in subsurface layers of aluminium alloys, *Surf. Coat. Technol.* 201 (2006) 2587–2598. doi:10.1016/j.surfcoat.2006.05.004.
- [22] G. Buytaert, H. Terryn, S. Van Gils, B. Kernig, B. Grzemba, M. Mertens, Study of the near-surface of hot- and cold-rolled AlMg0.5 aluminium alloy, *Surf. Interface Anal.* 37 (2005) 534–543. doi:10.1002/sia.2046.
- [23] G. Buytaert, H. Terryn, S. Van Gils, B. Kernig, B. Grzemba, M. Mertens, Investigation of the (sub)surface of commercially pure rolled aluminium alloys by means of total reflectance , r.f. GDOES , SEM/EDX and FIB/TEM analysis, *Surf. Interface Anal.* 38 (2006) 272–276. doi:10.1002/sia.
- [24] S. Van Gils, T. Dimogerontakis, G. Buytaert, E. Stijns, H. Terryn, P. Skeldon, et al., Optical properties of magnetron-sputtered and rolled aluminum, *J. Appl. Phys.* 98 (2005) 083505–1 – 9. doi:10.1063/1.2085315.
- [25] H. Zhu, M.J. Couper, A.K. Dahle, Effect of process variables on the formation of streak defects on anodized aluminum extrusions: An overview, *High Temp. Mater. Process.* 31 (2012) 105–111. doi:10.1515/htmp-2012-0024.
- [26] H. Zhu, X. Zhang, M.J. Couper, A.K. Dahle, Effect of initial microstructure on surface appearance of anodized aluminum extrusions, *Metall. Mater. Trans. A.* 40 (2009) 3264–3275. doi:10.1007/s11661-009-9976-0.
- [27] N. Tabrizian-Ghalehno, PhD thesis: Advanced anodizing technology, Technical University of Denmark, 2011.
- [28] G.E. Thompson, R.C. Furneaux, G.C. Wood, J.A. Richardson, J.S. Goode, Nucleation and growth of porous anodic films on aluminium, *Nature.* 272 (1978) 433–435.
- [29] G.C. Wood, J.P. O’Sullivan, B. Vaszko, The Direct Observation of Barrier Layers in Porous Anodic Oxide Films, *J. Electrochem. Soc.* 115 (1968) 618–620.
- [30] G.E. Thompson, R.C. Furneaux, G.C. Wood, Electron microscopy of ion beam thinned porous anodic films formed on aluminium, *Corros. Sci.* 18 (1978) 481–498.
- [31] J.D. Edwards, F. Keller, The structure of anodic oxide coatings, *Trans. Am. Inst. Min. Metall. Eng.* 156 (1944) 288–299.
- [32] S.J. Feliu, M.J. Bartolomé, J.A. González, S. Feliu, XPS characterization of porous and sealed anodic films on aluminum alloys, *J. Electrochem. Soc.* 154 (2007) C241–C248. doi:10.1149/1.2712148.

- 
- [33] K. Shimizu, G.M. Brown, K. Kobayashi, P. Skeldon, G.E. Thompson, G.C. Wood, Ultramicrotomy-a route towards the enhanced understanding of the corrosion and filming behaviour of aluminium and its alloys, *Corros. Sci.* 40 (1998) 1049–1072.
- [34] Skanaluminium, Aluminium: Overfladebehandling, Universitetsforlaget AS, Oslo, Norway, 1972.
- [35] H. Kuo, Y. Wang, L. Iglesia-Rubianes, H.-Y. Lee, S.F. Kia, Interference-Colored Finishes for Automotive Aluminum Alloys, *Plat. Surf. Finish.* (2004).
- [36] Aluminium Anodizers Council, Interference Coloring, Accessed Dec. 6. (2013) [anodizing.org/Publications/interfer.html](http://anodizing.org/Publications/interfer.html).
- [37] L. Chesterfield, Products Finishing: Interference Coloring, Accessed Dec. 6. (2013) [pfonline.com/articles/interference-coloring](http://pfonline.com/articles/interference-coloring).
- [38] L. Hao, B.R. Cheng, Sealing Processes of Anodic Coatings-Past, Present, and Future, *Met. Finish.* 98 (2000) 8–18. doi:10.1016/S0026-0576(01)80002-7.
- [39] A. Bautista, J.A. González, V. Lopez, Influence of triethanolamine additions on the sealing mechanism of anodised aluminium, *Surf. Coat. Technol.* 154 (2002) 49–54.
- [40] The Global Aluminium Recycling Committee (GARC), Report: Global Aluminium Recycling : A Cornerstone of Sustainable Development, London, UK, 2009.
- [41] M.E. Schlesinger, Aluminum Recycling, CRC Press, Missouri, USA, 2006.
- [42] M.A. Dewan, M.A. Rhamdhani, J.B. Mitchell, C.J. Davidson, G.A. Brooks, M. Easton, et al., Control and Removal of Impurities from Al Melts: A Review, *Mater. Sci. Forum.* 693 (2011) 149–160. doi:10.4028/www.scientific.net/MSF.693.149.
- [43] Y. Chino, M. Mabuchi, S. Otsuka, K. Shimojima, H. Hosokawa, Y. Yamada, et al., Corrosion and Mechanical Properties of Recycled 5083 Aluminum Alloy by Solid State Recycling, *Mater. Trans.* 44 (2003) 1284–1289. doi:10.2320/matertrans.44.1284.
- [44] M. Scharun, C. Fricke-Begemann, R. Noll, Laser-induced breakdown spectroscopy with multi-kHz fibre laser for mobile metal analysis tasks — A comparison of different analysis methods and with a mobile spark-discharge optical emission spectroscopy apparatus, *Spectrochim. Acta Part B At. Spectrosc.* 87 (2013) 198–207. doi:10.1016/j.sab.2013.05.007.
- [45] P. Werheit, C. Fricke-Begemann, M. Gesing, R. Noll, Fast single piece identification with a 3D scanning LIBS for aluminium cast and wrought alloys recycling, *J. Anal. At. Spectrom.* 26 (2011) 2166. doi:10.1039/c1ja10096c.
- [46] E. Hecht, *Optics* (4th Edition), Addison-Wesley, San Francisco, USA, 2001.
- [47] R.J.D. Tilley, *Colour and The Optical Properties of Materials: An Exploration of the Relationship Between Light, the Optical Properties of Materials and Colour*, John Wiley & Sons, West Sussex, UK, 2011.
- [48] J.E.R. Frisvad, *Light , Matter , and Geometry The Cornerstones of Appearance Modelling*, Technical University of Denmark, 2008.

- 
- [49] B.T. Phong, Illumination for computer generated pictures, *Commun. ACM.* 18 (1975) 311–317. doi:10.1145/360825.360839.
- [50] X.D. He, K.E. Torrance, F.X. Sillion, D.P. Greenberg, A comprehensive physical model for light reflection, *ACM SIGGRAPH Comput. Graph.* 25 (1991) 175–186. doi:10.1145/127719.122738.
- [51] R. C. Weast, *Handbook of Chemistry and Physics*, 67th Edition, CRC Press, San Diego, USA, 1986.
- [52] A.C. Nyce, L.P. Skolnick, Optical constants of bulk and thin-film aluminum at 6328 Å, *J. Opt. Soc. Am.* 65 (1975) 792. doi:10.1364/JOSA.65.000792.
- [53] E.D. Palik (editor), *Handbook of Optical Constants of Solids*, Academic Press, Boston, USA, 1991.
- [54] T.-S. Shih, P.-S. Wei, Y.-S. Huang, Optical properties of anodic aluminum oxide films on Al1050 alloys, *Surf. Coat. Technol.* 202 (2008) 3298–3305. doi:10.1016/j.surfcoat.2007.12.002.
- [55] M. Saito, S. Yasunori, M. Miyagi, K. Wada, O. Sachiko, Optical transmittance of anodically oxidized aluminum alloy, *J. Appl. Phys.* 34 (1995) 3134–3138.
- [56] M. Saito, Y. Shiga, M. Miyagi, Unoxidized aluminum particles in anodic alumina films, *J. Electrochem. Soc.* 140 (1993) 1907–1911.
- [57] N. Tabrizian, H.N. Hansen, P.E. Hansen, R. Ambat, P. Møller, Influence of annealing and deformation on optical properties of ultra precision diamond turned and anodized 6060 aluminium alloy, *Surf. Coat. Technol.* 204 (2010) 2632–2638. doi:10.1016/j.surfcoat.2010.02.002.
- [58] Premendra, J.H. Chen, F.D. Tichelaar, H. Terryn, J.H.W. DeWit, L. Katgerman, Optical and transmission electron microscopical study of the evolution of surface layer on recycled aluminium along the rolling mills, *Surf. Coat. Technol.* 201 (2007) 4561–4570. doi:10.1016/j.surfcoat.2006.09.090.
- [59] H. Zhu, X. Zhang, M. Couper, A.K. Dahle, Effect of primary intermetallic particles on surface microstructure and appearance of aluminium extrusions, *Mater. Chem. Phys.* 113 (2009) 401–406. doi:10.1016/j.matchemphys.2008.07.109.
- [60] T. Minoda, H. Yoshida, Effect of grain boundary characteristics on intergranular corrosion resistance of 6061 aluminum alloy extrusion, *Metall. Mater. Trans. A.* 33A (2002) 2891–2898.
- [61] L.E. Fratila-Apachitei, H. Terryn, P. Skeldon, G.E. Thompson, J. Duszczyk, L. Katgerman, Influence of substrate microstructure on the growth of anodic oxide layers, *Electrochim. Acta.* 49 (2004) 1127–1140. doi:10.1016/j.electacta.2003.10.024.
- [62] Y. Ma, X. Zhou, G.E. Thompson, J.-O. Nilsson, M. Gustavsson, A. Crispin, Origin of streaks on anodised aluminium alloy extrusions, *Trans. Inst. Met. Finish.* 91 (2013) 11–16. doi:10.1179/0020296712Z.00000000075.



- 
- [63] K.F. Karhausen, A.L. Dons, T. Aukrust, Microstructure control during extrusion with respect to surface quality, *Mater. Sci. Forum.* 217-222 (1996) 403–408. doi:10.4028/www.scientific.net/MSF.217-222.403.
- [64] H. Zhu, T. Wei, M.J. Couper, A.K. Dahle, Effect of extrusion profile on surface microstructure and appearance of aluminum extrusions with different Fe contents, *JOM.* 65 (2013) 618–624. doi:10.1007/s11837-013-0581-8.
- [65] L.-F. Huang, M. Saito, M. Miyagi, Polarization characteristics of alumina films anodized at low temperature, *Jpn. J. Appl. Phys.* 32 (1993) 3169–3174.
- [66] S. Van Gils, P. Mast, E. Stijns, H. Terryn, Colour properties of barrier anodic oxide films on aluminium and titanium studied with total reflectance and spectroscopic ellipsometry, *Surf. Coat. Technol.* 185 (2004) 303–310. doi:10.1016/j.surfcoat.2004.01.021.
- [67] Y. Liu, Y. Chang, Z. Ling, X. Hu, Y. Li, Structural coloring of aluminum, *Electrochem. Commun.* 13 (2011) 1336–1339. doi:10.1016/j.elecom.2011.08.008.
- [68] Q. Xu, Y. Yang, J. Gu, Z. Li, H. Sun, Influence of Al substrate on the optical properties of porous anodic alumina films, *Mater. Lett.* 74 (2012) 137–139. doi:10.1016/j.matlet.2012.01.076.
- [69] X. Hu, Y.J. Pu, Z.Y. Ling, Y. Li, Coloring of aluminum using photonic crystals of porous alumina with electrodeposited Ag, *Opt. Mater. (Amst).* 32 (2009) 382–386. doi:10.1016/j.optmat.2009.09.009.
- [70] H.M. Chen, C.F. Hsin, R.-S. Liu, S.-F. Hu, C.-Y. Huang, Controlling Optical Properties of Aluminum Oxide Using Electrochemical Deposition, *J. Electrochem. Soc.* 154 (2007) K11. doi:10.1149/1.2728147.
- [71] X. Wang, H. Zhang, D. Zhang, Y. Ma, H.-J. Fecht, J.Z. Jiang, Color tuning by local sputtering metal nanolayer on microstructured porous alumina, *Microsc. Res. Tech.* 75 (2011) 698–701. doi:10.1002/jemt.21114.
- [72] X. Wang, D. Zhang, H. Zhang, Y. Ma, J.Z. Jiang, Tuning color by pore depth of metal-coated porous alumina., *Nanotechnology.* 22 (2011) 305306. doi:10.1088/0957-4484/22/30/305306.
- [73] M. Pourbaix, *Atlas of electrochemical equilibria in aqueous solutions*, NACE, Houston, USA, 1974.
- [74] F. Eckermann, T. Suter, P.J. Uggowitzer, A. Afseth, M. Stampanoni, F. Marone, et al., In Situ Microtomographically Monitored and Electrochemically Controlled Corrosion Initiation and Propagation in AlMgSi Alloy AA6016, *J. Electrochem. Soc.* 156 (2009) C1–C7. doi:10.1149/1.2996269.
- [75] A. Afseth, J.H. Nordlien, G.M. Scamans, K. Nisancioglu, Filiform corrosion of binary aluminium model alloys, *Corros. Sci.* 44 (2002) 2529–2542. doi:10.1016/S0010-938X(02)00029-X.
- [76] R.W. Revie, *Uhlig's Corrosion Handbook*, John Wiley & Sons, Ottawa, Canada, 2000.

- 
- [77] G.E. Thompson, H. Habazaki, K. Shimizu, M. Sakairi, P. Skeldon, X. Zhou, et al., Anodizing of aluminium alloys, *Aircr. Eng. Aerosp. Technol.* 71 (1999) 228–238.
- [78] R. Ambat, A.J. Davenport, A. Afseth, G. Scamans, Electrochemical Behavior of the Active Surface Layer on Rolled Aluminum Alloy Sheet, *J. Electrochem. Soc.* 151 (2004) B53. doi:10.1149/1.1635828.
- [79] R.L. Twite, G.P. Bierwagen, Review of alternatives to chromate for corrosion protection of aluminum aerospace alloys, *Prog. Org. Coatings*. 33 (1998) 91–100. doi:10.1016/S0300-9440(98)00015-0.
- [80] S.M. Cohen, Review: Replacements for Chromium Pretreatments on Aluminum, *Corrosion*. 51 (1995) 71–78. doi:10.5006/1.3293580.
- [81] R. Akid, M. Gobara, H. Wang, Corrosion protection performance of novel hybrid polyaniline/sol–gel coatings on an aluminium 2024 alloy in neutral, alkaline and acidic solutions, *Electrochim. Acta*. 56 (2011) 2483–2492. doi:10.1016/j.electacta.2010.12.032.
- [82] M.R. Kalantary, D.R. Gabe, D.H. Ross, A model for the mechanism of nickel fluoride cold sealing of anodized aluminium, *J. Appl. Electrochem.* 22 (1992) 268–276.
- [83] V. López, M.J. Bartolomé, E. Escudero, E. Otero, J.A. González, Comparison by SEM, TEM, and EIS of Hydrothermally Sealed and Cold Sealed Aluminum Anodic Oxides, *J. Electrochem. Soc.* 153 (2006) B75. doi:10.1149/1.2163811.
- [84] M.L. Zheludkevich, I.M. Salvado, M.G.S. Ferreira, Sol–gel coatings for corrosion protection of metals, *J. Mater. Chem.* 15 (2005) 5099. doi:10.1039/b419153f.
- [85] D. Wang, G.P. Bierwagen, Sol–gel coatings on metals for corrosion protection, *Prog. Org. Coatings*. 64 (2009) 327–338. doi:10.1016/j.porgcoat.2008.08.010.
- [86] M. Sheffer, A. Groysman, D. Mandler, Electrodeposition of sol–gel films on Al for corrosion protection, *Corros. Sci.* 45 (2003) 2893–2904. doi:10.1016/S0010-938X(03)00106-9.
- [87] P.C.R. Varma, J. Colreavy, J. Cassidy, M. Oubaha, C. McDonagh, B. Duffy, Corrosion protection of AA 2024-T3 aluminium alloys using 3, 4-diaminobenzoic acid chelated zirconium–silane hybrid sol–gels, *Thin Solid Films*. 518 (2010) 5753–5761. doi:10.1016/j.tsf.2010.05.088.
- [88] N.N. Voevodin, N.T. Grebasch, W.S. Soto, L.S. Kasten, J.T. Grant, F.E. Arnold, et al., An organically modified zirconate film as a corrosion-resistant treatment for aluminum 2024-T3, *Org. Coat.* 41 (2001) 287–293.
- [89] Y. Zhang, H. Ye, H. Liu, K. Han, Preparation and characterisation of aluminium pigments coated with silica for corrosion protection, *Corros. Sci.* 53 (2011) 1694–1699. doi:10.1016/j.corsci.2011.01.027.
- [90] S. Hirai, K. Shimakage, S. Aizawa, K. Wada, Alkaline Corrosion Resistance of Anodized Aluminum Coated with Zirconium Oxide by a Sol–Gel Process, *J. Am. Ceram. Soc.* 81 (1998) 3087–3092.
- [91] A. Afseth, R&D Manager, Constellium, Private communication, (2014).

- 
- [92] Timet corporation, Report: Corrosion resistance of titanium, Denver, USA, 1997.
- [93] J.R. Davis, ASM Handbook, Volume 13: Corrosion, 9th ed., ASM International, Ohio, USA, 1989.
- [94] T.B. Massalski, J.L. Murray, L.H. Bennet, H. Baker, Binary phase diagrams vol. 1, 1st ed., ASM International, Ohio, USA, 1986.
- [95] J. Douin, A. Girard, M. Hantcherli, F. Pettinari-Sturm, Weak-beam study of dislocations in D022-Al<sub>3</sub>Ti deformed at 400°C, *Philos. Mag.* 93 (2013) 38–49. doi:10.1080/14786435.2012.712222.
- [96] C. Colinet, A. Pasturel, Ab initio calculation of the formation energies of L12, D022, D023 and one dimensional long period structures in TiAl<sub>3</sub> compound, *Intermetallics*. 10 (2002) 751–764.
- [97] K. Yamashita, I. Fujimoto, S. Kumai, A. Sato, Plastic deformation of D022 ordered Al<sub>3</sub>Ti in a centrifugally cast Al-Al<sub>3</sub>Ti composite, *Mater. Trans.* 39 (1998) 824–833.
- [98] J. Cissé, H.W. Kerr, G.F. Bolling, The nucleation and solidification of Al-Ti alloys, *Metall. Trans.* 5 (1974) 633–641. doi:10.1007/BF02644659.
- [99] I. Langmuir, Oscillations in ionized gases, *Proc. N. A. S.* 14 (1928) 627–637.
- [100] M. Ohring, Materials Science of Thin Films, Second Edition, Academic Press, San Diego, USA, 2001.
- [101] National Physical Laboratory, Ar Sputtering Yields at 0°, Accessed Oct. 9. 2013. (2005) resource.npl.co.uk/docs/science\_technology/.
- [102] G. Bräuer, B. Szyszka, M. Vergöhl, R. Bandorf, Magnetron sputtering – Milestones of 30 years, *Vacuum*. 84 (2010) 1354–1359. doi:10.1016/j.vacuum.2009.12.014.
- [103] P. Kelly, A. R.D., Magnetron sputtering: a review of recent developments and applications, *Vacuum*. 56 (2000) 159–172. doi:10.1016/S0042-207X(99)00189-X.
- [104] J.A. Thornton, Influence of substrate temperature and deposition rate on structure of thick sputtered Cu coatings, *J. Vac. Sci. Technol.* 12 (1975) 830–835.
- [105] R. Messier, Revised structure zone model for thin film physical structure, *J. Vac. Sci. Technol. A Vacuum, Surfaces, Film*. 2 (1984) 500. doi:10.1116/1.572604.
- [106] J.A. Thornton, The microstructure of sputter-deposited coatings, *J. Vac. Sci. Technol. A*. 4 (1986) 3059–3065. doi:10.1116/1.573628.
- [107] F. Sanchette, A. Billard, Main features of magnetron sputtered aluminium-transition metal alloy coatings, *Surf. Coat. Technol.* 142-144 (2001) 218–224.
- [108] J. Hampshire, P.J. Kelly, D.G. Teer, The structure of co-deposited aluminium–titanium alloy coatings, *Thin Solid Films*. 447-448 (2004) 418–424. doi:10.1016/j.tsf.2003.08.006.

- 
- [109] J. Hampshire, P.J. Kelly, D.G. Teer, The tribological properties of co-deposited aluminium – titanium alloy coatings, *Thin Solid Films*. 447-448 (2004) 392–398. doi:10.1016/S0040-6090.
- [110] J.C. Oliveira, A. Manaia, J.P. Dias, A. Cavaleiro, D. Teer, S. Taylor, Structure and mechanical properties of Ti–Al films deposited by magnetron sputtering, *Surf. Coat. Technol.* 200 (2005) 395–398. doi:10.1016/j.surfcoat.2005.01.078.
- [111] H. Tsuchiya, S. Berger, J.M. Macak, A. Ghicov, P. Schmuki, Self-organized porous and tubular oxide layers on TiAl alloys, *Electrochem. Commun.* 9 (2007) 2397–2402. doi:10.1016/j.elecom.2007.07.013.
- [112] S. Berger, H. Tsuchiya, P. Schmuki, Transition from nanopores to nanotubes : self-ordered anodic oxide structures on titanium-aluminides, *Chem. Mater.* 20 (2008) 3245–3247. doi:10.1016/j.cossms.2007.08.004.(22).
- [113] Q. Yan, H. Yoshioka, H. Habazaki, A. Kawashima, K. Asami, K. Hashimoto, Passivity and its breakdown on sputter-deposited amorphous Al-Ti alloys in a neutral aqueous solution with Cl<sup>-</sup>, *Corros. Sci.* 31 (1990) 401–406.
- [114] H. Yoshioka, Q. Yan, K. Asami, K. Hashimoto, Pitting potential and structure of sputter-deposited Al-Ti alloys, *Mater. Sci. Eng. A*. 134 (1991) 1054–1057.
- [115] K. Hashimoto, N. Kumagai, H. Yoshioka, J.H. Kim, E. Akiyama, H. Habazaki, et al., Corrosion-resistant amorphous surface alloys, *Corros. Sci.* 35 (1993) 363–370.
- [116] Q. Yan, H. Yoshioka, H. Habazaki, A. Kawashima, K. Asami, K. Hashimoto, The corrosion behavior of sputter-deposited Al-Ti alloys in 1 N HCl, *Corros. Sci.* 32 (1991) 327–335.
- [117] E. Akiyama, H. Habazaki, A. Kawashima, K. Asami, I.L. Hashimoto, K. Hashimoto, Corrosion-resistant amorphous aluminum alloys and structure of passive films, *Mater. Sci. Eng. A*. 226-228 (1997) 920–924.
- [118] H. Yoshioka, Q. Yan, H. Habazaki, A. Kawashima, K. Asami, K. Hashimoto, Passivity and its breakdown on sputter-deposited amorphous Al-early transition metal alloys in 1 M HCl at 30 °C, *Corros. Sci.* 31 (1990) 349–354.
- [119] K.G. Watkins, M.A. McMahon, W.M. Steen, Microstructure and corrosion properties of laser surface processed aluminium alloys: a review, *Mater. Sci. Eng. A*. 231 (1997) 55–61. doi:10.1016/S0921-5093(97)00034-8.
- [120] L. Pawlowski, Thick laser coatings: A review, *J. Therm. Spray Technol.* 8 (1999) 279–295.
- [121] P.L. Bonora, M. Bassoli, P.L. De Anna, G. Battaglin, G. Della Mea, P. Mazzoldi, et al., Electrochemical and corrosion behaviour of laser modified aluminium surfaces, *Electrochim. Acta*. 25 (1980) 1497–1499.
- [122] J.C. Ion, *Laser Processing of Engineering Materials: Principles, Procedure and Industrial Application*, Elsevier Butterworth-Heinemann, Oxford, UK, 2005.
- [123] U. de Oliveira, V. Ocelík, J.T.M. De Hosson, Analysis of coaxial laser cladding processing conditions, *Surf. Coat. Technol.* 197 (2005) 127–136. doi:10.1016/j.surfcoat.2004.06.029.

- 
- [124] M.D. da Silva, K. Partes, T. Seefeld, F. Vollertsen, Comparison of coaxial and off-axis nozzle configurations in one step process laser cladding on aluminum substrate, *J. Mater. Process. Technol.* 212 (2012) 2514–2519. doi:10.1016/j.jmatprotec.2012.06.011.
- [125] J.H. Abboud, R.D. Rawlings, D.R.F. West, Functionally gradient layers of Ti-Al based alloys produced by laser alloying and cladding, *Mater. Sci. Technol.* 10 (1994) 414–419.
- [126] J.H. Abboud, D.R.F. West, R.D. Rawlings, Functionally gradient titanium-aluminide composites produced by laser cladding, *J. Mater. Sci.* 29 (1994) 3393–3398. doi:10.1007/BF00352038.
- [127] B. Guo, J. Zhou, S. Zhang, H. Zhou, Y. Pu, J. Chen, Phase composition and tribological properties of Ti–Al coatings produced on pure Ti by laser cladding, *Appl. Surf. Sci.* 253 (2007) 9301–9310. doi:10.1016/j.apsusc.2007.05.056.
- [128] I. García, J. de la Fuente, J.J. de Damborenea, J. De Fuente, J.J. De Damborenea, (Ti,Al)/(Ti,Al)N coatings produced by laser surface alloying, *Mater. Lett.* 53 (2002) 44–51.
- [129] U. Wendt, S. Settegast, I.U. Grodrian, Laser alloying of aluminum with titanium wire, *J. Mater. Sci. Lett.* 22 (2003) 1319–1322.
- [130] L.A.B. Mabhali, S.L. Pityana, N. Sacks, Laser Surface Alloying of Aluminium AA1200, *Mol. Cryst. Liq. Cryst.* 555 (2012) 138–148. doi:10.1080/15421406.2012.635095.
- [131] J. Xu, W. Liu, Y. Kan, M. Zhong, Microstructure and wear properties of laser cladding Ti–Al–Fe–B coatings on AA2024 aluminum alloy, *Mater. Des.* 27 (2006) 405–410. doi:10.1016/j.matdes.2004.11.011.
- [132] A. Almeida, M. Anjos, R. Vilar, R. Li, M.G.S. Ferreira, W.M. Steen, et al., Laser alloying of aluminium alloys with chromium, *Surf. Coat. Technol.* 70 (1995) 221–229. doi:10.1016/0257-8972(94)02263-P.
- [133] M.G.S. Ferreira, R. Li, R. Vilar, Avoiding crevice corrosion by laser surface treatment, *Corros. Sci.* 38 (1996) 2091–2094.
- [134] R. Li, M.G.S. Ferreira, A. Almeida, R. Vilar, K.G. Watkins, M.A. McMahon, et al., Localized corrosion of laser surface melted 2024-T351 aluminium alloy, *Surf. Coat. Technol.* 81 (1996) 290–296.
- [135] E. McCafferty, P.G. Moore, G.T. Peace, Effect of laser-surface melting on the electrochemical behavior of an Al-1% Mn alloy, *J. Electrochem. Soc.* 129 (1982) 9–17. doi:10.1149/1.2123801.
- [136] K.G. Watkins, Z. Liu, M. McMahon, R. Vilar, M.G.S. Ferreira, Influence of the overlapped area on the corrosion behaviour of laser treated aluminium alloys, *Mater. Sci. Eng. A.* 252 (1998) 292–300. doi:10.1016/S0921-5093(97)00695-3.
- [137] S. Ocylok, A. Weisheit, I. Kelbassa, Increased wear and oxidation resistance of titanium aluminide alloys by laser cladding, *Adv. Mater. Res.* 278 (2011) 515–520. doi:10.4028/www.scientific.net/AMR.278.515.

- [138] T.M. Yue, K.J. Huang, H.C. Man, In-situ laser cladding of Al<sub>2</sub>O<sub>3</sub> reaction coating on aluminium alloy 7075 for corrosion resistance improvement, *Mater. Trans.* 47 (2006) 948–951.
- [139] SOCABIM, Software: EVA Application 6.0.0.1, (2000).
- [140] Image Metrology A/S, Software: SPIP 6.1.1, (2013).
- [141] M. Nonnenmacher, M.P. O’Boyle, H.K. Wickramasinghe, Kelvin probe force microscopy, *Appl. Phys. Lett.* 58 (1991) 2921–2923. doi:10.1063/1.105227.
- [142] Bruker, Software: Nanoscope v8.15, (2012).
- [143] Image Metrology A/S, Software: SPIP 6.0.4, (2012).
- [144] JISC Digital Media, Colour Theory: Understanding and Modelling Colour, Accessed Dec. 20. (2013) [jiscdigitalmedia.ac.uk/guides/a-z](http://jiscdigitalmedia.ac.uk/guides/a-z).
- [145] S.M. Luke, P. Vukusic, B. Hallam, Measuring and modelling optical scattering and the colour quality of white pierid butterfly scales., *Opt. Express.* 17 (2009) 14729–43.
- [146] P. Dutre, P. Bekaert, K. Bala, Advanced global illumination, 2nd Ed., A K Peters/CRC Press, Wellesley, USA, 2006.
- [147] R. Ambat, P. Møller, Corrosion investigation of material combinations in a mobile phone dome–key pad system, *Corros. Sci.* 49 (2007) 2866–2879. doi:10.1016/j.corsci.2006.12.013.
- [148] M. Jariyaboon, A.J. Davenport, R. Ambat, B.J. Connolly, S.W. Williams, D.A. Price, The effect of welding parameters on the corrosion behaviour of friction stir welded AA2024–T351, *Corros. Sci.* 49 (2007) 877–909. doi:10.1016/j.corsci.2006.05.038.





**DTU Mechanical Engineering**  
**Section of Materials and Surface Engineering**  
Technical University of Denmark

Produktionstorvet, Bld. 425  
DK- 2800 Kgs. Lyngby  
Denmark  
Phone (+45) 4525 2205  
Fax (+45) 4593 6213  
[www.mek.dtu.dk](http://www.mek.dtu.dk)  
ISBN: 978-87-7475-406-0